STUDIES ON SYNTHESIS OF PULLULAN AND ITS APPLICATION IN BIOMEDICAL ENGINEERING, COSMETICS AND FOOD PACKAGING

Thesis submitted in partial fulfilment of the requirements for the degree of

DOCTOR OF PHILOSOPHY

by

KUHELIKA DAS

(Roll No: 206106011)

Department of Biosciences & Bioengineering

Indian Institute of Technology Guwahati

Guwahati – 781039, Assam, India

(February 2026)

TH-3900_206106011

भारतीय प्रौद्योगिकी संस्थान गुवाहाटी
Indian Institute of Technology Guwahati

Dedication

This thesis is dedicated to my beloved Lord Laddu Gopal ji, Maa Kamakkhya devi, and my parents for their unconditional love, blessings, encouragement and support.

Kuhelika Das

भारतीय प्रौद्योगिकी संस्थान गुवाहाटी
Indian Institute of Technology Guwahati

Department of Biosciences and Bioengineering

Indian Institute of Technology Guwahati

CERTIFICATE

This is to certify that the research work in the thesis entitled "**Studies on synthesis of pullulan and its application in biomedical engineering, cosmetics and food packaging**", is carried out by me at the Department of Biosciences and Bioengineering and Centre for Sustainable Polymers, Indian Institute of Technology Guwahati, as partial fulfilment for the award of Doctor of Philosophy under the supervision of Dr. Vimal Katiyar, Professor at Department of Chemical Engineering and Centre for Sustainable Polymers, Indian Institute of Technology Guwahati, Assam, India. The research outcomes documented in this thesis are accomplished by me and has not been submitted to any other Institute or University for the award of any degree or diploma.

Kuhelika Das

(**Kuhelika Das**)

Roll No.: 206106011

Department of Biosciences and Bioengineering

Indian Institute of Technology Guwahati

Guwahati - 781039, Assam, India

Department of Chemical Engineering

Indian Institute of Technology Guwahati

CERTIFICATE

This is to certify that the thesis entitled "**Studies on synthesis of pullulan and its application in biomedical engineering, cosmetics and food packaging**", being submitted by Ms. Kuhelika Das (Roll No.: 206106011), a student of Department of Biosciences and Bioengineering, Indian Institute of Technology Guwahati, as partial fulfilment for the award of Ph.D. under my guidance and supervision. The research work documented in this thesis has not been submitted to any other University or Institute for the award of any degree or diploma.

Prof. Vimal Katiyar

Department of Chemical Engineering & Centre for Sustainable Polymers

Indian Institute of Technology Guwahati

Guwahati - 781039, Assam, India

ACKNOWLEDGEMENT

I am profoundly grateful to my doctoral advisor, Prof. Vimal Katiyar, whose constant support, generosity, and invaluable guidance have kept me motivated throughout this journey. I am also deeply thankful to my Doctoral Committee members, Prof. Priyadarshi Satpati, Prof. Sachin Kumar, and Prof. Rajkumar Paroshottambhai Thummer, for their critical feedback and valuable perspectives, which significantly enhanced the scientific rigour of my study. Furthermore, I also extend my heartfelt appreciation to Prof. Shinichi Sakurai, Prof. Huaizhong Xu and Mr. Jincheng Gu for the knowledge and insights that I have gained under their mentorship and for their immense support during my Student-Exchange program at Kyoto Institute of Technology, Japan.

I acknowledge with gratitude the facilities and support provided by the Department of Biosciences and Bioengineering, the Centre for Sustainable Polymers (Centre of Excellence-Sustainable Polymers, CoE-SusPol), the Department of Chemical Engineering, and the Central Instruments Facility (CIF), IIT Guwahati. My sincere thanks also go to Prof. Sanjay K Banerjee, NIPER Guwahati, for providing me the opportunity to carry out the cytocompatibility analyses with his team, Mr. Vikas Tiwari and Mr. Shriram Mahajan.

The assistance of my labmates at IITG-SusPol laboratory have been invaluable in this achievement. I extend my deepest appreciation to Ms. Shikha Sharma, Mr. Sonu Kumar, Mr. Vikrant Bodana, Dr. Bhanupriya Das, Dr. Tabli Ghosh, Dr. Sayan Bhattacharjee, and many others for their continuous motivation and support.

Everything I have achieved and all that I am is rooted in the love and sacrifices of my parents. My father, Dr. Kiron Sankar Das, and my mother, Dr. Lipika Saha (Das), being my greatest strength, kept motivating me to strive for goals beyond my imagination.

Above all, my ultimate gratitude is dedicated to my Lord Laddu Gopal ji and Maa Kamakhya devi—whose blessings have never abandoned me, shielding me through the challenges of life.

ABSTRACT

This thesis explores the microbial production of pullulan and its applications in biomedical, cosmetic, and food-packaging sectors. Pullulan, an extracellular polysaccharide synthesized by *Aureobasidium pullulans* (*A. pullulans*), has gained attention as a sustainable alternative to synthetic polymers due to its biodegradability, biocompatibility, water solubility, and film-forming property. The research was driven by the increasing need for environmentally safe and biologically compatible materials that can be used in various industrial and healthcare applications. Pullulan production was optimized by shake-flask fermentation of *A. pullulans* NCIM 1049 using liquid sugarcane jaggery as a cost-effective carbon source. A systematic study of media components including jaggery, yeast extract, NaCl, K_2HPO_4, $(NH_4)_2SO_4$, $MgSO_4.7H_2O$, and $ZnSO_4.5H_2O$, was performed using Plackett-Burman Design (PBD), which enabled the identification of significant factors influencing pullulan production. These significant factors were further optimized using Box–Behnken Design (BBD). The predicted pullulan production (5.106 g/L) under optimized conditions (jaggery = 49.09 g/L, yeast extract = 2.15 g/L, NaCl = 1.28 g/L) closely matched the experimentally observed production (4.923 ± 0.14 g/L), demonstrating the reliability of the statistical model. The produced pullulan was extracted and purified using ethanol precipitation, dialysis, and lyophilization. Structural characterization by Fourier Transform Infrared (FTIR) spectroscopy, Proton Nuclear Magnetic Resonance (^{1}H NMR), Carbon Nuclear Magnetic Resonance (^{13}C NMR), and Matrix-Assisted Laser Desorption Ionization-Time of Flight Mass Spectrometry (MALDI-TOF MS) confirmed its structural similarity to commercial pullulan. Beyond synthesis, the study explored the applications of pullulan in biomedical engineering, cosmetics, and food-packaging. A bilayered wound healing scaffold was prepared by combining an electrospun hydrophilic sublayer of pullulan/polyvinyl alcohol (PVA)/gum arabic containing gentamicin sulfate with a solvent-casted polylactic acid (PLA) top layer. This design addressed key challenges associated with traditional single-layered wound dressings, offering controlled gentamicin release and high swelling capacity for exudate absorption. The scaffold demonstrated antibacterial efficacy against *Staphylococcus aureus* (*S. aureus*) and *Escherichia coli* (*E. coli*), and drug release studies showed that 93.09 ± 2.63 % of gentamicin sulfate was released in a controlled manner over 48 hrs following Zero-Order kinetics (R^2 = 0.9850). It exhibited a high swelling index of 611.85 ± 15.05 %, a water vapour transmission rate (WVTR) of 94.20 ± 14.50 g/m²/day, and porosity of 70.56 ± 0.58 %, along with biocompatibility with human dermal fibroblasts, all of which are essential for accelerated healing. In another application-based study, coaxially

electro-centrifugally spun core/sheath nanofibers composed of pullulan and poly(lactic-co-glycolic acid) (PLGA) were fabricated to co-deliver ciprofloxacin (CIP) and paclitaxel (PTX). These nanofibers exhibited tunable release kinetics characterized by an initial burst release within 6 hrs followed by sustained drug delivery. They demonstrated significant *in vitro* cytotoxic effects against melanoma A375 cells, highlighting their suitability as a dual drug delivery system. The dual drug-loaded nanofibers with core-to-sheath ratios of 23G/1mm and 21G/1mm showed melanoma cell viabilities of 65.37 ± 1.96 % and 67.82 ± 1.31 %, respectively, after 72 hrs, highlighting their potential as dual drug delivery systems with tunable release properties. The functional properties of pullulan were also used in the preparation of an antibacterial skin-cream, where its film-forming ability and moisture retention were combined with the antimicrobial activity of turkey berry (*Solanum torvum, S. torvum*) leaf extract. The leaf extract exhibited antibacterial activity with zones of inhibition of 11.51 ± 0.92 mm against *S. aureus* and 10.45 ± 0.50 mm against *E. coli*, while the cream formulation showed enhanced zones of inhibition of 16.67 ± 0.40 mm and 14.83 ± 0.12 mm against *S. aureus* and *E. coli*, respectively. The formulation demonstrated good thermal stability with a pH of 6.10 ± 0.20, total fatty matter (TFM) of 8.5 %, moisture content of 65 %, shear-thinning behaviour, and absence of heavy metals, arsenic, and microbial contamination, all within acceptable limits for topical application. Additionally, active edible biocomposites were prepared using pullulan and gum arabic, functionalized with chitosan nanoparticles (NCS) and neem essential oil (NEO). The incorporation of NCS and NEO addressed the inherent high hydrophilicity and poor barrier properties of pullulan-based films. Among the formulations investigated, the PUL/GA/NCS3/NEO film (containing 3 % NCS and 1 % NEO) exhibited the most significant improvements in properties, with surface hydrophobicity increasing from a water contact angle of 55.49 ± 2.31° to 115.01 ± 1.86°. It also enhanced their tensile strength by ~ 12.77 MPa, elongation at break by ~ 6.26 %, barrier performance by ~ 45.95 %, while imparting antimicrobial, antioxidant, and UV-shielding properties. It was further applied as an edible coating for fresh-cut guava preservation, where it maintained quality attributes and extended shelf life under both ambient and refrigerated conditions.

CONTENTS

LIST OF FIGURES

LIST OF TABLES

ABBREVIATIONS

WHO-	World Health Organization
FDA-	Food and Drug Administration
GRAS-	Generally Recognized as Safe
PVC-	Polyvinyl chloride
DMSO-	Dimethyl Sulfoxide
DMF-	Dimethylformamide
UDPG-	Uridine 5′-diphosphate glucose
ATP-	Adenosine triphosphate
ADPG-	Adenosine diphosphate glucose
LPh-	Phospholipid intermediate
BNC-	Bacterial nanocellulose
A-g-BNC-	Aminoalkylsilane grafted BNC
TAMs-	Tumor-associated macrophages
CHP-	Cholesteryl pullulan
PE-	Pseudomonas Exotoxin A
TME-	Tumour microenvironment
BPPNPs-	Berberine-loaded 4-carboxyphenyl boronic acid-modified pullulan-stearic acid conjugate nanoparticles
GO-	Graphene oxide
CHPNH$_2$-	Amine-functionalized cholesteryl pullulan
NIR-PNG-	Near-infrared polymer nanogels
CAB-	Carbonic Anhydrase B
PEO-	Polyethylene oxide
MRI-	Magnetic Resonance Imaging
P-g-pAPTAC-	Pullulan-graft-poly(3-acrylamidopropyl trimethylammonium chloride)
ECH-	Epichlorohydrin
BEPE-	1,2-bis(2,3-epoxypropoxy)-ethane

TGDE-	Tetramethylene glycol diglycidyl ether
Gel-T-	TGDE-derived gel
STMP-	Trisodium trimetaphosphate
DOX-	Doxorubicin
MRSA-	Methicillin-resistant *Staphylococcus aureus*
PEIP-	Polyethylenimine pullulan
MSCs-	Mesenchymal stem cells
HGF-	Hepatocyte growth factor
ECFCs-	Endothelial colony-forming cells
CMV-TK-	Cytomegalovirus thymidine kinase
MERS-CoV-	Middle East respiratory syndrome coronavirus
PEI-	Polyethyleneimine
DEAEM-	Diethyl aminoethyl methacrylate
HUVECs-	Human umbilical vein endothelial cells
PHBV-	Poly (3-hydroxybutyrate-co-3-hydroxyvalerate)
PHMB-	Polyhexamethylene biguanide
Pul-PEI-	Pullulan-polyethyleneimine
Pul-TAEA-	Pullulan-tris(2-aminoethyl)amine
SPECT-	Single-photon emission computed tomography
QDs-	Quantum dots
CQDs-	Carbon quantum dots
DTPA-	Diethylene triamine pentaacetate
MMT-	Montmorillonite
NCL-	National Chemical Laboratory
OFAT-	One Factor At a Time
PBD-	Plackett Burman Design
RSM-	Response Surface Methodology
CCD-	Central Composite Design
BBD-	Box-Behnken Design
ANOVA-	Analysis of Variance
FTIR-	Fourier Transform Infrared Spectroscopy
^{13}C NMR-	Carbon Nuclear Magnetic Resonance
^{1}H NMR-	Proton Nuclear Magnetic Resonance

MALDI-TOF MS-	Matrix-Assisted Laser Desorption Ionization–Time of Flight Mass Spectrometry
DP-	Degree of polymerization
PVA-	Polyvinyl alcohol
PLA-	Polylactic acid
ECM-	Extracellular matrix
FESEM-	Field Emission Scanning Electron Microscope
EDX-	Energy-Dispersive X-ray
MTT-	3-(4,5-dimethylthiazol-2-yl)-2,5-diphenyltetrazolium bromide
DMEM-	Dulbecco's Modified Eagle's Medium
PBS-	Phosphate-buffered saline
HDF-	Human dermal fibroblasts
RBC-	Red blood cells
ATCC-	American Type Culture Collection
SD-	Standard deviation
CFU-	Colony-forming units
WVTR-	Water vapour transmission rate
WVP-	Water vapour permeability
LDPE-	Low density polyethylene
CDR-	Cumulative drug release
ECS-	Electro-centrifugal spinning
PLGA-	Poly(lactic-co-glycolic acid)
CIP-	Ciprofloxacin
PTX-	Paclitaxel
HPLC-	High Performance Liquid Chromatography
GPC-	Gas Permeation Chromatography
SCDA-	Soybean Casein Digest Agar
MSA-	Mannitol Salt Agar
BHIA-	Brain Heart Infusion Agar
TBLE-	Turkey berry leaf extract
TFM-	Total fatty matter
LVR-	Linear Viscoelastic Region
PUL-	Pullulan

GA-	Gum Arabic
CS-	Chitosan
NCS-	Chitosan nanoparticles
NEO-	Neem essential oil
STPP-	Sodium tripolyphosphate
LB-	Luria-Bertani
PDA-	Potato Dextrose Agar
PDB-	Potato Dextrose Broth
DRBC-	Dichloran Rose Bengal Chloramphenicol
DPPH-	2,2-diphenyl-1-picrylhydrazyl
ABTS-	2,2′-azino-bis (3-ethylbenzothiazoline-6-sulfonic acid)
HEK-	Human embryonic kidney
FETEM-	Field Emission Transmission Electron Microscope
UTM-	Universal Testing Machine
XRD-	X-Ray Diffractometer
TGA-	Thermogravimetric Analyzer
UV-	Ultra-Violet
TVC-	Total viable count
YMC-	Yeast and mold count

CHAPTER 1

INTRODUCTION AND LITERATURE REVIEW

This chapter explains the background and purpose of the study by focusing on the growing interest in natural materials that are safe to use and better for the environment. Pullulan, an exopolysaccharide produced by the fungus Aureobasidium pullulans (A. pullulans), is one such material. It has gained attention for being non-toxic, water-soluble, and able to form transparent, flexible films. These attributes make it useful in several biomedical, skincare, and food packaging applications. The chapter also looks at how pullulan is produced through fermentation and how the fermentation media components affect its production. In addition, it reviews how pullulan can be blended with other natural substances to improve its mechanical and water vapour barrier properties, or incorporation of antibacterial activity. Although pullulan has been studied before, there is still a need to make its production more cost-effective and to better understand how it can be used in versatile applications. This chapter reviews earlier studies to identify these gaps and explains how this research builds on that knowledge to explore new uses for pullulan.

The work in this chapter is under preparation of a review article titled as **"*Pullulan: A Comprehensive Review on its Production and Multifaceted Applications*"**.

1.1 Introduction

Proper waste management continues to be a significant challenge in both rural and urban areas of many developing countries, such as India. One potential solution is the bioconversion of these wastes, which not only mitigates environmental pollution but also offers economic benefits, such as the microbial synthesis of valuable products like enzymes, organic acids, and animal feed [1]. Plastics, widely utilized in daily life for packaging and manufacturing, have contributed significantly to environmental degradation due to their excessive use. This has led to growing global concern and interest in identifying sustainable alternatives to conventional plastic materials [2]. With increasing interest in environmentally friendly materials, bio-based polymers or biopolymers have gained interest as alternatives to petroleum-derived plastics. Biopolymers are naturally occurring polymers synthesized by microorganisms, plants, and animals. These macromolecules include polysaccharides, proteins, and nucleic acids, each with distinct structural and functional properties [3]. Due to their biodegradability, renewability, and biocompatibility, biopolymers have gained significant attention in several industrial sectors, including food packaging, agriculture, pharmaceuticals, and cosmetics. Their diverse physical and chemical properties allow them to serve as emulsifiers that stabilize mixtures of immiscible liquids, thickening agents that enhance viscosity, and binders that improve cohesion in formulations. They also function as suspending agents, stabilizers, lubricants, coagulants, film formers, and gelling agents, contributing to improved sustainability and product performance. Furthermore, the development of polymeric composites or blends has led to significant technological advancements. Polymer blends are created by physically combining two or more polymers, resulting in materials with improved thermal, mechanical, and other functional properties compared to the individual components. These blends can enhance durability, strength, flexibility, and other desirable characteristics, making them highly valuable in applications ranging from biomedical devices to packaging materials. The integration of biopolymers into polymeric blends further enhances their performance, offering sustainable alternatives to conventional synthetic polymers [4,5].

Microbial polymers are among the most promising alternatives to both synthetic and other biopolymers due to their sustainability, eco-friendliness, and ease of production. Various microorganisms are capable of synthesizing structurally diverse polymers, including polyesters, proteins, and polysaccharides [6]. These polymers can be classified into structural, intracellular and extracellular based on their localization within the microbial cell during production. Typically integrated within the cell wall, structural polysaccharides like cellulose and chitin are synthesized by both plants and animals. Cellulose, made of β-linked glucose

units, is plant-derived, while chitin is found in animals. These biodegradable materials are suitable for applications in pharmaceuticals, food, and biomedical devices. Intracellular polymers, or endopolysaccharides, are primarily polyesters that accumulate as granules within the microbial cytoplasm, serving as energy reserves. Located near or within the cytoplasmic membrane, they may also form complex matrices with lipids, proteins, polysaccharides, and nucleic acids. Their elastic-like properties, along with functional versatility, make them valuable in health, food, and medical applications [7]. In contrast, extracellular carbohydrate polymers or exopolysaccharides are secreted onto the outer surface of microbial cells, forming a loose slime layer. They are high molecular-weight polymers, produced by lactic acid bacteria such as *Leuconostoc*, *Lactobacillus*, and *Streptococcus*, and are utilized in food and pharmaceutical industries. These extracellular polymers are typically long-chain polysaccharides, which can be either homopolysaccharides or heteropolysaccharides, composed of repeating sugar units in varying ratios. The World Health Organization (WHO) classified probiotic exopolysaccharides as Generally Recognized as Safe (GRAS), indicating that they are safe for human consumption [8]. Exopolysaccharides can be classified as cationic, anionic, or neutral based on their ionic properties. They include pullulan, dextran, xanthan, gellan, alginate, bacterial cellulose, and others, many of which exhibit strong water retention and film-forming abilities [9,10]. Pullulan is a neutral exopolysaccharide with distinct characteristics that make it valuable for diverse applications. It is a water-soluble and biodegradable bipolymer produced extracellularly by the fungus *Aureobasidium pullulans* (*A. pullulans*) [11,12]. Pullulan was first reported in 1884, when it was described as a polysaccharide produced by microorganism initially referred to as *Dematium pullulans* by De Bary [13,14]. However, in the year 1958, Bernier successfully isolated the polysaccharide from *A. pullulans*, marking the first documented extraction of pullulan. The following year, further research led to its official naming as "pullulan" [15,16].

1.2 Occurrence, classification, and morphology of A. pullulans

A. pullulans is a widely distributed, polymorphic fungus isolated from diverse environments including soil, water, decaying plant material, etc. It is particularly known for colonizing early stages of organic decomposition, such as leaf litter and wood, and has also been implicated in the biodeterioration of materials like plasticized polyvinyl chloride (PVC) [17]. As a saprophyte, the fungus produces various extracellular enzymes including amylases, pectinases, xylanases, and hemicellulases [18,19]. According to the classification proposed by DeHoog and McGinnis (1987), *A. pullulans* is categorized under Kingdom Fungi, Phylum Ascomycota,

Class Dothideomycetes, Order Dothidiales, Family Dothididaceae, Genus *Aureobasidium* and Species *pullulans.* Earlier classifications placed it under the family Moniliaceae within the group of fungi imperfecti [20]. Although no perfect sexual stage has been observed, more recent literature places it firmly among the Ascomycetes, particularly within the Dothididaceae family. It exhibits five major morphological forms throughout its life cycle, namely yeast-like cells, young and swollen blastospores, chlamydospores, and mycelia. As colonies mature, they shift from a moist, smooth, and pale yeast-like appearance to darker shades of brown or black, often accompanied by filamentous, pigmented mycelia, slimy conidial masses, and septate hyphae. A distinctive feature of *A. pullulans* is its dimorphism, that enable transitions between budding yeast and filamentous forms in response to environmental conditions, with thick-walled chlamydospores indicating developmental stages [21].

1.3 Structure

The chemical composition of pullulan was fully explained in the 1960s, revealing it to be a linear α-D-glucan primarily composed of repeating units of maltotriose. These units are linked through α(1→6) glycosidic linkages, while the internal structure of each maltotriose consists of α(1→4) bonds.

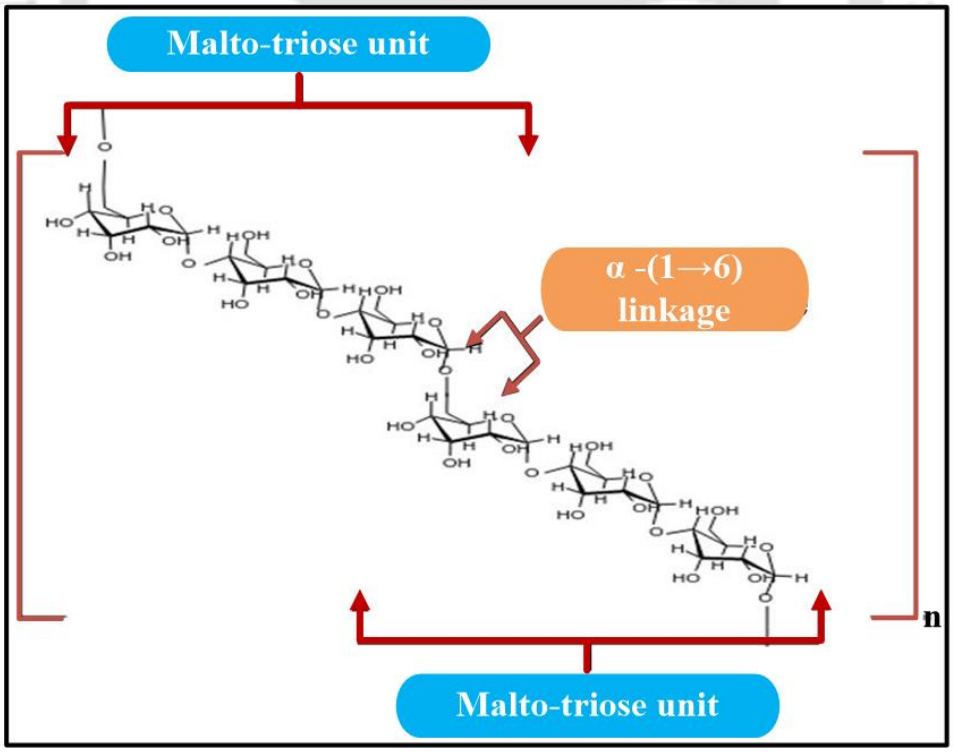

Figure 1.1 Structure of pullulan.

This alternating arrangement of α(1→4) and α(1→6) linkages imparts two significant properties to pullulan: enhanced solubility and structural flexibility. The molecular weight of pullulan varies between $4.5 \times 10^4 - 6 \times 10^5$ Da, and its general molecular formula is $(C_6H_{10}O_5)_n$ [22]. These structural attributes contribute to its diverse functional properties, making it useful in fields such as food packaging, pharmaceuticals, and other industrial sectors. The chemical structure of pullulan is illustrated in Figure 1.1. Despite being water soluble, it is insoluble in inorganic solvents, except for dimethyl sulfoxide (DMSO) and dimethylformamide (DMF). Pullulan has the capability to form highly viscous solutions, making it suitable for creating oxygen-impermeable films and fibers, as well as serve as thickening agents, adhesives, extenders, or encapsulating agents. Despite being an α-D-glucan, it resists α-D-amylolysis and can be used in the preparation of low-calorie food formulations [23]. A schematic representation of the overview of pullulan production and its different applications is shown in Figure 1.2.

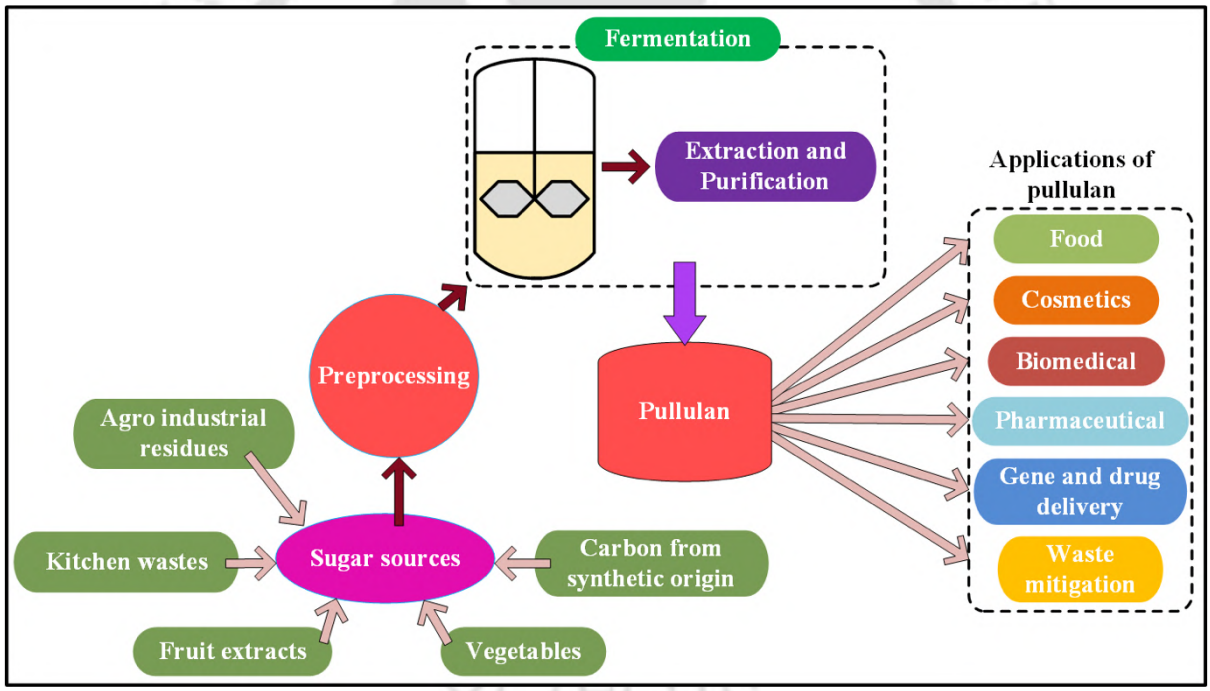

Figure 1.2 Overview of pullulan production by fermentation and its utilization in various applications.

1.4 Biosynthetic pathway for pullulan production

A. pullulans, being a polymorphic and metabolically versatile fungus, has been extensively studied for its unique cytological and physiological attributes. Despite significant research, the exact biosynthetic pathway of pullulan remains only partially understood. A variety of carbon sources, including glucose, galactose, fructose, sucrose, xylose, maltose, and

agricultural residues, are utilized as initial raw materials for pullulan production [16]. When agro-wastes are used as carbon source, they are first hydrolyzed into simple sugars by a multi-enzyme system comprising protease, amylase, xylanase, laccase and, cellulose [24]. Earlier studies demonstrated that pullulan can be synthesized from simple sugars such as sucrose using acetone-dried cells of *A. pullulans*, indicating that the biosynthetic machinery can function even in non-viable yet enzymatically active cells. Moreover, the cell-free enzymes of *A. pullulans* are capable of producing pullulan from sucrose in the presence of uridine diphosphoglucose (also known as uridine 5′-diphosphate glucose or UDPG) pyrophosphorylase and adenosine triphosphate (ATP) [22,25]. Inside the cell, saccharide molecules are stored, and glucose residues are converted into exopolysaccharides. These sugars accumulate within the cells and are subsequently utilized for pullulan synthesis during microbial growth and proliferation [26]. A schematic overview of the biosynthetic pathway of pullulan is presented in Figure 1.3.

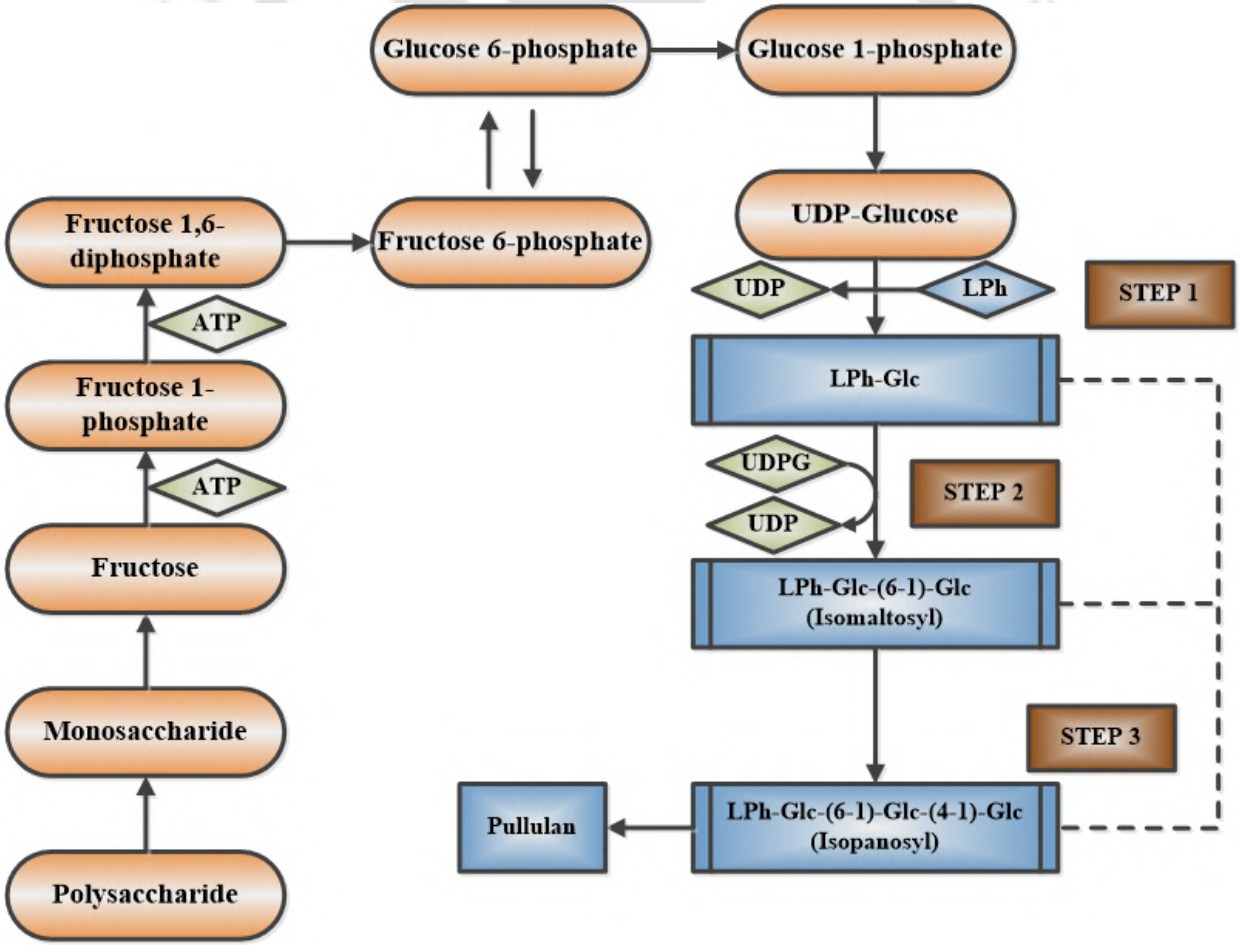

Figure 1.3 Biosynthetic pathway of pullulan.

At the biochemical level, glucose undergoes a series of transformations to yield the key precursor UDPG. Glucose is first isomerized into fructose, which is then phosphorylated by ATP to form fructose-1-phosphate. Subsequent phosphorylation and isomerization steps generate glucose-6-phosphate, which is converted to glucose-1-phosphate by α-phosphoglucose mutase. UDPG pyrophosphorylase then catalyzes the synthesis of UDPG from glucose-1-phosphate. More detailed biochemical investigations revealed that UDPG serves as a crucial glucose donor in the biosynthesis of pullulan [27,28], and adenosine diphosphate glucose (ADPG), another common glucose donor in microbial systems, cannot substitute for UDPG in this process. Furthermore, glucose-containing lipid intermediates (LPh-Glc) may play a crucial role in the biosynthesis and export of pullulan [29]. The biosynthetic process can be conceptually divided into two primary stages. In the first stage, a D-glucose residue from UDPG is transferred to a lipid molecule via a phosphoester linkage, resulting in the formation of lipid-linked glucose (LPh-Glc), and this step is catalyzed by specific glycosyltransferases. In the second stage, additional glucose residues are sequentially transferred from UDPG to form lipid-bound isomaltose. This disaccharide unit subsequently reacts with other lipid-linked glucose intermediates to yield pyranosyl or isopanosyl structures, which are polymerized into longer chains to produce pullulan. Importantly, isopanose, a trisaccharide consisting of two α(1→6) and one α(1→4) linked glucose residues, is identified as a key intermediate in this biosynthetic sequence. The formation of isopanose appears to require both glucose conjugates and a lipid-phospholipid (LPh) carrier system, further emphasizing the lipid-mediated nature of this process. This multi-step, enzyme-catalyzed, and lipid-facilitated pathway highlights the complex biochemical nature of pullulan production by *A. pullulans*. An increase in the activities of phosphoglucose mutase and UDPG-pyrophosphorylase has been associated with improved pullulan production [16,27]. The proposed mechanism has been summarized schematically in Figure 1.3, illustrating the key intermediates and steps involved in this complex biosynthetic network.

1.5 Production of pullulan

Pullulan production is often limited by the high cost of refined carbon and nitrogen sources required for microbial fermentation, which limits its large-scale commercialization. To address this, several studies have explored low-cost alternatives such as molasses, starch hydrolysates, fruit processing wastes, and agro-industrial residues, as these substrates contain fermentable sugars and nutrients that can support microbial growth. The use of such materials not only reduces production costs but also offers an eco-friendly approach to resource utilization.

However, their effectiveness depends on factors such as nutrient availability, composition consistency, and the requirement for pre-processing in some cases. Simpler sugar-rich feedstocks, such as jaggery, can also serve as efficient substrates without the need for extensive processing, offering a balance between cost-effectiveness and ease of use. Overall, the selection of substrate plays a crucial role in determining the cost-effectiveness of pullulan production.

Widyastuti et al. [30] reported the optimisation of pullulan production by *A. pullulans* Y428 using Melinjo seeds (*Gnetum gnemon*) as the substrate. The prepared pulluan was characterised as a glucose-fructose trisaccharide (~ 2.3×10^4 Da) with semi-crystalline structure, smooth layered morphology, and high thermal stability (~ 219 °C). Tagne et al. [31] explored the production of pullulan using sugarcane bagasse hemicellulosic hydrolysate in a bubble column reactor with *A. pullulans* ATCC 42023. The process yielded up to 28.62 ± 1.43 g/L of pullulan after 120 hrs. Mujdeci et al. [32] reported the optimisation of pullulan production by *A. pullulans* AZ-6 using Response Surface Methodology (RSM) in a defined synthetic medium. Under the optimal conditions (100 g/L sucrose, 11.31 g/L peptone, pH 6.48, and 24.2 °C), the strain achieved pullulan concentration of ~ 35.47 g/L with 54.48 % yield. Dsouza et al. [33] reported an iterative statistical optimization strategy for pullulan production by *A. pullulans* DSM 3042. Using One Factor At a Time (OFAT), Plackett-Burman Design (PBD), and RSM, sucrose was identified as the optimal carbon source, with pH 6 and 4 days incubation as favourable conditions. The process increased pullulan yield 6.34-fold, achieving 113.5 ± 3.5 g/L in shake-flask culture, representing the highest reported titer for this strain, and highlighting its industrial potential. Chen et al. [34] reported the isolation of a high-yielding pullulan-producing strain, RM1603, from rhizosphere soil, identified as *A. pullulans* through morphological and phylogenetic analysis. The strain produced 33.07 ± 1.03 g/L pullulan in shake flasks, which increased to 62.52 ± 0.24 g/L in a 5-L fermenter under optimized conditions (pH 6.5, 2 vvm aeration, 600 rpm, 2 % inoculum). Chen et al. [35] identified and engineered a novel strain, *A. pullulans* BL06, capable of high molecular weight (M_w = 3.3 × 10^6 Da) pullulan production, and developed a modified strain (BL06ΔPMAs) that produces moderate molecular weight (M_w = 1.3 × 10^5 Da) pullulan with significantly higher yield (140.2 g/L) compared to the wild strain (83.4 g/L). By manipulation of key genes involved in synthesis pathway, the researchers demonstrated precise control over M_w and purity of pullulan. Ganduri et al. [36] reported the statistical optimization of pullulan production by *A. pullulans* MTCC 2195 using jaggery as a carbon source. The Central Composite Design (CCD) model of RSM demonstrated that fermentation time had the most significant effect compared to initial pH, and

interaction plots highlighted the impact of parameters. Under the optimized fermentation conditions (50 g/L jaggery, initial pH 5.0, and 120 hrs), a maximum pullulan concentration of 15.589 g/L was achieved. Vijayendra et al. [37] reported pullulan production by a locally isolated strain *A. pullulans* CFR-77 using jaggery as the sole carbon source in batch fermentation. A maximum pullulan concentration of 51.90 g/L was obtained within 72 hrs at 5 % jaggery, which also yielded pigment-free, highly viscous polymer (160.50 cP, compared to 32.00 cP with sucrose). Table 1.1 shows an overview of different studies using various substrates and microbial strains for pullulan production.

Table 1.1 Different substrates and microbial strains used in pullulan production.

Substrates	**Microorganism**	**Fermentation parameters**				**Pullulan production**	**References**
		t (h)	**T (ºC)**	**pH**	**Agitation speed (rpm)**		
Melinjo seeds	*A. pullulans* Y428	120	25	7	-	0.42 g/L	[30]
Sugarcane bagasse hemicellulosic hydrolysate	*A. pullulans* ATCC 42023	120	26	5.50	200	28.62 ± 1.43 g/L	[31]
Sucrose	*A. pullulans* AZ-6	-	24.2	6.48	-	35.37 g/L	[32]
Sucrose	*A. pullulans* DSM 3042	96	28	6	140	113.50 ± 3.50 g/L	[33]
Sucrose	*A. pullulans* BL06 and BL06ΔPMAs	168	28	-	200	83.40 g/L and 140.20 g/L	[35]
Sucrose	*A. pullulans* RM1603	132	28	6.50	600	62.52 ± 0.24 g/L	[34]
Hazelnut husk hydrolysate	*A.pullulans* AZ-6	168	24.20	6.48	-	74.39 g/L	[38]
Sucrose	*A. pullulans* YQ65	144	28	6	180	42.70 g/L	[39]
Kitchen waste	*A. pullulans* MTCC 2013	-	28	5	150	24.77 ± 1.06 g/L	[1]
Deoiled rice bran	*A. pullulans* MTCC 6994	189.6	-	-	250	8.32 ± 0.02 % w/v	[40]

Cassava Bagasse	*A. pullulans* MTCC 1991	168	30	5.50	-	6.45 g/L	[41]
Sesame seed oil cake (SSOC)	*A. pullulans* KY767024	-	23	-	-	54.50 pullulan/kg substrate	[42]
Sugarcane bagasse hydrolysate	*A. pullulans* LB83	96	28	-	200	20 g/L	[43]
Jaggery	*A. pullulans* MTCC 2195	120	-	5	-	15.589 g/L	[36]
Jaggery	*A. pullulans* CFR-77	72	30	5	-	23.07 g/L	[37]
Corn steep liquor	*A. pullulans* RBF4A3	120	20	-	250	88.59 g/L	[44]
Molasses	*A. pullulans* MTCC 2195	120	35	-	150	45 g/L	[45]
Jaggery, corn steep liquor, deoiled jatropha seed cake	*A. pullulans* RBF4A3	72	28	-	250	61.17 g/L	[46]
Jackfruit seed powder	*A. pullulans* MTCC 2195	168	30	-	200	17.95 g/L	[47]
Hemicellulose hydrolysate	*A. pullulans* AY82	168	-	5	400	12.65 g/L	[48]
Potato starch hydrolysate	*A. pullulans* 201, 253	-	28	-	500	54.57 g/L	[49]
Cassava bagasse	*A. pullulans* MTCC 2670	120	30	7.50	-	19 g/L	[50]
Coconut milk	*A. pullulans* MTCC 2195	168	28		200	58 g/L	[51]
Coconut water	*A. pullulans* MTCC 2195	168	28	-	200	38.80 g/L	[51]
Jatropha seedcake	*A. pullulans* RBF 4A3	120	28	-	200	83.98 g/L	[52]
Palm kernel	*A. pullulans* MTCC 2670	168	30	-		18.43 g/L	[53]

Soybean pomace	*A. pullulans* MTCC 1991	168		-	210	27 125.70 g/L	[54]
Sweet potato hydrolysate	*A. pullulans* AP329	96	28	-	200	29.43 g/L	[55]
Whey	*A. pullulans* ATCC 42023	120	28	-	210	12 g/L	[56]
Kitchen waste	*A. pullulans* MTCC 2013	-	28	5	150	24.77 ± 1.06 g/L	[1]
Soyabean meal hydrolysate	*A. pullulans* NCPS2016	84	28	7	220	59.80 g/L	[57]
Cassava bagasse and Asian palm kernel	*A. pullulans* MTCC 2670	-	50 and 40	10	300 and 400	1.90 (% w/v) and 1.50 (% w/v) respectively	[58]
Cassava bagasse	*A. pullulans* MTCC 2670	-	-	5.50	-	39.42 mg/g of dry substrate	[59]
Cassava bagasse	*A. pullulans* MTCC 2670	96	-	5.50	-	23.60 mg/g of dry substrate	[60]
Asian palm kernel	*A. pullulans* MTCC 2670	168	30	6.50	-	16 g/L	[53]
Corn bran hydrolysate	*A. pullulans* KY767024	96	-	5.50	-	19.45 ± 0.40 g/L	[61]
Deoiled rice bran	*A. pullulans* 6994	168	30	-	150	54.80 g/L	[62]
Sugarcane bagasse	*A. pullulans* LB83	96	25.30	-	232	25.19 g/L	[63]
Sugarcane bagasse hydrolysate	*A. pullulans* LB83	96	28	-	200	20 g/L	[63]
Rice hull hydrolysate	*A. pullulans* CCTCC M 2012259	148	28	3.80	400	22.20 g/L	[64]

1.6 Factors influencing pullulan production

The fermentation parameters or factors that affect pullulan production are as follows:

- ***Carbon source:*** Pullulan can utilize a wide range of agricultural residues as substrates due to its multi-enzyme system. The optimal carbon source concentration is typically 10–15 %. Exceeding 20 % can inhibit pullulan production as enzymes are hindered at this concentration. Lower concentrations of carbon sources may prioritize biomass production over pullulan production. Sucrose is commonly used as the carbon source for *A. pullulans* growth [22,49,54,65–67]. Moreover, glucose has been identified as the most effective carbon source for pullulan production by mutant variant *A. pullulans* UVMU6–1 [68]. Other sources like glucose, corn syrup, molasses, and agricultural waste residues have also been utilized [50]. Xylose and lactose, however, result in lower pullulan yields [28]. It is noteworthy that an excessive increase in sugar concentration beyond a certain threshold has been shown to reduce pullulan production [62,69].

- ***Nitrogen source:*** The availability of nitrogen is a critical factor affecting pullulan production, with multiple studies noting its importance. Reduced nitrogen in the medium leads to higher pullulan production and vice-versa [50,62,70,71]. Different nitrogen sources yield varying production yields, and the type and concentration of nitrogen source play a pivotal role in pullulan production. It is noteworthy that while pullulan production decreases with the increase in nitrogen concentration in the medium, biomass tends to increase [72]. Agricultural waste-derived nitrogen sources have been utilized for the production of pullulan. Maximum pullulan production has been reported when nitrogen sources such as ammonium sulfate ($(NH_4)_2SO_4$) and ammonium nitrate (NH_4NO_3) were used [51]. Nitrogen sources also influence enzyme activity and has implications for incubation time and the activity of UDPG phosphorylase. Another study reported that limiting nitrogen in the medium led to peak production levels, which is attributed to increased activity of glucosyltransferase and α-phosphoglucomutase [73].

- ***pH:*** The optimal pH range for pullulan production is 5.5–7.5, as suggested by [70]. The highest yield of pullulan from *A. pullulans* MTCC 1991 was achieved within pH ranging from 6.5–7.5, as reported by [74]. However, the ideal pH for producing pullulan

has been documented as pH 5 [52] and pH 4 [68]. These varying optimum pH values for pullulan production can be attributed to the specific strain used and the culture conditions [37,68]. At very low pH of 2.5, pullulan production is suppressed, and insoluble glucan may be produced [70].

- ***Cell morphology:*** The connection between the cell morphology and its capacity to produce polysaccharides is a significant factor, given that polysaccharide production is closely linked to specific cell shapes. The exact type of cells responsible for synthesizing pullulan remains uncertain. In the majority of studies, pullulan production has been observed primarily in the yeast-like morphology of *A. pullulans*, as noted by [75]. On the other hand, in several other research papers, the ability to produce this polysaccharide has been associated with the chlamydospore population. On the other hand, yeast-like cells, when maintained at a neutral pH, yield pullulan with an exceptionally large molecular size [70].

- ***Temperature:*** *A. pullulans* is capable of thriving across a wide range of temperatures. For shake-flask experiments conducted under various physiochemical conditions using different agricultural residues, the optimal temperature for production of pullulan ranges from 25–35 °C [50]. Furthermore, when using the OVAT approach to optimize fermentation conditions for *A. pullulans*, it was determined that the ideal temperature for maximizing pullulan production is 27.5 °C [76].

- ***Aeration and agitation speed:*** Pullulan production by *A. pullulans* is highly dependent on aeration and agitation speed. Notably, increased aeration and lower agitation speed tend to improve pullulan production in bioreactor (Cheng et al., 2011a). A study on pullulan production using a solid-state fermentation matrix of Asian palm kernel and cassava bagasse found that optimal yields occurred at agitation speeds between 300–400 rpm [58]. In another study, it was reported that higher agitation speeds lead to the formation of a greater number of *A. pullulans* colonies, resulting in increased pullulan production [76]. It is noteworthy that changes in aeration speed were associated with alterations in cell morphology.

- ***Supplements:*** The introduction of tween-80 into the fermentation medium have been found to boost pullulan production, but it doesn't lead to increase in biomass [68,77–79]. In a different study, it was reported that incorporation of uracil into the growth medium enhances the production of pullulan. The pullulan yield was elevated from 37.72–49.07 g/L when 5 mM uracil was introduced after 48 hrs [80].

Overall, pullulan production is influenced by various factors that need to be carefully controlled to achieve optimal yields.

1.7 Downstream processing

The extraction procedure for pullulan from the fermentation broth comprises several stages: (1) removing of biomass by centrifugation, (2) cold ethanol or isopropanol addition to supernatant for precipitating the polysaccharide, (3) dissolution of precipitate in deionised water, (4) dialysis to remove low molecular weight impurities, and (5) freeze-drying (lyophilization), which is the final step of pullulan extraction in purified form. The biomass pellet is isolated through centrifugation of the broth at 10,000 rpm and 4 °C for 30 mins. The resultant supernatant is subjected to heat treatment at 80 °C for 20–30 mins to remove insoluble components and proteins sensitive to heat [55]. Various organic solvents such as ethanol [53,55,58,60,81], methanol [82], 2-propanol [83], isopropanol [37,84]; and acetone : ethanol (1 : 1) [85] have been used for precipitation of pullulan. In a study, Kachhawa et al. [86] noted the highest precipitation of polysaccharides by utilizing a mixture of ethanol and ethyl methyl ketone in a ratio of 60:40. Additionally, the purity of pullulan can be further enhanced through ultrafiltration or dialysis using membranes with appropriate molecular weight cut-offs, followed by lyophilisation of the dialysed sample. Cross-flow membrane separation methods may also be used for additional refinement.

1.8 Structural analysis of pullulan

The structure of the polysaccharide can be determined by Fourier Transform Infrared Spectroscopy (FTIR) and Nuclear Magnetic Resonance (NMR) techniques.

- ***FTIR analysis***

  By analyzing the infrared (IR) energy absorption at specific wave numbers associated with distinct functional groups or linkages within the sample, it is possible to make predictions about the structure of the exopolysaccharide [87]. FTIR spectroscopy is

used to identify functional groups, chemical bonding, and stretching in biopolymers [88]. The peaks observed at 1156 cm^{-1} and 856 cm^{-1} correspond to the presence of D-glucose in its pyranose configuration and the α-glycosidic bonds connecting the glycosyl units. Furthermore, the absorption peaks at 764 cm^{-1} and 931 cm^{-1} indicate the existence of α(1→6) and α(1→4) glycosidic bonds, respectively [50].

- ***NMR analysis***

  Researchers have conducted NMR spectroscopic examination on pullulan obtained through fermentation processes. In the proton NMR (^{1}H NMR) spectra, the peaks between 4.5 and 5.6 ppm correspond to the hydroxyl protons present in the sample [60,89,90]. The presence of 6-deoxy sugar is indicated by the peak at 16.8 ppm in the carbon NMR (^{13}C NMR), as reported by [60] and [91]. Additionally, the presence of the anomeric carbon α(1→6) is evidenced by the peak at 100.1 ppm [89].

1.9 Applications of pullulan

Pullulan is a natural polysaccharide with many useful applications in different areas. Being a biodegradable and biocompatible polymer, it is used in food, pharmaceutical, and cosmetic applications. Beyond these, pullulan also finds use in electronics, oil recovery, and water purification. It can be formulated or fabricated into coatings, fibers, gels, and particles, making it a valuable material for both everyday products and advanced technologies. The applications of pullulan in different domains have been discussed in detail as follows:

1.9.1 Biomedical applications

Pullulan and its derivatives have been widely recognized as versatile biomaterials with various applications in the biomedical field. With their biocompatibility and biodegradability, they have found utility in various medical applications. One notable area is drug delivery, where pullulan-based nanoparticles function as effective delivery systems for the controlled release of drugs, improving therapeutic outcomes and reducing adverse effects. Furthermore, pullulan coatings have been used in tissue engineering to facilitate cell adhesion and proliferation, helping in damaged tissue regeneration [92]. In wound healing, pullulan dressings exhibit excellent moisture retention properties, creating an optimal environment for wound repair. Moreover, pullulan-based hydrogels have demonstrated promise in creating scaffolds for regenerative medicine and tissue engineering, offering support for cell growth and tissue regeneration [93,94]. Different biomedical applications of pullulan and its derivatives have

been depicted in Table 1.2, with selected recent examples discussed below to emphasize key findings and advancement.

1.9.1.1 Wound healing

Kang et al. [95] reported that oxidized pullulan, obtained through sodium periodate oxidation, introduces aldehyde groups capable of forming crosslinked networks with polymers such as chitosan, polyvinyl alcohol (PVA), or collagen, thereby enhancing mechanical properties, cell viability, and antibacterial activity. At higher oxidation levels, the films significantly promoted wound healing in methicillin-resistant *Staphylococcus aureus* (MRSA)-infected mouse models, indicating strong potential for use in advanced skincare and wound treatment applications. Liu et al. [96] developed a multifunctional conductive hydrogel composed of quaternized chitosan, oxidized pullulan, *Chlorella vulgaris*, and dopamine-coated polypyrrole, offering antimicrobial, anti-inflammatory, oxygen-releasing, and wound-monitoring functions. The enhanced solubility, mechanical strength, and conductivity of the hydrogel, combined with microalgae-driven oxygenation and photothermal therapy, significantly improved healing in chronic diabetic wounds. This integrated approach presents a promising strategy for simultaneous wound treatment and monitoring. Li et al. [97] developed a sustainable 3D nanofiber sponge dressing using quaternized chitosan derived from housefly pupa shells, pullulan, and citric acid, utilizing gas foaming for environmentally friendly fabrication. This biodegradable dressing exhibited strong haemostatic, antibacterial, and pro-angiogenic properties, with high porosity and extracellular matrix (ECM)-mimicking architecture that supports fluid absorption and cellular growth. Its potential as a drug delivery platform further enhances its promise for advanced wound healing applications. In another study, Li et al. [98] introduced a fully natural hydrogel composed of quaternary chitosan, oxidized pullulan, and cuttlefish-ink nanoparticles for treatment of bacteria-infected diabetic oral ulcers. The hydrogel combines anti-inflammatory, antibacterial, pro-angiogenic, and antioxidant properties within a 3D network, significantly promoting healing in diabetic rat models. This multifunctional platform demonstrated the potential of naturally derived components in oral ulcer treatment. Reinoza et al. [99] developed pullulan-chitosan nanofibers via high-speed rotational spinning, achieving uniform, bead-free structures with enhanced hydrophilicity and permeability due to strong hydrogen bonding between components. These nanofibers demonstrated excellent haemocompatibility and significant haemostatic properties, suggesting their application in wound healing and bleeding control. Plugariu et al. [100] reported the development of PVA/pullulan hydrogels with and without clay, evaluating their structural, rheological, and

drug release properties under physiological conditions. Hydrogels without clay showed enhanced swelling and more effective neomycin release, best described by the Peppas-Sahlin model, while clay-containing networks followed the Korsmeyer-Peppas model. The incorporation of pullulan improved biocompatibility and drug diffusion, making these hydrogels promising candidates for antibiotic delivery in wound dressing applications. Jiang et al. [101] developed a multifunctional hydrogel composed of catechol-quaternized chitosan, methacrylate-dialdehyde pullulan, and gallium ions, offering antibacterial, haemostatic, self-healing, and injectable properties. The hydrogel exhibited strong mechanical performance, effective activity against drug-resistant bacteria (including MRSA), and enhanced wound healing through collagen synthesis and vascular regeneration. Its photo-crosslinkable and bioactive composition demonstrated its potential as an advanced dressing for infected wound care. Wang et al. [102] reported the development of chitosan/hyaluronic acid-grafted pullulan succinate (HA-st-Pu) polymers through electrostatic interaction between HA-st-Pu and chitosan, aiming at superficial wound healing applications. Characterization confirmed successful synthesis, and the composite exhibited favourable properties such as a porous structure, high swelling capacity, rapid haemostasis, biocompatibility, and antibacterial and antioxidant activity. *In vivo* studies further demonstrated its ability to accelerate wound healing, suggesting its potential as an effective wound dressing material. Khalaji et al. [103] reported the fabrication of a functional wound dressing by silylating bacterial nanocellulose (BNC) with 3-aminopropyltrimethoxysilane, followed by grafting electrospun pullulan-zinc oxide (ZnO) hybrid nanofibers onto the modified surface. The resulting aminoalkylsilane grafted BNC (A-g-BNC) membrane/pullulan-ZnO dressing exhibited superior antibacterial activity, enhanced mechanical strength, and significantly improved wound healing performance compared to pristine BNC and A-g-BNC, while maintaining good biocompatibility.

Table 1.2 Biomedical applications of pullulan and pullulan derivatives/composites.

Pullulan derivatives/ composites	Formulation	Biomedical applications	References
Curcumin grafted hyaluronic acid pullulan polymers	Chemical modification	Wound dressing	[104]
Poly (vinyl alcohol)/pullulan	Hydrogel	Wound dressing	[100]
Pullulan	Hydrogel	Sutureless wound healing	[105]

Chitosan/hyaluronic acid/pullulan	Film	Wound dressing	[106]
Pullulan/collagen	Hydrogel	Wound dressing	[107]
Chitosan-and hyaluronic acid-grafted pullulan succinate	Film	Wound healing	[102]
Algae-inspired chitosan/pullulan	Multifunctional hydrogel	Wound healing	[96]
Hyaluronic acid grafted pullulan	Film	Wound healing	[108]
Pullulan-grafted copolymer hydrogel formed through UV copolymerization and crosslinking.	Hydrogel	Wound healing	[109]
Bacterial cellulose (BC)/pullulan/vitamin-C/vitamin-E	Bilayer membrane	Wound healing	[110]
Alginate/pullulan/hyaluronic acid	Hydrogel	Wound healing	[111]
Chitosan/pullulan/sodium hydroxide	Hydrogel	Wound healing	[112]
Pullulan	Gel	Wound healing	[113]
Chitosan/carboxymethyl pullulan/bioglass	Film	Wound healing	[114]
Propolis-loaded photocurable methacrylated pullulan	Film	Wound healing	[115]
Pullulan/ poly (3-hydroxybutyrate-co-3-hydroxyvalerate) (PHBV)	Bilayer scaffold	Wound healing	[116]
Collagen-oxidized pullulan loaded with polydatin	Scaffold	Chronic wound healing	[117]

Oxidized pullulan/ PVA/chitosan/collagen	Film	MRSA-infected wound healing	[95]
Cross-linked pullulan/polyhexamethylene biguanide (PHMB)	Powder that transforms into gel upon contact with wound exudate	Wound healing	[118]
Pullulan/ε-poly-l-lysine	Hydrogels	Burn wound healing	[119]
2D molybdenum disulfide (MoS_2) functionalized with quaternary pullulan	Glycosheets	Wound disinfection and healing	[120]
Chitosan-fucoidan nanoparticle/pullulan	Nanoparticle-loaded microneedle patch	Wound healing	[121]
Ulmus davidiana var. *japonica* root bark/pullulan	Superabsorbing hydrogel film	Wound healing	[122]
Curcumin-loaded methacrylate pullulan with grafted carboxymethyl-β-cyclodextrin	Hydrogels	Wound healing	[123]
Aminoalkylsilane-grafted bacterial nanocellulose with ZnO-nanoparticles-doped pullulan nanofibers	Nanofibers	Multifunctional wound dressing.	[103]
Chitosan and hyaluronic acid-grafted pullulan succinate	Film	Wound healing	[102]
Insect chitosan/pullulan/gallium	Hydrogels	MRSA-infected wound healing	[101]
Pullulan/chitosan	Fiber membranes	Haemostasis	[99]

Eumelanin-assisted pullulan/chitosan	Hydrogel	Diabetic oral ulcers treatment	[98]
Insect quaternized chitosan/pullulan/citric acid	3D nanofiber sponge	Wound healing	[97]
Oxidized pullulan polysaccharide/carboxymethyl chitosan	Injectable hydrogel	Open abdominal wound treatment	[124]
Amoxicillin-loaded multilayer pullulan	Nanofibers	Topical drug delivery in skin treatments and wound healing	[125]
Silk fibroin coated Pullulan microspheres, crosslinked by trisodium trimetaphosphate (STMP)	Microcarriers	Bone tissue regeneration	[126]
Pullulan-g-poly(L-lactide)	Nanoparticles	Cancer cells treatment	[127]
Gold (Au) nanoparticles using pullulan as reducing/ stabilizing/ capping agent	Nanoparticles	Demonstrate efficient uptake, non-toxicity toward normal cells, and increased toxic effects on gastric cancer cell lines	[128]
Tannic acid/ chitosan/ pullulan	Nanofibers	Wound dressing	[129]
Cholesterol modified pullulan nanoparticles loaded with mitoxantrone	Nanoparticles	Facilitated rapid mitoxantrone release at pH 5.6 within 9 hrs post- administration	[130]
Carboxymethyl pullulan	Nanoparticles	Controlled drug release system	[131]
Carboxymethyl pullulan	Nanocomplexes	DNA and pH-sensitive drug delivery for cancer treatment	[132]
Oxidized pullulan	Conjugate	Improved targeting specifically toward hepatocellular carcinoma HepG2 cells within the liver	[133]

Oxidised pullulan	Hydrogels	Targeted delivery of drug to colon tumour HCT116 cells	[134]
Polyethylenimine pullulan (PEIP) nanomicelles modified with deoxycholic acid	Nanomicelles	High encapsulation efficiency (84.05 %) enabled sustained drug release and enhanced cytotoxicity against MCF-7 breast cancer cells	[135]
PEIP nanoplexes connected via a mercaptosuccinic acid disulfide bond	Nanoplexes	Enhanced doxorubicin (DOX) retention via glutathione-induced disulfide bond reduction in C6 cells	[136]
Core-crosslinked pullulan lipoic acid	Nanoparticles	Prolonged systemic retention and gradual plasma clearance observed in the human hepatocellular carcinoma SMMC-7721 cell line	[137]
Hydroxypropyl cyclosophoraose-pullulan	Microspheres	Resulted in a release system influenced by pH, which enhanced drug entrapment. The microspheres maintained the naproxen levels in the plasma of Sprague-Dawley rats for up to 72 hrs of oral administration	[138]
Pullulan-g-poly (N-isopropylacrylamide)	Nanoparticles	Thermo-responsive drug release from nanoparticles at pH 7.4 or 5 varies with polymer molecular weight and drug loading.	[139]
Core-shell stearyl pullulan	Nanostructures	Prolonged drug release under simulated gastrointestinal conditions and effectively controlled hyperglycemia over time.	[140]
pH-sensitive pullulan-1,1,2-trichlorotrifluoroethane	Nanoparticles	Improved tumour ablation and therapeutic effectiveness of drug.	[141]
NH_2 functionalized mesoporous silica nanoparticles with oxidized pullulan coating	Nanoparticles	Acid-triggered release of 5-fluorouracil from nanoparticles.	[142]

Carboxylated pullulan	Hydrogels	Insulin is released from carboxylated pullulan-concanavalin A-insulin hydrogels in a controlled manner, through specific binding of concanavalin A to glucose.	[143]

1.9.1.2 Cancer treatment and stem cell therapy

In cancer treatment, precise targeting of cells or tissues is frequently necessary to minimize adverse effects on healthy tissues in the body. Pawara et al. [144] reported the development of surface-functionalized, resveratrol-loaded pullulan nanoparticles for targeted drug delivery in lung cancer treatment. The nanoparticles demonstrated high drug entrapment efficiency, optimal size for deep lung deposition, and prolonged retention *in vivo*. Their findings demonstrated the potential of these biocompatible, stable nanoparticles as a sustainable, green alternative for cancer therapy, emphasizing the need for further research and clinical validation to optimize personalized medicine approaches for lung cancer. Nakatsukasa et al. [145] reported that M2 tumour-associated macrophages (TAMs) in CT26 and CMS5a tumour models showed high CD209b expression and preferentially internalized cholesteryl pullulan (CHP) nanogels via this receptor. CHP nanogels complexed with Pseudomonas Exotoxin A (PE) selectively depleted CD209b-positive M2 TAMs, likely due to targeted binding and uptake. Beyond depletion, CHP nanogels showed potential as drug delivery systems for modulating TAM function, offering a promising approach for tumour immunotherapy. Sheikhi et al. [146] reported that supercritical CO_2 technology effectively enhanced the solubility and dissolution rate of the hydrophobic anti-cancer drug regorafenib by impregnating it into the hydrophilic pullulan polymer. Process conditions, particularly temperature, significantly influenced drug loading, with the highest loading achieved at 328 K and 280 bar. The resulting amorphous regorafenib exhibited improved dissolution (up to 80 % over 60 hrs), attributed to increased surface area and Fickian diffusion as the primary release mechanism. Lopez-Vince et al. [147] reported the development of a green, polysaccharide-based hydrogel platform using 3D-printed molds for scalable and reproducible cancer spheroid formation. The non-adhesive, porous hydrogels supported spheroid growth across multiple cancer cell types and enabled drug testing with doxorubicin (DOX) and paclitaxel (PTX), revealing cell-type-specific responses in 3D versus 2D cultures. This system offers a customizable, biomimetic microenvironment suitable for drug screening and further tumour microenvironment (TME) modelling. Thomas

et al. [148] reported that pullulan-based nanoparticles represent a promising platform for targeted and controlled drug delivery, owing to biocompatibility, non-toxicity, and biodegradability of pullulan. These nanoparticles enhance drug solubility, stability, and therapeutic efficacy, with demonstrated applications in cancer and antimicrobial therapies. Despite challenges such as size uniformity and scalability, ongoing research is optimizing synthesis and characterization methods to improve reproducibility and clinical potential. Varadhan et al. [149] developed hyalgan-coated pullulan acetate nanoparticles loaded with ferulic acid, which showed significantly enhanced anti-tumour activity, approximately three times more effective than free ferulic acid, against gastrointestinal cancer cell lines. The nano-formulation showed favourable drug release kinetics (95 % in 22 hrs), optimal particle size (425 ± 5.2 nm), excellent biocompatibility and haemocompatibility, highlighting its potential for targeted gastrointestinal cancer therapy. Solanki et al. [150] reported the development of a novel drug delivery system based on berberine-loaded 4-carboxyphenyl boronic acid-modified pullulan-stearic acid conjugate nanoparticles (BPPNPs) for targeted delivery of berberine to treat skin cancer. The nanoparticles exhibited favourable physicochemical properties, including nanoscale size, high encapsulation efficiency, sustained drug release, and excellent colloidal stability. *In vitro* studies using 2D and 3D cell culture models demonstrated significantly enhanced anticancer activity and apoptosis induction compared to free berberine, highlighting the potential of BPPNPs as an effective therapeutic strategy for skin cancer. Barer et al. [151] developed a novel system combining microspheres and hydrogels for localized postoperative delivery of doxorubicin (DOX)-loaded polycaprolactone microspheres in the treatment of breast cancer. They used an innovative method to embed the microspheres onto the hydrogel surface, which enabled controlled drug release and sustained anticancer activity, as shown in both 2D and 3D MCF-7 breast cancer models. Fard et al. [152] reported the formulation of polysaccharide-based nano-emulsions using blends of charged polymers—chitosan (positive), alginate (negative), and pullulan (neutral), to optimize drug delivery for melanoma treatment. Among various combinations, a nano-emulsion made from pullulan and chitosan in a 1 : 2 ratio demonstrated the most favourable drug release profile. When modified with folate, it enhanced cellular uptake and significantly reduced the viability of A375 melanoma cells. Asgari et al. [153] reported the development of an oxygen-rich graphene oxide (GO)-based nanocarrier with high dispersibility, co-loaded with paclitaxel (PTX) and curcumin, two hydrophobic anticancer agents. This dual-drug nanocarrier was incorporated into pullulan nanofibers via electrospinning, enabling localized, sustained drug release and reduced systemic toxicity. The formulation showed an enhanced ability to inhibit the growth

of MCF-7 breast cancer cells and potential for localized breast cancer treatment or prevention of post-surgical recurrence. Emam et al. [154] reported the green and cost-effective synthesis of carbon quantum dots (CQDs) using a hydrothermal method, comparing carrageenan and pullulan as nucleating agents. The resulting monodispersed CQDs (~ 2.1 nm) exhibited distinct bioactivities. Pullulan-derived CQDs showed superior anticancer effects against human breast cancer cells, whereas carrageenan-derived CQDs demonstrated enhanced antiviral activity against Middle East respiratory syndrome coronavirus (MERS-CoV), highlighting their potential as an effective therapeutic agent. Huang et al. [137] developed nanoparticles derived from pullulan to transport PTX with reversible cross-linking, demonstrating notable cytotoxic effects and a capacity for targeting the liver. Furthermore, to overcome the limitations of using DOX in cancer therapy, Chen et al. [155] created an innovative copolymer micelle based on pullulan. This micelle was modified with folate to target tumours and was able to simultaneously deliver DOX and shRNA targeting Beclin1. The delivery system exhibited efficient cellular uptake in folate-positive HepG2 and HeLa cells, leading to cytotoxicity and induction of apoptosis, thereby displaying encouraging anti-tumour efficacy. In another study, Wang et al. [156] developed a nanoparticle-based system to co-deliver PTX and IR780, enabling a synergistic combination of photothermal and photodynamic therapy with chemotherapy for hepatocellular carcinoma. Hepatic cancer cells were observed to uptake pullulan-DOX conjugates, with DOX being released within the acidic pH environment of the endosome/lysosome. This facilitated the delivery of DOX to the nuclei of tumour cells, where it hindered proliferation and stimulated apoptosis owing to its affinity to nucleic acids [157].

Utilization of stem cells for disease treatment or prevention presents significant potential in both scientific investigation and medical practice. Mesenchymal stem cells (MSCs) are highly regarded in stem cell therapy for their capacity to transform into diverse cell types. Researchers have discovered that porous scaffolds composed of pullulan and dextran serve as effective substrates for cultivating cord-blood endothelial colony-forming cells (ECFCs). Porous nature of the material facilitated enzymatic degradation, allowing for the recovery of cultivated cells. This showed the potential of such biocompatible permeable substance in delivering stem cells for the treatment of vascular diseases [158]. MSC-derived exosomes were functionalized with cationic spermine-pullulan, enabling targeted delivery to hepatocytes, and accumulating in liver tissues. These modified exosomes exhibited therapeutic effects with anti-inflammatory and protective properties [159]. Hydrogels derived from a combination of pullulan and silk fibroin were utilized to encapsulate rabbit bone marrow MSCs. Assessment of cell viability and morphological observations indicated excellent compatibility between the

hydrogels and the cells. These results indicated that pullulan-based hydrogels hold promise as vehicles for delivering stem cells in musculoskeletal tissue engineering applications [160]. Pullulan underwent modification to form spermine-pullulan, which was then combined with plasmid DNA encoding hepatocyte growth factor (HGF). Upon introduction into MSCs, this compound enabled the synthesis of HGF. Implantation of these altered MSCs into a rat model led to a noteworthy decrease in liver fibrosis [161]. In a separate investigation, spermine-pullulan was mixed with the cytomegalovirus thymidine kinase (CMV-TK) gene and ganciclovir, and subsequently introduced into bone marrow MSCs to assess its influence on pulmonary melanoma metastasis. This strategy demonstrated cytotoxic effects and successfully suppressed tumour proliferation both in laboratory settings and within living organisms [162]. Researchers have explored the utilization of pullulan-based compositions in MSC therapy. Among these compositions is a hydrogel made of pullulan and collagen bio-scaffold, utilized for delivering MSCs to wound locations. Applying MSCs through this hydrogel resulted in increased expression of genes related to angiogenesis, enhanced viability of adipose-derived stem cells, accelerated wound healing, and an increase in blood vessel [163].

1.9.1.3 Gene delivery

Pullulan-derived carriers have been thoroughly researched for gene delivery because of their biocompatible characteristics, minimal immunogenicity and great adaptability. Reichel et al. [164] developed a hydrophobic and pH-responsive cationic polymer based on pullulan, synthesized via esterification with 5-norbornene-2-carboxylic acid and subsequent thiol-ene functionalization with a tertiary amine. The modified pullulan exhibited enhanced gene delivery capabilities by improving endosomal escape, promoting protein interaction, and balancing transfection efficiency with low cytotoxicity. Sherly et al. [165] reported the synthesis of dextran- and pullulan-based polymer derivatives (DPD I/II and PPD I/II) conjugated with polyethyleneimine (PEI) and diethyl aminoethyl methacrylate (DEAEM) using Michael addition reaction at varying grafting densities. Among them, DPD II and PPD II showed high cytocompatibility, efficient cellular internalization, and selective transfection in cancer cell lines (C6 and HeLa), with no activity in non-cancerous L929 cells. *In vivo* biodistribution studies in BALB/c mice confirmed good renal clearance and no accumulation in major organs, indicating favourable safety profiles. Moraes et al. [166] reported development of nanosized, stable polyplexes in aqueous medium by simply mixing miRNA with cationized pullulan derivatives. These nanoparticles, developed without toxic reagents or

organic solvents, showed no cytotoxicity in human umbilical vein endothelial cells (HUVECs) and represented a novel, safe approach for miRNA delivery systems, building on prior work with pullulan-modified nanoparticles. Caroline et al. [167] reported that cationized pullulan modified with PEI and cross-linked using ethylene glycol dimethacrylate exhibited high cytocompatibility and reduced interactions with plasma proteins, enhancing its potential for systemic gene delivery. The crosslinked pullulan-PEI (PPE) polyplexes showed selective uptake and effective p53-mediated apoptosis in C6 cancer cells, highlighting their promise as targeted gene delivery vectors for cancer therapy. Farahpour et al. [168] reported the conjugation of pullulan with poly(β-amino esters) to develop gene delivery nanocarriers with favourable transfection efficiency and low toxicity. The resulting polyplexes exhibited appropriate particle size, positive zeta potential, and effective DNA condensation, making them promising candidates for further development in gene delivery applications. In another study, a gene delivery agent was synthesized by functionalizing lysine dendrons with octaguanidine and attaching them to pullulan. The carrier system incorporated the plasmid pKillerRed-mem, serving as a photosensitizer. Compared to control groups, this system exhibited notably enhanced gene transfection efficiency without inducing haemolysis. It was suggested that the carriers were internalized via macropinocytosis, and the photosensitizer triggered reactive oxygen species production, thereby inducing cytotoxicity in tumour cells [169]. In another study, nanoplexes were formed by cationically modifying pullulan with disulfide linkages, resulting in particles of around 150 nm in size that exhibited redox sensitivity and susceptibility to reductive cleavage. The nanoplexes demonstrated safety towards C6 glioma cells and had the capability to target the cell nucleus, releasing DNA following reduction with dithiothreitol. This system facilitated the combined delivery of both DOX and the p53 gene, resulting in increased intracellular drug retention through the inhibition of efflux pumps. This simultaneous drug and gene delivery approach enhanced cell death [136,170].

1.9.1.4 Tissue engineering and drug delivery

Numerous studies have explored the use of pullulan-based scaffolds in tissue engineering, with particular emphasis on bone regeneration. de Carvalho et al. [171] reported the development of poly (3-hydroxybutyrate-co-3-hydroxyvalerate) (PHBV) filaments incorporating pullulan and ketoprofen via hot-melt extrusion, with pullulan enhancing drug release and degradation due to its hydrophilic and amorphous nature. The addition of pullulan shifted the drug release mechanism from erosion-controlled (non-Fickian) to diffusion-controlled (Fickian), while all formulations demonstrated good biocompatibility, suggesting their potential for bone tissue

engineering applications. Qin et al. [172] reported the development of a biocompatible methacrylated pullulan/polyethylene (glycol) diacrylate composite (PulMA/PEGDA) hydrogel synthesized via UV photo-crosslinking. The hydrogel supported rabbit mesenchymal stem cell viability, promoted glycosaminoglycan synthesis, and enhanced chondrogenic differentiation, highlighting its potential for cartilage repair and regeneration applications. Chauhan et al. [173] developed an injectable, biodegradable, and self-healing hydrogel composed of pullulan and poly(ethylene glycol), crosslinked through pH-responsive hydrazone bonds and incorporated with a poly(ethylene glycol)-dexamethasone conjugate. The hydrogel showed high porosity, provided sustained drug release for up to 28 days, and promoted osteogenic differentiation and mineralization in murine osteoblast precursor cells. Le et al. [174] synthesized polyaminated pullulan derivatives by attaching low molecular weight polyamines to the pullulan backbone, which improved their mucoadhesive behaviour and ability to sustain drug release. These derivatives, particularly pullulan-polyethyleneimine (Pul-PEI) and pullulan-tris(2-aminoethyl)amine (Pul-TAEA), demonstrated significantly increased tensile strength, mucoadhesion time, and reduced drug flux, while maintaining biocompatibility and biodegradability. Moris et al. [175] developed a pullulan/polyvinylpyrrolidone (PVP) nanocomposite scaffold integrated with anisotropic Ag-silica Janus particles displaying a ball-stick morphology for bone regeneration applications. Incorporation of these particles improved the antibacterial performance, mechanical strength, and osteogenic potential of the scaffold, as evidenced by enhanced MG-63 cell viability, alkaline phosphatase activity, and increased calcium mineralization. The scaffolds also supported apatite formation, indicating promising bioactivity for bone repair applications. Su et al. [176] reported the development of a pullulan-based hydrogel incorporating fibers via a one-step crosslinking strategy to enhance its mechanical and viscoelastic properties. The polydopamine fibers imparted pH-responsive drug loading and release capabilities, while maintaining good cytocompatibility. In another study conducted on rats with femoral bone defects utilized implants made from dextran-pullulan biomaterials enriched with hydroxyapatite and fucoidan. Researchers used a specialized Magnetic Resonance Imaging (MRI) protocol to observe bone regeneration and the formation of new blood vessels following implantation [177]. Pullulan and dextran were used to fabricate a scaffold designed for astaxanthin administration to treat injury caused by ischemic-reperfusion in a specific animal model. Through subjecting the animals to femoral artery clamping and repeated reperfusion periods, the implant demonstrated enhanced antioxidant properties and efficiently mitigated muscle damage resulting from the injury [178]. Another investigation focused on creating macroporous beads by combining pullulan, dextran, and

hydroxyapatite, which were then implanted into rats with defects in their femoral condyles. Interestingly, there were no signs of inflammation due to the implant, and over time, cellular structures formed between the scaffolds, facilitating space filling. By the 70th day, both the density and amount of mineralization significantly enhanced [179].

1.9.1.5 Medical imaging

Pullulan has been found to have significant applications as a contrast agent in MRI, a technique that uses magnetic field to image parts of the body. The effectiveness of MRI relies significantly on magnetic nanoparticles, which exhibit sensitivity to the magnetic field gradients of the instrument. Extensive research has been focused on developing pullulan-based magnetic nanoparticles that are biocompatible and suitable for imaging techniques such as MRI, ultrasound imaging and single-photon emission computed tomography (SPECT). Medical imaging enables visualization of internal body structures by using fluorescent probes to label cells and subcellular components. Among these, quantum dots (QDs), that are semiconductor nanocrystals, are widely recognized for real-time cellular imaging, owing to their broad excitation range, intense fluorescence, narrow emission spectra and excellent photostability [180–182]. Despite this, achieving the successful introduction of QDs into live cells presents a substantial difficulty, given the typically low uptake efficiency of cells for QDs. To address this limitation, cationic liposomes have been explored as potential QD carriers since they can interact with negatively charged cell membranes and promote endocytosis [183,184]. However, their tendency to form large cytoplasmic aggregates reduces imaging efficiency. A promising alternative is the use of amine-functionalized cholesteryl pullulan ($CHPNH_2$), which overcomes these drawbacks and supports precise intracellular labelling [185]. The cellular uptake efficiency of QDs conjugated with CHP exceeds that of traditional carriers, rendering monodisperse hybrid nanoparticles of QDs-$CHPNH_2$ suitable for use as fluorescent probes in medical imaging across diverse human cell types. In a study by Biliuta et al. [186], pullulan was oxidised to its carboxylated form through the (2,2,6,6-tetramethylpiperidine-1-yl)-oxyl (TEMPO) radical reaction, and this modified iteration was used to stabilize and cover magnetic Fe_3O_4 nanoparticles, rendering it a fitting contrast agent for MRI. Upon administration into pig liver, the formulated contrast agent displayed a reduced diffusion factor compared to conventional agents, rendering it suitable for specific scenarios where lower diffusion properties are preferred. In another study, Kong et al. [187] developed CHP-based nanoparticles linked with infrared dye 900 as near-infrared polymer nanogels (NIR-PNG), showing limited dispersion and extended retention within sentinel nodes. These nanogels

provided high sensitivity and specificity for sentinel node detection, indicating their potential use as tracers in navigation surgery for gastric cancer. Jenjob et al. [188] engineered a novel MRI contrast agent, gadolinium-diethylene triamine pentaacetate (DTPA)-pullulan, by conjugating pullulan with gadolinium-DTPA, exhibiting improved and prolonged contrast effects for more than 30 mins in comparison to a commercial agent. Chen et al. [189] demonstrated the incorporation of calcium carbonate and pullulan into a copolymer-based nanoparticle platform which improved ultrasound imaging resolution at hepatic tumour regions. Another study by Huang et al. [190] developed cationic pullulan-based nanoparticles, incorporating ethanolamine-functionalized poly(glycidyl methacrylate) together with gadolinium, that showed strong potential as MRI contrast agents, especially in HepG2 cells. They also demonstrated notable gene transfection efficacy and were efficiently taken up by both HeLa and HepG2 cells.

1.9.1.6 Plasma expander

Plasma expander, also known as a blood plasma substitute, is a colloidal substance designed to mimic the properties of blood plasma, including appropriate colloidal osmotic effect, osmotic pressure, and viscosity. For it to be considered appropriate for medical use, the plasma expander needs to be free from pyrogens, non-toxic, and compatible with the human body [191]. In cases of polytrauma resulting from severe accidents or other circumstances, significant blood loss occurs, leading to a decrease in osmotic pressure. In such cases, blood plasma volume expanders are essential for restoring blood circulation and sustaining osmotic pressure within blood vessels. Highly water-soluble polymers are suitable for use as plasma expanders, and pullulan falls into this category being a water-soluble polymer. Pullulan, known for its non-toxicity and high compatibility with the human body, has been reported to be valuable in maintaining the osmotic pressure within blood vessels and facilitating adequate blood circulation. It possesses the ability to metabolize and thereby counterbalance blood loss, while still being easily removable after achieving the desired therapeutic effects [192,193]. Modified pullulan, recognized as a colloidal component, has emerged as a highly promising therapeutic candidate to function as a substitute for blood plasma [194,195], as depicted in Figure 1.4. Its efficacy as a plasma expander is closely linked to its molecular weight (M_w). Researchers discovered that for pullulan to be effective as a blood plasma expander, it should possess a M_w of approximately 60 kDa. They noted that pullulan with higher M_w raised venous pressure, whereas pullulan with lower M_w was rapidly cleared from the body, resulting in secondary haemorrhagic shock [191]. Therefore, pullulan intended for this purpose should fall

within the effective therapeutic M_w range, avoiding both very low and very high molar mass fraction. Modified pullulan fractionated within 30,000–90,000 M_w distribution range has been shown to effectively treat and, in some cases, prevent haemorrhage [191,196]. Fractionation can be achieved using water-miscible organic solvents such as ethanol, isopropanol, methanol, and acetone, while isotonic agents like glucose, sodium chloride, xylitol, sorbitol, etc. are used for dilution. To improve its therapeutic performance, chemical modifications of pullulan have been developed. These resist amylase action, thereby slowing degradation in blood vessels. Gamma (γ)-irradiated pullulan with reduced M_w and viscosity has been identified as a suitable plasma expander candidate [197]. Furthermore, conjugation of cationic and anionic surfactants with γ-irradiated pullulan have been reported to produce fractions with narrower M_w distributions [198–200], enhancing its suitability for plasma substitution [194].

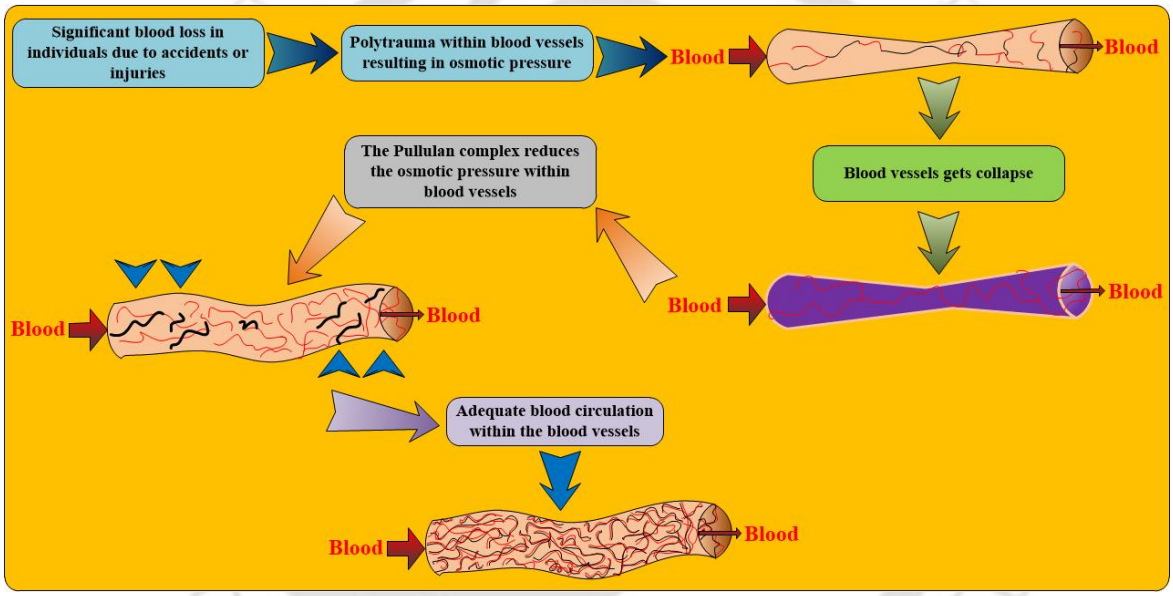

Figure 1.4 Application of pullulan as plasma expander.

1.9.1.7 Molecular chaperons

Molecular chaperones are unique supramolecular arrangements formed by the interaction of self-aggregated hydrophobic polymers with soluble proteins. These chaperones play a crucial role in improving the thermal stability and enzymatic activities of protein structures. By using the self-assembling technique, which involves assembling polymers as fundamental units, scientists have effectively developed functional nanogels and nanobiomaterials. Chaperone-like activity involves the ability to capture and release proteins. Molecular chaperones have the capability to selectively bind denatured proteins, preventing irreversible aggregation through host-guest interactions. Once bound, the host chaperone releases the protein in its refolded state. To improve the recovery yield of native proteins during refolding, researchers attempted

to use water-soluble polymers like polyethylene oxide (PEO) [201]. These polymers function by blocking the exposed hydrophobic surfaces on denatured proteins, effectively preventing protein aggregation. However, it is crucial not to bind too strongly to intermediates, as it could hinder the folding process into the native confirmation. Cholesteryl pullulan (CHP) nanoparticles modified to be hydrophobic have shown properties similar to molecular chaperones, especially in enzyme engineering. CHP has been reported to effectively enhance the thermal stability of proteins by capturing the denatured state of α-chymotrypsin within its self-aggregate and then releasing the restructured protein [202]. Even after being subjected to heat, the restructured chymotrypsin retains its stability, preserving 74 % of its initial enzyme activity without experiencing thermal unfolding. Likewise, hydrogel nanoparticles made from hydrophobized CHP have demonstrated the capacity to improve the thermal stability and reconfiguration of heat-denatured Carbonic Anhydrase B (CAB) [192]. CHP helped in refolding the heat-denatured CAB, leading to ~ 100 % recovery of enzyme activity and further stabilizing the refolded form of CAB, protecting it from irreversible heat denaturation. Certain CHP nanogels responsive to both heat and light have been known to function as molecular chaperones, significantly boosting the activity of citrate synthase [201]. Additionally, it has been discovered that CHP nanogels effectively inhibit the aggregation of enzymes such as citrate synthase, lipase, and horseradish peroxidase. When CHP was combined with 2-methacryloyloxyethyl phosphorylcholine, it enhanced the capture of denatured insulin or CAB, followed by the subsequent release of these proteins in their restructured states [203]. Figure 1.5 depicts an overview of the application of pullulan as molecular chaperones.

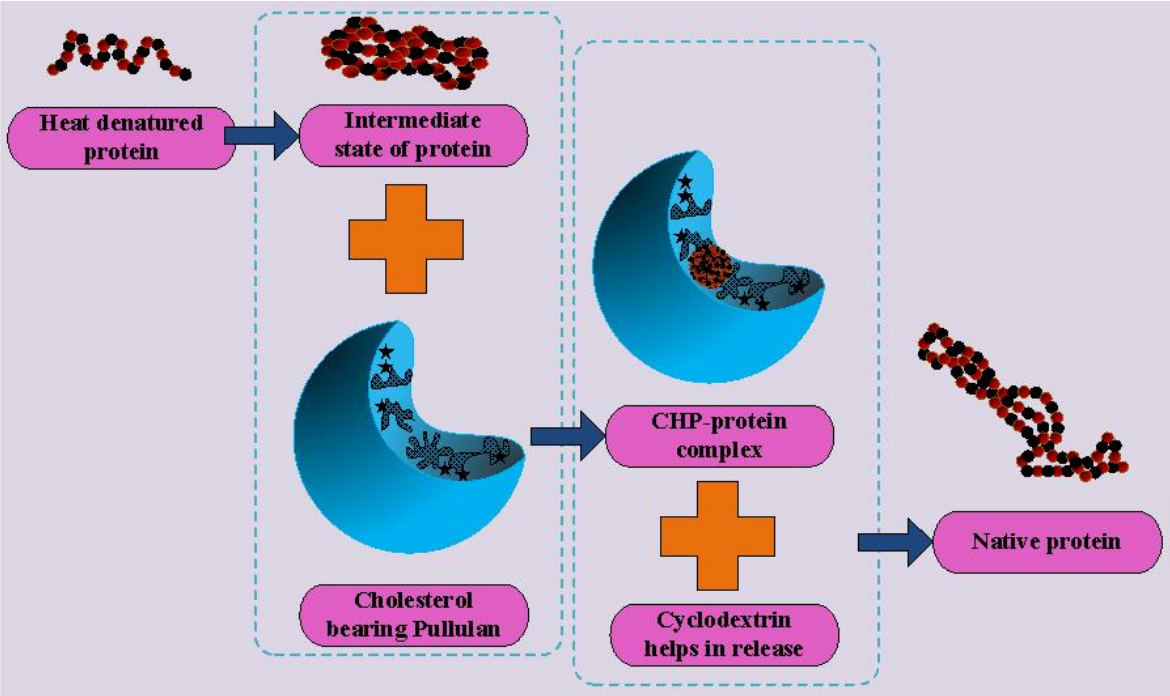

Figure 1.5 Application of pullulan as molecular chaperones.

1.9.2 Cosmetics and pharmaceuticals

Pullulan, recognized for its biocompatibility, skin-friendly properties, and environmental sustainability, has attracted considerable attention within the cosmetic sector [50,204]. Due to its non-toxic nature and environmentally friendly characteristics, pullulan is frequently used in producing biopolymer nanocomposites. In cosmetics, pullulan shows promising potential to reduce photoirritancy and photoactinic responses, skin irritation and sensitivity caused by sunlight, which can happen when certain ingredients are absorbed into the body. It has been reported that sunscreen formulations containing pullulan-dioxybenzone provided protection against harmful UV rays, while shielding dioxybenzone from the hypochromic impact caused by noncovalent π-π molecular stacking. Unlike free dioxybenzone, which readily penetrated the epidermis and dermis, pullulan–dioxybenzone largely remained on the skin surface in hairless mice, thereby offering effective UVA/UVB protection without systemic absorption [205]. Its durability and resistance to gas penetration allow it to function as a clear and environmentally friendly material for cosmeceutical uses [206–209]. Researchers have found that skin penetration is influenced by molecular weight, with components under 500 Da capable of having systemic effects [210,211]. Xiao et al. [212] prepared PVA/pullulan aerogels with tunable composition that demonstrated high water absorption and retention, mechanical softness, and flexibility in both dry and wet states, making them well-suited for skin-contact applications. Their rapid release of loaded ascorbic acid (> 90 % within 30 mins) demonstrated

their potential as delivery systems in facial masks. Pullulan has a significant role in cosmetics, particularly in addressing concerns related to phototoxicity and photoallergic reactions resulting from the systemic absorption of certain ingredients. By utilizing pullulan in cosmetic products, it is possible to create safer and chemical-free options, minimizing allergic and inflammatory reactions. These products may contribute positively to skin cell proliferation and lifespan, potentially mitigating aging effects [213]. Facial masks containing pullulan have been shown to possess rejuvenating effects on the structural integrity of the skin, providing significant cosmeceutical advantages [214]. Self-dissolving microneedles made from pullulan have been used for the transdermal distribution of various cosmetic biomolecules, regardless of their size [215]. Pullulan has been used in creating cosmetic products aimed at skin rejuvenation, shampoos, eye creams, facial powders, hair treatments, and facial masks blended with diverse ingredients for skin brightening and addressing hyperpigmentation concerns [216–218]. Its capacity to disperse across a surface, create films, and hold liquids, such as water, makes it suitable for these applications [22,50,219–221]. Pullulan, in conjunction with other biomaterials such as chitin nanofibrils and nanolignin, has been reported to be beneficial in rejuvenating the skin of elderly individuals [222]. The rising demand for effective and revitalizing cosmeceutical items aimed at preserving youthful looks indicates a promising future market for anti-aging cosmeceuticals. By blending pullulan with low molecular weight polymers, inorganic substances, fragrances, and preservatives, superior cosmeceutical products can be formulated, enhancing the structural characteristics of human skin [223]. Furthermore, pullulan can also be used in the dental field as a dental adhesive and dental powder owing to its stabilizing and adhesive characteristics. A patent has been submitted for a pullulan-based ingestible film integrated with essential oils (thymol, menthol, eucalyptol, and methyl salicylate), serving as an antimicrobial agent against bacteria responsible for gingivitis, halitosis, and dental plaque [224].

1.9.3 Food industry

The food packaging sector has experienced notable advancements due to increasing demands for food safety. Over the past few decades, polymers, such as plastic, have dominated food packaging due to their numerous advantages, such as cost-effectiveness, lightweight nature, heat-sealing capabilities, and adaptability to various packaging requirements. However, their non-biodegradable nature poses a major environmental concern as they accumulate and spread as waste, posing a threat to both humans and the environment. To address these concerns, the adoption of naturally degradable materials has emerged as the most effective solution. Natural

polysaccharides have gained considerable attention for their film-forming ability, nutritional functionality, and chemical stability. Being abundant, non-toxic, biodegradable, and biocompatible, these biopolymers offer promising potential for sustainable food packaging applications [225,226]. Among these, pullulan, a fungal exopolysaccharide, is considered an ideal raw material for producing food packaging materials owing to its remarkable biodegradability, biocompatibility, and thermal stability. Moreover, the Food and Drug Administration (FDA) has recognized pullulan as safe for use in food products due to its Generally Recognized as Safe (GRAS) status, making it suitable for incorporation into food items [227] and the effective production of edible films [228,229]. These unique characteristics of pullulan contribute to its various uses in the food and related industries. Being odourless, tasteless, and biodegradable, it offers excellent properties for creating high-quality films that can be used as non-polluting food packaging material [230,231]. Films made from pullulan exhibit unique characteristics including transparency, lack of pigmentation and odour, and low permeability to oil and oxygen. Pullulan can be utilized to create a clear and distinct frosting layer on frozen food, acting as a protective glaze. It also serves as a low-calorie dietary fiber substitute for starch in food preparations. Moreover, its exceptional oxygen barrier properties help extend the shelf-life of sensitive food items, reducing waste and enhancing product sustainability. Additionally, it functions as a dispersing agent in beverages, effectively inhibiting the occurrence of turbidity and the formation of sediment [232]. Table 1.3 summarizes previous studies on the use of pullulan-based composites in food packaging and edible coatings, and a few recent examples are discussed below to highlight important results and developments.

Enhancing food safety and extending shelf life can be achieved through the use of antimicrobial food-packaging films. Kraśniewska et al. [233] developed a polyethylene terephthalate/polypropylene-based active packaging film coated with pullulan and enriched with clove essential oil. The film demonstrated improved UV-light barrier, antioxidant, and antibacterial properties; particularly against Gram-negative bacteria, while maintaining transparency and preserving the visual quality of packaged spinach. Another study by Liu et al. [234] developed soluble soybean polysaccharide/pullulan films incorporating lavender or clove essential oils with enhanced antioxidant, antibacterial, and UV-barrier properties. The clove essential oil-enriched films exhibited superior performance, particularly in free radical scavenging and bacterial inhibition, making them more suitable for active food packaging. Mayakrishnan et al. [235] prepared bio-nanocomposite films using pullulan, lignin and silicon carbide for high-performance active food packaging applications. The incorporation of silicon

carbide enhanced film properties by increasing hydrophobicity, tensile strength, antibacterial activity, and opacity, while reducing moisture content, porosity, and gas/water vapour transmission rates. Afzia et al. [236] prepared biocomposite films from pectin/pullulan, reinforced with cassava peel-derived cellulose nanofibers, and optionally combined with olive oil, which showed improved thermal stability, barrier properties and mechanical strength. These films effectively preserved chicken meat quality by reducing weight loss, slowing bacterial growth, and maintaining texture, highlighting their potential as sustainable alternatives to conventional plastic packaging. In another study by Sul et al. [237] nitrogen-doped carbon dots derived from tangerine peel were incorporated into chitosan/pullulan films, resulting in active packaging with enhanced antibacterial, antioxidant, and UV-blocking properties. These films helped preserve sliced bread during refrigerated storage by suppressing microbial contamination, thereby prolonging its shelf life. This study highlights the potential of using food waste-derived carbon dots as functional additives in sustainable packaging. Bian et al. [238] developed pullulan-based films incorporating gellan gum and extracts from *Broussonetia papyrifera* with strong antioxidant, antibacterial, and UV-blocking properties, along with good mechanical strength and biodegradability. The films also showed clear colour changes in response to pH and amine levels, making them suitable for monitoring fish freshness. These features demonstrated their potential as multifunctional, eco-friendly packaging materials with built-in spoilage indicators. Madihalli et al. [239] developed chitosan/pullulan films integrated with quinic acid and montmorillonite (MMT) that showed improved mechanical, UV-protective, and antimicrobial properties. It also demonstrated superior performance in preserving tofu by minimizing weight loss, maintaining nutrient content, and inhibiting microbial growth over 72 hrs. In another study, Dong et al. [240] prepared edible composite films by combining pullulan with soy protein amyloid fibrils, achieving about a threefold improvement in mechanical strength through hydrogen bonding. The films also showed improved antimicrobial activity, hydrophobicity, and moisture resistance compared to those made with soy protein isolate. Additionally, when loaded with epigallocatechin gallate, the films demonstrated effective release in simulated oral conditions, suggesting their potential for oral rapid-release applications. Gan et al. [241] developed edible films incorporating bacterial levan with pullulan, chitosan, and ε-polylysine that showed UV-blocking, water resistance, oxygen barrier properties, and flexibility with higher levan content. These films also demonstrated strong antimicrobial activity, biodegradability, and effectively preserved strawberries by reducing water loss and microbial growth during storage. Gasti et al. [242] developed a sustainable nanocomposite film by incorporating hybrid nanoparticles

composed of chitosan and zinc oxide (ZnO), infused with clove essential oil, into a chitosan/pullulan matrix for use in food packaging. The inclusion of these nanoparticles significantly enhanced the UV-blocking capability, barrier efficiency, mechanical strength, and water resistance of the film, while also providing strong antioxidant and antimicrobial properties. When applied to chicken meat storage, it extended shelf life by up to five days under refrigeration, demonstrating its potential for sustainable food preservation. Kumar et al. [243] reported the development of a composite edible coating consisting of chitosan and pullulan in a 50 : 50 ratio, enhanced with pomegranate peel extract. This specific blend of chitosan and pullulan demonstrated its efficacy in preserving the quality and prolonging the post-harvest shelf life of litchi fruits during storage under both room temperature of 23 ºC and cold storage conditions of 4 ºC (Figure 1.6).

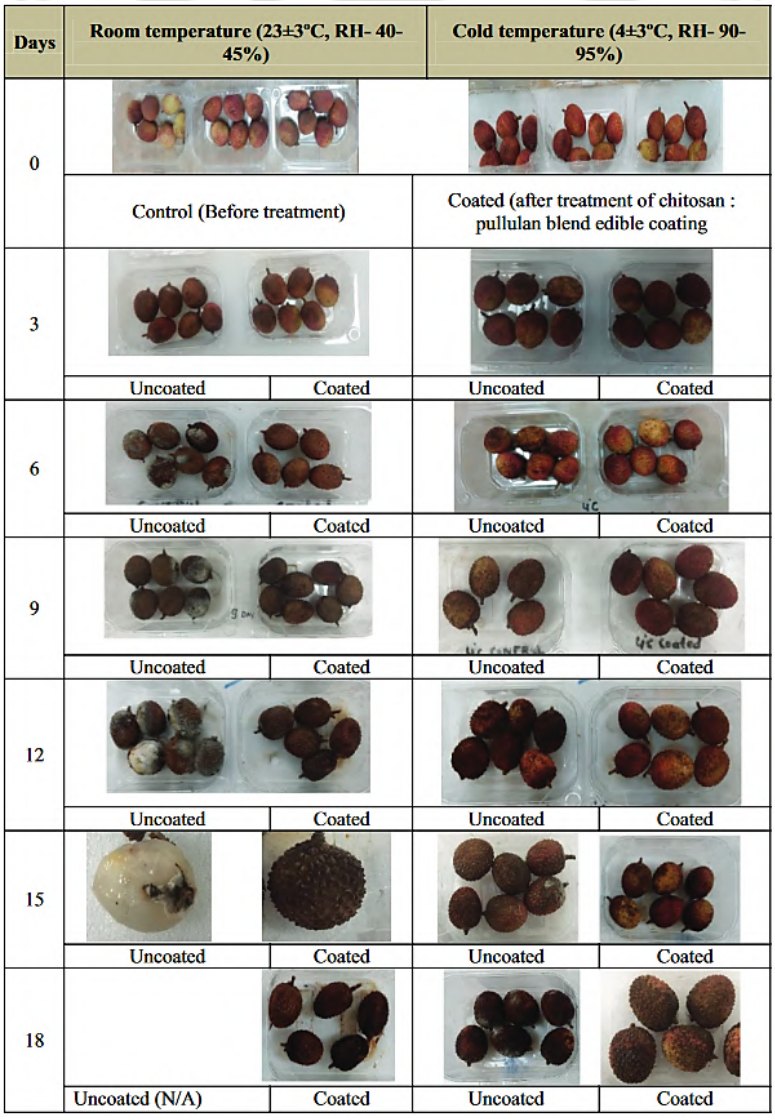

Figure 1.6 Chitosan/ pullulan composites for improvement of shelf life and quality of litchi [243].

Silva et al. [244] demonstrated a cost-efficient solvent casting method to prepare transparent films consisting of pullulan reinforced with lysozyme nanofibers (Figure 1.7). These resulting nanocomposite films exhibited a high degree of uniformity, transparency, and gloss, along with impressive mechanical strength and thermal stability. The incorporation of lysozyme nanofibers to pullulan not only improved its strength but also introduced new functionalities, including notable antioxidant and antibacterial properties.

Table 1.3 Different pullulan-based composites for use in food grade applications.

Composites	Applications	References
Polyethylene terephthalate/polypropylene/pullulan/clove essential oil	Preservation of packaged spinach	[233]
Soluble soybean polysaccharide /pullulan/lavender or clove essential oils	Food packaging	[234]
Pullulan/lignin/silicon carbide	Food packaging	[235]
Pectin/pullulan/cassava peel-derived cellulose nanofibers/olive oil	Chicken meat preservation	[236]
Chitosan/pullulan/nitrogen-doped carbon dots derived from tangerine peel	Sliced bread preservation	[237]
Gella gum/ pullulan/ *Broussonetia papyrifera extract*	Food packaging	[238]
Chitosan/pullulan/quinic acid/ montmorillonite	Tofu preservation	[239]
Soy protein amyloid fibrils/pullulan	Food packaging	[240]
Carvacrol/cyclodextrin/gelatin/pullulan nanofibers	Food packaging	[245]
Levan/pullulan/chitosan/ε-polylysine	Food packaging	[241]
Chitosan/pullulan/ chitosan-ZnO hybrid nanoparticles loaded with clove essential oil	Food packaging	[242]
Pectin/pullulan	Enhance shelf life of peanuts	[246]
Pullulan/pectin/grape seed extract	Diminished lipid oxidation in both uncooked and roasted peanuts	[246]
Pullulan/chitin nanofibers containing curcumin and anthocyanins	Intelligent food packaging	[247]
Pectin/pullulan	Food packaging	[231,246]

Carboxymethyl chitosan/pullulan	Mango preservation	[248]
Chickpea protein isolate/pullulan	Food packaging	[249]
Chitosan/pullulan/pomegranate peel extract	Enhance shelf life and quality of tomato, green bell pepper and mango	[250–252]
Pea protein isolate/pullulan	Extension of shelf life of foods/delivery system for enhancement of food products with added value	[253]
Lysozyme nanofibers/pullulan	Food packaging	[244]
Chitosan/pullulan and carboxymethyl chitosan/pullulan	Edible films	[254]
Carboxymethyl-gellan/pullulan	Edible films	[255]
Casein/pullulan	Food packaging	[256]
Whey protein/pullulan	Entrapment of probiotic *Lactobacillus acidophilus*	[257]
Amaranth protein/pullulan	Encapsulation of bioactives	[258]
Nanofibrillated cellulose/pullulan	Dry food packaging	[259]
Whey protein isolate/pullulan films with nano-SiO_2	Improve food shelf life and in packaging	[260]
Pullulan/sodium alginate	Edible films	[261]
Pullulan/alginate incorporated with capsaicin	Edible films	[262]
Esterification of pullulan using octenyl succinylation	Enhance shelf life of sapota fruits (*Manilkara zapota*)	[263]
Pullulan/sorbitol/sucrose fatty acid ester	Enhance shelf life of fruits	[264]
Whey protein isolate/pullulan	Extension of shelf life of chestnut fruits	[265]
Pullulan/glutathione/chitooligosaccharides	Extension of shelf life of fresh-cut ‘Fuji’ apples	[266]

Oligosaccharides derived from *Laminaria japonica* /pullulan	Extend shelf life of cherry tomato	[267]
Chitosan/pullulan	Enhance quality and shelf life of litchi	[243]

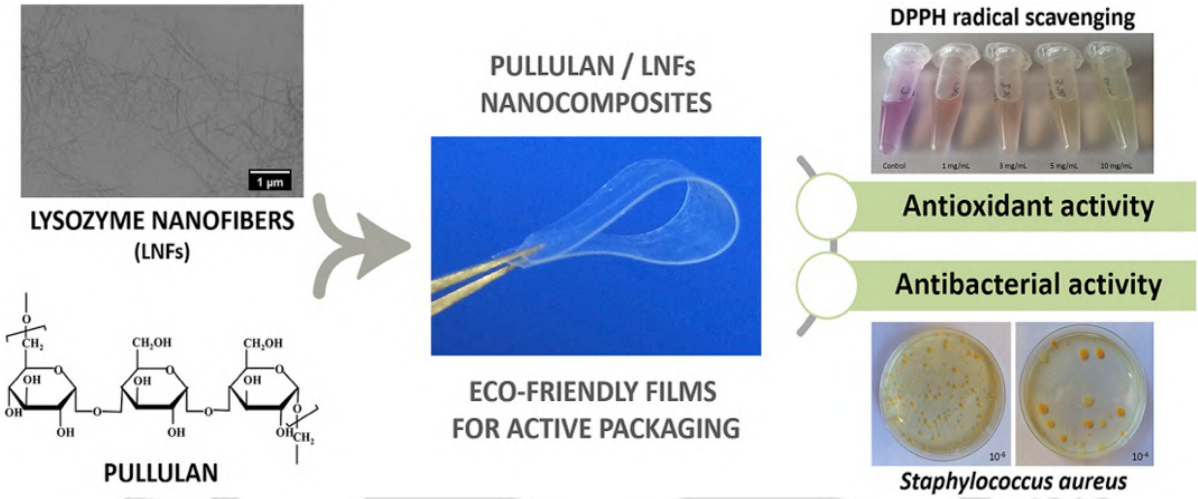

Figure 1.7 Pullulan-based nanocomposites for food packaging with antioxidant and antibacterial properties [244].

1.9.4 Other applications

- ***Waste mitigation and water purification***

  Water contamination from industrial effluents, heavy metals, aromatic compounds, and synthetic dyes remains a major environmental challenge. As a result, there is an increasing need for efficient and high-value treatment of heavy metal-containing effluents [268,269]. Microbial strains producing extracellular polysaccharides have shown promise in water remediation because of their ability to sequester heavy metals through biosorption. This process involves the interaction between metal cations and the acidic functional groups of the polysaccharide [270,271]. In response to the challenge of eliminating anionic dyes from water, scientists developed microspheres made of pullulan-graft-poly(3-acrylamidopropyl trimethylammonium chloride) (P-g-pAPTAC). These microspheres were produced through suspension cross-linking of pullulan that had been pre-modified with cationic components. The uptake of Azocarmine B by the microspheres served as a model system to demonstrate their effectiveness in eliminating anionic dyes from aqueous solutions. This study provides details on the preparation and characterization of these cross-linked pullulan

microspheres with grafted cationic properties, as well as their capability to absorb sulfonated anionic dyes [272]. Sectors such as paper, textile, dye, and plastic manufacturing produce substantial volumes of contaminated wastewater owing to their extensive water consumption and the utilization of chemicals and dyes for product colouring. This wastewater, loaded with dyes, has the potential to significantly degrade water quality and pose risks to human health due to its carcinogenic, teratogenic, and mutagenic characteristics [273–275]. Managing wastewater containing dyes cause difficulties because the dyes resist aerobic digestion and remain stable against oxidizing agents. A range of physical, biological, and chemical techniques have been utilized for treating dye wastewater. However, often a combination of multiple approaches is required to attain the desired water quality in an economically feasible manner [276,277]. Therefore, there is a demand for the development of effective and industrially viable decolouration methods. Pullulan was chemically crosslinked separately with 1,2-bis(2,3-epoxypropoxy)-ethane (BEPE), tetramethylene glycol diglycidyl ether (TGDE) and epichlorohydrin (ECH). The TGDE-derived gel (Gel-T) exhibited a macro-porous structure and desirable swelling capacity while maintaining relative rigidity. The Gel-T being biocompatible, was combined with montmorillonite (MMT) to form a nanocomposite hydrogel system. This pullulan-constructed nanocomposite hydrogel exhibited an excellent adsorption capacity (80 mg/g) for crystal violet, making it an effective adsorption system for removing dyes from aqueous media [278]. In another study, pullulan hydrogels containing MMT and polydopamine have been utilized in the elimination of crystal violet [279]. A composite nanogel, consisting of gellan and pullulan, was created using chemical crosslinking with 2,2-diphenyl-1-picrylhydrazyl (DPPH). This nanogel was used for the adsorption of methylene blue from aqueous media [280]. Cationized pullulan demonstrated enhanced pesticide flocculation with decreasing emulsion pH and increasing degree of substitution [281,282]. The sodium salt of succinylated pullulan exhibited a remarkable 90 % removal of Cadmium (Cd) from spiked water within the initial 15 mins [283]. During fermentation on acid peat hydrolysate, metals accumulate in the *A. pullulans* CH-1 biomass, making this microorganism appropriate for decreasing metal levels. This technology effectively combined the biosynthesis of pullulan using the *A. pullulans* strain CH-1 with simultaneous biosorption of metals, offering a practical solution for mitigating metal pollution. Moreover, the excellent attributes of pullulan such as its comparable transparency, roughness, hardness, and gloss make it a

sustainable alternative to synthetic polymers such as polystyrene and polyvinyl chloride (PVC), which pose environmental hazards when carelessly disposed of [284,285]. Pullulan is also known to serve as a reducing, stabilizing, and capping agent in the production of metallic nanoparticles, showing promise in photo-decolorization applications. Isa et al. [286] examined the amalgamation of pullulan and zinc oxide (ZnO) nanoparticles for the swift photo-decolorization of Methyl Orange and Rhodamine B. Pullulan acted as a capping agent, while ZnO nanoparticles served as catalyst. The synthesis conditions of ZnO nanoparticles, particularly at 400 °C and 1 hr of calcination, significantly influenced the degradation of dyes, leading to effective photocatalytic removal of dyes such as Methyl Orange and Rhodamine B. In another study by Isa et al. [287], pullulan-assisted porous ZnO microflowers were prepared through a precipitation approach for the photocatalytic degradation of Methyl Orange. Additionally, cationic derivatives of pullulan have been reported as efficient flocculants for industrial wastewater treatment, particularly in the removal of metal oxides, dyes, and pesticide residues [291]. Sonmez et al [288] prepared pullulan-based hydrogels through free radical solution polymerization. As shown in Figure 1.8, these hydrogels exhibited significant capability in adsorbing five different metal ions (cadmium(II), mercury(II), nickel(II), copper(II) and zinc(II) ions) and demonstrated favourable reusability characteristics, making them promising options for applications in metal removal from water.

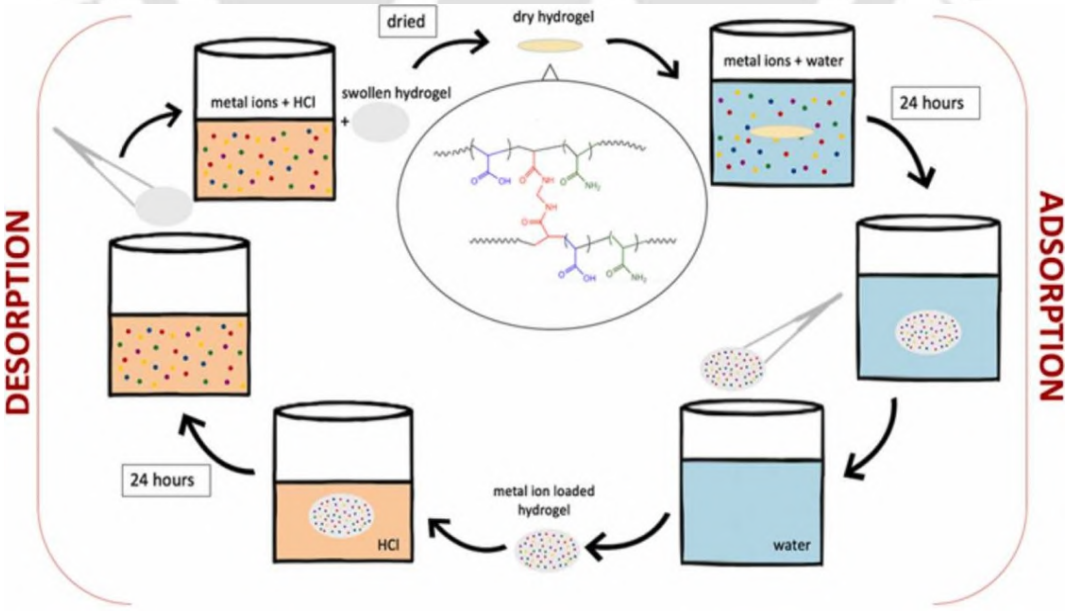

Figure 1.8 Pullulan based hydrogels for metal ions removal from water [288]**.**

- ***Electronics, oil recovery, and fiber formation***

  It has been reported that cyanoethylated pullulan offers promising applications in sensors and low-frequency amplifiers [289]. Furthermore, this natural polymer has been acknowledged for its capacity to improve the retrieval of crude oil in the petroleum extraction process [290]. Pullulan can also be spun into fibers with characteristics similar to rayon or nylon through dry or wet spinning, and can be extruded into materials resembling polystyrene or polyvinyl alcohol (PVA) [6,15].

1.10 Chapter summary

Pullulan has been recognized as a versatile and sustainable biopolymer, finding applications across diverse industries. Its unique properties, such as being non-toxic, biodegradable, and water-soluble, make it an promising alternative to synthetic polymers. Throughout this chapter, we have explored its production process and discussed its diverse applications in different fields. In the field of production, significant improvements have been made in optimizing pullulan extraction techniques. Advancements in microbial fermentation, particularly using different strains of *A. pullulans*, have led to increased yields and cost-effectiveness. Moreover, the development of novel bioreactor designs and the utilization of agro-industrial waste as feedstock have further enhanced the eco-friendliness of the production process. These advancements play a crucial role in promoting sustainability by mitigating the environmental burden associated with the polymer industry. The applications of pullulan are vast and continue to expand, driven by progressive research and technological advancements. In the food industry, pullulan has proven to be an excellent stabilizer, thickener, and film-forming agent, replacing synthetic additives and promoting healthier and safer products [231,292]. Its ability to form transparent and oxygen-permeable films makes it suitable for use in the packaging industry, offering a sustainable solution for enhancing the shelf life of perishable goods. Pharmaceutical and biomedical applications of pullulan have shown promise as well. Its biocompatibility and biodegradability make it a valuable material for drug delivery systems [131,132,134] and tissue engineering scaffolds [160]. As research in nanotechnology progresses, pullulan-based nanoparticles hold potential for targeted drug delivery, enabling more efficient and controlled treatments [139]. In the cosmetic sector, the film-forming and moisturizing properties of pullulan have gained attention. It has found application in skincare products, hair care formulations, [50,204] and even in the development of eco-friendly and biodegradable microbeads/ microspheres, replacing harmful plastic microbeads that pollute

water bodies [272]. Overall, this biodegradable polysaccharide has been widely explored in medicinal and other industrial applications, and its potential in drug delivery opens up new possibilities for the future.

1.11 Research gaps in prior literature

Although pullulan is a sustainable biopolymer known for its non-toxic, biodegradable, and excellent film-forming properties, there exists a research gap in its limited large-scale application due to its high production cost. To address this, extensive research is being explored on use of low-cost sugar sources such as agro-industrial residues, naturally derived sugars etc. Although many low-cost substrates have been explored, existing studies often lack optimization strategies or fail to assess performance across different microbial strains. Additionally, there is not much exploration of fermentation parameters that directly impact pullulan production and cost-effectiveness when using such alternative substrates.

For wound healing applications, single-layered scaffolds often fail to meet all the essential requirements, such as moisture regulation, exudate absorption, breathability, mechanical strength, and controlled drug release. For example, a purely hydrophilic scaffold may effectively absorb wound exudates but can be mechanically weak and may adhere to the wound surface, causing pain during removal of the wound dressing. On the other hand, a purely hydrophobic scaffold may offer better mechanical strength but often lacks adequate exudate absorption, potentially leading to excessive moisture build-up on the wound and impaired healing. To overcome these limitations, bilayered wound dressing scaffolds have emerged as a promising alternative. These scaffolds are designed to mimic the natural architecture of healthy skin, which consists of two specialized layers: the epidermis (a dense outer layer) and the dermis (an inner layer composed of loosely organized connective tissue with collagen, elastic fibers, and extracellular matrix components). Typically, bilayered scaffolds consist of a hydrophilic sublayer that promotes cell adhesion and proliferation, closely simulating the regenerative properties of the dermis. Above this, a dense hydrophobic top layer provides structural integrity, regulates moisture loss, and serves as a protective barrier against external contaminants, including microorganisms and fluids, thus maintaining an optimal healing environment. Despite many advancements in design of wound dressing materials, many existing wound dressings still lack either antimicrobial efficacy or sufficient mechanical properties. Therefore, there remains a critical need for the development of advanced wound dressing materials that combine these essential properties to enhance overall wound healing effectiveness.

For drug delivery applications, there remains the lack of an effective localized drug delivery system that can simultaneously deliver multiple drugs or therapeutic agents with distinct properties, such as hydrophilic and hydrophobic drugs. The conventional drug delivery systems often face several challenges, including systemic toxicity, poor drug targeting, limited control over drug release kinetics, and an increased risk of developing drug resistance. Notably, the cancerous tissues, especially those in skin-related malignancies like melanoma, are susceptible to secondary infections, which further complicate the process of treatment. There has been limited exploration of advanced nanofibrous systems that combine both anticancerous and antimicrobial agents within a single system while ensuring biocompatibility and sustained release.

For application in cosmetic formulations, pullulan has been explored in earlier literature for its film-forming and moisture-retentive properties. However, most of these either combined pullulan with synthetic or unspecified antibacterial agents or focused mainly on texture and moisturizing effects rather than antimicrobial action. Additionally, many topical skincare formulations often contain strong chemical preservatives including parabens, triclosan, and formaldehyde-releasing compounds. Although these ingredients are effective in reducing microbial load, their continued and prolonged use raise concerns about side effects such as allergic contact dermatitis, skin irritation, and disruption of the skin microbiome. More critically, the overuse of antibiotics in cosmetics has been linked to the development of antimicrobial resistance, which is a growing global health concern.

For food packaging applications, especially in preservation of fresh-cut fruits, there is an increasing demand to develop biodegradable, multifunctional materials that not only provide physical protection but also offer antimicrobial, antioxidant, and UV-blocking properties. Traditional plastic packaging poses serious environmental hazards and often lack active functional properties. Fresh-cut fruits are particularly susceptible to microbial spoilage, oxidation, and quality loss due to increased surface exposure. Although biopolymer-based edible coatings have shown promise as sustainable alternatives, many still lack sufficient functional properties for practical use.

Based on these research gaps, the following research objectives were designed to address the limitations.

1.12 Research objectives

- ***Objective 1:*** Shake-flask optimization of pullulan production by fungal fermentation of *Aureobasidium pullulans* NCIM 1049 using sugarcane jaggery as substrate.
- ***Objective 2:*** Preparation of bilayered wound healing scaffold with electrospun gentamicin-loaded pullulan/PVA/gum arabic nanofibers and solvent-casted PLA.
- ***Objective 3:*** Preparation of pullulan/PLGA dual drug-loaded core/sheath nanofibers by coaxial electro-centrifugal spinning and their *in vitro* cytotoxic efficacy towards melanoma cells.
- ***Objective 4:*** Formulation and characterization of antibacterial cosmetic skin-cream infused with pullulan and turkey berry (*Solanum torvum*) leaf extract.
- ***Objective 5:*** Preparation of chitosan nanoparticles and neem essential oil-functionalized pullulan/gum arabic biocomposites for edible food packaging.

Figure 1.9 presents a mind-map outlining the key research objectives of the present study within a structured framework.

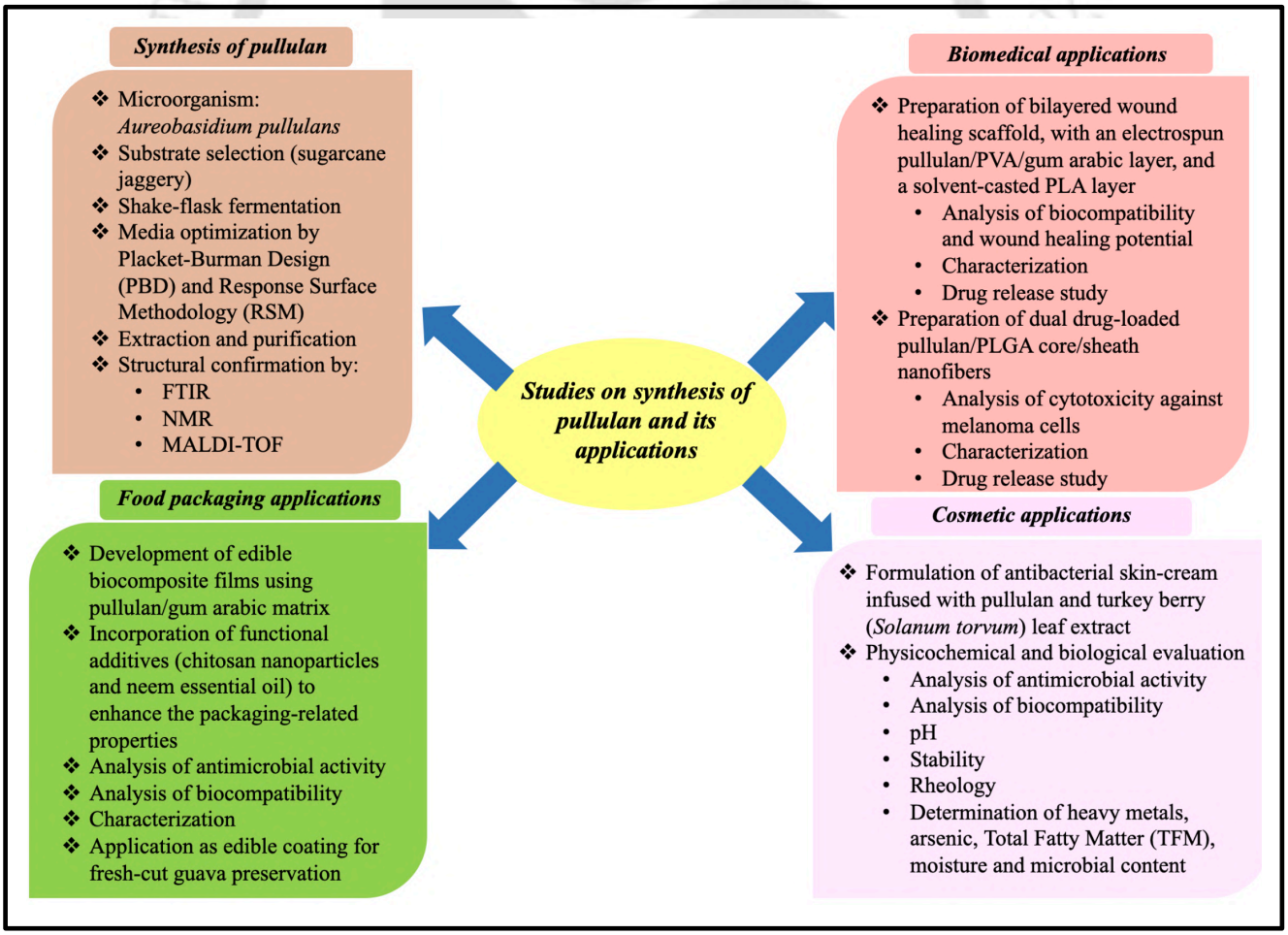

Figure 1.9 Mind-map illustrating the research objectives of the present study.

CHAPTER 2

MATERIALS AND METHODS

This chapter describes in detail the materials used, the step-by-step experimental procedures followed, and the techniques applied to analyze and evaluate the results across all phases of the study. The research was conducted in a series of interconnected stages, beginning with the optimization of pullulan production using shake-flask fermentation with the fungal strain A. pullulans NCIM 1049. It also explores the practical application of pullulan in preparing various functional products, including biomedical scaffolds, topical cosmetic formulations, and food packaging films. Each area of application required a different approach, carefully chosen to meet the specific goals of that part of the research. For example, the development of bilayered wound dressing scaffolds and dual drug-loaded nanofibers for possible melanoma treatment involved fabrication methods like electrospinning and solvent casting, as well as biological tests to check their safety and effectiveness. Similarly, the formulation of skin-cream and edible films involved blending pullulan with natural additives, followed by tests to assess their physical properties, skin compatibility, and antimicrobial activity. Throughout the study, standardized and widely accepted methods were used to prepare and test the samples. These included evaluations of physical appearance, surface morphology, mechanical properties, drug release, antimicrobial effects, and in vitro biocompatibility with living cells. Different analytical instrumentation techniques were used to validate the quality and performance of the developed materials. To ensure accuracy and reliability, all experiments were carried out in triplicate, with results recorded and analyzed accordingly.

The chapter is organized into six major sections, corresponding to the different experimental phases of the study. Section 2.1 describes the shake-flask optimization of pullulan production by *Aureobasidium pullulans* NCIM 1049 using sugarcane jaggery as a cost-effective carbon source. It includes details of microbial culture conditions, preparation and characterization of the substrate, screening of significant variables using Plackett–Burman Design (PBD), and media optimization using Response Surface Methodology (RSM), followed by extraction and purification procedures. Section 2.2 discusses about the preparation of a bilayered wound healing scaffold comprising an electrospun pullulan/PVA/gum arabic sublayer loaded with gentamicin sulfate and a solvent-casted PLA top layer. The section further details the physicochemical characterization, swelling behaviour, water vapour transmission rate, porosity, antibacterial properties, *in vitro* degradation analysis, biocompatibility studies, wound healing assay, and drug release kinetics. Section 2.3 describes the fabrication of dual drug-loaded pullulan/PLGA core-sheath nanofibers using coaxial electro-centrifugal spinning. The methodology includes nanofiber preparation, drug loading, *in vitro* drug release study, hydrolytic degradation analysis, and cytotoxicity evaluation against melanoma cells. Section 2.4 presents the formulation and characterization of an antibacterial cosmetic skin-cream infused with pullulan and turkey berry (*Solanum torvum*) leaf extract. The procedures include extract preparation, cream formulation, antibacterial activity assessment, cytotoxicity analysis, evaluation of physicochemical properties, determination of heavy metals and arsenic, total fatty matter (TFM), moisture content, microbial load, and rheological characterization. Section 2.5 details the preparation of chitosan nanoparticles and neem essential oil-functionalized pullulan/gum arabic biocomposites for edible food packaging applications. The section includes synthesis of chitosan nanoparticles, film preparation, evaluation of mechanical, thermal, water vapour barrier, antioxidant and antimicrobial properties, and biocompatibility. It also describes the application of the prepared filmogenic solution as edible coating for shelf-life enhancement of fresh-cut guava. Finally, Section 2.6 describes the analytical instrumentation and characterization techniques used throughout the study.

2.1 Shake-flask optimization of pullulan production by fungal fermentation of Aureobasidium pullulans NCIM 1049 using sugarcane jaggery as substrate

2.1.1 Materials

Yeast extract, ammonium sulfate ($(NH_4)_2SO_4$), potassium phosphate dibasic anhydrous (K_2HPO_4), magnesium sulfate heptahydrate ($MgSO_4 \cdot 7H_2O$), zinc sulfate pentahydrate

($ZnSO_4$.$5H_2O$), sodium chloride (NaCl), potato dextrose agar (PDA), potato dextrose broth (PDB), and D (+) glucose anhydrous were supplied by HiMedia Laboratories, India. Acetone, diethyl ether, and acetonitrile were procured from FINAR chemicals, India. The commercial pullulan standard was procured from Sisco Research Laboratories Pvt. Ltd. (SRL), India. Phenol, sulfuric acid (H_2SO_4) and deuterium oxide (D_2O) were procured from Sigma-Aldrich, USA. 2, 5-dihydroxybenzoic acid was purchased from Tokyo Chemical Industry (TCI). Fresh sugarcane stalks were purchased from Amingaon local market in Guwahati, Assam, India. Lyophilized culture of the yeast-like fungal strain, *A. pullulans* NCIM 1049 was obtained from National Chemical Laboratory (NCL), Pune, India.

2.1.2 Microorganism culture conditions

The fungal stock culture was maintained on PDA plates at 4 °C and sub-cultured after an interval of every 15 days. The *A. pullulans* cells from the PDA plate were then transferred to conical flasks containing PDB. This is the sterilized seed-culture medium, which was incubated at 30 °C, 200 rpm for 48 hrs in an orbital shaker and was used to inoculate the fermentation media.

2.1.3 Preparation of liquid sugarcane jaggery

Fresh sugarcane stalks were procured from the local market, thoroughly washed with distilled water, peeled, and crushed using a mechanical crusher to extract juice. The raw juice was filtered through a muslin cloth to remove suspended solids and fibers. The resulting juice was transferred to a glass beaker and concentrated by heating at 90°C for 3 hrs under constant stirring, until a viscous dark brown liquid (jaggery) was obtained. The concentrated syrup was then allowed to cool down to room temperature, aseptically transferred to sterile glass container, and stored at 4 °C for later use as a carbon source in the fermentation media.

2.1.4 Determination of total sugar content in the jaggery

Total sugar content in the jaggery was estimated using the phenol-sulfuric acid method, as reported by Dubois et al. [293] and Pathirana et al. [294] , with slight modifications. A standard calibration curve was prepared using known concentrations of D (+) glucose. For the assay, the diluted jaggery sample (1:500 v/v) was mixed with 1 ml of 5 % phenol solution, followed by addition of 5 ml of concentrated H_2SO_4. The reaction mixture was allowed to stand for 30 mins at room temperature to enable colour development. A blank solution containing 1 mL of distilled (Millipore) water in place of the jaggery sample was used as the control. Absorbance

was then measured at 490 nm using a UV–Vis spectrophotometer (Make: PerkinElmer, Model: Lambda 45) and the sugar concentration was calculated based on the standard curve. Based on this measured sugar content, the required volume of liquid jaggery was added to the fermentation medium to achieve the desired initial sugar concentrations, as discussed later under PBD and BBD experimental setups (Sections 2.1.5 and 2.1.6, respectively).

2.1.5 Screening of significant process variables using Plackett-Burman Design (PBD)

The experimental approach involved two main stages: an initial screening using the Plackett-Burman Design (PBD), followed by optimization using the Box-Behnken Design (BBD). PBD was used to identify which media components had a significant effect on pullulan production. Seven media components were examined in the study: jaggery, yeast extract, NaCl, K_2HPO_4, $(NH_4)_2SO_4$, $MgSO_4.7H_2O$, and $ZnSO_4.5H_2O$. This phase included 12 experiments, with each factor tested at two levels, represented as −1 and +1. The PBD method assumes a linear relationship and does not account for interactions among variables, making it suitable for screening the most significant factors. The design and statistical analysis of the PBD experiments were done using Minitab software (trial version), using the equation (1):

$$Y = \beta_0 + \sum \beta_i x_i \qquad (1)$$

where Y represents the response (pullulan production in g/L), x_i indicates the level of each variable, and β_0 and β_i are the intercept and coefficients, respectively. Based on analysis of variance (ANOVA), only the variables with p-values below 0.05 were considered statistically significant and selected for further optimization using Response Surface Methodology (RSM). The variables for pullulan production along with their corresponding coded levels used in the PBD have been presented in Table 2.1.

Table 2.1 Variables and their corresponding coded levels used in PBD for pullulan production by *A. pullulans*.

Variables (g/L)	**Coded levels**	
	Low (−1)	**High (+1)**
Jaggery	30	60

Variables (g/L)	Coded levels	
	Low (−1)	High (+1)
K_2HPO_4	1	4
Yeast extract	1	4
$(NH_4)_2SO_4$	0.5	1.5
NaCl	0.5	2.5
$MgSO_4.7H_2O$	0.1	0.5
$ZnSO_4.5H_2O$	0.01	0.05

2.1.6 Media optimization by Response Surface Methodology (RSM)

The key variables found to significantly influence pullulan production during the Plackett-Burman screening, namely jaggery, yeast extract and NaCl, were selected as the independent variables for further optimization using a Box-Behnken Design (BBD). The remaining components in the growth medium (K_2HPO_4, $(NH_4)_2SO_4$, $MgSO_4.7H_2O$, $ZnSO_4.5H_2O$), along with the initial pH of 6 and incubation period of 7 days, were held constant at the levels identified in the PBD phase for maximising pullulan production. The BBD model consisted of 17 experimental runs, including five replicates at the center point. The concentration ranges for jaggery, yeast extract, and NaCl were set based on prior experimental trials for pullulan production: jaggery (30–60 g/L), yeast extract (1–4 g/L), and NaCl (0.5–2.5 g/L). Variables were coded at three levels (−1, 0, +1) to represent low, mean, and high values, respectively. Each experimental run was conducted as per the software-generated combinations, and the corresponding pullulan production (responses) were recorded. The design and statistical analysis of the BBD experiments were done using Minitab software (trial version).

For statistical analysis, the variables were coded using the following equation (2):

$$x_i = (X_i - X_0)/\Delta X \qquad (2)$$

Where x_i is the coded value, X_i is the actual value of the variable, X_0 is the value at the center point, and ΔX represents the step change in the uncoded variable.

A quadratic regression model, as shown in equation (3), was used in Response Surface Methodology (RSM) to capture the relationship between the dependent (response) and independent variables:

$$y = a_0 + \sum a_i x_i + \sum a_{ii} x_i^2 + \sum\sum a_{ij} x_i x_j \quad (3)$$

In this equation, y represents the response variable, a_0, a_i, a_{ii}, and a_{ij} are the regression coefficients, and x_i and x_j are the independent variables. According to the ANOVA, only those variables with p-values less than 0.05 were considered to have a statistically significant effect. The model's fit was assessed using the coefficient of determination (R^2). Minitab response optimizer tool was used to find the optimal conditions for maximising pullulan production, with the values of the independent variables kept within ranges of their various levels. The optimized condition, having a desirability value close to 1, was validated in triplicate experiments. The 3D surface and contour plots were made using the Design Expert software (trial version) at the same conditions for better visual representation. A summary of the variables and their coded levels is presented in Table 2.2.

Table 2.2 Selected variables along with their corresponding coded levels used in BBD for pullulan production by *A. pullulans*.

Variables (g/L)		**Coded levels**	
	Low (−)	**Center (0)**	**High (+1)**
Jaggery	30	45	60
Yeast extract	1	2.5	4
NaCl	0.5	1.5	2.5

2.1.7 Fermentation conditions

The required amount of sugar source (liquid sugarcane jaggery) was taken along with production media containing each of the components (yeast extract, $(NH_4)_2SO_4$, K_2HPO_4, $MgSO_4.7H_2O$, $ZnSO_4$ $.5H_2O$ and NaCl) according to the PBD and BBD models. The prepared media were autoclaved for 15 min at 121 ºC. After sterilization, the media were allowed to cool before being inoculated with 2 % (v/v) of a 48-hr-old *A. pullulans* culture, resulting in an

initial cell concentration of approximately 1×10^7 cells/mL. The fermentation was carried out for a period of 7 days, conducted in 250 mL Erlenmeyer flasks sealed with cotton plugs, each containing 100 mL of the sterilized production medium.

2.1.8 Extraction and purification of pullulan

The A. pullulans cells were separated from the fermentation broth by centrifugation at 2500 × g for 10 mins at 4 °C. Pullulan was then precipitated from the cell-free supernatant or broth by adding two volumes of ice-cold ethanol [53,295]. In the present study, additional purification steps were included. The precipitate was washed three times with acetone and diethyl ether, followed by dissolution in deionized water. Dialysis was carried out at 4 °C for 3 days using tubing with a 12,000–14,000 Da molecular weight cutoff, with five changes of deionised water to remove residual salts and impurities. The dialyzed solution was finally lyophilized to obtain purified pullulan in powdered form. The lyophilised pullulan powder was then weighed to estimate its concentration, which was expressed in grams per liter (g/L).

Analytical instrumentation and characterization techniques used: Fourier Transform Infrared (FTIR) spectroscopy, Proton Nuclear Magnetic Resonance (^{1}H NMR), Carbon Nuclear Magnetic Resonance (^{13}C NMR), and Matrix-Assisted Laser Desorption Ionization-Time of Flight Mass Spectrometry (MALDI-TOF MS) analyses.

2.2 Preparation of bilayered wound healing scaffold with electrospun gentamicin-loaded pullulan/PVA/gum arabic nanofibers and solvent-casted PLA

2.2.1 Materials

Pullulan was supplied by Sisco Research Laboratories Pvt. Ltd. (SRL), India. PVA (Molecular weight (M_w): 89,000–98,000, percentage of hydrolysis: 99+ %), gum arabic (Source: from acacia tree), Dulbecco's Modified Eagle's Medium (DMEM), 3-(4,5-dimethylthiazol-2-yl)-2,5-diphenyltetrazolium bromide (MTT), poly-D-lysine, phosphate-buffered saline (PBS) and dimethyl sulfoxide (DMSO) were procured from Sigma-Aldrich, USA. Extrusion grade 2003D PLA (NatureWorks® LLC, USA, density- 1.24 g/cc) was used for the study. Chloroform and glutaraldehyde were procured from Merck, Germany. Gentamicin sulfate, Luria–Bertani (LB) agar and broth were supplied by HiMedia Laboratories, India. The human dermal fibroblast (HDF) cell line and the bacterial strains (*Staphylococcus aureus* (*S. aureus*), ATCC 29213 and

Escherichia coli (*E. coli*), ATCC 25922) were purchased from American Type Culture Collection (ATCC), USA.

2.2.2 Preparation of top layer by solvent-casting

The casting solution was formulated by dissolution of 1 % (w/v) PLA in chloroform and subjected to stirring overnight. Then, the resultant solution was solvent-casted on glass Petri plate and dried in a fume hood at room temperature (25 ± 2 °C) for a period of 24 hrs to prepare the solvent-casted hydrophobic top layer, as shown in Figure 2.1 (a).

2.2.3 Preparation of sublayer by electrospinning

The nanofibrous layer (or the hydrophilic sublayer) composed of pullulan, PVA and gum arabic was prepared using the electrospinning technique performed at 20 kV (Make: ESpin Nanotech, Model: ES-2).

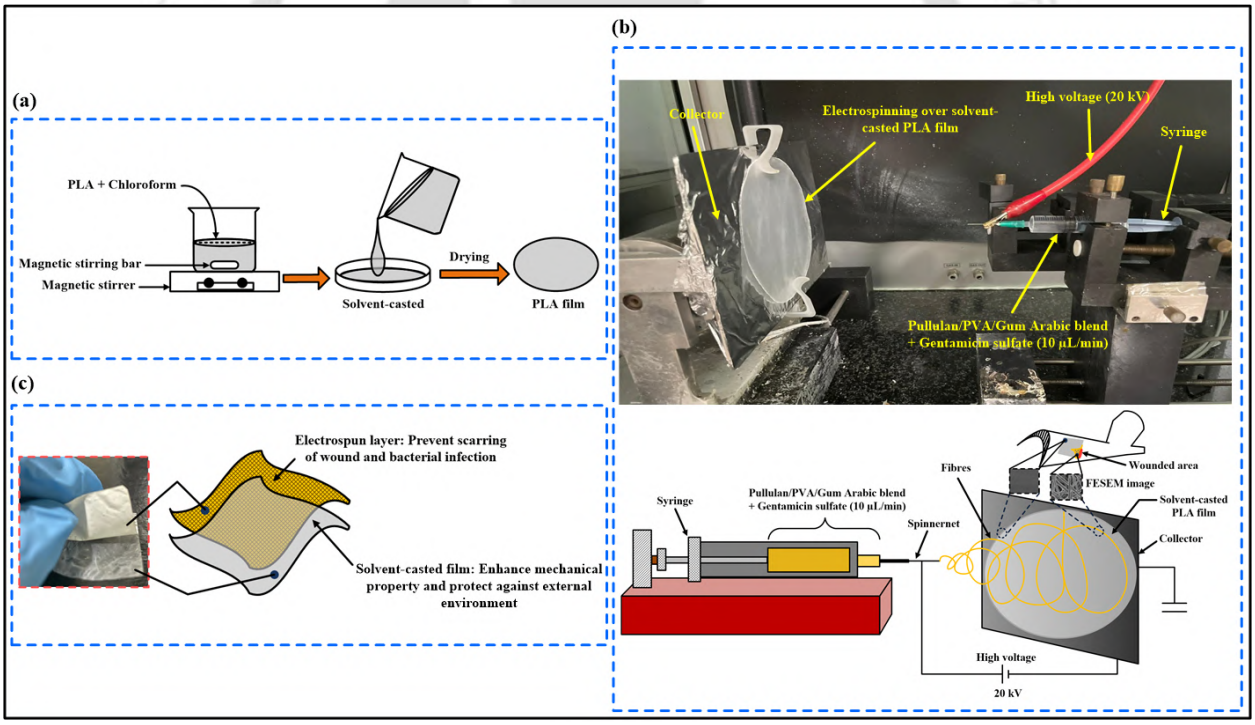

Figure 2.1 Steps involved in the preparation of the bilayered scaffold.

Pullulan, PVA and gum arabic were mixed to form the blend solution in distilled water (Millipore), having a ratio of 30/60/10. The solution underwent stirring at 90 °C for 4 hrs, followed by incorporation of 25 % aqueous glutaraldehyde (2 % v/v) to introduce crosslinking. The drug delivery system in wound healing scaffolds should consist of a bioabsorbable component with a large surface area to promote cell adhesion and proliferation. Therefore, an

antibacterial drug, gentamicin sulfate (0.5 mg/ml) was loaded into the nanofibers during electrospinning. Two sets of solutions were prepared (one with and another without gentamicin sulfate), and a 10 µL/min flow rate was maintained in each case. The resulting fibers were collected over the solvent-casted PLA layer (Figure 2.1 (b)), which was positioned horizontally to the spinning needle tip, with the tip at a 12 cm distance from the collector. A visual representation of the fabricated bilayered scaffold is depicted in Figure 2.1 (c).

2.2.4 Thickness, swelling index and moisture content

The average thickness of the scaffold was calculated using a digital micrometer at eight random locations [296]. The swelling index and moisture content were calculated, as reported in prior studies [297,298]. The moisture content is defined as the scaffold volume occupied by water molecules [299]. Initially, a known quantity of scaffold was dried at 105 °C till it attained the constant weight (m_1). Next, the dry scaffold was kept in distilled water (pH 7) at 37 °C for 24 hrs. Following this, the wet weight (m_2) was measured at specific time intervals [297,300,301]. The measurements were taken in triplicates, and the particulars were calculated using equations (4) and (5).

$$\text{Swelling index } (\%) = \left(\frac{m_2 - m_1}{m_1} \right) \times 100 \tag{4}$$

$$\text{Moisture content } (\%) = \left(\frac{m_2 - m_1}{m_2} \right) \times 100 \tag{5}$$

2.2.5 WVTR characterization

Water vapour transmission rate (WVTR) of the fabricated scaffold was determined using cup method (ASTM E96 standard), and the measurements were taken in triplicates. Sample containers filled with distilled water (Millipore) were taken to conduct this analysis. The fabricated scaffolds were attached to the mouth of each container (outer diameter: 44.31 mm, inner diameter: 42.60 mm), and a low density polyethylene (LDPE) film was used as the control. The containers were retained in an environmental chamber maintained at 40 ± 2 % relative humidity and a temperature of 37 °C for 6 days. Over this period, the weight of the containers was recorded after every 24-hr interval. The amount of water vapour lost from the cups was determined by calculating their weight losses over time. Equation (6) was used to determine the WVTR:

$$\text{WVTR}\,(\text{g/m}^2/\text{day}) = \left(\frac{\text{Change in sample weight}}{\text{Area of opening of the container} \times \text{Time}} \right) \quad (6)$$

2.2.6 Porosity

The porosity of the bilayered scaffold and the electrospun layer was measured using the liquid displacement method, with ethanol chosen as the displacement medium due to its non-swelling, non-degrading properties and ease of penetration. Prior to analysis, the samples were weighed and placed in a graduated cylinder containing a known volume (V_1) of ethanol for 5 mins. Following this, evacuation–pressurization cycles were applied to drive ethanol into the sample pores, repeating until air bubbles have ceased to form, and the final volume (V_2) was recorded. After removing the ethanol-impregnated samples from the cylinder, the volume (V_s) was determined and the porosity was calculated using the following equation (7) as reported by Khan et al. [302]:

$$\text{Porosity} = \left(\frac{V_1 - V_s}{V_2 - V_s} \right) \times 100 \quad (7)$$

2.2.7 Antibacterial property

The antibacterial effectiveness of the bilayered scaffold was examined against *S. aureus* and *E. coli*. Firstly, LB agar and broth media were prepared in distilled water (Millipore), then sterilised at 121 °C and 15 psi for 20 mins. After bringing the media to room temperature, the LB agar was casted into a petri plate and given time to solidify. Meanwhile, the LB broth was inoculated with the bacterial cultures and grown overnight in a shaking incubator at 37 °C. The cultures grown overnight were diluted and used as inoculum for the antimicrobial assay to achieve 2×10^{10} colony-forming units (CFU)/mL concentration for *S. aureus* and 2×10^{9} CFU/mL for *E. coli*. Circular pieces of the scaffold samples (both drug-loaded and the one without drug) were cut and subjected to 1 hr of UV sterilization prior to use. Then, the samples were placed onto LB agar plates inoculated with model bacteria, followed by a 24-hr incubation at 37 °C. The analysis was performed in triplicates, and the inhibition zones were measured in millimetres (mm) in each case. The average zone of inhibition was determined using the mean values of the triplicates. An antibiotic disc of gentamicin (10 µg) was used as the positive control, and a circular piece of prepared scaffold without any drug loaded in it was used as the negative control in each case.

2.2.8 In vitro hydrolytic degradation

The prepared samples of identical size and weight were immersed in PBS solution (pH 7.4), to assess the rate of *in vitro* hydrolytic degradation. The samples were removed at specific intervals, followed by drying at 60 °C. The percentage weight loss due to degradation was calculated using the equation (8):

$$\text{Weight loss } (\%) = \left(\frac{W_0 - W_t}{W_0} \right) \times 100 \quad (8)$$

where W_0 is the initial weight of scaffold, and W_t is the weight measured at specific intervals.

2.2.9 Biocompatibility test

Biocompatibility testing was carried out to evaluate the safety and suitability of the fabricated bilayered scaffold for potential wound healing applications. The study involved haemolytic assay, cell viability, and cell adhesion assessments to determine its haemocompatibility, cytocompatibility, and ability to support cellular attachment and growth.

- ***Haemolytic assay***

  The fabricated scaffold was made into 1 × 1 cm^2 pieces and kept in the saline solution (800 µL) at 37 °C for 30 mins. The scaffold pieces were then treated with diluted blood (200 µL) for 1 hr at 37 °C. In this study, the positive control (PC) with 100 % haemolysis followed the ratio of 4:5 (human blood and distilled water), and the negative control (NC) was the physiological saline solution, as reported by Pandey et al. [303]. Following a 15-min centrifugation at 5000 rpm, the supernatant aliquots were pipetted into a 96-well plate, as represented in Figure 2.2 (a). Finally, the absorbance was calculated by a microplate reader (Make: Molecular Probes, Model: SpectraMax iD3) at 540 nm [304]. The haemolytic index was determined using equation (9) [305]:

$$\text{Haemolytic index } (\%) = \left(\frac{\text{Absorbance of bilayered scaffold} - \text{Absorbance of NC}}{\text{Absorbance of PC} - \text{Absorbance of NC}} \right) \times 100 \quad (9)$$

- ***Cell viability (MTT assay)***

  In a 96-well plate, the fabricated bilayered scaffold was placed at the bottom of three wells. HDF cells were introduced into the wells, grouped as control, poly-D-lysine, and

bilayered scaffold, and each well was left to incubate for 24, 48, and 72 hrs, as represented in Figure 2.2 (b). Following each exposure period with the bilayered scaffold or poly-D-lysine, the cell culture media was aspirated entirely, followed by addition of MTT (0.4 mg/ml) in plain DMEM to each of the wells. After a 4-hr incubation, followed by dissolution of the formazan crystals in DMSO, the absorbance was calculated by a microplate reader (Make: Molecular Probes, Model: SpectraMax iD3) at 570 nm [306].

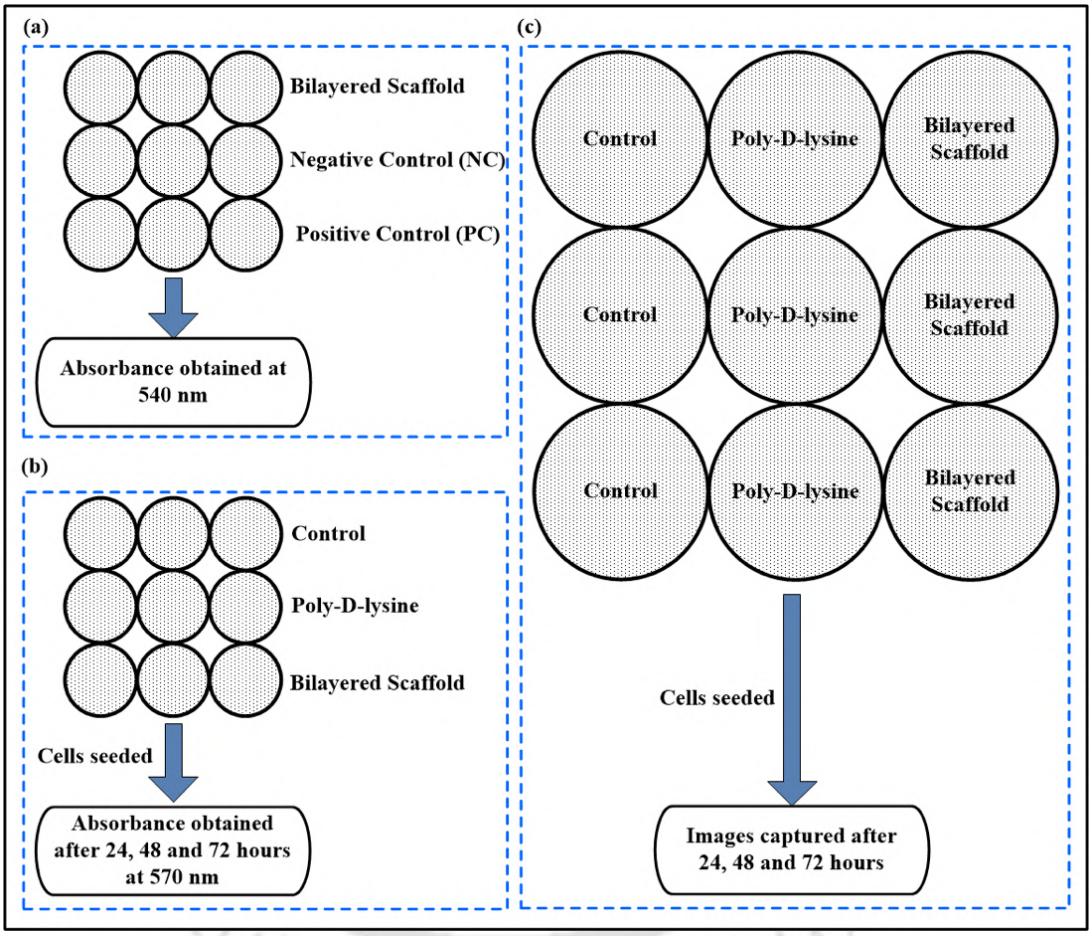

Figure 2.2 Experimental design for **(a)** haemolytic assay on human blood, **(b)** MTT assay, and **(c)** cell adhesion study of the scaffold on HDF cell lines.

- ***Cell adhesion***

The bilayered scaffold was put into three wells of a 24-well plate. Similarly, poly-D-lysine coating was done at the bottom surface of another three wells, as represented in Figure 2.2 (c). Subsequently, around 10,000 cells were seeded in each well, grouped as control, poly-D-lysine, and bilayered scaffold; and left for an exposure period of 24, 48, and 72 hrs. Following the completion of the exposure period, cell images were

captured using a 100X inverted microscope (Make: Nikon). These collected images were then analyzed to assess the impact on cell adhesion.

2.2.10 In vitro wound healing (scratch assay)

HDF cells were grown at a density of 1×10^5 cells/well in 6 wells of a 6-well tissue culture plate under standard conditions (37 °C, 5 % CO_2). When a confluence of 90 % was attained, a pipette tip (200 µL) was taken to create a straight-line scratch to mimic a cell-free wounded area within the monolayer. Following this, cellular debris was eliminated by rinsing the cells twice with PBS. Subsequently, the fabricated scaffold samples were placed into the wells and maintained under the aforementioned conditions to facilitate cell migration. The wound healing progress was observed at 0, 12, 24 and 48 hrs and was captured using a 100X inverted microscope (Make: Nikon). The wound closure percentage was obtained with equation (10), as reported by Hussein et al. [301]:

$$\text{Wound closure } (\%) = \left(\frac{\text{Wound area } (0\,\text{hr}) - \text{Wound area } (x\,\text{hr})}{\text{Wound area } (0\,\text{hr})} \right) \times 100 \qquad (10)$$

where Wound area (0 hr) denotes the initial wound area, and Wound area (x hr) denotes the wound area at x hr. The wound area was measured with the help of Image J v1.48 software.

2.2.11 In vitro drug release

For the *in vitro* release study, PBS solution (10 ml, pH 7.4) was mixed with 80 mg of the drug-loaded scaffold. The vial was then incubated at 37 °C temperature and 80 rpm agitation speed. At regular intervals, 0.5 ml sample was collected and immediately restored by fresh buffer solution of same quantity to maintain the sink condition. A UV-Vis spectrometer (Make: PerkinElmer, Model: Lambda 25) was used to calculate the percentage of cumulative drug release (CDR) from the scaffold into PBS solution. The absorbance was recorded at 232 nm wavelength [307].

2.2.12 Release kinetics of gentamicin sulfate

The *in vitro* release kinetics of gentamicin sulfate in PBS solution (pH 7.4) was studied as a function of time against various mathematical models depicted in equations (11) to (15):

$$\text{Zero-Order: } Q_t = \{Q_0 + (k_0 \times t)\} \qquad (11)$$

$$\text{First-Order: } Q_t = Q_0 \times \{1 - e^{-(k \times t)}\} \qquad (12)$$

Higuchi-Crowell model: $Q = (K_H \times t^{\frac{1}{2}})$ (13)

Korsmeyer-Peppas model: $\ln\left(\frac{Q_t}{Q_0}\right) = \{n \times \ln(t)\} + \ln(K)$ (14)

Hixson-Crowell model: $Q_0^{\frac{1}{3}} - Q_t^{\frac{1}{3}} = (K \times t)$ (15)

where

Q_t - amount of drug released at the time *t*,

Q_0 - initial amount of the drug,

k_0, k, K_H, and K - rate constants and, n - release exponent.

If, $n \leq 0.5$, it indicates Fickian diffusion; and if $0.5 < n \leq 1$, it indicates a non-Fickian behaviour.

2.2.13 Statistical analysis

The mean ± standard deviation (SD) was used to report the results, all measured in triplicates. The statistical tests were performed using the GraphPad Prism 9.0 software with $p < 0.05$. Student's t-test was conducted to statistically analyse the results of porosity, antibacterial activity and haemolytic assay. One-way ANOVA was performed for the statistical analysis of mechanical properties, contact angle measurement, WVTR, MTT assay and CDR. Ordinary two-way ANOVA followed by Bonferroni-sidak multiple comparison test was performed for analysis of *in vitro* wound healing assay. Brown-Forsythe and Welch ANOVA followed by Dunnett's T3 multiple comparison test was performed for analysis of moisture content and swelling index. Two-way RM ANOVA with Geisser-greenhouse correction followed by Turkey's multiple comparison test was performed for analysis of the *in vitro* degradation rate. ***Analytical instrumentation and characterization techniques used:*** Field Emission Scanning Electron Microscope (FESEM), Energy-Dispersive X-ray (EDX), Universal Testing Machine (UTM), and surface wettability.

2.3 Preparation of pullulan/PLGA dual drug-loaded core/sheath nanofibers by coaxial electro-centrifugal spinning and their in vitro cytotoxic efficacy towards melanoma cells

2.3.1 Materials

Pullulan was purchased from Tokyo Chemicals, Japan and PLGA (molecular weight (M_w) = 136000, L : G ratio = 5 : 5) was purchased from BMG, Japan. Chloroform was procured from Nacalai Tesque Ltd., Japan. Ciprofloxacin (CIP, 98% purity) and paclitaxel (PTX) were purchased from Thermo Scientific, U.S.A. Dimethyl sulfoxide (DMSO), 3-(4,5-dimethylthiazol-2-yl)-2,5-diphenyltetrazolium bromide (MTT) and Dulbecco's Modified Eagle's Medium (DMEM) were procured from Sigma-Aldrich, U.S.A. Acetonitrile was supplied by Kanto Chemical Co., Inc., Japan and phosphate-buffered saline (PBS) was supplied by Nacalai Tesque, Ltd., Japan. The human melanoma A375 cell line was supplied by American Type Culture Collection (ATCC), U.S.A.

2.3.2 Fabrication and drug loading of pullulan/PLGA core/sheath nanofibers by electro-centrifugal spinning (ECS)

The nanofibers were fabricated by the in-house built coaxial ECS setup as reported by Gu et al. [308]. For the study, a temperature of ~ 25 °C and a relative humidity of ~ 35 % were selected. To examine the drug release behaviour of the fabricated core/sheath nanofibers, CIP and PTX were chosen as the model drugs. For fabrication of the drug-loaded nanofibers, two distinct polymeric solutions were formulated as follows:

(a) The core solution was prepared by dissolving pullulan in distilled (Millipore) water at 20 wt. % concentration with the incorporation of CIP at a 1/100 (CIP/pullulan) weight ratio, and

(b) The sheath solution was prepared by dissolving PLGA in chloroform at 7 wt. % concentration, incorporating PTX at a 1/100 (PTX/PLGA) weight ratio.

Initially, the solutions had numerous bubbles following vigorous stirring. However, these bubbles completely dissipated, and a uniform solution was obtained after allowing it to stand for 8–10 hrs. For each coaxial ECS run, spinning dopes of ~ 0.7 mL core solution and ~ 1.5 mL sheath solution were used. To maintain the desired core-to-sheath ratio of the nanofibers, the sheath needle diameter was kept fixed at 1 mm, and the core needle diameter was varied as 0.34 mm (23G) and 0.51 mm (21G). The spinning parameters such as the distance from needle to collector, positive and negative high voltage, and spinneret rotational speed were optimized to 10 cm, 15 kV, –5 kV, and 960 rpm, respectively, to ensure the production of homogeneous fibers. Additionally, for optical microscopic visualization, thicker fibers were produced. For this, the inner needle diameter of 21G was used, and positive high voltage and the rotational speed were maintained at 12 kV and 250 rpm, respectively. The collector was maintained at 2 mm/s translation speed to facilitate the scaling up of the nanofiber production.

For subsequent characterization, the as-spun nanofibers were collected over an aluminium foil positioned on a stainless-steel plate (for SEM observation) or on a steel rod collector (for mechanical testing). The resultant dual drug-loaded core/sheath nanofibers were produced for subsequent analysis of drug release behaviour *in vitro*. Additionally, non-drug-loaded pullulan/PLGA core/sheath nanofibers, CIP-loaded pullulan nanofibers and PTX-loaded PLGA nanofibers were separately prepared to determine the cytotoxic efficacy of the individual drugs towards A375 melanoma cells. A schematic representation of the coaxial ECS setup and the spinneret have been shown in Figure 2.3 (a, b), respectively.

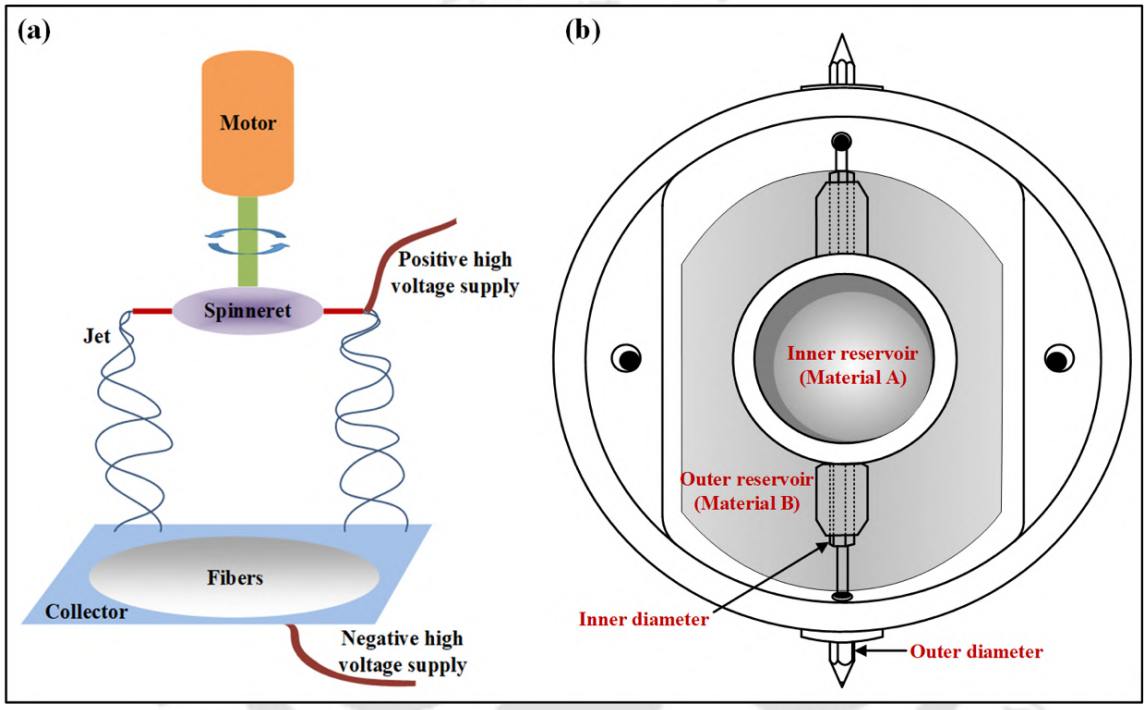

Figure 2.3 Schematic images of **(a)** the coaxial ECS setup and **(b)** the spinneret.

2.3.3 In vitro drug release

The fabricated nanofibers were kept in desiccator for more than 24 hrs to eliminate any residual solvent prior to the drug release analysis. Subsequently, 15 mg of each of the nanofiber samples were submerged in 20 mL PBS solution enclosed within glass vials and maintained at 37 °C, 60 rpm. The fiber specimens were kept immersed in the PBS solution for durations of 0.5, 1, 2, 4, 6, 12, 48, 96 and 168 hrs. All PBS solutions containing released CIP (from core) and PTX (from sheath) were then subjected to drying at 60 °C for 24 hrs, followed by re-dissolution in 1 mL of acetonitrile. This resulting solution was then passed through a filter with 0.45 µm mean pore size, thereby eliminating any unwanted impurities. To determine the quantity of released CIP and PTX present in the solution, High Performance Liquid Chromatography (HPLC) (Model: LC10AD, Make: Shimazu) was performed using a chromatographic column (Model:

COSMOSIL 3C18-EB, Make: Nacalai Tesque). As the UV-detection wavelength is different for CIP and PTX, each sample was chromatographed twice. The flow rate was maintained at 1.0 mL/min, with a column temperature of 50 °C, and the UV detection was performed at wavelength of 280 nm (for CIP) and 227 nm (for PTX), as reported by Wu et al. [309].

2.3.4 In vitro hydrolytic degradation

- ***Weight loss of as-spun nanofibers***

  To determine the weight loss of the as-spun nanofibers resulting from hydrolytic degradation, about 50 mg of the nanofibers were immersed in 20 mL PBS (pH 7.4) solution at 37 °C. Following specified time intervals of 0.5, 1, 2, 4, 6, 12, 48, 96, and 168 hrs, the nanofibers were removed from the PBS solution. They were then washed with distilled (Millipore) water and dried at 40 °C for 24 hrs before their mass change was measured.

- ***Molecular weight reduction of PLGA sheath***

  The core material pullulan being highly hydrophilic would readily dissolve in the PBS solution. Hence, to further confirm the hydrolytic degradation of the core/sheath nanofibers, the sheath material PLGA was examined for any reduction in its molecular weight. A Gel Permeation Chromatography (GPC) instrument (Make: Shimadzu) was used to determine the molecular weight of PLGA following its immersion in a PBS solution for durations of 1, 3, 6, 12, 24, 72, and 168 hrs. The GPC setup comprised of a LC-20AD pump and a RID-10A refractive index detector. PLGA was dissolved in chloroform at 5 mg/mL concentration and chromatographed at 40 °C using TSK gel Super HZM-N and HZM-L columns, and chloroform was used as the mobile phase at 0.25 mL/min flow rate. The GPC column was calibrated using polystyrene standards.

2.3.5 In vitro cytotoxicity study

- ***MTT assay***

  The MTT assay was used to determine the viability of A375 cells in presence of the drug-loaded and non-drug-loaded nanofiber test samples. For this study, the standard DMEM solution without any test sample was used as the control. All the test samples were placed in triplicates at the bottom of the corresponding wells of a 96-well plate. The A375 melanoma cells were then placed onto the wells, grouped as control, non-drug-loaded core/sheath nanofibers, CIP-loaded pullulan nanofibers, PTX-loaded

PLGA nanofibers and CIP/PTX or dual drug-loaded 23G/1mm and 21G/1mm pullulan/PLGA nanofibers. Each well was then incubated for 24, 48, and 72 hrs; and following each incubation period, the cell culture media was completely aspirated, and MTT solution (0.4 mg/ml in plain DMEM) was added to each well. After an incubation period of 4 hrs and dissolution of the formazan crystals in DMSO, the absorbance was measured with a microplate reader (Molecular Probes, SpectraMax iD3 model) at 570 nm [306].

- ***Cell adhesion***

  The test samples in triplicates were placed onto the corresponding wells of a 24-well plate. Subsequently, around 10,000 cells were seeded in each well, grouped as control, non-drug-loaded core/sheath nanofibers, CIP-loaded pullulan nanofibers, PTX-loaded PLGA nanofibers and dual drug-loaded 23G/1mm and 21G/1mm pullulan/PLGA nanofibers; and left to be incubated for 24, 48, and 72 hrs. Upon the completion of the incubation period, cell images were taken using an inverted (100X) microscope (Make: Nikon). Subsequently, these images were analyzed to determine the effect of the nanofibers on A375 cell adhesion.

2.3.6 Statistical analysis

All the data were measured in triplicates and the results were represented as mean ± SD. The statistical analysis was conducted using GraphPad Prism 9.0 with significance determined at $p < 0.05$. One-way ANOVA was used to analyze the mechanical properties and unpaired one-way ANOVA followed by Dunnett's test was used for surface wettability analysis. The MTT assay results were analyzed using two-way RM ANOVA followed by Tukey's multiple comparison test. The weight loss due to hydrolytic degradation was analysed using two-way RM ANOVA followed by Sidak's multiple comparison test.

Analytical instrumentation and characterization techniques used: Scanning Electron Microscope (SEM), optical microscopy, Universal Testing Machine (UTM), Fourier Transform Infrared (FTIR) spectroscopy, and surface wettability.

2.4 Formulation and characterization of antibacterial cosmetic skin-cream infused with pullulan and turkey berry (Solanum torvum) leaf extract

2.4.1 Materials

Pullulan was purchased from Sisco Research Laboratories Pvt. Ltd. (SRL), India. Stearic acid and cetyl alcohol were purchased from Sigma Aldrich. Glycerol, propylene glycol and phenoxyethanol were purchased from FINAR chemicals, India. Ethylenediaminetetraacetic acid (EDTA), potassium hydroxide (KOH), isopropyl palmitate (IPP), octyl methoxy cinnamate (OMC), dimethicone (DC 350), butylated hydroxytoluene (BHT), titanium dioxide (TiO_2), zinc oxide (ZnO), niacinamide, methylene blue, methyl orange, petroleum ether, sodium chloride (NaCl), Soybean Casein Digest Agar (SCDA), Potato Dextrose Agar (PDA), MacConkey Agar, Mannitol Salt Agar (MSA) and Brain Heart Infusion Agar (BHIA) were supplied by HiMedia Laboratories. Lead nitrate ($Pb(NO_3)_2$), arsenic trioxide (As_2O_3), hydrochloric acid (HCl), hydrogen sulfide (H_2S), acetic acid (CH_3COOH), sulfuric acid (H_2SO_4), sodium sulfate (Na_2SO_4), ferric ammonium sulfate ($NH_4Fe(SO_4)_2.12H_2O$), stannous chloride ($SnCl_2.2H_2O$) and toluene were purchased from Merck. 3-(4,5-dimethylthiazol-2-yl)-2,5-diphenyltetrazolium bromide (MTT) and Dulbecco's Modified Eagle's Medium (DMEM) for cytotoxicity analysis were procured from Sigma-Aldrich, U.S.A.

2.4.2 Preparation of turkey berry leaf extract (TBLE)

The TBLE was obtained using an ultrasonic method as reported by Kumar et al. [310]. After collection, the leaves were thoroughly washed with distilled water, sun-dried at 25 ± 5 °C for 2 days, and then ground into fine, uniform powder using a mixer grinder, as shown in Figure 2.4. Around 50 gms of the powder was soaked in 500 mL of an ethanol (80 % v/v) and water (20 % v/v) solution, and the mixture was kept at 4 °C for 24 hrs before ultrasonic treatment. The treatment was performed in an ultrasonic bath (Make: Labman Scientific Instrument, India, Model: LMUC-12) at a frequency of 40 kHz and a temperature of 30 °C for 30 mins, followed by centrifugation of the solution at 5000 rpm and 10 °C for 20 mins. After centrifugation, the supernatant was filtered using Whatman No. 1 filter paper, and the filtrate was concentrated using a rotary vacuum evaporator at 40 °C under reduced pressure to remove the solvent (ethanol), followed by lyophilisation, leaving behind only the dried leaf extract powder. The resulting powder was then collected and stored at −20 °C for later use.

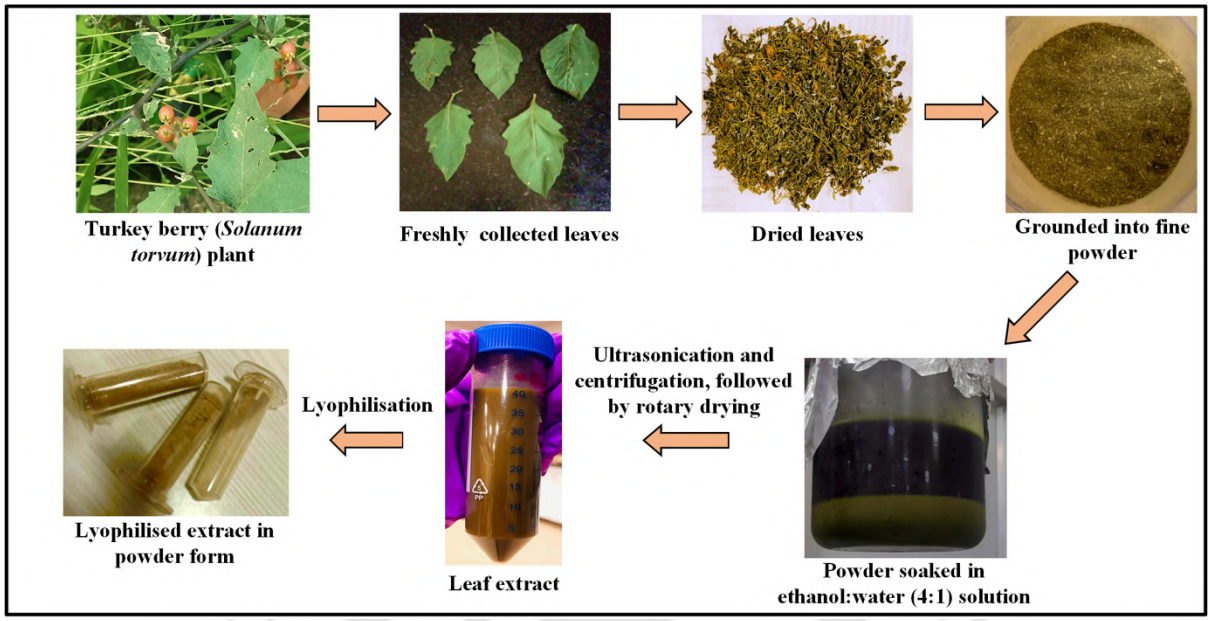

Figure 2.4 Preparation process of turkey berry leaf extract (TBLE).

2.4.3 Antibacterial activity of TBLE

The antibacterial activity of TBLE was determined against *S. aureus* (Gram-positive bacteria) and *E. coli* (Gram-negative bacteria). The bacterial cultures were grown in sterilized LB broth at 37 °C for 24 hrs in shaking incubator, and the suspensions were adjusted to 2×10^{10} CFU/mL for *S. aureus* and 2×10^{9} CFU/mL for *E. coli*. Circular filter paper discs were cut and sterilized under Ultra-Violet (UV) light for 1 hr, then immersed in 0.5 % w/w TBLE solution prepared in deionised (Millipore) water. The discs were placed on LB agar plates inoculated with the respective bacteria and incubated at 37 °C for 24 hrs, as reported by Mondal et al [311]. After incubation, the zones of inhibition around the discs were measured to assess antibacterial activity.

2.4.4 In vitro cytotoxicity analysis (MTT assay) of the TBLE

The TBLE was put into the wells of a 96-well plate, in different concentrations of 0.005, 0.01, 0.015, 0.02, 0.025, 0.03, 0.04 and 0.05 mg/mL. Each concentration was tested in triplicates. Human Dermal Fibroblast (HDF) cells were introduced into the wells, grouped as control (0 mg/mL) and the corresponding extract concentrations, and each well was left to incubate for 24, 48 and 72 hrs. After the exposure period with the extract samples, the cell culture media was aspirated entirely, followed by addition of MTT (0.4 mg/mL) in plain DMEM to each of the wells. After a 4-hr incubation, followed by dissolution of the formazan crystals in dimethyl sulfoxide (DMSO), the absorbance was calculated by a microplate reader (Make: Molecular

Probes, Model: SpectraMax iD3) at 570 nm [306]. Based on the cytotoxicity results of TBLE, its concentration to be incorporated into the cream formulation was determined.

2.4.5 Preparation of pullulan-infused antibacterial cream

Pullulan (1.00 % w/w) was dissolved in 5 mL of deionized water (Millipore) to prepare a thick solution. Simultaneously, in a separate beaker, the aqueous phase was prepared by mixing deionized water (70.00 % w/w), EDTA (0.10 % w/w), glycerol (1.50 % w/w), propylene glycol (0.10 % w/w), and KOH (0.40 % w/w). On the other hand, the oil phase was prepared by mixing stearic acid (14.40 % w/w), cetyl alcohol (0.60 % w/w), IPP (1.00 % w/w), phenoxyethanol (0.30 % w/w), OMC (0.40 % w/w), DC 350 (0.74 % w/w), and BHT (0.05 % w/w), followed by heating and melting the ingredients at a temperature of 65–75 °C. Once both phases were ready, the aqueous phase was gradually combined with TiO_2 (0.30 % w/w) and ZnO (0.01 % w/w) under stirring to ensure proper dispersion. Subsequently, the oil phase was added to the resulting mixture, stirred using an anchor (25 rpm) and cowl (1000 rpm) for 5 mins, and allowed to cool to room temperature. Once cooled, it was subjected to further processing under a vacuum pressure of 500–600 mm Hg, with continued stirring using the anchor (25 rpm), cowl (1000 rpm), and homogenizer (1200 rpm). The previously prepared pullulan solution was then added into the resultant mixture and mixed for 5 mins using only the anchor. Finally, a blend containing deionized water (2.00 % w/w), niacinamide (1.00 % w/w), perfume J 145 (0.60 % w/w), and *Solanum torvum* leaf extract (0.50 % w/w) was prepared separately and added to the formulation at a temperature below 40 °C. The detailed formulation of the prepared cream is depicted in Table 2.3.

Table 2.3 Detailed formulation of the cream.

Formulation (for 1000 g batch size)		**Quantity (% w/w)**	**Actual Quantity**	**Texture and Appearance**
Pullulan solution	Deionised water	5.00	50.00	
	Pullulan	1.00	10.00	
Aqueous phase	Deionised water	70.00	700.00	
	EDTA salt	0.10	1.00	
	Glycerine/Glycerol	1.50	15.00	
	Propylene glycol (PG)	0.10	1.00	
	Potassium hydroxide (KOH)	0.40	4.00	
	Titanium dioxide (TiO_2)	0.30	3.00	
	Zinc oxide (ZnO)	0.01	0.10	

Oil phase	Stearic acid	14.40	144.00	 Smooth texture, have a moisturising effect on the skin.
	Cetyl alcohol	0.60	6.00	
	Isopropyl palmitate (IPP)	1.00	10.00	
	Phenoxyethanol	0.30	3.00	
	Ocetyl methoxy cinnamate (OMC)	0.40	4.00	
	Dimethicone (DC 350)	0.74	7.40	
	Butylated hydroxytoluene (BHT)	0.05	0.50	
Niacinamide and *Solanum torvum* leaf extract	Deionised water	2.00	20.00	
	Niacinamide	1.00	10.00	
	Perfume J145	0.60	6.00	
	Solanum torvum leaf extract	0.50	5.00	
	TOTAL	100.00	1000.00	

2.4.6 Characterization of the formulated cream

2.4.6.1 Determination of the type of emulsion, pH and stability of cream

The emulsion type, pH and stability was determined in accordance with the Indian Standard for Skin Creams (IS 6608: 2004). To determine the type of emulsion (Oil in Water (O/W) or Water in Oil (W/O)), few drops of water-soluble dye, such as methylene blue was added to the cream. In case of O/W emulsion (where water is the continuous phase), dye would get uniformly dissolved throughout the system, and in case of W/O emulsion (where oil is the continuous phase), dye would appear as clusters on the surface of the cream. For further confirmation, the cream was tested for its electrical conductivity. In case of O/W emulsion, it would conduct electricity. To measure the pH, precisely 5 ± 0.01 g of the cream was weighed in a 100 mL beaker, followed by its dispersion in 45 mL of deionized water. The pH of the suspension was assessed using a pH meter at a temperature of 27 °C. The cream sample was kept at 4 °C, 37 °C and 45 °C for around 24 hrs to test for thermal stability.

2.4.6.2 Determination of heavy metals

The determination of heavy metals was performed in accordance with the Indian Standard for Skin Creams (IS 6608: 2004). Firstly, a standard lead solution was prepared by dissolving 1.6 g of ($Pb(NO_3)_2$) in water and the volume was adjusted to 1000 mL. Then 10 mL of the resulting solution was pipetted out and further diluted to 1000 mL with water. It was estimated that 1 mL of this solution contain 0.01 mg of lead (as Pb). For the estimation of heavy metals, about 2000 g of the cream was weighed in a crucible and heated on a hot plate, followed by its ignition in a muffle furnace until it reached 600 °C and a constant mass was maintained. Then 3 mL of

dilute HCl was added and warmed till no further dissolution occurred and the volume was adjusted to 100 mL. The resulting solution was then filtered and 25 mL of the filtrate was transferred into a measuring cylinder. In a separate measuring cylinder, 2 mL of dilute CH_3COOH was mixed with 1 mL of standard lead solution and the volume was adjusted with water to 25 mL. Then 10 mL of H_2S solution was added to each of the measuring cylinders and the volume was adjusted with water to 50 mL. Finally, both the solutions were allowed to stand for 10 mins to compare the colouration in both the measuring cylinders. A blank determination without samples was also performed to prevent errors that may arise from the reagents.

2.4.6.3 Determination of arsenic

The determination of arsenic was performed in accordance with the Indian Standard for Skin Creams (IS 6608: 2004). Firstly, a mixed acid solution was prepared, for which 1 volume of concentrated H_2SO_4 was diluted with 4 volumes of deionized water, followed by addition of 10 g of NaCl for each 100 mL of the solution. Then, 64 g of $NH_4Fe(SO_4)_2.12H_2O$ was dissolved in water containing 10 mL of the mixed acid solution and volume was adjusted to 1 L. Then, a $SnCl_2.2H_2O$ solution was prepared by dissolving 80 g of $SnCl_2.2H_2O$ in 100 mL water containing 5 mL of concentrated HCl. The test was then performed in a Gutzeit bottle, by adding 2 mL of $NH_4Fe(SO_4)_2.12H_2O$ solution, 0.5 mL of $SnCl_2.2H_2O$ solution and 25 mL of the sample cream solution as prepared in (2.4.6.2) discussed above. For comparison of the stain colour, a standard stain using 0.001 mg of As_2O_3 was prepared.

2.4.6.4 Determination of total fatty matter (TFM)

The TFM determination was performed in accordance with the Indian Standard for Skin Creams (IS 6608: 2004). For determination of TFM content, about 2 g of the cream was weighed and put into a conical flask, followed by addition of 25 mL of dilute HCl. Then a reflux condenser was fitted into the flask, and the contents were boiled until a clear solution was obtained. Then the contents of the flask were poured into a 300 mL separating funnel and allowed to cool down to room temperature. The conical flask was then rinsed with 50 mL of petroleum ether in portions of 10 mL. Following this, the petroleum ether rinsings were poured into the separating funnel, and the funnel was shaked well and left until the layers got separated. Then the aqueous phase was carefully separated out and shaked out twice with 50 mL portions of petroleum ether. Finally, all the ether extracts were combined and washed with deionized water until complete removal of acid (when tested with methyl orange indicator solution). Then the petroleum ether extracts were filtered out through a filter paper containing Na_2SO_4 into a

conical flask previously dried at 90 °C. The Na_2SO_4 on the filter was then washed with petroleum ether and the washings were combined with the filtrate. The petroleum ether was then distilled off and the residual material in the flask was dried to constant mass at a temperature of 90 °C. The total fatty substance was measured using the following equation (16):

$$\text{Total fatty substance (\% by mass)} = \frac{M_1}{M_2} \times 100 \quad (16)$$

where M_1 = mass in g of the residue, and M_2 = mass in g of the material taken for the test.

2.4.6.5 Determination of moisture content

Moisture content is a critical parameter in cosmetic formulations, particularly in creams, as it influences product texture, stability, shelf life, and skin hydration capability. A well-balanced moisture content ensures the cream maintains a smooth and spreadable consistency, facilitates active ingredient delivery, and supports skin hydration without causing greasiness or dryness. In the present study, the moisture content in the formulated cream was determined using Dean-Stark Apparatus, which comprises of a flask, a condenser, and a graduated moisture trap, as shown in Figure 2.5. It involves azeotropic distillation for separation of water from samples using an organic solvent (such as toluene). In the present study, 1 g of the cream sample was weighed and mixed with 20 mL toluene, followed by placing it on an oil bath to ensure uniform heating and gentle boiling at around 110 °C. The reaction was run for a period of 7 hrs, during which the water present in the cream was evaporated along with toluene vapour. The vapours travelled up the condenser, where they got cooled and condensed back into a liquid. The moisture content was calculated using the following equation (17):

$$\text{Moisture content (\%)} = \left(\frac{\text{Volume of water extracted}}{\text{Amount of cream sample taken}} \right) \times 100 \quad (17)$$

Figure 2.5 Dean-Stark apparatus used for determination of moisture content.

2.4.6.6 Determination of microbial content

The microbial content of the formulated cream was evaluated in accordance with the Indian Standard IS 14648:2011. Approximately 500 mg of the cream formulation was dissolved in autoclaved PBS to ensure sterility. The mixture was vortexed for 10 mins to achieve uniform dispersion, followed by centrifugation at 200 rpm for 5 mins at room temperature. The supernatant obtained after centrifugation was subjected to serial dilution up to 10^{-6}. Aliquots from each dilution were then aseptically spread onto selective agar media to detect and quantify specific microbial populations. Soybean Casein Digest Agar (SCDA) was used for total aerobic bacterial count, Potato Dextrose Agar (PDA) for fungal (yeast and mold) colonies, MacConkey Agar for *Escherichia coli* and *Salmonella* spp., Mannitol Salt Agar (MSA) for *Staphylococcus aureus*, and Brain Heart Infusion Agar (BHIA) for *Pseudomonas aeruginosa*. To ensure reliability and validity of the results, three types of control plates were included in the study: negative control plates inoculated with only sterile PBS, positive control plates exposed to open air to represent environmental contamination, and test plates inoculated with the cream formulation diluted with PBS. All bacterial culture plates were incubated at 37 °C for 24 hrs, while fungal culture plates were incubated at 30 °C for 120 hrs. After the incubation period, the number of colony-forming units (CFU) on each plate was counted manually, and the microbial load in the cream formulation was determined based on these counts.

2.4.6.7 Antibacterial activity of the cream formulation

The antibacterial activity of the prepared cream was determined against *S. aureus* (Gram-positive bacteria) and *E. coli* (Gram-negative bacteria), using the same method as described under Section 2.4.3.

2.4.6.8 In vitro cytotoxicity analysis (MTT assay) of the cream formulation

The formulated cream was put into the wells of a 96-well plate, in different concentrations of 0.1, 0.25, 0.5, 0.75, 1.0, 1.5, 2.0, 2.5 and 3.0 mg/mL. Each concentration was tested in triplicates, and the MTT assay was performed on human dermal fibroblast (HDF) cells using the same method as that of the TBLE as described under Section 2.4.4.

2.4.7 Statistical analysis

All the measurements were taken in triplicates (N = 3) and the results were represented as mean ± SD. The SPSS 25.0 software was used for the statistical analysis with a significance level of $p < 0.05$. The data were analyzed using ANOVA and the statistically significant differences among the mean values were determined by Tukey's post-hoc test. Different letters in superscript represent statistically significant ($p < 0.05$) differences and the same letters represent statistically non-significant ($p > 0.05$) differences for each data.

Analytical instrumentation and characterization techniques used: Rheological analyses (viscosity, amplitude sweep and frequency sweep measurements).

2.5 Preparation and characterization of chitosan nanoparticles and neem essential oil-functionalized pullulan/gum arabic biocomposites for edible food packaging

2.5.1 Materials

Pullulan (PUL, polymaltotriose, extrapure) was purchased from Sisco Research Laboratories (SRL) Pvt. Ltd., India. Chitosan (CS, from shrimp shells, practical grade, deacetylated chitin, poly (D-glucosamine)) and gum arabic (GA, from acacia tree, branched polysaccharide) were procured from Sigma-Aldrich, USA. Neem essential oil (NEO, specific gravity: 0.91 g/mL, refractive index: 1.476) was purchased from Veda Oils, India. Glacial acetic acid (extrapure) and glycerol were procured from FINAR chemicals, India. Sodium tripolyphosphate (STPP) was supplied by Otto Chemie Pvt. Ltd., India. Luria-Bertani (LB) agar and broth, Potato Dextrose Agar (PDA), plate count agar, Dichloran Rose Bengal Chloramphenicol (DRBC)

agar, peptone water, potassium persulfate ($K_2S_2O_8$), sodium chloride (NaCl), sodium hydroxide (NaOH), calcium chloride ($CaCl_2$), 2,2-diphenyl-1-picrylhydrazyl (DPPH), 2,2′-azino-bis (3-ethylbenzothiazoline-6-sulfonic acid) (ABTS), dimethyl sulfoxide (DMSO), Dulbecco's Modified Eagle's Medium (DMEM) and MTT (3-(4,5-dimethylthiazol-2-yl)-2,5-diphenyltetrazolium bromide) were obtained from HiMedia laboratories, India. The guava fruits in fresh condition were purchased from a fruit store at IIT Guwahati, Assam, India.

2.5.2 Preparation of chitosan nanoparticles (NCS)

The NCS was prepared using the ionic gelation method as reported by Ghosh et al. [312], with few modifications. In this study, STPP was used as the cross-linking agent and NaOH was used as the stabilizer, facilitating interaction between the polycation CS and the polyanion STPP. The CS solution was first prepared by dissolution of CS in acetic acid (1% v/v), followed by stirring for 4 hrs at 600 rpm. Subsequently, STPP (0.09 wt.%) solution was gradually added to the CS solution under stirring condition, followed by addition of 1% w/v aqueous NaOH solution and then subjected to ultrasonication for 5 mins. The resulting solution was then washed with ethanol and distilled (Millipore) water to purify the NCS. Finally, the prepared NCS was characterized for its particle size, crystallinity and thermal stability.

2.5.3 Preparation of PUL-based edible biocomposites

For preparation of neat PUL film, an aqueous solution of PUL (4 % w/v) containing glycerol (30 % w/w relative to the total PUL content) was stirred for 2 hrs at 750 rpm, 25 °C. The PUL/GA edible biocomposite was prepared using 2 % w/v each of PUL and GA in distilled (Millipore) water, with glycerol added at 30 % w/w relative to the combined PUL and GA content. The resulting solution was stirred under conditions as mentioned above. Additionally, for preparation of the PUL/GA/NCS1, PUL/GA/NCS2, and PUL/GA/NCS3 biocomposites, NCS solution was prepared in 0.2 % acetic acid with concentration of 1, 2 and 3 % w/v respectively, and subjected to vigorous stirring for 2 hrs at 800 rpm, 25 °C. The resulting NCS solution was then mixed with solution containing PUL, GA and glycerol. Similarly, the NEO-containing biocomposites were prepared with the incorporation of 1 % v/v NEO to each of the solutions. The NEO-containing solutions were further subjected to homogenization using a homogenizer (Make: IKA, Model: T25 digital ULTRA TURRAX) at 6500 rpm for 30 mins. After homogenization, the prepared solutions were allowed to stand for 1–2 hrs for removal of entrapped bubbles and then casted on teflon petri plates, followed by drying at 40 °C in hot-air oven. The dried films were then characterized for their morphological, optical, mechanical and

thermal properties. A tabular representation of the film formulations have been mentioned in Table 2.4.

Table 2.4 Formulations of different PUL-based biocomposites.

Films/Biocomposites	PUL (% w/v)	GA (% w/v)	NCS (% w/v)	NEO (% v/v)	Glycerol (% w/w)
PUL	4	-	-	-	30
PUL/GA	2	2	-	-	30
PUL/GA/NEO	2	2	-	1	30
PUL/GA/NCS1	2	2	1	-	30
PUL/GA/NCS1/NEO	2	2	1	1	30
PUL/GA/NCS2	2	2	2	-	30
PUL/GA/NCS2/NEO	2	2	2	1	30
PUL/GA/NCS3	2	2	3	-	30
PUL/GA/NCS3/NEO	2	2	3	1	30

2.5.3.1 Water vapour permeability (WVP)

The WVP of the prepared edible films were analysed using the cup method, following ASTM E398-03 standard, as reported in previous studies [312,313]. For this, cups were filled with anhydrous $CaCl_2$ (0 % relative humidity) and sealed using the film samples. Prior to the analysis, area of opening of the cup and the film thickness were measured. Following this, the permeation cells along with the film composites were kept inside a desiccator containing saturated solution of NaCl (75 % relative humidity). The increase in weight of permeation cell was measured over specific time intervals. The water vapour transmission rate (WVTR) and the WVP were determined using equations (18) and (19), respectively:

$$\text{WVTR} = \left(\frac{\Delta m / \Delta t}{A} \right) \tag{18}$$

$$\text{WVP} = \left(\frac{\text{WVTR} \times L}{\Delta P} \right) \tag{19}$$

where WVTR denotes water vapour transmission rate (g/m^2/day), $\Delta m / \Delta t$ denotes the slope (change in weight of permeation cell per unit time, g/day), A denotes film area through which

water vapour permeation occurs (m^2), WVP denotes water vapour permeability (g/m/day/Pa), L denotes thickness of film (m), and ΔP denotes partial water vapour pressure difference across the film (Pa).

2.5.3.2 Antioxidant activity

The antioxidant activity of the film samples, the uncoated and coated guava samples was determined using the DPPH and ABTS radical scavenging assays. For preparation of the film extracts, 50 mg of each of the prepared films was added to 2 mL of distilled (Millipore) water, and stirred overnight. For preparation of the guava extracts, 10 g of guava were taken in 40 mL of distilled water and homogenized using a homogenizer (Make: IKA, Model: T25 digital ULTRA TURRAX). Following this, the extracts were subjected to filtration and centrifugation to obtain clear extract. Subsequently, 0.5 mL of the test sample extract (film or guava) was mixed with DPPH or ABTS solution to obtain a final volume of 2.5 mL, and vortexed for proper mixing, as reported by Adame et al. [314]. For the DPPH assay, the sample to be tested was mixed with DPPH solution (4 mg/100 mL ethanol) and incubated for 30 mins in darkness at room temperature. Absorbance was measured using an UV-Vis spectrophotometer at 517 nm. For the ABTS assay, ABTS (7 mM) solution with $K_2S_2O_8$ (2.45 mM) was incubated overnight in darkness, diluted to an absorbance of 0.99 at 734 nm, and mixed with the test sample. After 30 mins, absorbance was measured at 734 nm. A control test (DPPH or ABTS without the sample) was conducted simultaneously using the same method [315]. The radical scavenging activity was calculated using equation (20):

$$\text{DPPH or ABTS radical scavenging activity}\ (\%) = \left(\frac{\text{Absorbance}_{\text{DPPH or ABTS}} - \text{Absorbance}_{\text{Sample in DPPH or ABTS}}}{\text{Absorbance}_{\text{DPPH or ABTS}}} \right) \times 100 \quad (20)$$

2.5.3.3 Antimicrobial property

The antimicrobial properties of the filmogenic solutions were tested against both bacterial and fungal food pathogens. For antibacterial testing, *Staphylococcus aureus* or *S. aureus* (Gram-positive bacteria) and *Escherichia coli* or *E. coli* (Gram-negative bacteria) were used. Bacterial cultures were grown in sterilized LB broth at 37 °C for 24 hrs in a shaking incubator, and the bacterial suspensions were diluted to 2×10^{10} CFU/mL for *S. aureus* and 2×10^{9} CFU/mL for *E. coli*. Filter papers were cut into circular pieces and subjected to UV sterilization for 1 hr. The circular filter paper discs were then dipped into filmogenic test solutions, placed on LB

agar plates, and incubated at 37 °C for 24 hrs, as reported by Mondal et al. [311]. Chloramphenicol was used as the positive control. The zones of inhibition formed around the test samples were measured.

For antifungal testing, *Aspergillus niger or A. niger*, a common mold causing food spoilage, was used. Fungal spore suspensions were prepared in sterilized 0.85 % NaCl solution and diluted to 10^6 spores/mL, as reported by Ma et al. [316]. The prepared suspensions were then inoculated onto sterilized PDA plates. UV-sterilized filter paper discs were dipped into the filmogenic test solutions, placed on the inoculated PDA plates, and incubated at 30 °C for 3 weeks. Voriconazole was used as the positive control in this case, and the zones of inhibition were similarly measured.

2.5.3.4 In vitro biocompatibility analysis (MTT assay)

The viability of human embryonic kidney (HEK-293) cells in filmogenic/ coating solutions was determined using the MTT assay at 24, 48, and 72 hrs, as reported by Eze et al. [317] with some modifications. The standard DMEM (without test solution) served as the control. The test solutions were prepared at a 10 % v/v concentration in standard DMEM. Around 100 µL of each test solution and control were added in triplicate to the wells of a 96-well plate, and incubated at 37 °C with 5 % CO_2 for the specified intervals. After each incubation period, the culture media was aspirated and 100 µL of MTT solution (0.5 mg/mL in standard DMEM) was added to each of the wells and incubated for 4 hrs. The MTT solution was then removed, 100 µL of DMSO was added, and incubated for 10 mins to dissolve formazan crystals. The cell viability was estimated by measuring absorbance with a microplate reader at 570 nm (Make: Molecular Probes, Model: SpectraMax iD3).

2.5.4 Edible coating on fresh-cut guava

The efficacy of the optimized filmogenic solution or edible coating formulation (PUL/GA/NCS3/NEO) was applied on fresh-cut guava and the quality parameters were determined during its storage time. The guava fruits were first washed thoroughly with water and subjected to air-drying at room temperature. The guava fruits were then cut, dipped for 5 mins into the edible coating solution and again air-dried at room temperature. Finally, the coated and uncoated guava pieces were stored for a period of 6 days under ambient condition, and 14 days under refrigerated condition. The cut guava fruits were then tested for various parameters such as visual appearance, colour factors (L, a*, b*, Chroma and hue), firmness and weight loss with respect to time.

2.5.5 Microbiological shelf-life analysis

The microbiological shelf-life of the uncoated and coated guava fruits was assessed following the protocol outlined in [318,319], with few modifications. Guava samples (10 g) were mixed with 90 mL of 0.1 % peptone water and subjected to homogenization for 5 mins. Serial dilutions were made by transferring 1 mL of the mixture into 9 mL of 0.1 % peptone water. Subsequently, 0.1 mL of each of the diluted homogenate was used as the inoculum for determining the total viable count (TVC) and the yeast and mold count (YMC). The TVC was determined using pour plate technique and plate count agar as the medium and the plates were incubated at 37 °C for 2 days. The YMC was determined using spread plate technique and DRBC agar as the medium and the plates were incubated at 30 °C for 5 days. Colony numbers were then counted and reported as $\log_{10}$ colony-forming units per mL ($\log_{10}$ CFU/mL), as per the ASTM-E2149 standard, as reported by Shiekh et al. [320].

2.5.6 Statistical analysis

All the measurements were taken in triplicates (N = 3) and the results were represented as mean ± SD. The SPSS 25.0 software was used for the statistical analysis with a significance level of $p < 0.05$. The data were analyzed using ANOVA and the statistically significant differences among the mean values were determined by Tukey's post-hoc test. Different letters in superscript represent statistically significant ($p < 0.05$) differences and the same letters represent statistically non-significant ($p > 0.05$) differences for each data.

Analytical instrumentation and characterization techniques used: Field Emission Scanning Electron Microscope (FESEM), Energy-Dispersive X-ray (EDX), Field Emission Transmission Electron Microscope (FETEM), Fourier Transform Infrared (FTIR) spectroscopy, X-ray diffraction (XRD) analysis, Thermogravimetric analysis (TGA), Universal Testing Machine (UTM), surface wettability, colour factors, weight loss, and firmness.

2.6 Analytical instrumentation and characterization techniques

2.6.1 Nuclear Magnetic Resonance (NMR) analysis

Samples analysed: Lab-made polysaccharide and commercial pullulan.

The ^{1}H NMR and ^{13}C NMR analyses were performed using 600MHz NMR spectrometer (Make: Bruker, Model: AVANCE III HD). For the study, ~ 20 mg each of the purified lab-

made polysaccharide sample and commercial pullulan were separately dissolved in 0.5 mL of D_2O, as reported by Liu et al. [321] and Chen et al. [77].

2.6.2 Matrix-Assisted Laser Desorption Ionization-Time of Flight Mass Spectrometry (MALDI-TOF MS) analysis

Samples analysed: Lab-made polysaccharide and commercial pullulan.

For matrix preparation, 20 mg of 2, 5-dihydroxybenzoic acid was dissolved in a mixture containing 500 µL of acetonitrile, 500 µL of deionized water, as reported by Mitić et al. [322], followed by addition of 10 µL of 0.5 % aqueous NaCl solution. The resulting solution was vortexed and then centrifuged for 10 mins at 10,000 rpm. For sample preparation, both the lab-made polysaccharide and commercial pullulan samples were individually dissolved in deionized water at a concentration of 10 mg/mL. The solution was then subjected to ultrasonication to ensure complete dissolution. The analysis was performed using a MALDI-TOF mass spectrometer (Make: Bruker, Model: Autoflex Speed) operated at an accelerating voltage of 19 kV, with each spectrum averaged over ~2000 laser shots, as reported by Mitić et al. [322]. For the study, 1:1 (v/v) mixture of the sample and matrix solutions were drop-casted onto a stainless-steel target plate, and air-dried prior to analysis. The spectral reproducibility was confirmed by collecting data from four distinct spots on each sample.

2.6.3 Fourier Transform Infrared (FTIR) spectroscopy

Samples analysed: Lab-made polysaccharide, commercial pullulan, pullulan/PVA/gum arabic electrospun nanofibrous layer of the bilayered wound healing scaffold (both before and after glutaraldehyde crosslinking), chitosan (CS), chitosan nanoparticles (NCS), edible films (PUL, PUL/GA, PUL/GA/NEO, PUL/GA/NCS1, PUL/GA/NCS2, PUL/GA/NCS3, PUL/GA/NCS1/NEO, PUL/GA/NCS2/NEO and PUL/GA/NCS3/NEO), monolithic pullulan nanofibers, CIP-loaded pullulan nanofibers, pure CIP powder, monolithic PLGA nanofibers, PTX-loaded PLGA nanofibers and pure PTX powder.

The FTIR analysis of the lab-made polysaccharide, commercial pullulan, pullulan/PVA/gum arabic electrospun nanofibrous layer (both before and after crosslinking), CS, NCS and edible films was performed using a FTIR spectrometer (Make: PerkinElmer, Model: Spectrum Two), in ATR mode. However, the monolithic pullulan nanofibers, CIP-loaded pullulan (represented as pullulan + CIP) nanofibers, pure CIP powder, monolithic PLGA nanofibers, PTX-loaded PLGA (represented as PLGA + PTX) nanofibers and pure PTX powder were assessed using the KBr pellet mode. For the lab-made and commercial pullulan samples, the purpose was to

identify and compare the functional groups present in the lab-made polysaccharide with those of the commercial pullulan. For the nanofibrous layer of wound healing scaffold, the purpose was to confirm the successful crosslinking by glutaraldehyde. For CS, NCS, and the edible films, the purpose was to identify chemical bonding or possible interactions among the components. For the pullulan + CIP and PLGA + PTX nanofibers, the purpose was to determine whether drug-polymer interactions were present in the drug-loaded nanofibers by comparing them with non-drug-loaded nanofibers and the corresponding pure drug powders. For the analysis, the dried samples were scanned for wavenumber ranging from 4000 to 500 cm^{-1}, as reported by Wani et al. [323] and Mondal et al. [324].

2.6.4 Morphological analysis

Samples analysed: Bilayered wound healing scaffold, edible films (PUL, PUL/GA, PUL/GA/NEO, PUL/GA/NCS3, and PUL/GA/NCS3/NEO), NCS, pullulan/PLGA core/sheath 23G/1mm and 21G/1mm nanofibers.

The morphology of the samples was analysed using various microscopy techniques. Field Emission Scanning Electron Microscopy (FESEM, Make: Zeiss, Model: Gemini) analysis was done to examine the surface morphology and fractured cross-sections of the bilayered scaffold and the edible films, including PUL, PUL/GA, PUL/GA/NEO, PUL/GA/NCS3, and PUL/GA/NCS3/NEO. Prior to imaging, samples were dried at 60 °C for 24 hrs and mounted on stubs using double-sided carbon tape. For the electrospun layer, nanofiber morphology was observed via FESEM, and the average fiber diameter was estimated by analysing at least 100 individual fibers using ImageJ v1.48, based on FESEM image magnification and scale. Additionally, the pullulan/PLGA core/sheath nanofiber morphology was studied using a Scanning Electron Microscope (SEM) operated at 10 kV after gold coating with a sputtering device (Model: IB-2, Make: Eiko Engineering) using 7 mA current for 5 mins. The core/sheath structure of the nanofibers was further confirmed using an optical microscope (Model: VHX-200 with VH-Z500 lens, Make: Keyence). Energy Dispersive X-ray (EDX) analysis was performed to evaluate the elemental composition of the wound healing scaffold and the edible films, as reported by Ghosh et al. [27]. To assess the nanoscale morphology of the prepared NCS, Field Emission Transmission Electron Microscopy (FETEM, Make: JEOL, Model: 2100F) was used.

2.6.5 Thermogravimetric analysis (TGA)

Samples analysed: CS, NCS and edible films (PUL, PUL/GA, PUL/GA/NEO, PUL/GA/NCS1, PUL/GA/NCS2, PUL/GA/NCS3, PUL/GA/NCS1/NEO, PUL/GA/NCS2/NEO and PUL/GA/NCS3/NEO).

The thermal stability of the samples was determined using Thermogravimetric Analyzer (TGA) (Make: PerkinElmer, Model: TGA-4000) for a temperature range of 28 to 700 °C at 10 °C/min heating rate, as reported by Sun et al. [325]. Each sample weighing ~ 10 mg was taken for the study.

2.6.6 Surface wettability

Samples analysed: The electrospun hydrophilic and solvent-casted hydrophobic layers of the bilayered wound healing scaffold, pullulan/PLGA core/sheath nanofibers and edible films (PUL, PUL/GA, PUL/GA/NEO, PUL/GA/NCS1, PUL/GA/NCS2, PUL/GA/NCS3, PUL/GA/NCS1/NEO, PUL/GA/NCS2/NEO and PUL/GA/NCS3/NEO).

The surface wettability was estimated using water contact angle measurement. A drop-shape analyzer (Make: Kruss GmbH, Model: DSA25) was used to measure the contact angle of the samples cut into pieces (10 mm × 10 mm) and placed onto a glass slide using double-sided tape. For the study, ~ 2 µL of distilled (Millipore) water was carefully poured on the sample surface, with 0.16 mL/min flow rate, as reported by Mondal et al. [326]. This allowed for the observation of how the behaviour of the water droplet changed over time from 0 to 60 secs (for the bilayered scaffold layers and the edible films), and from 0 to 300 secs for the core/sheath nanofibers, when in contact with the sample at a temperature of 25 °C.

2.6.7 Mechanical properties

Samples analysed: Bilayered wound healing scaffold, edible films (PUL, PUL/GA, PUL/GA/NEO, PUL/GA/NCS1, PUL/GA/NCS2, PUL/GA/NCS3, PUL/GA/NCS1/NEO, PUL/GA/NCS2/NEO and PUL/GA/NCS3/NEO), dual drug-loaded and non-drug-loaded pullulan/PLGA core/sheath nanofibers.

The mechanical characteristics of the bilayered wound healing scaffold and prepared edible films (cut into 30 mm × 100 mm) were assessed using the ASTM D882 standard in a 5 kN Electromechanical Universal Testing Machine (UTM, Make: ZwickRoell, Model: Z005TNProLine), as reported by Mondal et al. [32]. The mechanical properties of the dual drug-loaded and non-drug-loaded nanofibers having pullulan/PLGA core-to-sheath ratios of 21G/1mm and 23G/1mm were determined using a tensile testing machine (Model: STA-1150,

Make: Orientec). The stretching rate was maintained at 5 mm/min for the wound healing scaffold and core/sheath nanofibers, and at 15 mm/min for the edible films. All tests were conducted under room conditions of 22 ºC temperature and 40 % relative humidity.

2.6.8 Rheological analyses

Sample analysed: Cream formulation.

The rheological properties of the cream formulation were determined using a rheometer (Make: Thermo Scientific, Model: HAAKE MARS iQ Air) equipped with a cone-and-plate geometry (2° cone angle, 35 mm diameter, 0.1 mm gap), and all measurements were performed at 25 °C. To determine the flow behaviour, steady shear testing was conducted by measuring viscosity across a shear rate range of 0.1–1000 s^{-1}. The resulting data were analyzed using the Ostwald–de Waele (power-law) model with the equation (21) as follows:

$$\eta = K(\dot{\gamma})^{n-1} \tag{21}$$

where η is the viscosity, $\dot{\gamma}$ is the shear rate, K is the consistency index and n is the flow behaviour index, helping to categorize the cream as a Newtonian or pseudoplastic fluid. For identifying the linear viscoelastic region (LVR), an amplitude sweep test was carried out at a constant angular frequency of 10 rad/s with shear strain ranging from 0.01–1000 %, and the key parameters such as storage modulus (G′), loss modulus (G″), tan δ (ratio of G″ to G′), and the critical strain (γ_L) defining the LVR boundary were measured. Additionally, a dynamic frequency sweep test was performed at a constant strain of 0.1 % (within the LVR, as determined from the amplitude sweep) while varying the angular frequency from 0.1–100 rad/s to observe the changes in G′ and G″ with increasing frequency.

2.6.9 X-ray diffraction (XRD) analysis

Samples analysed*:* CS, NCS, STPP and the edible films (PUL, PUL/GA, PUL/GA/NEO, PUL/GA/NCS1, PUL/GA/NCS2, PUL/GA/NCS3, PUL/GA/NCS1/NEO, PUL/GA/NCS2/NEO and PUL/GA/NCS3/NEO).

XRD analysis of the samples were performed using X-ray diffractometer (Make: Rigaku, Model: Smartlab) with 2θ ranging from 5 to 70°, at scanning rate of 0.5°/min to analyse the type of material and the efficacy of NCS and NEO on the biocomposites. The crystallinity index (I_{CR}) was determined using equation (22), as reported by Guo et al. [327] :

$$\%\ \text{Crystallinity index}\ (I_{CR}) = \left(\frac{\text{Area of crystalline peaks}}{\text{Area of crystalline peaks} + \text{Area of amorphous peaks}}\right) \times 100 \tag{22}$$

2.6.10 Optical properties

Samples analysed for transparency: Edible films (PUL, PUL/GA, PUL/GA/NEO, PUL/GA/NCS1, PUL/GA/NCS2, PUL/GA/NCS3, PUL/GA/NCS1/NEO, PUL/GA/NCS2/NEO and PUL/GA/NCS3/NEO).

Samples analysed for colour factors: Edible films (PUL, PUL/GA, PUL/GA/NEO, PUL/GA/NCS1, PUL/GA/NCS2, PUL/GA/NCS3, PUL/GA/NCS1/NEO, PUL/GA/NCS2/NEO and PUL/GA/NCS3/NEO) and the uncoated and coated cut guava fruits.

The optical properties of the prepared samples were determined to interpret the efficacy of the incorporated NCS and NEO. The transparency and colour factors (L, a*, b*, Chroma and hue) were determined using an UV-Vis spectrophotometer (Make: PerkinElmer, Model: Lambda 45) and a colorimeter (Make: Datacolor Technology Suzhou Co., Ltd., Model: Datacolor 550), respectively [311,328]. For the transparency assessment, each film was cut into a 10 mm × 40 mm rectangular piece and placed in a cuvette perpendicular to the Ultra-Violet (UV) light beam to ensure proper light passage through the film surface. The films were sized to fully cover the light path of the spectrophotometer, avoiding any bubbles or wrinkles. The transparency was assessed in transmittance mode, with a scanning wavelength range from 200 to 800 nm.

2.6.11 Weight loss

Samples analysed: Uncoated and coated fresh-cut guava fruits.

The weight loss from the uncoated and coated guava fruits was determined by measuring the initial weight and the change in weight after specific time interval, as reported by Mondal et al. [311]. The results were reported as weight loss percentage using equation (23):

$$\text{Weight loss (\%)} = \left(\frac{\text{Initial weight} - \text{Final weight}}{\text{Initial weight}} \right) \times 100 \quad (23)$$

2.6.12 Firmness

Samples analysed: Uncoated and coated fresh-cut guava fruits.

The firmness of the uncoated and coated guava fruits was determined using a texture analyser (Make: Stable Microsystems, Model: TA.XT.plusC) as reported by Ghosh et al. [329], with some modifications. A cylindrical probe (P/5) with 5 mm diameter was used for the study. The test speed was maintained at 10 mm/min and the firmness was measured in newton (N).

CHAPTER 3

SHAKE-FLASK OPTIMIZATION OF PULLULAN PRODUCTION BY FUNGAL FERMENTATION OF *Aureobasidium pullulans* NCIM 1049 USING SUGARCANE JAGGERY AS SUBSTRATE

Motivation

Pullulan is a versatile biopolymer with significant industrial value due to its non-toxic, biodegradable, and film-forming properties. However, its large-scale application is limited by the high cost of production, particularly from the use of purified sugars as carbon sources. While liquid sugarcane jaggery has been previously reported as a potential alternative, many studies lack detailed optimization or do not evaluate its performance with different microbial strains. In this context, the present study focuses on using A. pullulans NCIM 1049 to investigate pullulan production from liquid sugarcane jaggery under shake-flask conditions. By systematically optimizing the fermentation media components, this work aims to evaluate the feasibility and efficiency of sugarcane jaggery as a practical cost-effective substrate. Although no cost estimation was performed, the study identifies the key parameters influencing pullulan production.

The work in this chapter is under preparation of a research article titled as: **"*Shake-flask Optimization of Pullulan Production by Aureobasidium pullulans NCIM 1049 Fermentation Using Sugarcane Jaggery as Substrate*"**.

Abstract

Pullulan is a natural, biodegradable polysaccharide produced by the fungus *Aureobasidium pullulans* (*A. pullulans*) valued for its excellent film-forming and water-soluble properties. Its wide application in food, pharmaceutical, and biomedical fields is limited by high production costs, largely due to the use of expensive refined sugars. Liquid sugarcane jaggery (concentrated sugarcane juice), a low-cost, nutrient-rich sugar syrup, has been explored in previous studies as an alternative carbon source. However, many of those studies lacked systematic optimization or used different fungal strains. In this study, shake-flask fermentation of *A. pullulans* NCIM 1049 was performed to maximize pullulan production using liquid sugarcane jaggery as substrate. The fermentation media components such as carbon source (jaggery), nitrogen sources (yeast extract, $(NH_4)_2SO_4$), and essential salts (K_2HPO_4, NaCl, $MgSO_4.7H_2O$, $ZnSO_4.5H_2O$) were varied to maximize pullulan production. The Plackett–Burman Design (PBD) of experiments identified jaggery, yeast extract, and NaCl as the significant factors influencing pullulan production. These factors were further optimized using a Box-Behnken Design (BBD). The predicted pullulan production (5.106 g/L) under the optimized BBD conditions (jaggery = 49.09 g/L, yeast extract = 2.15 g/L, NaCl = 1.28 g/L) closely matched the observed production (4.923 ± 0.14 g/L), thereby demonstrating the reliability and accuracy of the BBD model. The prepared pullulan was extracted and purified using standard techniques, including ethanol precipitation, dialysis, and lyophilization. Its structural properties were characterized using Fourier Transform Infrared (FTIR) spectroscopy, Proton Nuclear Magnetic Resonance (^{1}H NMR), Carbon Nuclear Magnetic Resonance (^{13}C NMR), and Matrix-Assisted Laser Desorption Ionization-Time of Flight Mass Spectrometry (MALDI-TOF MS), confirming its close similarity to commercial pullulan in terms of structure and composition.

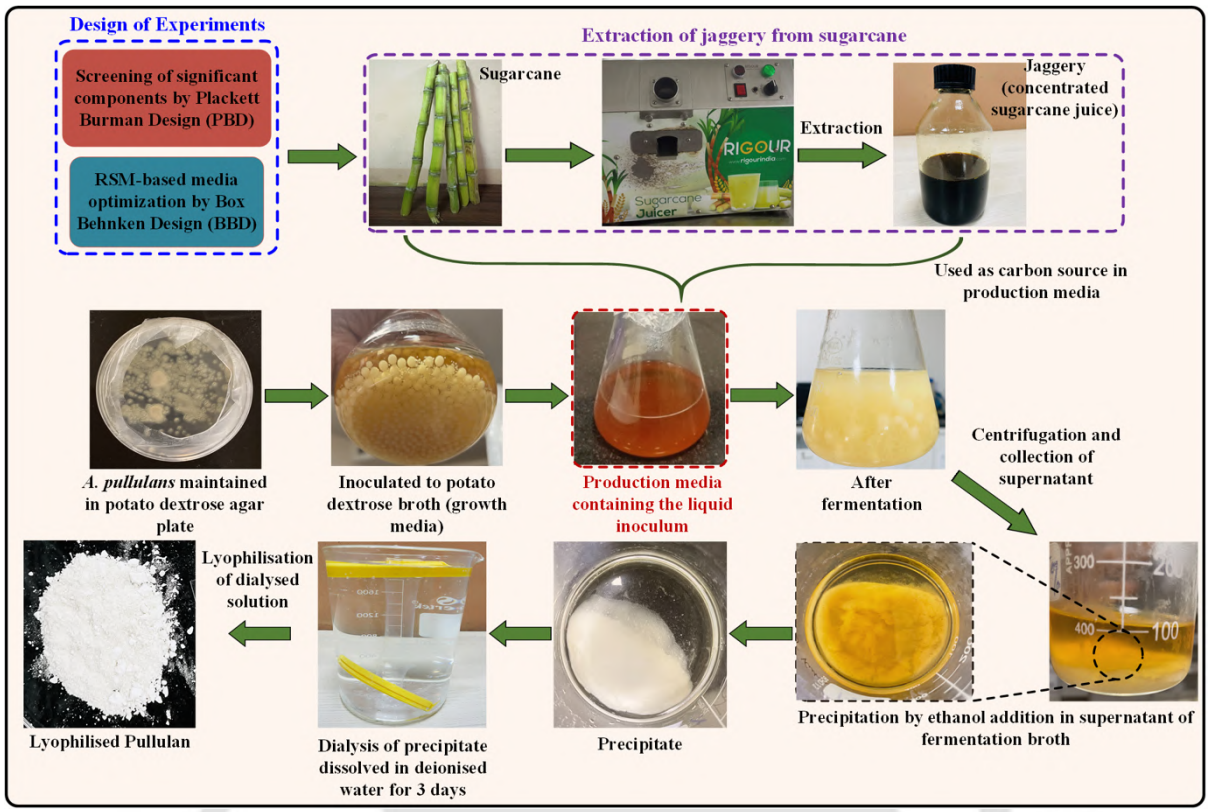

Figure 3.1 Scheme of chapter 3.

3.1 Introduction

Pullulan is a unique extracellular polysaccharide produced primarily by the fungus *Aureobasidium pullulans (A. pullulans)*, possessing desirable properties such as high water solubility, film-forming ability, non-toxicity, biodegradability, and oxygen impermeability [11,12]. Due to these functional attributes, pullulan has found wide applications in the food, pharmaceutical, and biomedical industries [148,330]. However, despite its promising industrial potential, the high production cost of pullulan remains a major limitation to its large-scale commercial exploitation. Among the major contributors to production cost, the carbon source alone can account for up to 30–50 % of the total fermentation expenses. Traditionally, pure and refined sugars such as glucose, sucrose, and maltose are used, offering high yields but at a premium cost. Consequently, there has been a growing research focus on exploring alternative, low-cost carbon sources such as agro-industrial residues, fruit processing wastes, and other non-conventional substrates to make pullulan production more economically viable. Agro-industrial by-products are intensively used as fermentation substrates due to their low cost and abundance; however, many such residues require extensive pre-treatment or enzymatic hydrolysis, which introduce additional complexities and costs into the process.

Therefore, the search continues for substrates that are not only inexpensive and readily available but also directly fermentable without significant pre-processing. In this context, liquid sugarcane jaggery, which is a concentrated form of sugarcane juice, serves to be a promising alternative. It contains high concentration of fermentable sugars, primarily sucrose, along with glucose, fructose, and naturally occurring minerals and micronutrients. Importantly, it is widely available, especially in sugarcane-producing regions, and remains significantly cheaper than refined sugars. Several studies have explored the use of sugarcane juice and jaggery for pullulan production, demonstrating the potential of these sugar-rich substrates in microbial fermentation. However, some studies have not focused deeply on process optimization and production enhancement strategies associated with jaggery-based fermentations [37,331]. The use of liquid sugarcane jaggery offers distinct advantages due to its stable, concentrated, and uniform composition, which makes it more suitable for industrial-scale applications compared to fresh sugarcane juice. Liquid jaggery contains high levels of readily fermentable sugars, which eliminates the need for pre-hydrolysis. Therefore, liquid sugarcane jaggery represents a promising cost-effective substrate for pullulan production, with the potential to enhance process efficiency and make production more economical. To the best of our knowledge, no prior studies reported the production of pullulan by *Aureobasidium pullulans* NCIM 1049 using sugarcane jaggery as the carbon source.

3.2 Results and discussion

3.2.1 Preliminary screening of significant factors using Plackett–Burman Design (PBD)

The pullulan production under various experimental conditions was determined, and the data are summarized in Table 3.1. It is usually assumed that all the fermentation medium components influence pullulan production; however, some of the components are particularly crucial. The Plackett–Burman Design (PBD) is useful for identification of these crucial components, as shown in the ANOVA results in Table 3.2. Additionally, among the tested components, jaggery, yeast extract, and $(NH_4)_2SO_4$ demonstrated positive effects on pullulan production, while the remaining factors negatively influenced production. These findings are in line with previously reported literature [47]. Statistical analysis was performed at a 95 % confidence level using Minitab software (trial version). The Pareto chart (shown in Figure 3.2) highlights the key factors and their standardized effects on pullulan production. The analysis demonstrated that jaggery, yeast extract, and NaCl had a significant influence ($p < 0.05$) on pullulan production. According to the chart, jaggery emerged as the most influential factor, with the highest confidence level (99.20 %), followed by yeast extract (95.70 %) and NaCl

(95.40 %), as shown in Table 3.2. The highest significance of jaggery may be attributed to its dual role as both a carbon and energy source for the microorganism.

Table 3.1 Predicted and experimental pullulan production under media conditions as determined by Plackett-Burman Design (PBD).

Run	Jaggery (g/L)	K_2HPO_4 (g/L)	Yeast extract (g/L)	$(NH_4)_2SO_4$ (g/L)	NaCl (g/L)	$MgSO_4.7H_2O$ (g/L)	$ZnSO_4.5H_2O$ (g/L)	Observed pullulan production (g/L)	Predicted pullulan production (g/L)
1	60	1	4	0.5	0.5	0.1	0.05	4.080	3.977
2	60	4	1	1.5	0.5	0.1	0.01	3.396	3.239
3	30	4	4	0.5	2.5	0.1	0.01	2.077	2.355
4	60	1	4	1.5	0.5	0.5	0.01	3.800	4.014
5	60	4	1	1.5	2.5	0.1	0.05	2.560	2.715
6	60	4	4	0.5	2.5	0.5	0.01	3.480	3.201
7	30	4	4	1.5	0.5	0.5	0.05	2.742	2.848
8	30	1	4	1.5	2.5	0.1	0.05	2.863	2.643
9	30	1	1	1.5	2.5	0.5	0.01	2.240	2.136
10	60	1	1	0.5	2.5	0.5	0.05	2.780	2.945
11	30	4	1	0.5	0.5	0.5	0.05	2.410	2.303
12	30	1	1	0.5	0.5	0.1	0.01	2.580	2.623

Additionally, high yeast extract and low K_2HPO_4 levels demonstrated increase in production efficiency. This may further be attributed to the requirement of the microorganism for sufficient nitrogen and essential minerals for optimal growth and metabolism [47]. The factors K_2HPO_4, $(NH_4)_2SO_4$, $MgSO_4.7H_2O$ and $ZnSO_4.5H_2O$ demonstrated p-value exceeding 0.05, indicating that variations in these components did not significantly affect pullulan production under the tested conditions [69,332–337]. The analysis of variance (ANOVA)

showed that the overall model was significant (p-value = 0.049), suggesting that some media components had a measurable impact on the response. Among the tested variables, three components (jaggery, yeast extract, and NaCl) were found to be statistically significant factors. Jaggery had a positive effect on pullulan production, with a coefficient of 0.4320 and a p-value of 0.008, indicating that an increase in jaggery concentration significantly enhances pullulan production. Yeast extract also showed a positive influence (coefficient = 0.2563 and p-value = 0.043), contributing favourably to pullulan production, likely due to its content of nitrogen, vitamins, and growth factors. In contrast, NaCl had a statistically significant negative effect (coefficient = –0.2507 and p-value = 0.046), indicating that elevated salt concentrations may exert osmotic stress or inhibitory effects on microbial growth. A negative coefficient, when statistically significant, implies that the factor inversely affects the response, as in this case, increasing NaCl led to a decrease in pullulan production. Thus, only the three factors affecting pullulan production (jaggery, yeast extract, and NaCl) were selected for further detailed optimization using Response Surface Methodology (RSM).

Table 3.2 Analysis of Variance (ANOVA), estimated regression coefficients and significance of factors for the PBD for pullulan production.

Source	Coefficient	Adj SS	Adj MS	F-value	DF	p-value	Confidence level (%)
Model	-	4.02224	0.57461	6.20	7	0.049 **(s)**	95.10
Constant	3.205	-	-	-	-	-	-
Jaggery	0.4320	2.23949	2.23949	24.16	1	0.008 **(s)**	99.20
K_2HPO_4	–0.1398	0.23464	0.23464	2.53	1	0.187 **(ns)**	81.30
Yeast extract	0.2563	0.78848	0.78848	8.51	1	0.043 **(s)**	95.70
$(NH_4)_2SO_4$	0.0162	0.00314	0.00314	0.03	1	0.863 **(ns)**	13.70
NaCl	–0.2507	0.75401	0.75401	8.14	1	0.046 **(s)**	95.40
$MgSO_4.7H_2O$	–0.0087	0.00090	0.00090	0.01	1	0.926 **(ns)**	7.40
$ZnSO_4.5H_2O$	–0.0115	0.00159	0.00159	0.02	1	0.902 **(ns)**	9.80

Error	-	0.37073	0.09268	-	4	-	-
Total	-	4.39297	-	-	11	-	-

***Note:** s = significant, ns = non-significant.*

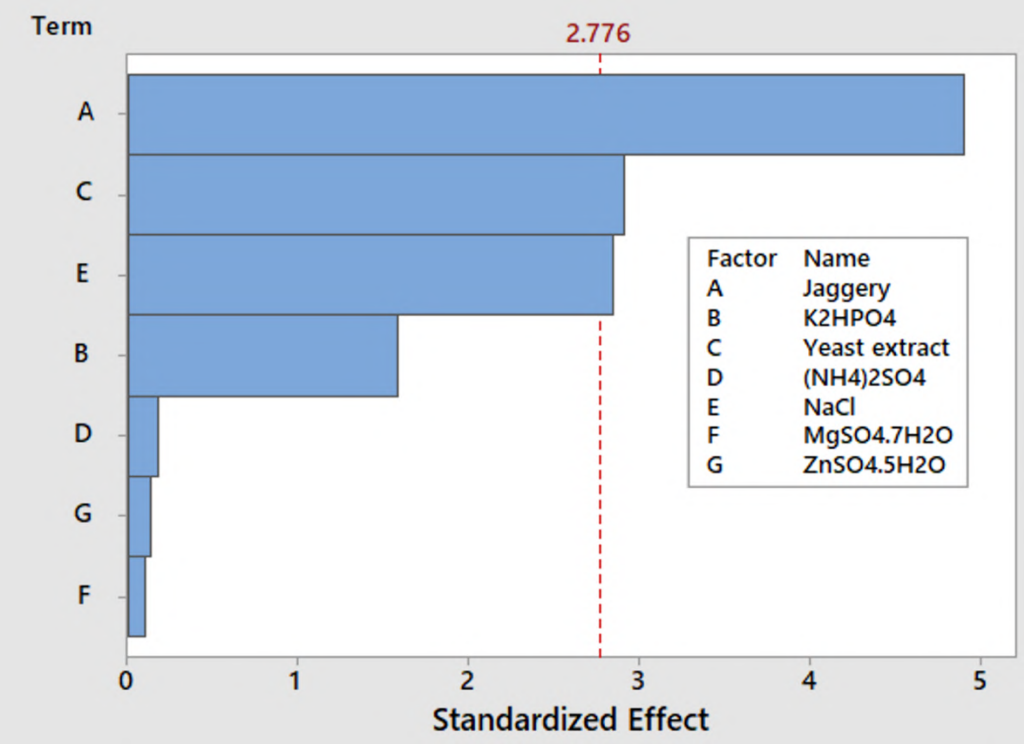

Figure 3.2 Pareto chart showing the standardized effects of medium components on pullulan production based on PBD analysis.

3.2.2 RSM-based media optimization using Box-Behnken Design (BBD)

Following the identification of key parameters, jaggery, yeast extract and NaCl (designated as A, B and C, respectively), affecting pullulan production, optimization was carried out using the Box-Behnken statistical approach. The experimental design for optimizing pullulan production is presented in Table 3.3, and the corresponding regression coefficients and p-values are provided in Table 3.4 (a–b). Coefficients with p-values below 0.05 were considered statistically significant at the 95 % confidence level. According to the p-values presented in Table 3.4 (a), the interactions between jaggery (A) and NaCl (C), as well as between yeast extract (B) and NaCl (C), were not statistically significant, as their p-values exceeded 0.05 at the 95 % confidence level. Specifically, the p-values for these interactions were 0.170 and 0.643, respectively. Consequently, these interaction terms were excluded from the regression

model. The regression analysis and ANOVA were then performed again using the reduced model and the results are as shown in Table 3.4 (b). The results demonstrate that all variables in the reduced model had a statistically significant influence on the response variable (pullulan production), as indicated by their corresponding p-values. The reduced BBD model demonstrated R^2 value of 0.9708, indicating that the model closely matched the experimental data. All linear, quadratic, and interaction terms included in the reduced model had p-values below 0.05, signifying statistical significance. The lack-of-fit p-value was 0.161, suggesting that the lack of fit was not significant and that the model was appropriate. The regression coefficients were then applied to the polynomial model using coded variables, expressed as:

Pullulan production (g/L) = $5.00 + 0.5337\ A - 0.1557\ B - 0.1603\ C - 0.2548\ A*B - 1.05\ A^2 - 0.4733\ B^2 - 0.3843\ C^2$

The carbon source plays a crucial role in the fermentation medium, acting as the primary energy supply necessary for the metabolic functions of *A. pullulans*. It supports cellular growth and significantly influences pullulan production. High concentrations of readily metabolizable sugars like sucrose have been reported to enhance pullulan biosynthesis by increasing the activity of enzymes such as glucosyltransferase and phosphofructo-2-kinase, which play key roles in exopolysaccharide formation [65]. In the present study, liquid sugarcane jaggery (a complex sugar source comprising sucrose, glucose and fructose) was used as the sole carbon source. The initial sugar concentration from jaggery was found to have a statistically significant impact ($p < 0.05$) on pullulan production, as shown in Table 3.4. However, deviations from optimal sugar concentration, either higher or lower, led to relatively lower pullulan production. This reduction in production may be attributed to osmotic stress and decreased water activity at non-optimal sugar concentrations, as noted by Shin et al. [338]. Similar findings have been reported by Göksungur et al. [69], who observed that increasing the initial sugar concentration improved pullulan production only up to a certain threshold, beyond which production decreased. These results are consistent with earlier studies on *A. pullulans* [62,89,339]. Furthermore, an excess supply of carbon has been reported to potentially inhibit both cell growth and the synthesis of pullulan [340]. Additionally, it has been reported that the nitrogen sources contribute to the metabolite production in the fermentation medium and have significant effect on the polysaccharide production by *A. pullulans*. Yeast extract, which serves as a nitrogen source for production of pullulan, comprises of amino acids, peptides, minerals, vitamins, etc. [62]. Furthermore, nitrogen availability has been reported to enhance biomass

production by stimulating glycolysis through activation of phosphofructokinase, a key enzyme in the pathway [341]. It also serves as a substrate for the synthesis of pullulan-degrading enzymes, thereby contributing to a reduction in pullulan accumulation. In the present study, the addition of yeast extract (nitrogen source) resulted in an initial increase in pullulan production followed by decrease in pullulan production as its concentration was increased further. This is consistent with previously reported studies [342,343]. Notably, the negative linear coefficient of NaCl indicates that increasing NaCl concentrations adversely affected pullulan production. This observation is consistent with previous findings, where the negative influence of NaCl was attributed to its inhibitory effects on microbial growth and enzyme activity essential for polysaccharide biosynthesis [344,345].

3.2.3 Predicted optimal conditions and experimental validation of the model

To identify the optimal conditions more efficiently for maximising pullulan production, the response optimizer tool in Minitab was used, which gave the following optimal concentrations: jaggery (A) = 49.09 g/L, yeast extract (B) = 2.15 g/L, and NaCl (C) = 1.28 g/L. To validate the accuracy of the proposed model, experiments were conducted in triplicate using these optimal conditions. The desirability of the optimized solution was found to be 0.982. The observed pullulan production was 4.923 ± 0.14 g/L, which was slightly lower than the predicted value (5.106 g/L), thereby confirming the reliability, stability and accuracy of the model. The experimental results were further visualized using contour plots and three-dimensional (3D) surface plots, as shown in Figure 3.3 and 3.4, respectively. These plots not only enabled identification of the optimal combination of the medium components but also revealed their pairwise interactive effects on pullulan production. In each of the plots, the effect of two components on pullulan production was illustrated while keeping the other component at its middle optimum level.

Table 3.3 Predicted and experimental pullulan production under media conditions as determined by Box-Behnken Design (BBD).

Run	Jaggery (g/L)	Yeast extract (g/L)	NaCl (g/L)	Observed pullulan production (g/L)	Predicted pullulan production (g/L)
1	30	1.0	1.5	2.751	2.840
2	60	1.0	1.5	4.276	4.418
3	30	4.0	1.5	3.180	3.040

4	60	4.0	1.5	3.686	3.599
5	30	2.5	0.5	3.365	3.189
6	60	2.5	0.5	4.218	4.257
7	30	2.5	2.5	2.640	2.869
8	60	2.5	2.5	4.026	3.938
9	45	1.0	0.5	4.458	4.454
10	45	4.0	0.5	4.000	4.143
11	45	1.0	2.5	4.360	4.134
12	45	4.0	2.5	3.733	3.824
13	45	2.5	1.5	5.022	4.996
14	45	2.5	1.5	4.900	4.996
15	45	2.5	1.5	4.840	4.996
16	45	2.5	1.5	5.150	4.996
17	45	2.5	1.5	5.065	4.996

Table 3.4 (a) Analysis of Variance (ANOVA), estimated regression coefficients and significance of factors for the full BBD for pullulan production.

Source	Coefficient	Adj SS	Adj MS	F-value	DF	p-value
Model	-	9.75869	1.08430	35.65	9	0.000 **(s)**
Constant	4.9954	-	-	-	-	0.000 **(s)**
A	0.5337	2.27911	2.27911	74.93	1	0.000 **(s)**
B	–0.1558	0.19406	0.19406	6.38	1	0.039 **(s)**
C	–0.1602	0.20544	0.20544	6.75	1	0.035 **(s)**
A^2	–1.0488	4.63172	4.63172	152.27	1	0.000 **(s)**
B^2	–0.4733	0.94331	0.94331	31.01	1	0.001 **(s)**
C^2	–0.3843	0.62192	0.62192	20.45	1	0.003 **(s)**
AB	–0.2548	0.25959	0.25959	8.53	1	0.022 **(s)**
AC	0.1332	0.07102	0.07102	2.33	1	0.170 **(ns)**

BC	–0.0423	0.00714	0.00714	0.23	1	0.643 **(ns)**
Error	-	0.21292	0.03042	-	7	-
Lack-of-Fit	-	0.15022	0.05007	3.19	3	0.146 **(ns)**
Pure Error	-	0.06270	0.01568	-	4	-
Total	-	9.97161	-	-	16	-

$\mathbf{R^2}$ = 0.9786, $\mathbf{R^2}$ **(adj)** = 0.9512, $\mathbf{R^2}$ **(pred)** = 0.7491.

***Note:** s = significant, ns = non-significant.*

Table 3.4 (b) Analysis of Variance (ANOVA), estimated regression coefficients and significance of factors for the reduced BBD for pullulan production.

Source	**Coefficient**	**Adj SS**	**Adj MS**	**F-value**	**DF**	**p-value**
Model	-	9.68052	1.38293	42.76	7	0.000 **(s)**
Constant	4.9954	-	-	-	-	0.000 **(s)**
A	0.5337	2.27911	2.27911	70.47	1	0.000 **(s)**
B	–0.1558	0.19406	0.19406	6.00	1	0.037 **(s)**
C	–0.1602	0.20544	0.20544	6.35	1	0.033 **(s)**
A^2	–1.0488	4.63172	4.63172	143.21	1	0.000 **(s)**
B^2	–0.4733	0.94331	0.94331	29.17	1	0.000 **(s)**
C^2	–0.3843	0.62192	0.62192	19.23	1	0.002 **(s)**
AB	–0.2548	0.25959	0.25959	8.03	1	0.020 **(s)**
Error	-	0.29108	0.03234	-	9	-
Lack-of-Fit	-	0.22838	0.04568	2.91	5	0.161 **(ns)**
Pure Error	-	0.06270	0.01568	-	4	-
Total	-	9.97161	-	-	16	-

$\mathbf{R^2}$ = 0.9708, $\mathbf{R^2}$ **(adj)** = 0.9481, $\mathbf{R^2}$ **(pred)** = 0.8311.

***Note:** s = significant, ns = non-significant.*

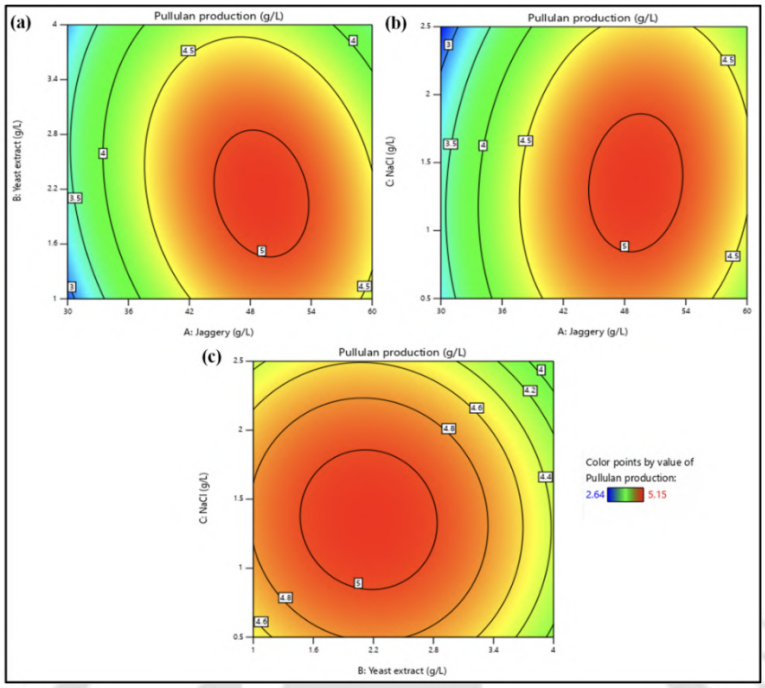

Figure 3.3 Contour plot showing interaction between **(a)** jaggery and yeast extract, **(b)** jaggery and NaCl, and **(c)** yeast extract and NaCl.

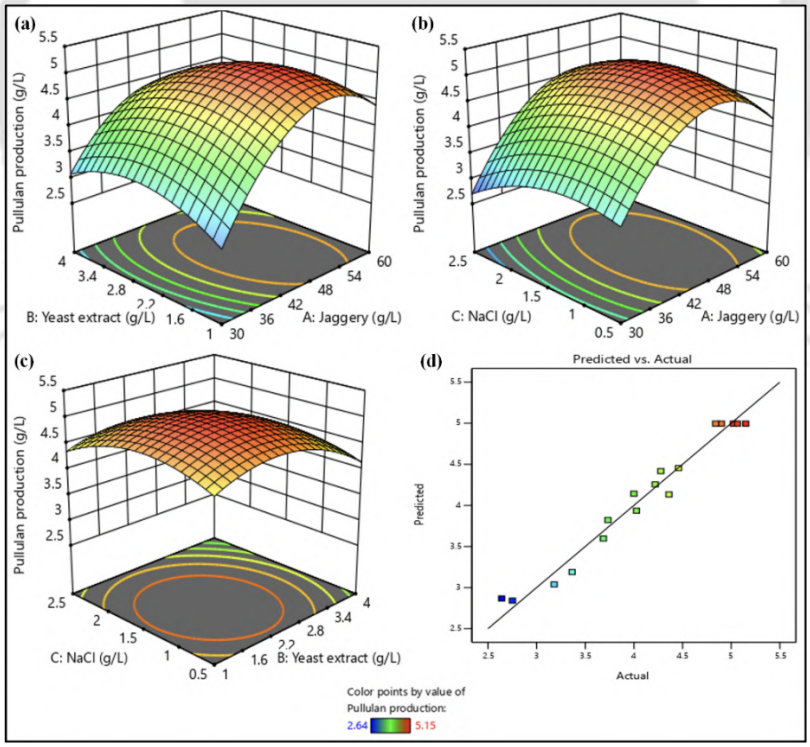

Figure 3.4 3D surface plot showing interaction between **(a)** jaggery and yeast extract, **(b)** jaggery and NaCl, and **(c)** yeast extract and NaCl. Additionally, **(d)** scatter plot showing correlation between predicted and actual values of pullulan production.

3.2.4 FTIR analysis

The FTIR spectral analysis was performed to compare the structural features of commercial pullulan with the lab-made polysaccharide. Both spectra exhibit characteristic absorption bands of polysaccharides, affirming the presence of similar functional groups and molecular frameworks. As depicted in Figure 3.5, a broad absorption band corresponding to O–H stretching vibrations was observed near 3299 cm^{-1} for commercial pullulan and appeared at 3316 cm^{-1} for the lab-made polysaccharide. The C–H stretching vibrations, attributed to aliphatic –CH and $–CH_2$ groups in the glucose ring, appeared at 2929 cm^{-1} in the commercial sample and at 2927 cm^{-1} in the lab-made sample, indicating overall structural similarity in the carbohydrate backbone. Peaks corresponding to the O–C–O stretching vibrations were present at 1640 cm^{-1} in the commercial pullulan and at 1647 cm^{-1} in the lab-made polysaccharide. The peaks at 1350 cm^{-1} in the commercial pullulan and at 1339 cm^{-1} in the lab-made polysaccharide may be attributed to the C–O–H bending vibrations. The C–O–C and C–O stretching vibrations were evident at 1145 and 1002 cm^{-1} in the commercial pullulan, and at 1140 and 1026 cm^{-1} in the lab-made polysaccharide, respectively. These peaks are fundamental characteristics of glucose-based polysaccharides and confirm the integrity of the glucopyranose units in the synthesized material. Despite slight positional differences, the consistent pattern across this region suggests that the fundamental ring structure is preserved. The peaks at around 849, 758 and 929 cm^{-1} in the commercial pullulan, and those at around 845, 754 and 928 cm^{-1} in the lab-made polysaccharide are characteristic of α-D-glucopyranose units, α(1→4) glycosidic bonds and α(1→6) glycosidic bonds, respectively. These findings are in line with previously reported literature [62,346–348]. Thus, the FTIR spectral profile of the lab-synthesized polysaccharide closely aligns with that of commercial pullulan, representing all the vibrational bands corresponding to hydroxyl groups, aliphatic chains, glycosidic linkages, and pyranose rings. The minor differences in band positions and intensities do not imply compositional deviation but are more likely reflective of differences in molecular interactions, chain conformation, or processing conditions. The alignment of these characteristic peaks in the lab-made polysaccharide with those of the commercial pullulan confirms the identification of the polysaccharide as pullulan.

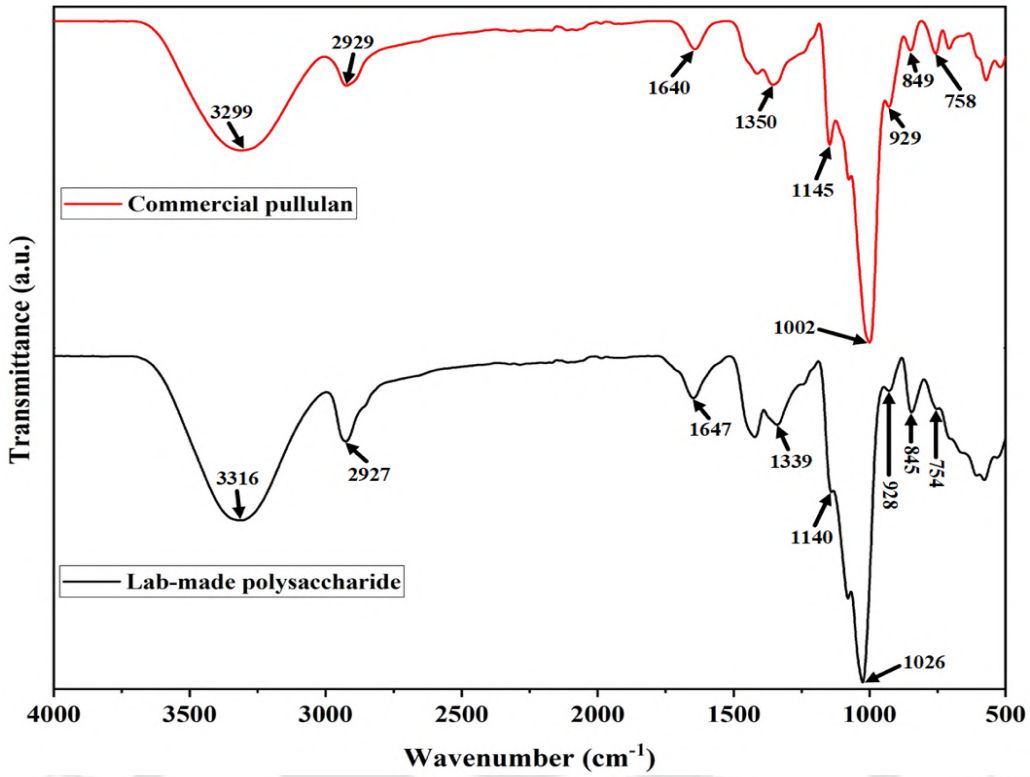

Figure 3.5 FTIR analysis of lab-made polysaccharide and commercial pullulan.

3.2.5 NMR analysis

The structural identity of the produced pullulan was further confirmed through both ^{1}H NMR and ^{13}C NMR analyses, as shown in Figure 3.6 (a–d). Both spectra were recorded in deuterium oxide (D_2O), the preferred solvent for polysaccharide characterization due to its excellent solubility and minimal background signal in the relevant spectral regions. The comparative analysis of the ^{1}H and ^{13}C NMR spectra of commercial pullulan and lab-made polysaccharide indicates strong structural similarity, with only minor chemical shift variations. In the ^{1}H NMR spectra, the anomeric proton associated with the α(1→6) glycosidic linkage appears at 4.83 ppm for commercial pullulan (Figure 3.6 (c)) and slightly downfield at 4.88 or 4.87 ppm for the lab-made variant (Figure 3.6 (a)). Similarly, the α(1→4) anomeric proton is observed at 5.28–5.24 ppm in commercial pullulan and 5.32–5.28 ppm in the lab-made sample. The H4 proton shifts marginally from 3.35–3.32 ppm in the commercial pullulan to 3.40–3.37 ppm in the lab-made sample, while the ring protons (H2–H5) and methylene protons at C6 appear in comparable ranges (3.90–3.47 ppm in commercial pullulan and 3.95–3.52 ppm in lab-made polysaccharide). The D_2O solvent peak remains consistent at 4.7 ppm in both spectra. These results are in agreement with previously reported studies [61,84,342]. In the ^{13}C NMR spectra, the α(1→6) linkage carbon shifts from 97.90 ppm in the commercial sample (Figure 3.6 (d))

to 97.94 ppm in the lab-made sample (Figure 3.6 (b)) and the α(1→4) linkage carbons show slight downfield shifts as well (~ 100.19 or 100.14 & 99.74 ppm in commercial to ~ 100.24 or 100.15 & 99.78 ppm in lab-made). The C4 and C6 carbon signals also shift slightly, with C4 moving from 77.72–77.33 ppm (commercial) to 77.76–77.38 ppm (lab-made), and the C6 (CH_2OH) group shifting from 60.67–60.36 ppm (commercial) to 60.72–60.41 ppm (lab-made). All other ring carbons (C2–C5) appear within similar ranges for both samples, (73.41–66.44 ppm for commercial, and 73.46–66.49 ppm for lab-made). Such minor chemical shift variations may be attributed to the slight differences in polymer chain conformations, hydration states, or degree of polymerization, which are inherently influenced by biological fermentation conditions, as also reported by Chen et al. [77]. Additionally, the minor variations in signal resolution and broadness suggest subtle differences in sample homogeneity. The results confirm that the pullulan synthesized using liquid sugarcane jaggery as substrate by the strain NCIM 1049 shares the same structural characteristics as that of the commercial pullulan.

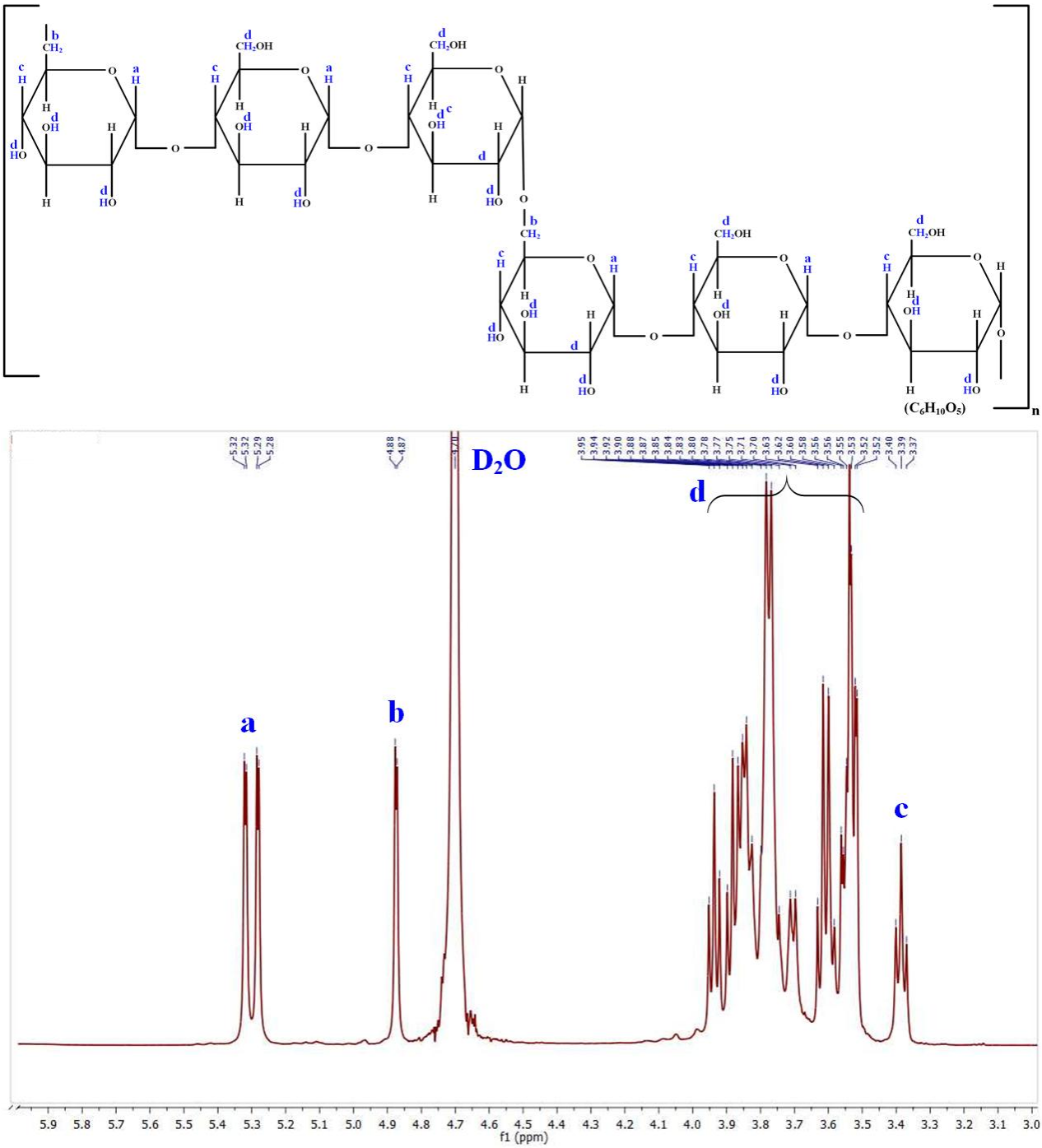

Figure 3.6 (a) ^{1}H NMR spectra of lab-made polysaccharide.

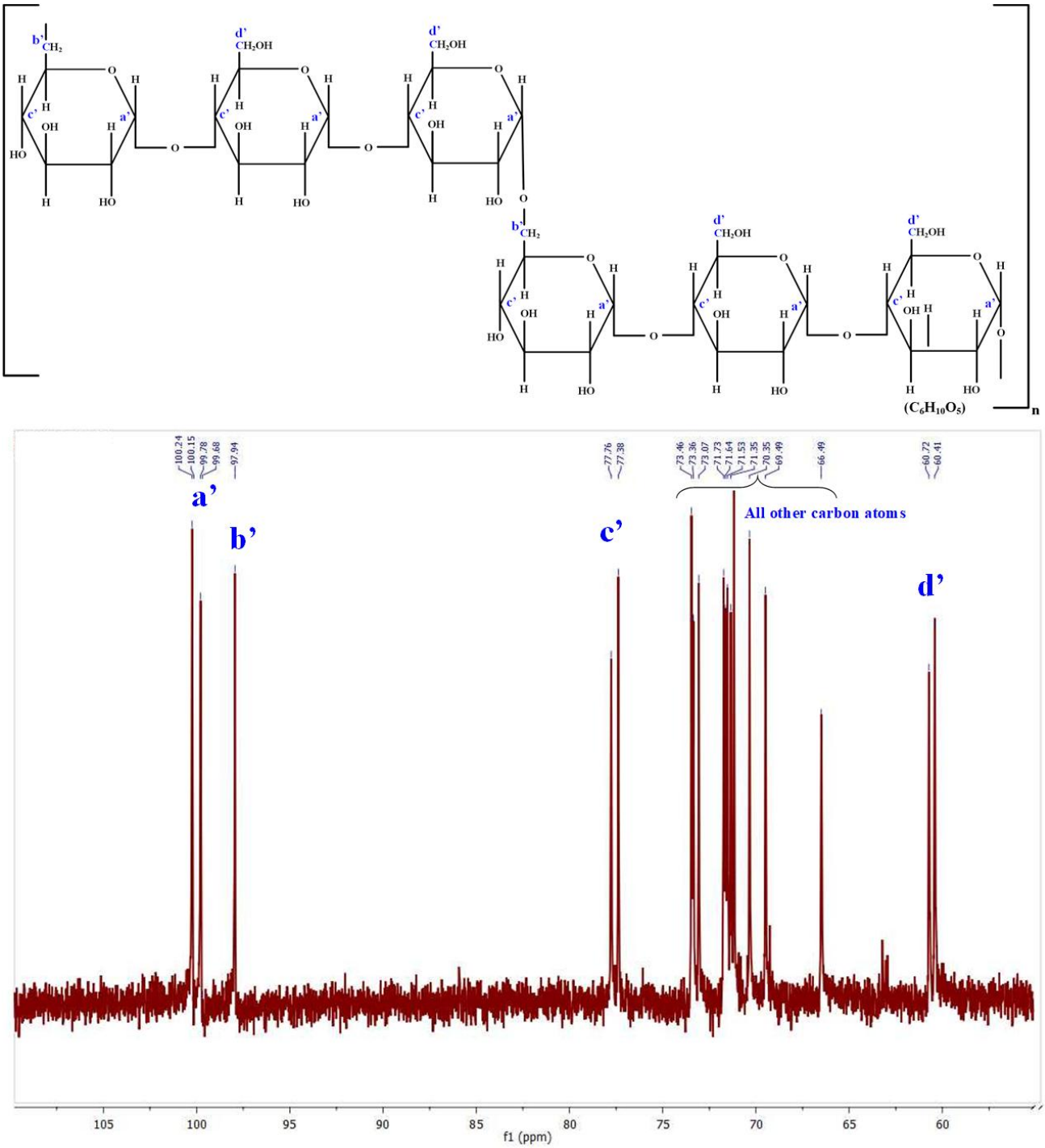

Figure 3.6 (b) ^{13}C NMR spectra of lab-made polysaccharide.

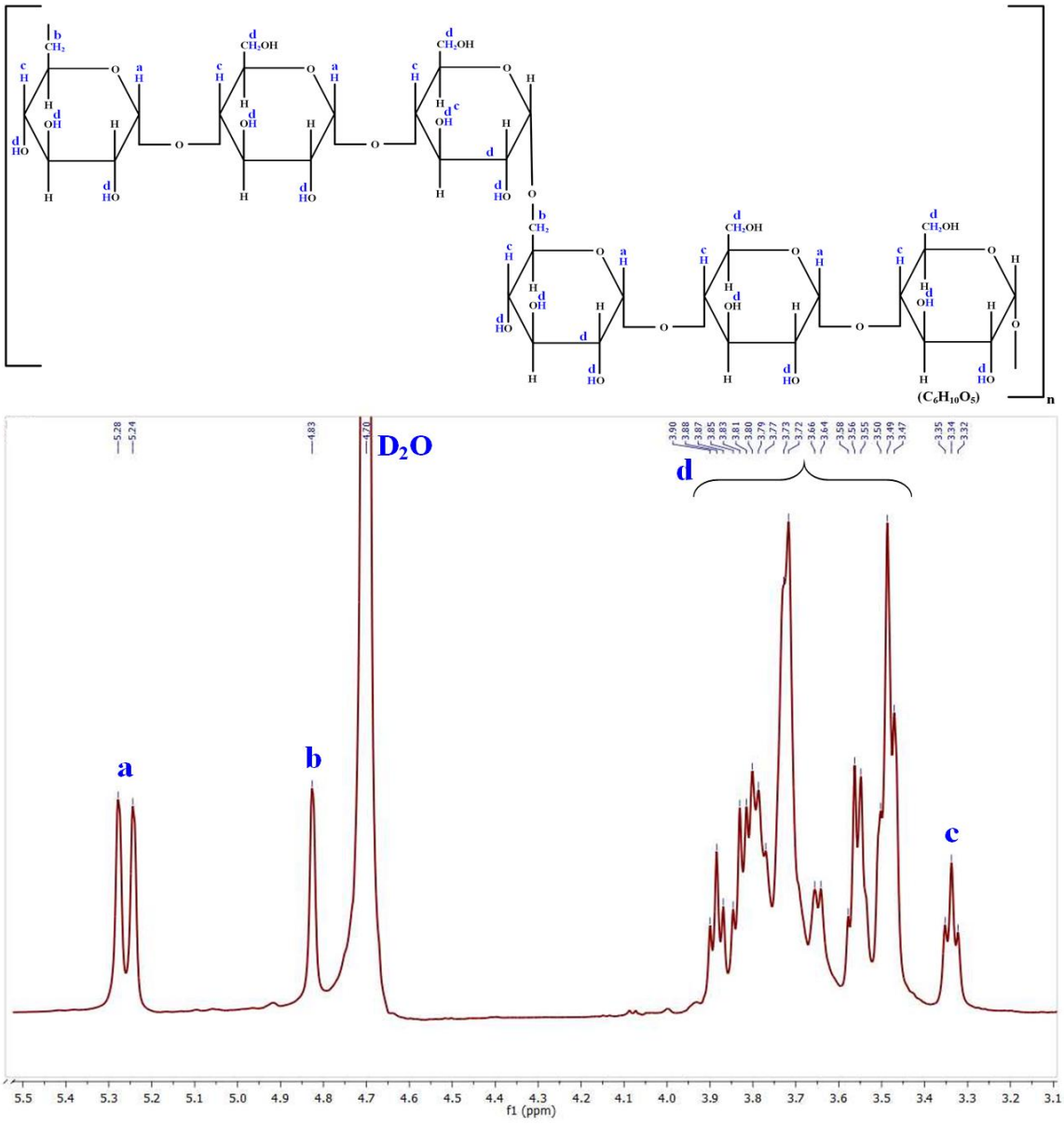

Figure 3.6 (c) ^{1}H NMR spectra of commercial pullulan.

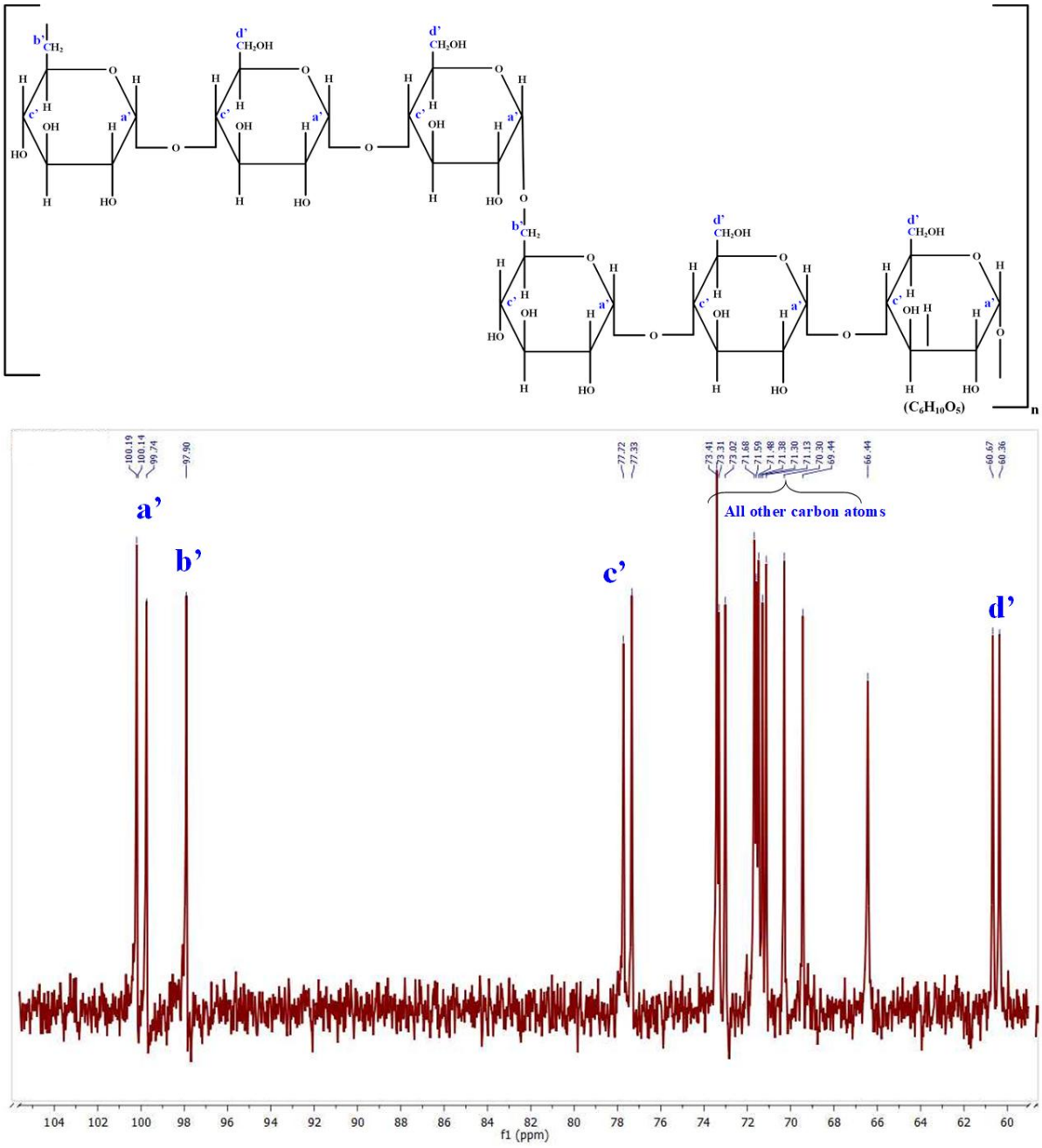

Figure 3.6 (d) ^{13}C NMR spectra of commercial pullulan.

3.2.6 MALDI-TOF MS analysis

The MALDI-TOF mass spectra of lab-made polysaccharide and commercial pullulan have been depicted in (Figure 3.7 (a, b)), respectively. Each peak in the spectra can be described using the equation (24):

$$m/z = 162\,x + M_{\text{adduct}} \qquad (24)$$

where m/z is the mass-to-charge ratio of ion, x is the number of glucose units and M_{adduct} is the mass of adduct ion such as 23 Da (Na^+), 39 Da (K^+), or even unknown adducts (as in the case of lab-made polysaccharide).

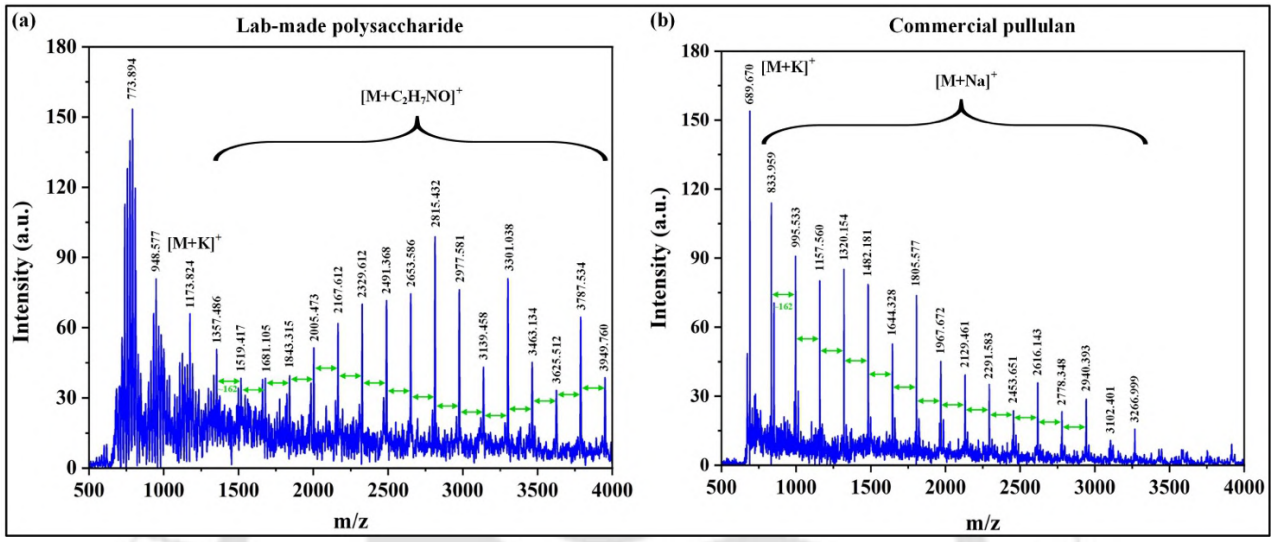

Figure 3.7 MALDI-TOF spectra of **(a)** lab-made polysaccharide and **(b)** commercial pullulan.

In the lab-made polysaccharide spectrum (Figure 3.7 (a)), the peak at m/z 1173.824 corresponded to a potassium adduct $[M+K]^+$, followed by a series of peaks each corresponding to a mass adduct of ~ 61 Da. This consistent ~ 61 Da shift may be attributed to some unknown ion adducts possibly originating from ethanolamine-related adduct $[M+C_2H_7NO]^+$ formation, resulting from the presence of yeast extract in the fermentation medium. As depicted in Figure 3.7 (a), the series of peaks occurred at regular spacing of ~ 162 Da. This repeating mass difference of ~ 162 Da between peaks confirms the presence of glucose-based repeating units in the polymer. On the other hand, the MALDI-TOF mass spectrum of commercial pullulan (Figure 3.7 (b)), demonstrated a relatively clear pattern, with a series of peaks spaced ~ 162 Da apart. This spacing is consistent with the stepwise addition of glucose monomer units. The first prominent peak appeared at m/z 689.670, corresponding to a degree of polymerization (DP) of 4 and was attributed to a potassium adduct $[M+K]^+$. Interestingly, all the subsequent peaks observed at m/z 833.959–3266.999 followed the sodium adduct $[M+Na]^+$ pattern corresponding to DP 5–20, respectively (Figure 3.7 (b)). The presence of a single potassium adduct at the lower mass range may be due to minor variations in ionization or trace levels of potassium remaining in the matrix. Thus, these findings demonstrate that the MALDI-TOF MS

analysis of both the lab-made polysaccharide and commercial pullulan showed a series of peaks, with each successive peak separated by ~ 162 Da, corresponding to one glucose unit ($C_6H_{10}O_5$). This pattern confirms the polymeric structure of pullulan and further verifies that the lab-made polysaccharide is pullulan.

3.3 Summary

In this chapter, pullulan was successfully synthesized using shake-flask fermentation of *A. pullulans* NCIM 1049 under statistically optimized medium conditions, utilizing liquid sugarcane jaggery as a cost-effective carbon source. Jaggery, which is a concentrated sugar-rich form of sugarcane juice, serves as an economical and sustainable option compared to commercially refined sugars. Although jaggery has been used before for pullulan production, this study is the first to report its use with the specific strain NCIM 1049. To improve pullulan production, a two-step statistical approach was used to optimize the fermentation medium. First, the PBD was used to screen and identify the most significant factors influencing pullulan production. Based on these results, the RSM-based media optimization was carried out using BBD to determine the optimal levels and combinations of these key nutrients. This approach enabled a more efficient formulation of the medium, thereby enhancing the pullulan production. The prepared pullulan was extracted and purified using standard techniques, including ethanol precipitation, dialysis, and lyophilization. Its structural properties were characterized using FTIR, ^{1}H NMR, ^{13}C NMR, and MALDI-TOF MS, confirming its close similarity to commercial pullulan in terms of structure and composition.

CHAPTER 4

PREPARATION OF BILAYERED WOUND HEALING SCAFFOLD WITH ELECTROSPUN GENTAMICIN-LOADED PULLULAN/PVA/GUM ARABIC NANOFIBERS AND SOLVENT-CASTED PLA

Motivation

Effective wound healing is often difficult to achieve, especially in severe or chronic cases where infection, excess fluid, and tissue damage complicate recovery. Conventional single-layered dressings often fail to meet these complex requirements, leading to prolonged healing and patient discomfort. This highlights the urgent need for advanced, multifunctional wound dressings that can address these limitations. The development of a bilayered scaffold, integrating a bioactive, hydrophilic sublayer and a protective, hydrophobic top layer, offers a strategic approach to overcoming these challenges. By utilizing the biocompatibility of pullulan and its blends, along with the structural integrity of polylactic acid, this research aims to fabricate and characterize a bilayered scaffold that effectively supports wound healing through sustained drug release, superior exudate absorption, and barrier protection.

The work in the chapter has received the scientific recognition as follows:

Das, K., *Tiwari, V., Prasannavenkadesan, V., Banerjee, S.K. and Katiyar, V., 2025. In Vitro Biocompatibility and Wound Healing Potential of Bilayered Scaffold With Electrospun Gentamicin-Loaded Pullulan/PVA/Gum Arabic Nanofibers and Solvent-Casted PLA. Journal of Applied Polymer Science, p.e56731.*

Abstract

Severe wound healing requires specialized dressings that can effectively absorb exudate, prevent infections, and facilitate tissue regeneration while minimizing trauma during removal. Traditional single-layered wound dressings often fail to maintain the optimal balance between moisture retention and protection, leading to delayed healing. To overcome these limitations, a bilayered scaffold was developed, integrating both hydrophilic and hydrophobic components to enhance wound healing properties. The fabricated scaffold consisted of an electrospun hydrophilic sublayer composed of a pullulan/polyvinyl alcohol (PVA)/gum arabic blend, loaded with the antibiotic gentamicin sulfate, and a solvent-casted hydrophobic top layer composed of polylactic acid (PLA). The hydrophilic layer was designed for direct contact with the wound to facilitate easy removal of the dressing. On the other hand, the hydrophobic PLA layer was designed to enhance the mechanical stability of the scaffold, thereby reducing excessive moisture loss, and provide a protective barrier against external environmental contaminants. The antibacterial efficacy of the scaffold was demonstrated against *Staphylococcus aureus* (*S. aureus*) and *Escherichia coli* (*E. coli*). The drug release studies showed that 93.09 ± 2.63 % of gentamicin sulfate was released in a controlled manner over 48 hrs. The release profile followed Zero-Order kinetics ($R^2 = 0.9850$), indicating a consistent and sustained release of the antibiotic. Additionally, the scaffold exhibited a high swelling index of 611.85 ± 15.05 %, confirming its superior exudate absorption capability; an essential property for wound dressing materials. The water vapour transmission rate (WVTR) was 94.20 ± 14.50 g/m²/day, while the porosity measured 70.56 ± 0.58 %, both of which fall within the acceptable range for effective wound healing. *In vitro* biocompatibility and wound healing assays using human dermal fibroblast (HDF) cells further validated the non-cytotoxic nature of the scaffold, confirming its safety and suitability for wound dressing applications.

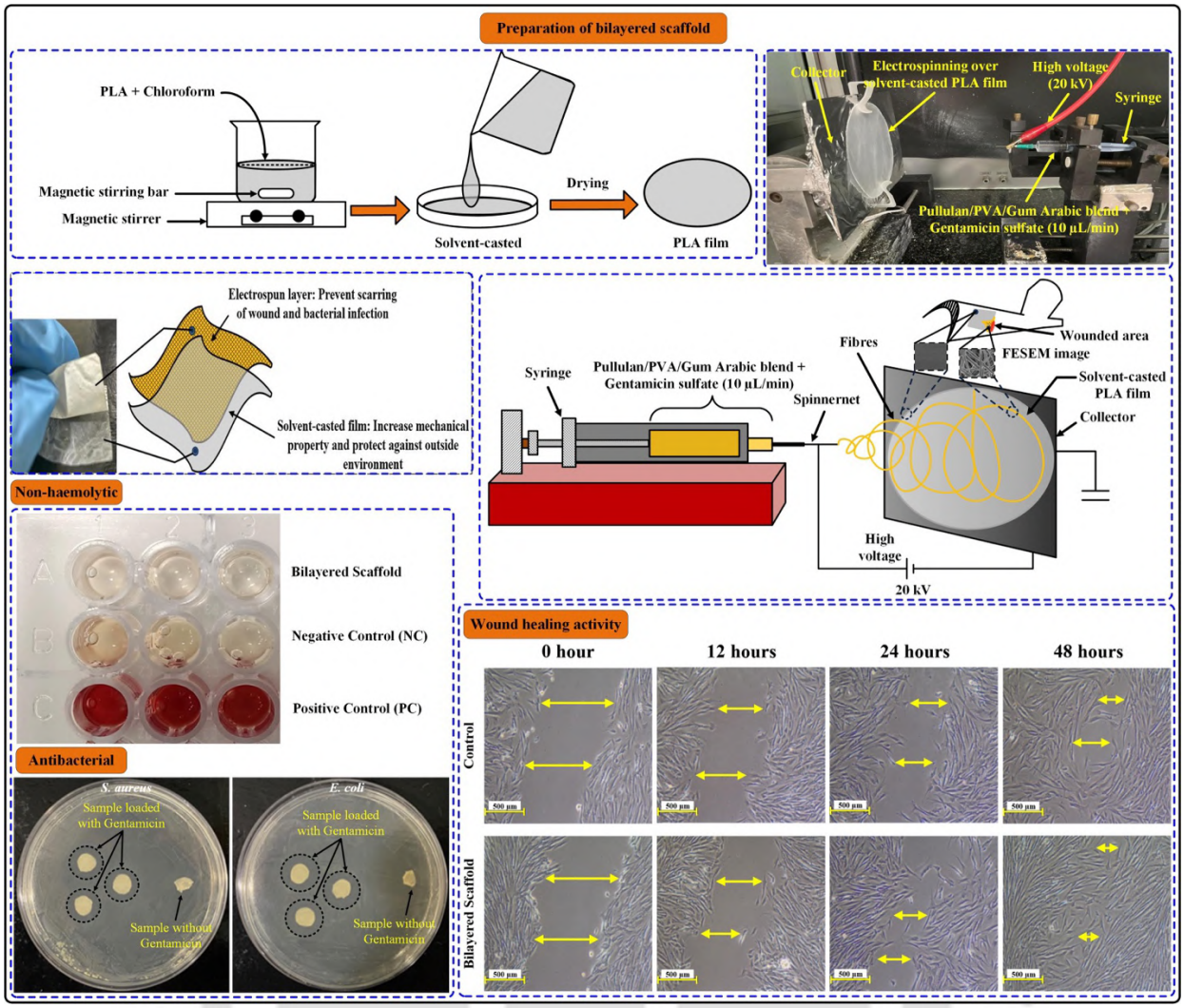

Figure 4.1 Scheme of chapter 4.

4.1 Introduction

Skin is the largest organ of the human body that acts as a protective shield, safeguarding internal organs from outside environment [349,350]. It regulates body temperature, prevents moisture loss, and protects against harmful pathogenic agents. The skin comprises of the outermost layer, the epidermis, which is responsible for generating melanin for pigmentation, shedding dead skin cells, and protecting the skin against Ultra-Violet (UV) rays. The middle layer, the dermis, which comprises of sebaceous glands, sweat glands, blood vessels and nerves, is responsible for thermoregulation and sensation. The deepest layer, the hypodermis, comprises of adipose and connective tissues that insulate and cushion vital organs. Even though the skin can withstand various environmental challenges, it is still vulnerable to injuries. This is where the importance of wound healing comes into place. The wound healing process includes haemostasis, which stops bleeding by clotting; followed by inflammation, during

which immune cells remove waste products and release growth factors. Then proliferation occurs, when new blood vessels are formed, and collagen builds up within the injury. Finally, remodelling occurs during which the injured tissue matures and strengthens over weeks or months, depending on the wound severity [351]. A schematic representation of the wound healing process have been depicted in Figure 4.2.

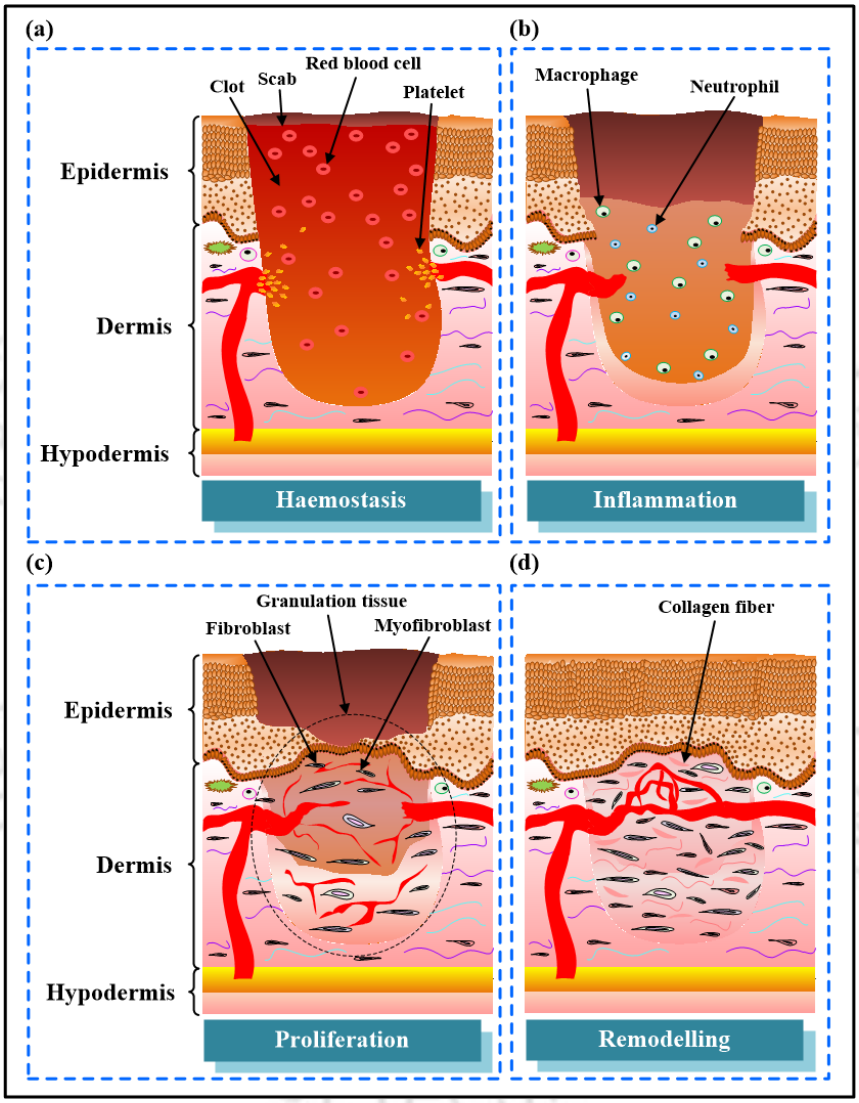

Figure 4.2 Schematic representation showing the different stages in wound healing process.

It is essential for wound dressing scaffolds to be non-cytotoxic, non-antigenic, elastic, flexible, resistant to shear forces, permeable to gaseous exchange, and have antibacterial properties [352,353]. Traditional foams and hydrogels are known for their high absorption capacity, often resulting in a dry wound environment and adhering firmly to the dry surface, making their removal uncomfortable [354]. Scaffolds fabricated using electrospinning are better alternatives when compared with the traditional wound dressing approach in terms of

surface area, gaseous exchange and exudate absorption [355–358]. Also, the nanofiber scaffolds with active components can be fabricated using electrospinning [349,359,360]. Researchers reported that the structure of skin could be mimicked with the electrospun fibers as they have an excellent extracellular matrix (ECM) analogue [353,361–363] promoting cell growth and skin regeneration [354,364]. In addition, the porosity of the scaffold helps the oxygen permeability, which in turn improves drug transportation, tissue regeneration and shields against bacterial infections [360,364].

Pullulan, a biodegradable polymer synthesized through fungal fermentation of *Aureobasidium pullulans* (*A. pullulans*), has been reported to exhibit high water absorption capacity, excellent drug delivery and moisture retention potential [15,365]. It also possess excellent film and fiber-forming properties, non-toxicity and biocompatibility, making it a suitable material for various biomedical applications including wound dressing, tissue engineering, drug and gene delivery [96,129]. Furthermore, it is known to enhance the spinnability of electrospinning solutions by increasing viscosity, reducing surface tension and conductivity [366]. It has been used along with other polymers to create blends or composites for several biomedical applications [367,368]. Polyvinyl alcohol (PVA), another biodegradable polymer, has been reported to enhance the mechanical strength and stability of the electrospun fibers, while demonstrating excellent capacity for absorbing excess wound exudates. Furthermore, its non-toxicity, biocompatibility, chemical resistance, and water solubility, make it an effective carrier for hydrophilic bioactive agents. These properties also contribute to its superior fiber-forming capacity, further supporting its role in wound care by providing structural integrity and stability [301,369–373]. However, the poor stretchability and high hydrophilic nature of PVA limit its applicability. This issue could be addressed by using composite polymers in biomedical applications. Additionally, researchers have reported improved mechanical properties of pullulan/PVA composite nanofiber [374]. Gum arabic is another biodegradable polymer recognized for its beneficial properties in wound healing. It is non-toxic and biocompatible, and it exhibits haemostatic, antioxidant, and hydrophilic characteristics that support tissue repair and regeneration. It has been shown to facilitate effective absorption of wound exudates while preserving a moist environment, which is crucial for promoting optimal wound healing and skin regeneration [375–378]. Similarly, polylactic acid (PLA) is recommended for various biomedical applications due to its ability to enhance wound healing [379–382]. Furthermore, researchers reported that wounds treated using gentamicin (an antibacterial drug) accelerated wound recovery [383]. Thus, the incorporation of gentamicin into wound dressing scaffolds would enhance their healing efficiency and

protect against secondary infections. Although, the efficiency of the individual materials has been extensively documented in the literature; to the best of author's knowledge, there is no study reported on combining all these materials for a practical wound healing application.

Single-layered scaffolds often compromise one or more key properties, such as moisture regulation, exudate absorption, breathability, mechanical strength, or controlled drug release. For instance, a purely hydrophilic scaffold could absorb exudates but might be prone to mechanical failure and adhere to the wound causing pain during dressing changes. In contrast, a purely hydrophobic scaffold might enhance the mechanical properties but could lead to inadequate exudate absorption and wound maceration, thereby hindering the healing process. However, researchers have reported that bilayered wound dressing scaffolds are highly promising for addressing the limitations associated with traditional hydrogels and single-layered scaffolds [302,384–386]. The bilayered scaffold structure is designed after the natural organization of healthy skin, which includes two distinct layers with specialized functions: the epidermis (dense outer layer) and the dermis (inner layer) [387]. In contrast to the densely structured epidermis, the dermis primarily consists of loosely organized acellular connective tissue, incorporating collagen fibers, elastic fibers, and extracellular matrix components [388]. The bilayered wound healing scaffolds usually comprise a hydrophilic sublayer that simulates the properties of natural skin, facilitating cell adhesion and proliferation. In addition to this, there is a dense hydrophobic top layer that provides structural support and helps regulate moisture in the wound area. Additionally, this hydrophobic layer protects the tissue from external factors, serves as an effective barrier, prevents external liquids and microbial contaminants from penetrating the dressing, and maintains an optimal healing environment [384,389–395].

Hence, this study addressed an electrospun gentamicin-loaded hydrophilic pullulan/PVA/gum arabic sublayer and a solvent-casted hydrophobic top layer (or film) of PLA fabricated to be utilized as an antibacterial bilayered wound dressing scaffold. The hypothesis of the bilayered structure was to utilize the hydrophilic electrospun sublayer to easily treat critical wounds and the hydrophobic solvent-casted top layer to enhance mechanical properties of the scaffold, prevent rapid moisture loss and protect against external environment. Moreover, impregnation of the hydrophilic layer with gentamicin would contribute antibacterial properties to the resultant scaffold.

4.2 Results and discussion

4.2.1 Morphological and compositional analyses

The combined effect from both the electrospun and solvent-casted layers of the fabricated bilayered scaffold is illustrated in the cross-sectional FESEM image, as shown in Figure 4.3 (a). Additionally, the morphology of both the layers were separately observed by FESEM, as shown in Figure 4.3 (b, c).

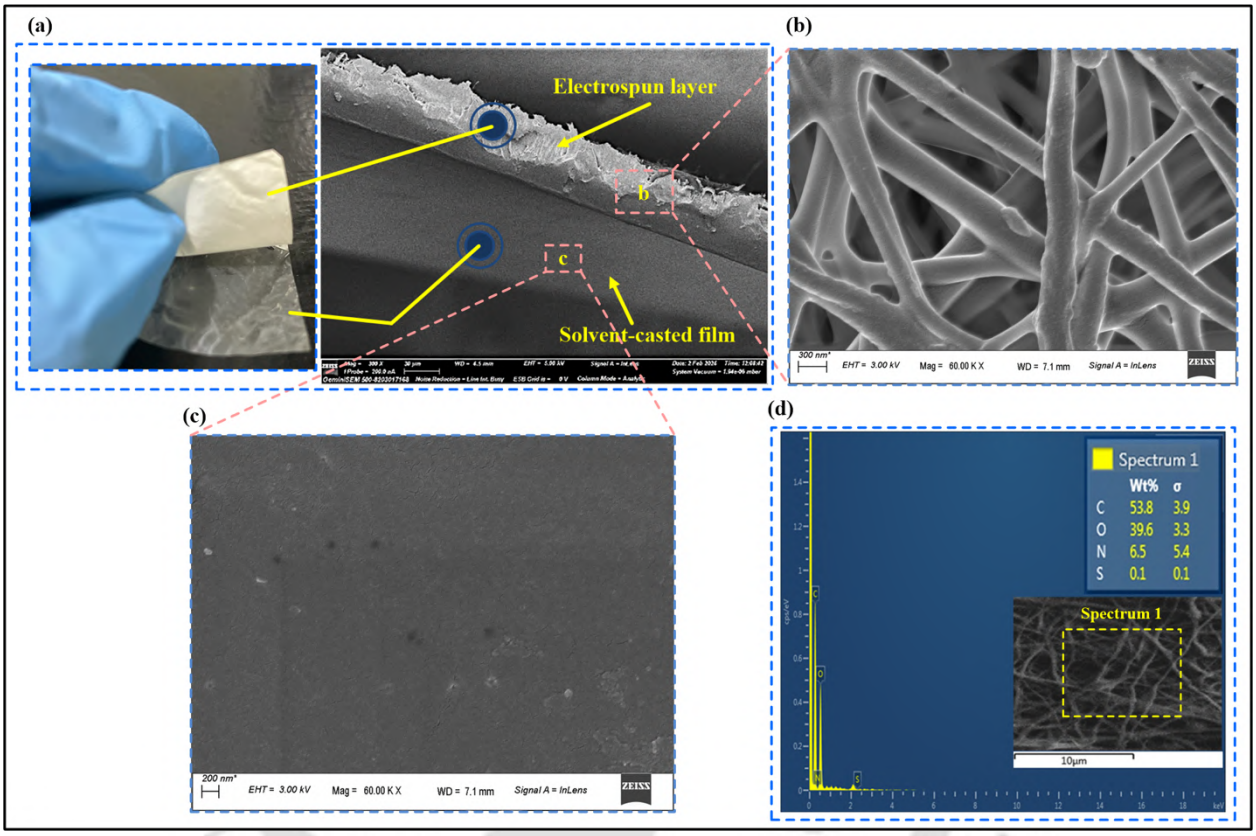

Figure 4.3 FESEM images of the fabricated scaffold showing **(a)** the cross-sectional view of the bilayered structure, **(b)** electrospun hydrophilic layer, **(c)** solvent-casted hydrophobic layer, and **(d)** EDX spectra.

The electrospun layer demonstrated an average nanofiber diameter of 349 ± 52 nm, as shown in Figure 4.3 (b). The overall morphology of the nanofibers appeared smooth, continuous, and free from bead formation, indicating a successful electrospinning process. The uniformity and smooth morphology of nanofibrous surface would facilitate cell growth, adhesion and proliferation, thereby enhancing the cytocompatibility and healing efficacy of the material [396]. Additionally, the FESEM image of the solvent-casted layer (Figure 4.3 (c)) reveals a smooth and continuous film with a homogeneous appearance. The solvent-casting process thus appears to have resulted in an even distribution of the PLA polymer across the film surface.

The EDX study provide information about the weight percentages of different elements present in the scaffold, including Carbon (C), Oxygen (O), Nitrogen (N), and Sulfur (S). The weight percentages of the elements were found to be as follows: C - 53.8 %, O - 39.6 %, N - 6.5 %, and S - 0.1 % (Figure 4.3 (d)). The presence of N in the scaffold can be attributed to the aminoglycosidic antibiotic (gentamicin sulfate) used. Aminoglycosides contain an amine group, which justifies the existence of N in the scaffold. The detection of S further validates the successful incorporation of gentamicin sulfate into the scaffold, supporting its potential application as an antibacterial wound dressing material.

4.2.2 Analysis of thickness, swelling index and moisture content

Moisture in wounds is crucial as it enables quicker wound healing, prevents invasion by microorganisms, and reduces the pain associated with removing wound dressings [397]. Improved absorption or retention qualities of wound dressing help efficiently absorb wound exudates and retain moderately moist conditions over time [398]. The thickness, swelling index and moisture content of the scaffold were determined to evaluate its exudate absorbing capacity when used for wound dressing purpose. The thickness of the bilayered scaffold, electrospun sublayer, solvent-casted top layer and control low density polyethylene or LDPE film (for WVTR characterization) was measured to be 0.36 ± 0.05, 0.29 ± 0.02, 0.07 ± 0.01 and 0.10 ± 0.02 mm, respectively.

The scaffold was immersed in distilled water (pH 7) for a 24-hr duration to determine the swelling index and moisture content using the formulae in equations (4) and (5), respectively (discussed in chapter 2). The swelling index was found to initially increase with time up to 12 hrs (from 109.11 ± 9.07 % to 611.09 ± 21.06 %), after which no significant increase in the swelling index was observed (611.85 ± 15.05 % up to 24 hrs), as shown in Figure 4.4 (a). Notably, it has been reported in the literature that a minimum swelling index of 300 % is recommended for a super-absorbent wound dressing material [399–402]. Thus, the scaffold presented in this study may be regarded to exhibit an excellent swelling index. Similarly, an initial increase in the moisture content was noted with time up to 12 hrs (from 52.61 ± 2.96 % to 85.92 ± 1.76 %) and became nearly constant after that (85.94 ± 1.86 % up to 24 hrs), as shown in Figure 4.4 (b). Moreover, statistically significant changes were observed in the swelling index ($p < 0.01$) and moisture content ($p < 0.05$) with respect to time. The increase in swelling ratio and moisture content may be attributed to the hydrophilicity of the electrospun layer comprising pullulan, PVA and gum arabic.

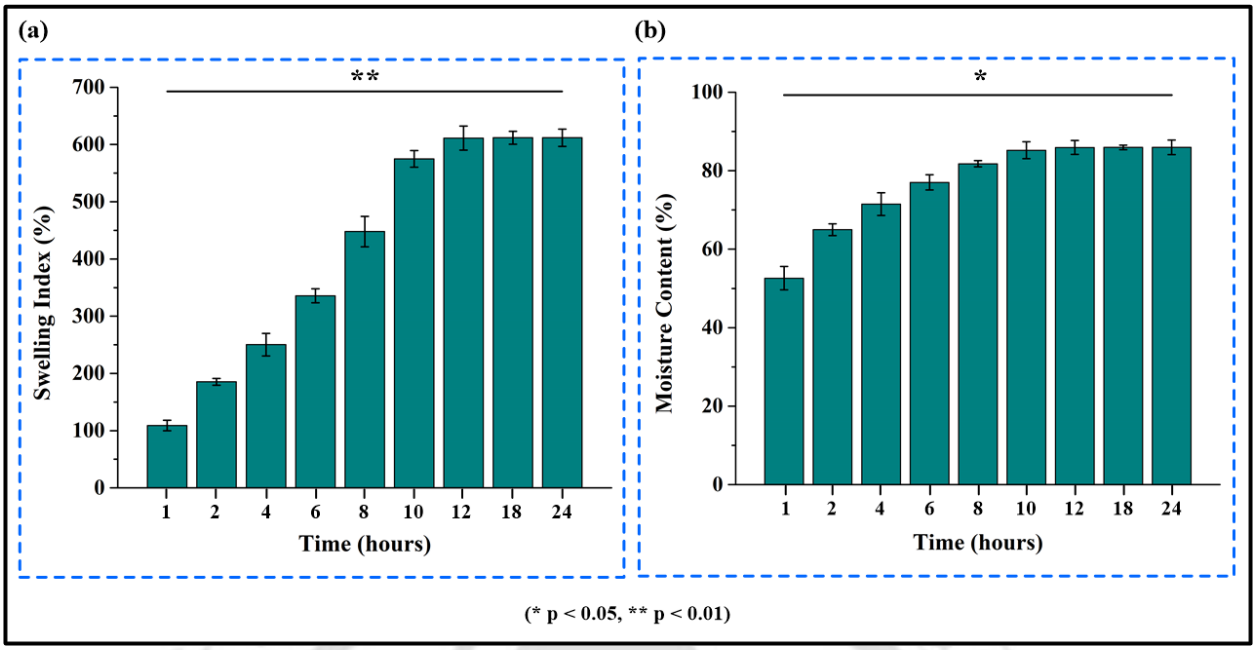

Figure 4.4 Rate of change of **(a)** swelling index and **(b)** moisture content of the bilayered scaffold with respect to time. Results are shown as mean ± SD.

4.2.3 Mechanical testing

The fabricated scaffold was subjected to tensile tests to determine its mechanical strength and integrity against external forces. Additionally, both the individual layers (electrospun layer and solvent-casted layer) were separately tested for their mechanical properties to better understand the significance of the bilayered structure in maintaining the strength of the resultant scaffold, as shown in the stress-strain curves (Figure 4.5 (a)). The electrospun layer ruptured easily at an elongation of 29.92 ± 0.76 %. On the other hand, the bilayered scaffold, which included both the electrospun and the solvent-casted layers, demonstrated excellent durability and sustained elongation up to 91.74 ± 1.16 % before rupturing. The bilayered scaffold had a higher tensile strength (25.12 ± 0.27 MPa) than the electrospun layer (21.55 ± 0.42 MPa), as listed in Table 4.1. The solvent-casted PLA layer demonstrated tensile strength of 35.82 ± 0.12 MPa, Young's modulus of 12.83 ± 0.15 MPa and elongation at break of 63.52 ± 2.31 %, which are similar to previously reported studies [403]. It was observed that without the solvent-casted layer, the tensile strength of the electrospun layer alone was comparatively lower. Thus, the solvent-casted PLA layer enhanced the mechanical strength of the fabricated scaffold. Mechanical properties of wound dressing materials are considered satisfactory within the ranges desirable for normal skin in terms of the tensile strength (5 to 30 MPa), Young's modulus (4.6 to 20 MPa), and percentage of elongation (35 to 115 %) [404–406]. Therefore, the fabricated bilayered scaffold meets the requirement for substantial mobility of a wound

dressing material. Furthermore, the incorporation of PLA has been reported to enhance mechanical properties of scaffold by several researchers [379,380]. Notably, it was observed that the bilayered scaffold demonstrated higher elongation at break than that of electrospun layer and solvent-casted layer. This may be attributed to the fact that the bilayered scaffold benefitted from the combined mechanical properties of both the electrospun layer and solvent-casted layer. The porous electrospun layer typically showed high flexibility and an ability to deform before breaking due to the nature of its fibrous network. The solvent-casted layer, on the other hand, being more dense, provided rigidity. Both the layers together formed a complementary structure where the electrospun layer provided flexibility, and the solvent-casted layer enhanced strength, resulting in a scaffold with improved overall elongation at break.

Table 4.1 Mechanical properties of the electrospun layer, bilayered scaffold and the solvent-casted layer.

Layer/Scaffold	**Tensile strength (MPa)**	**Young's modulus (MPa)**	**Elongation at break (%)**
Electrospun layer	21.55 ± 0.42	1.68 ± 0.85	29.92 ± 0.76
Bilayered scaffold	25.12 ± 0.27	6.79 ± 1.24	91.74± 1.16
Solvent-casted layer	35.82 ± 0.12	12.83 ± 0.15	63.52 ± 2.31

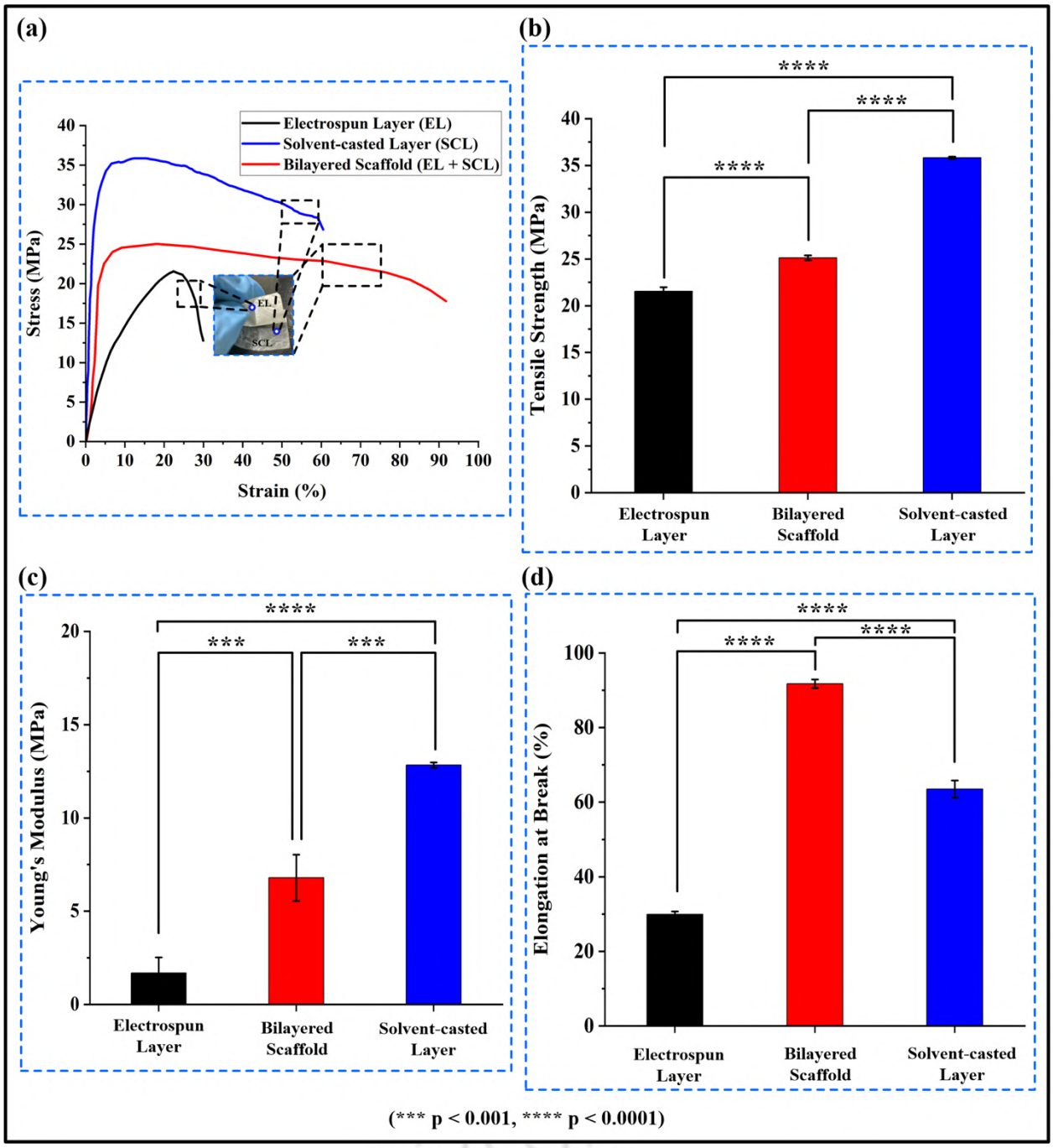

Figure 4.5 (a) Stress-strain curve of bilayered scaffold, electrospun layer and solvent-casted layer. Bar graphs showing statistical differences of bilayered scaffold, electrospun layer and solvent-casted layer in: **(b)** tensile strength, **(c)** Young's modulus, and **(d)** elongation at break. Results are shown as mean ± SD.

As the bilayered scaffold underwent stretching, the fibrous network of the electrospun layer extended and redistributed the applied stress, while the solvent-casted layer provided

structural support. This interaction allowed the scaffold to withstand more strain before breaking, leading to a higher elongation at break compared to either layer alone. In the present study, the differences in mechanical properties were statistically significant in case of bilayered scaffold, electrospun layer and solvent-casted layer. Additionally, the differences in tensile strength and elongation at break were statistically highly significant ($p < 0.0001$), as shown in Figure 4.5 (b, d) respectively. However, in case of Young's modulus, as shown in Figure 4.5 (c), the difference was statistically highly significant ($p < 0.0001$) when comparing the electrospun layer to the solvent-casted layer, and relatively less significant ($p < 0.001$) when comparing the electrospun layer to the bilayered scaffold, and the bilayered scaffold to the solvent-casted layer.

4.2.4 Surface wettability and WVTR

The surface wettability or hydrophilicity of wound dressings enable better absorption of exudates and maintain an optimum moist environment at the wound site, thereby accelerating the wound healing process [407,408]. Moreover, the surface hydrophilicity enhances the cytocompatibility of the material by facilitating the cell growth, attachment and proliferation [409]. For effective wound healing, an adequate hydrophilicity is very essential for the surface of wound dressing, that is to be in direct contact with the wound site [410]. Researchers have reported that surfaces with contact angle less than 65° are considered hydrophilic and those above 65° are considered hydrophobic [411,412]. The water contact angles of both the electrospun and solvent-casted layers of the fabricated scaffold were separately measured until they became constant after 60 secs (Figure 4.6 (a, b)).

The electrospun layer of the scaffold, that is to be in direct contact with the wound site, was made of a pullulan/PVA/gum arabic blend, each containing abundant –OH groups within their structures. These –OH groups facilitate the formation of extensive hydrogen bonding (–OH···O–) within the layer, resulting in a highly hydrophilic surface. When a water droplet is placed on the hydrophilic surface, it is rapidly absorbed due to the strong affinity between the water molecules and the –OH groups. As a result, the contact angle is relatively low, measuring approximately 63.53° ± 2.01° to 45.82° ± 1.99° within a duration of 0 to 60 secs (Figure 4.6 (a)). The decrease in contact angle indicates that the water droplet spreads out and is readily absorbed by the hydrophilic electrospun layer. The change in contact angle after 60 secs when compared to that at 0 sec was highly significant ($p < 0.0001$). Additionally, when the contact angle after 60 secs was compared to that after 30 secs, and after 30 secs to that at 0 sec, a statistically significant difference ($p < 0.01$) was observed in each case (as shown in Figure 4.6

(a)). This is because the contact angle changes significantly over time due to the high affinity of the hydrophilic layer towards water. Notably, it has been reported that a water contact angle within the range of 40° to 70° is considered suitable for wound dressing applications [307]. Thus, the observed hydrophilicity of the electrospun layer (45.82° ± 1.99° contact angle) can significantly enhance cytocompatibility and wound healing efficacy of the scaffold.

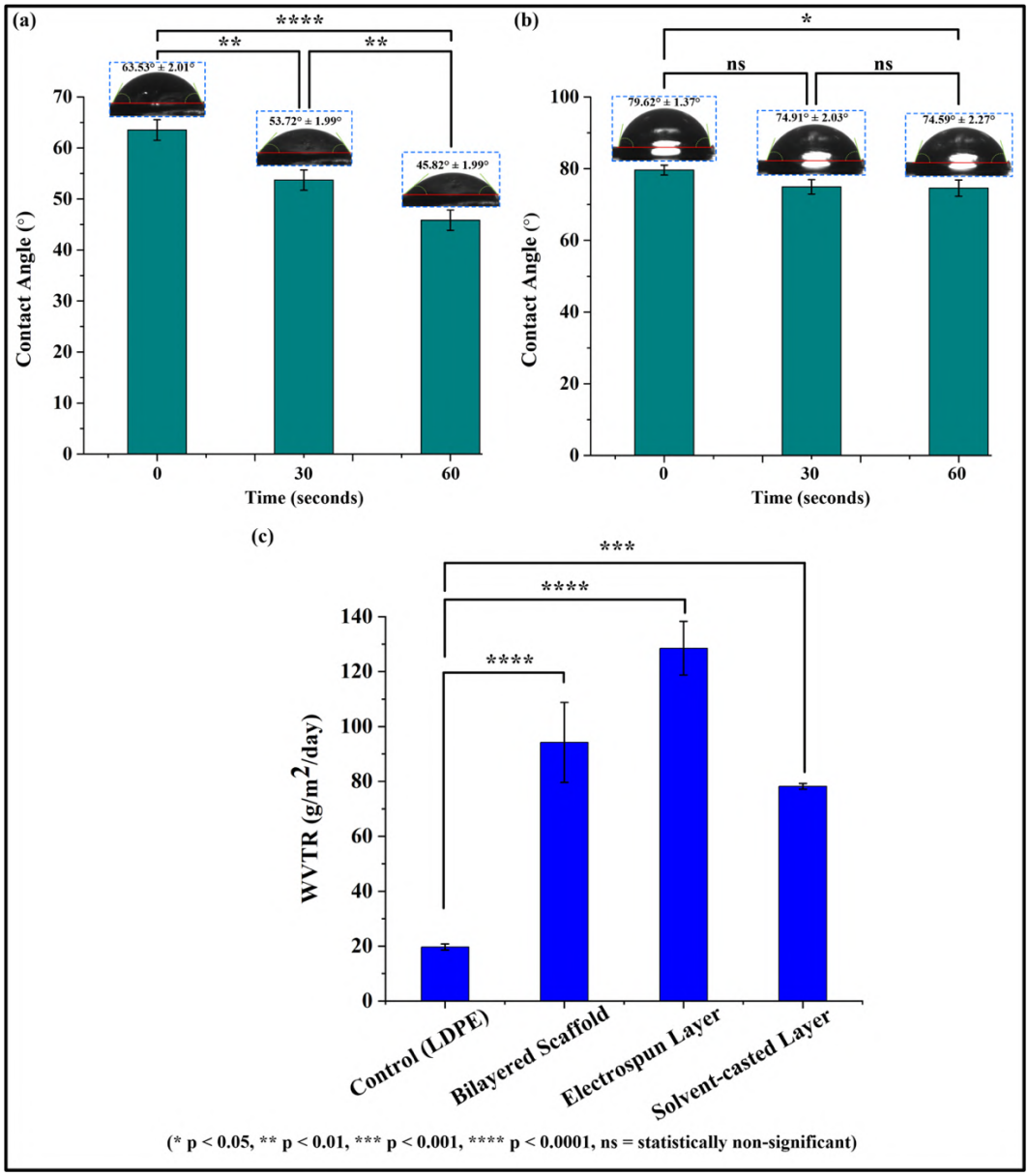

Figure 4.6 Bar graphs showing the statistical analysis of **(a)** contact angle for the hydrophilic layer, **(b)** contact angle for the hydrophobic layer of the scaffold, and **(c)** WVTR comparing the bilayered scaffold and its individual layers with the control (LDPE film). Results are shown as mean ± SD.

In contrast, the solvent-casted layer made of PLA does not contain the same abundance of –OH groups and hydrogen bonding capabilities as the hydrophilic layer. Consequently, when a water droplet is placed on the solvent-casted layer, it is less readily absorbed, leading to a higher contact angle of approximately 79.62° ± 1.37° to 74.59° ± 2.27° within a duration of 0 to 60 secs (Figure 4.6 (b)). Additionally, the contact angle results obtained for the PLA film is similar to the literature [413,414]. The higher contact angle indicates that the water droplet remains more localised and does not quickly spread or absorb into the solvent-casted layer. In this case, the change in contact angle after 60 secs when compared to that at 0 sec was statistically significant ($p < 0.05$). However, when the contact angle after 60 secs was compared to that after 30 secs, and after 30 secs to that at 0 sec, the difference was statistically non-significant (ns) in each case (Figure 4.6 (b)). This is because the contact angle changes slightly over time due to the surface hydrophobicity of this layer.

WVTR is another important parameter to determine the efficacy of wound dressing scaffolds. It helps in moisture regulation at the wound surface by enabling water vapour passage through the scaffold [415]. Moreover, wound dressings with a high value of WVTR cause dryness at the wound surface due to rapid moisture loss; whereas, those with low WVTR values cause accumulation of exudates, thereby slowing down the healing process [416,417]. Thus, maintaining an optimum WVTR is essential for accelerated wound healing. In the present study, the WVTR of the pure LDPE film control group was 19.70 ± 1.10 g/m^2/day, which is similar to previously reported study [418]. Notably, the solvent-casted PLA top layer despite being dense and non-porous, still allowed small amounts of water molecules to diffuse through it, with a WVTR of 78.24 ± 1.02 g/m^2/day (Figure 4.6 (c)), which aligns with values reported in prior studies [419]. This is especially due to its low thickness (0.07 ± 0.01 mm) and semi-crystalline structure, which helped to minimize water loss by maintaining the WVTR and moisture levels suitable for wound healing. This may be attributed to the fact that when PLA is cast as a thin film, the diffusion pathway for moisture is relatively short, thereby increasing the rate of moisture permeability through the material. Wound healing scaffolds with WVTR ranging from 76 to 9360 g/m^2/day have been reported to possess faster healing characteristics [420,421]. In the present study, the WVTR of the bilayered scaffold, electrospun layer and solvent-casted layer was found to be 94.20 ± 14.50, 128.53 ± 9.76 and 78.24 ± 1.02 g/m^2/day, all of which lie within the permissible range for materials used in wound dressing. As shown in Figure 4.6 (c), the fabricated bilayered scaffold and the electrospun layer exhibited statistically highly significant differences in WVTR ($p < 0.0001$) compared to the control

LDPE film. In contrast, the solvent-casted layer showed a relatively less significant difference ($p < 0.001$) compared to the control LDPE film.

4.2.5 Porosity

Efficient exchange of nutrients, gases and waste products through the pores of dressing materials is essential for effective wound healing. A porous biomaterial enhances fibroblast adhesion, proliferation, and mobility, while also facilitating the exchange of micronutrients, the delivery of therapeutic agents, and the absorption of exudate at the wound site [422]. As depicted in Figure 4.7, the electrospun nanofibrous layer demonstrated significant porosity (86.98 ± 1.22 %), which contributed to a high surface area-to-volume ratio that supported fibroblast interaction and migration.

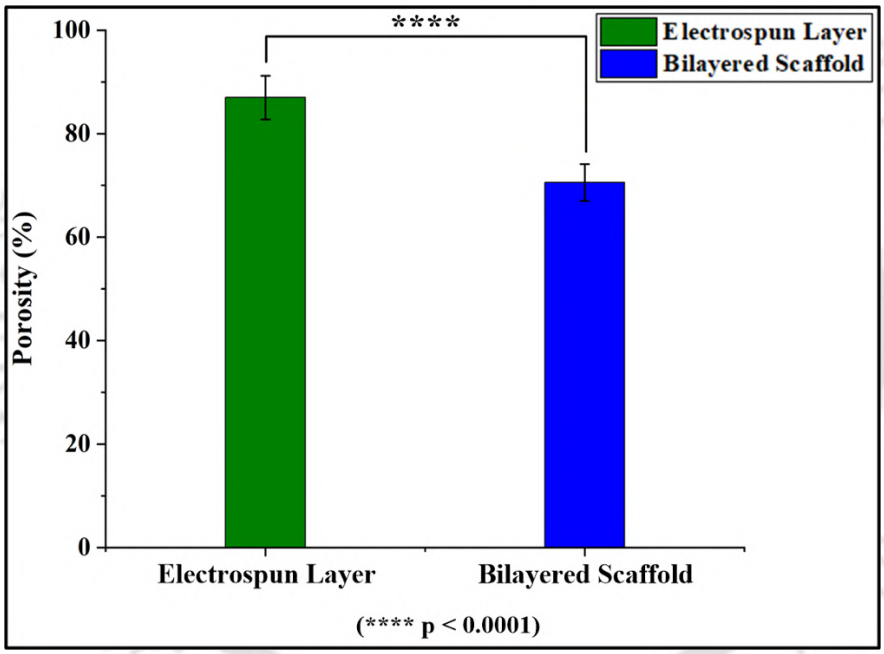

Figure 4.7 Bar graphs representing statistical difference in porosity between the electrospun layer and the bilayered scaffold. Results are shown as mean ± SD.

This high porosity may be attributed to the porous architecture of the layer generated by electrospinning that led to random alignment of nanofibers, creating interconnected voids that enhanced cellular mobility, nutrient diffusion, and exudate management. However, the bilayered scaffold, which included an additional non-porous solvent-casted PLA top layer, exhibited a reduced overall porosity (70.56 ± 0.58 %). This lower porosity may be attributed to the dense and hydrophobic nature of the PLA layer. Notably, it has been reported that wound dressing scaffolds with a porosity range of 60–90 % enhances cellular interactions and

facilitates the effective exchange of biomolecules, proteins, and growth factors, which promotes fibroblast proliferation and migration essential for wound healing [355,423,424]. Although the difference in porosity between the electrospun layer and the bilayered scaffold was statistically highly significant ($p < 0.0001$), as shown in Figure 4.7, both structures demonstrated adequate porosity for use in wound healing applications. Additionally, the non-porous solvent-casted PLA top layer also allowed diffusion of water molecules through it, as evident from its WVTR (shown in Figure 4.6 (c)). This further indicates that the fabricated bilayered scaffold effectively maintained a balance between porosity and barrier properties, without comprising the overall wound healing process.

4.2.6 Analysis of antibacterial activity

The antibacterial activity of the scaffold was determined using disc diffusion method, as reported by Bonadies et al. [425]. For each sample disc (fabricated scaffold cut into circular shapes), the diameters of the inhibition zone were measured.

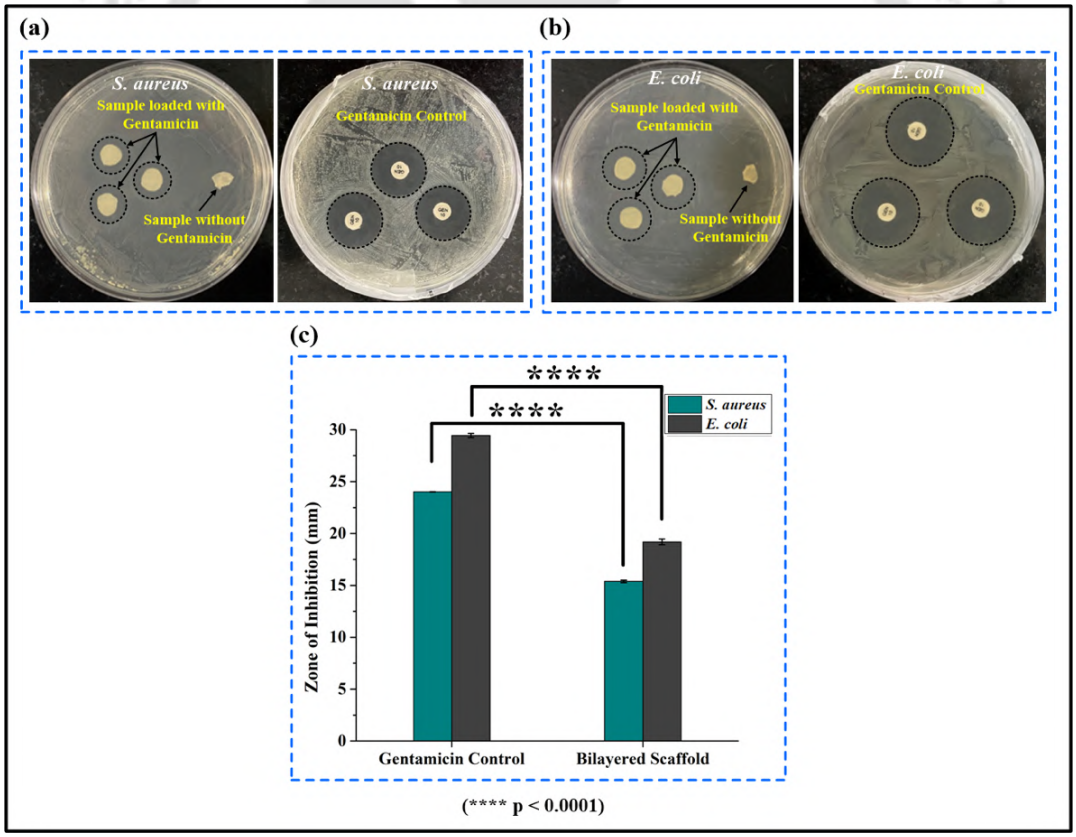

Figure 4.8 Images showing zones of inhibition around the bilayered scaffold and gentamicin control, against **(a)** *S. aureus* and **(b)** *E. coli*. Additionally, **(c)** bar graphs representing statistical differences between the zones of inhibition around the bilayered scaffold and gentamicin control, against *S. aureus* and *E. coli*. Results are shown as mean ± SD.

These zones appear as clear areas around the sample discs, indicating the effectiveness of the drug-loaded bilayered scaffold in inhibiting bacterial growth. The antibacterial activity was attributed to gentamicin sulfate incorporated into the scaffold. The mean diameters of the zone of inhibition around the scaffold were 15.38 ± 0.12 mm against *S. aureus* and 19.18 ± 0.28 mm against *E. coli*. In addition, those around the gentamicin control were 24.01 ± 0.02 mm against *S. aureus* and 29.44 ± 0.20 mm against *E. coli* (Figure 4.8 (a, b)). The inhibition zone around the scaffold when compared to that around the gentamicin control was statistically highly significant ($p < 0.0001$) against both *S. aureus* and *E. coli* (as depicted in Figure 4.8 (c)). The results demonstrate that the fabricated bilayered scaffold showed significant antibacterial activity against *S. aureus* and *E. coli*, as evidenced by the measured zone of inhibition diameters.

4.2.7 In vitro degradation study

The *in vitro* hydrolytic degradation study of the bilayered scaffold was conducted to assess its stability when in contact with the wound surface. The scaffold was found to undergo degradation after immersion in PBS, as shown in the FESEM images and weight loss (rate of degradation) data in Figure 4.9. For calculating the degradation rate, the weight loss was monitored at specific time intervals (Figure 4.9 (c)). In the case of electrospun layer, the diameter of the nanofibers increased during degradation compared to their initial size. This indicates that the bilayered scaffold underwent degradation in PBS. Despite the increase in diameter from 349 ± 52 nm (Figure 4.3 (b)) to 583 ± 78 nm (Figure 4.9 (a)), the nanofibers retained their fibrous structure even after 7 days of degradation. This suggests that the nanofibers possessed favourable biodegradability and dimensional stability, making them applicable to tissue engineering applications [426]. However, no significant changes were noted in the FESEM image of the PLA layer after 7 days of PBS immersion (Figure 4.9 (b)) as compared to that before immersion (Figure 4.3 (c)). Notably, no layer separation was observed in the case of the bilayered scaffold upon its immersion in PBS. In order to better understand the degradation of the two layers, the degradation analysis was conducted for the bilayered scaffold and the two individual layers separately. Additionally, the weight loss assessment was conducted to quantitatively determine the extent of degradation. This data was obtained by assessing the weight of the material before and after degradation; thus, the difference indicated the material lost due to degradation in PBS. As shown in Figure 4.9 (c), the electrospun layer experienced weight losses of 11.85 ± 0.77 %, 26.95 ± 1.74 %, 37.54 ± 1.20 %, and 63.76 ± 2.35 % on the 1st, 3rd, 5th, and 7th day post-PBS immersion. In contrast, the solvent-casted PLA

layer showed much slower degradation, with weight losses of 0.07 ± 0.01 %, 0.28 ± 0.03 %, 0.56 ± 0.53 %, and 0.87 ± 0.43 % over the same period.

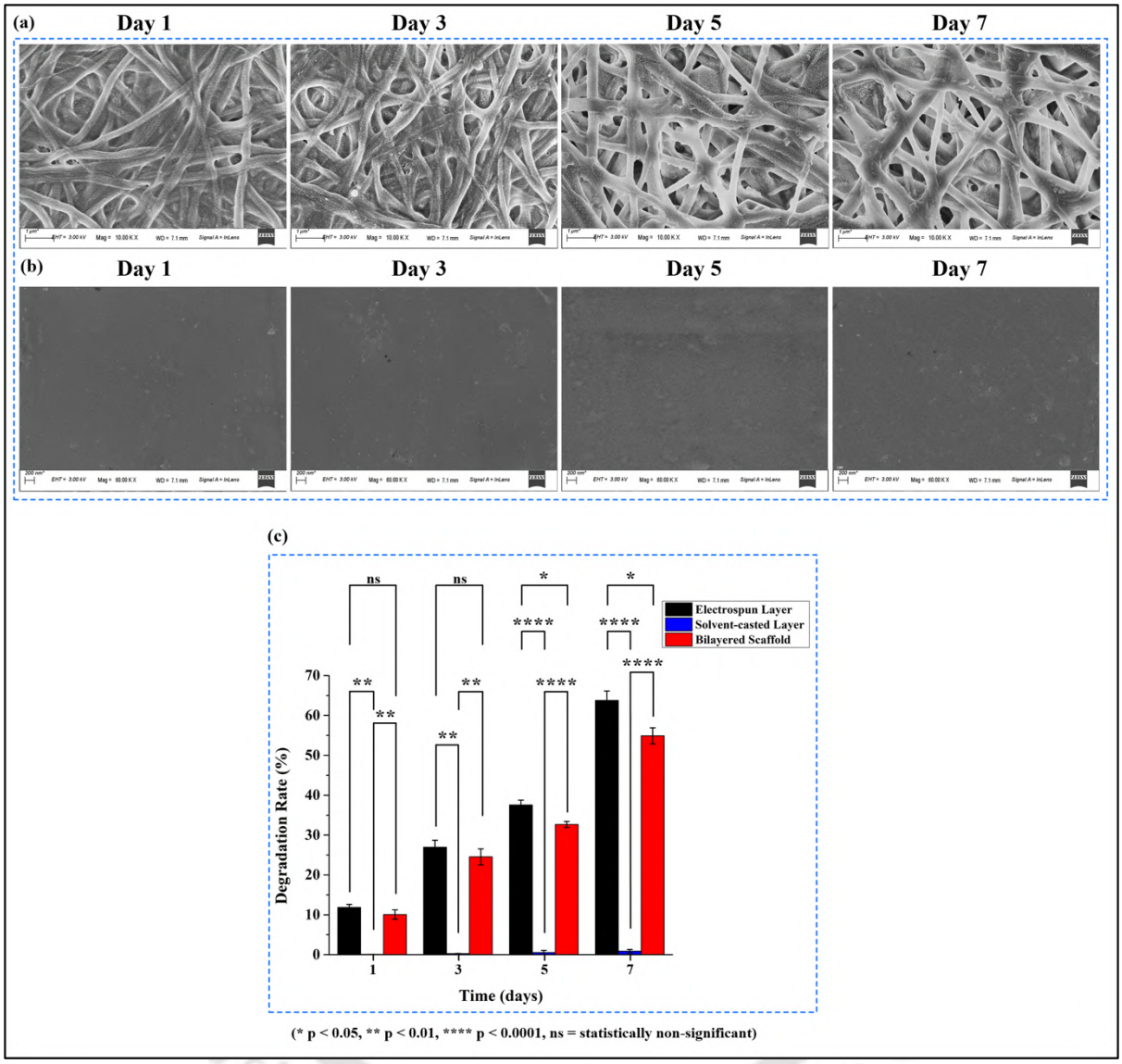

Figure 4.9 FESEM images of **(a)** electrospun layer and **(b)** solvent-casted layer, after 1st, 3rd, 5th and 7th days of degradation in PBS, respectively. Additionally, **(c)** the graphical representation illustrates the rate of weight loss of electrospun layer, solvent-casted layer and bilayered scaffold, after immersion in PBS. Results are shown as mean ± SD.

Additionally, the weight loss of the PLA layer is similar to previously reported study [427]. On the other hand, the bilayered scaffold exhibited weight losses of 10.07 ± 1.17 %, 24.53 ± 2.01 %, 32.65 ± 0.74 %, and 54.88 ± 2.00 % over the same duration. The weight loss of the bilayered scaffold with respect to the electrospun layer was statistically non-significant (ns) on the 1st and 3rd day, and statistically significant ($p < 0.05$) on the 5th and 7th day of degradation. However, with respect to the solvent-casted layer, the weight loss rate of the

scaffold was statistically significant throughout the tested period of degradation, $p < 0.01$ on the 1st and 3rd day, and $p < 0.0001$ on the 5th and 7th day, as shown in Figure 4.9 (c). The rapid weight loss in the case of the electrospun layer could be related to the hydrophilicity of pullulan, PVA and gum arabic [428]. Furthermore, the hydrophilicity of polymers accelerate the weight loss by building up osmotic pressure in the scaffold [429,430]. However, the weight loss of the bilayered scaffold was comparatively lower than that of the electrospun layer. This may be attributed to the incorporation of the hydrophobic PLA layer in the bilayered scaffold. Similarly, the least weight loss observed in the case of the solvent-casted PLA layer may be due to the hydrophobic nature of PLA. In the present study, the cell adhesion test performed on the fabricated bilayered scaffold demonstrated adequate cell growth and proliferation within 3 days (72 hrs), as depicted in Figure 4.10 (c). Notably, the corresponding weight loss of the scaffold was 24.53 ± 2.01 % up to the 3rd day of degradation. Thus, the outcomes indicate that the rate of degradation exhibited by the scaffold could be considered as optimum and acceptable, with respect to the observed cell proliferation and cytocompatibility.

4.2.8 In vitro biocompatibility analysis of the bilayered scaffold

4.2.8.1 Haemolytic index

Determination of haemocompatibility is essential for assessing the safety of the fabricated scaffold on red blood cells (RBCs) [303]. The fabricated bilayered scaffold was tested for its haemolytic activity on healthy human peripheral blood, as shown in Figure 4.10 (a). In comparison to the positive control, which exhibited 100 % haemolysis, the bilayered scaffold exhibited 0.52 ± 0.30 % haemolysis. The difference in haemolytic index of the scaffold with respect to the positive control was statistically highly significant ($p < 0.0001$). These outcomes indicate that the observed haemoglobin concentration was low, suggesting that a very less number of erythrocytes (RBCs) were disrupted. Additionally, Pandey et al. [303] reported that materials showing less than 2 % haemolysis are non-haemolytic, whereas those exceeding this threshold are considered haemolytic. Thus, these results indicate the haemocompatibility of the fabricated bilayered scaffold, an essential criterion for use in wound healing applications [431].

4.2.8.2 Cell viability

The fabricated bilayered scaffold was made of pullulan, PVA, gum arabic, and PLA, which are non-cytotoxic. Still, the *in vitro* cytotoxicity study of the bilayered scaffold was conducted to ensure its biocompatibility after its fabrication. The viability of HDF cells on the fabricated bilayered scaffold was analysed using an MTT assay. The relative percentage of cell viability

on the bilayered scaffold after 24, 48, and 72 hrs was 85.56 ± 4.63 %, 89.35 ± 3.15 %, and 93.95 ± 2.67 %, respectively.

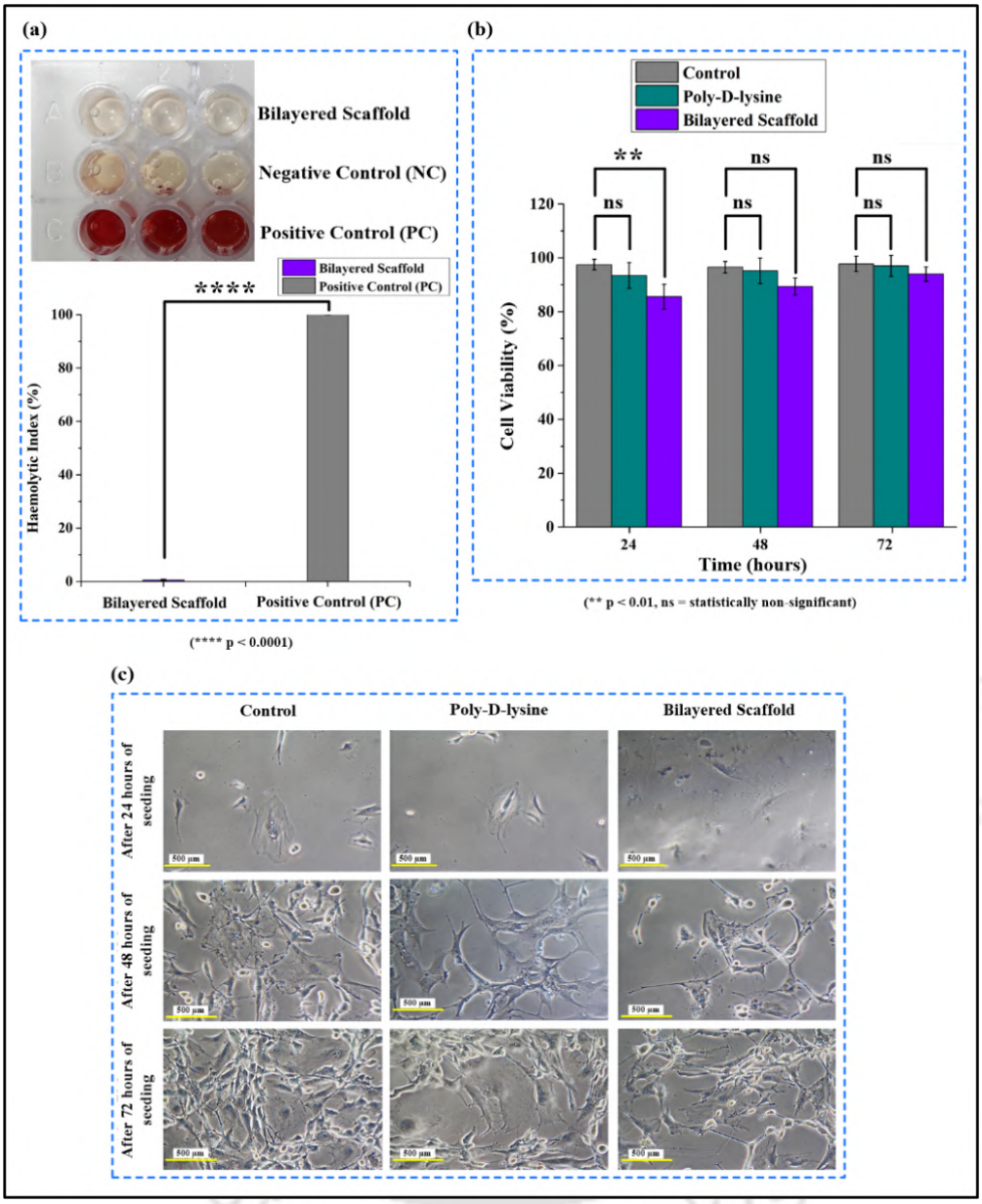

Figure 4.10 (a) Human blood treated with the bilayered scaffold, PC and NC for haemolysis assay and its statistical analysis, **(b)** relative viability percentage of the HDF cells on the bilayered scaffold after 24, 48, and 72 hrs of cell seeding and, **(c)** effect of the fabricated bilayered scaffold on HDF cell adhesion. Results are shown as mean ± SD.

The relative cell viability percentage on the bilayered scaffold when compared to control showed statistically significant difference ($p < 0.01$) after 24 hrs. However, it was found to be statistically non-significant (ns) after 48 and 72 hrs, as the viability percentage of cells on the bilayered scaffold increased over time. On the other hand, the relative viability percentage of

cells in the case of control and poly-D-lysine coated wells being almost equal, the differences among them were found to be statistically non-significant (ns) in all the cases, as represented in Figure 4.10 (b). All the relative cell viability exceeded 75 %, indicating that none of them displayed significant cytotoxicity based on the cytotoxicity grading criteria [432]. Notably, the criteria for grading cytotoxicity states that cell viability above 75 % is non-cytotoxic, and values between 50% and 74% are regarded as slightly toxic. Viability between 25% and 49% suggests moderate toxicity, while viability less than 24% denotes high toxicity [433]. Furthermore, substances are regarded as non-cytotoxic if their cell viability is atleast 75% of the control group, as per ISO10993-5:2009 criteria [434–437].

4.2.8.3 Cell adhesion study

To assess the adhesion property of the HDF cells on the fabricated bilayered scaffold, the cells were incubated into the wells containing the scaffold, the control wells, and those coated with poly-D-lysine. The images were collected after three different time intervals of seeding (24, 48, and 72 hrs). The cells have shown similar adhesion on the bilayered scaffold as that in the poly-D-lysine coated wells and the control wells, as shown in Figure 4.10 (c). Thus, the results indicate that the fabricated bilayered scaffold allows adequate cell adhesion and proliferation, and hence is non-cytotoxic to the HDF cells.

4.2.9 In vitro biocompatibility analysis of the individual layers of the scaffold

It was observed that both the layers individually demonstrated cell viability of more than 75 % (Figure 4.11 (a)) and supported HDF cell adhesion and proliferation (Figure 4.11 (b)), thereby indicating their non-cytotoxic nature. The relative cell viability percentage on the electrospun and solvent-casted layers of the scaffold when compared to control showed statistically significant difference ($p < 0.001$) after 24 and 48 hrs. However, after 72 hrs, it was found to be statistically non-significant (ns) for electrospun layer and relatively less significant ($p < 0.05$) for the solvent-casted layer, as the cell viability percentage on both the layers increased over time. On the other hand, the relative viability percentage of cells in the case of control and poly-D-lysine coated wells being almost equal, the differences among them were found to be statistically non-significant (ns) in all the cases, as represented in Figure 4.11 (a).

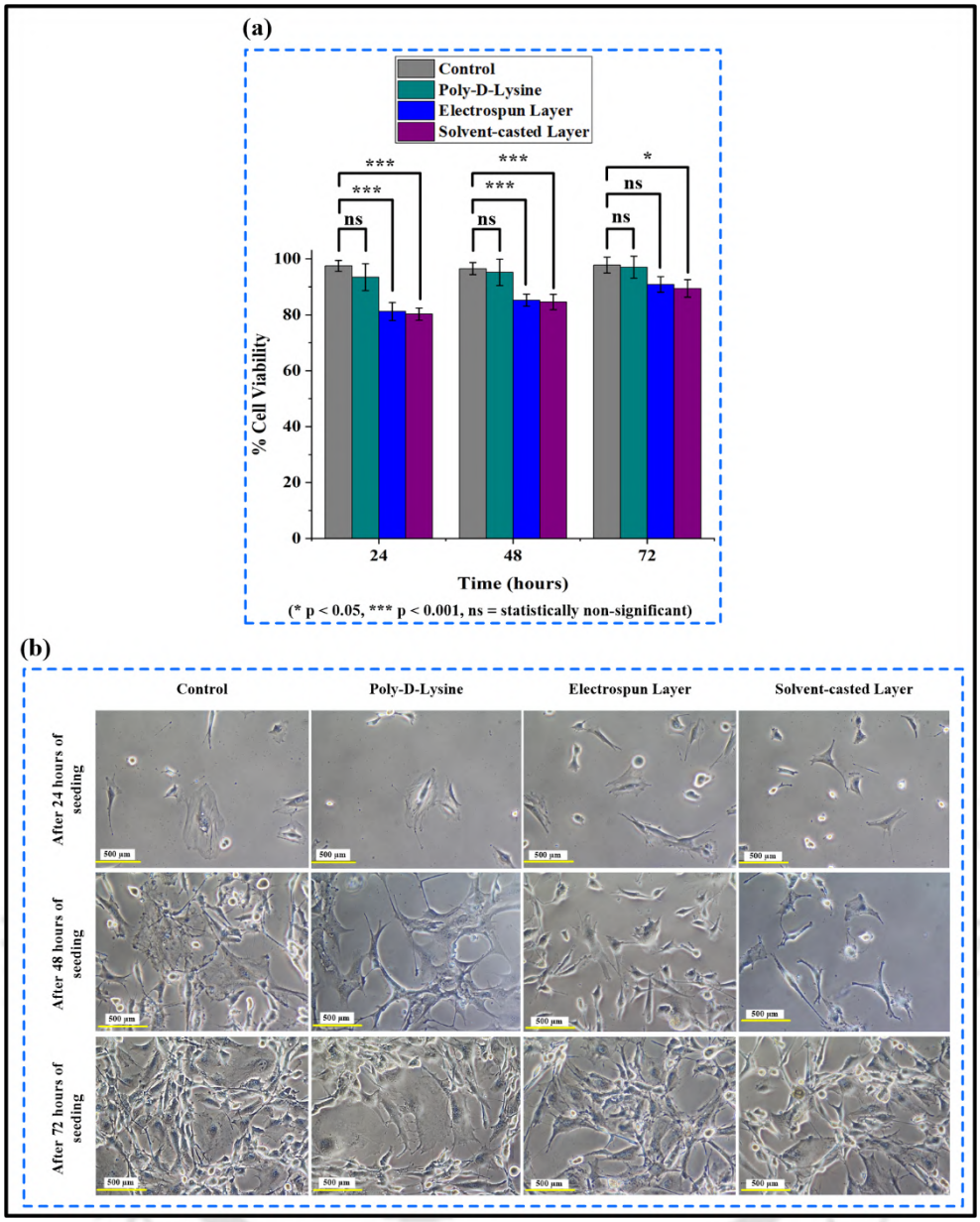

Figure 4.11 (a) Relative viability percentage of the HDF cells on the electrospun layer and solvent-casted layer of the bilayered scaffold after 24, 48, and 72 hrs of cell seeding and, **(b)** effect of the electrospun layer and solvent-casted layer on HDF cell adhesion. Results are shown as mean ± SD.

4.2.10 In vitro wound healing analysis of the bilayered scaffold

Fibroblasts play a crucial role in wound healing by constricting the wound and forming new collagen and ECM structures, which support other cells involved in wound healing or closure [438]. To determine the cell migration or wound healing potential of the fabricated bilayered scaffold, an *in vitro* scratch assay was conducted to mimic cell migration during the wound healing process. Briefly, a gap was created in a cell monolayer, and the migration of cells into

this gap was observed. The rate of cell migration was then quantified from the captured images, expressed as the percentage of wound closure, as reported in prior studies [439].

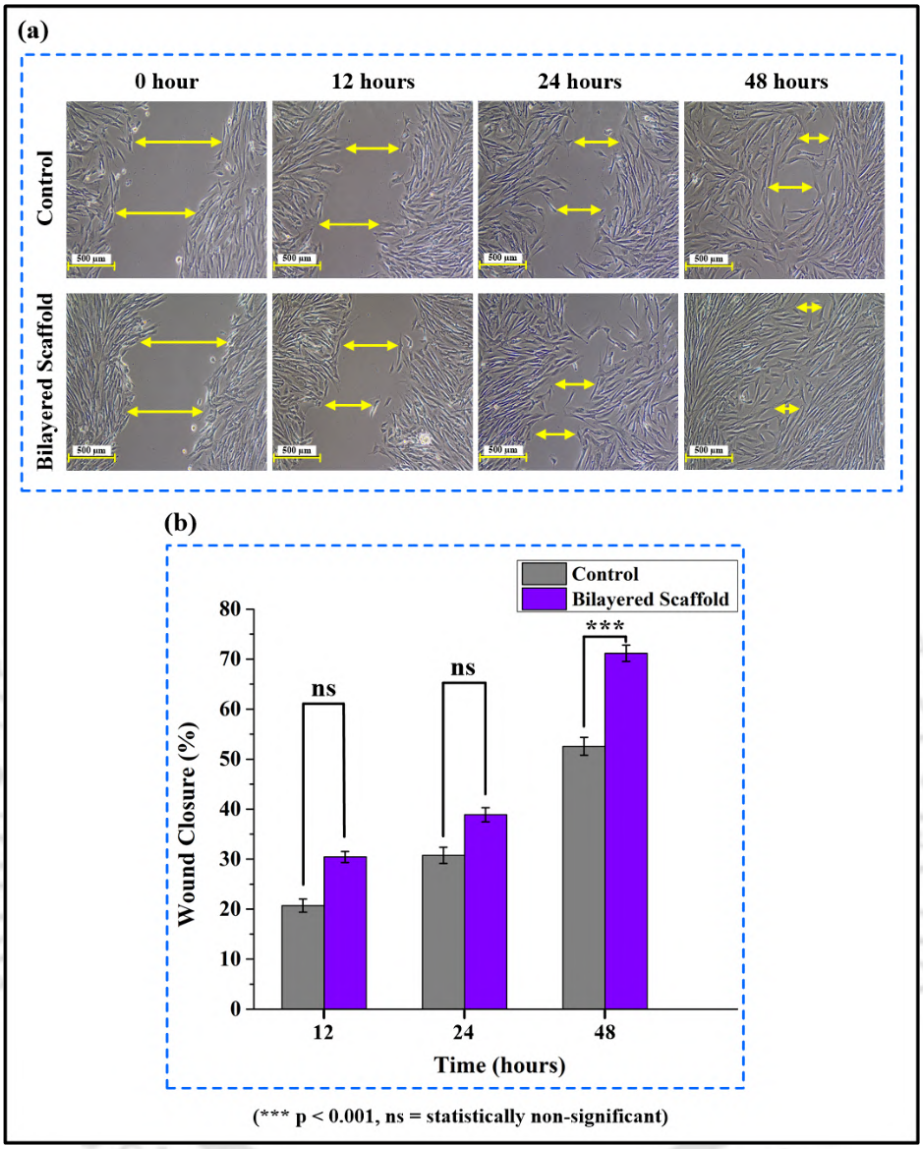

Figure 4.12 (a) Bilayered scaffold showing better wound healing activity compared to control, and **(b)** Statistical analysis of wound closure rate. Results are shown as mean ± SD.

The images of *in vitro* scratch assay performed on HDF cells at specific time intervals (0, 12, 24 and 48 hrs) post-injury, demonstrated the wound healing capabilities of the cells treated with the fabricated bilayered scaffold as compared to those of the untreated (control) cells, as shown in Figure 4.12 (a). All the images illustrate the gradual progression of wound closure in scratch-injured HDF cells. It was observed that cells treated with the bilayered scaffold exhibited improved wound closure compared to the untreated cells, where the wound healing process was relatively slow. As observed in Figure 4.12 (b), at initial time points (12 and 24 hrs) post-injury, the relative wound closure percentages in treated cells were comparable to

those in the control group, with no statistically significant difference (ns). However, by the 48-hr time point, a statistically significant difference ($p < 0.001$) was observed, where the relative wound closure in the treated cells (71.15 ± 1.62 %) was significantly higher than that of the control (52.55 ± 1.79 %). The results demonstrate the effectiveness of the bilayered scaffold in accelerating wound healing, confirming its potential as a suitable material for promoting cell migration and wound closure, which are essential for wound healing applications.

4.2.11 In vitro wound healing analysis of the individual layers of the scaffold

The scratch assay was separately performed on each of the individual layers of the bilayered scaffold to investigate their healing potential. As depicted in Figure 4.13, the electrospun layer exhibited a better wound healing potential (or wound closure rate) compared to the solvent-casted layer. Moreover, the wound closure rate of the electrospun layer was similar to that of the bilayered scaffold, while that of the solvent-casted layer was close to that of the control (as shown in Figure 4.12). The observed wound closure rates may be attributed to the inherent properties and design purposes of each layer in the bilayered scaffold. The electrospun hydrophilic layer, composed of pullulan/PVA/gum arabic, is designed to contact the wound directly, creating a moist environment that facilitates cell proliferation and migration. Its porosity and hydrophilicity enhance cellular attachment and proliferation, critical for wound healing, while the embedded gentamicin provides antibacterial action, preventing infection and supporting tissue regeneration. This layer alone achieves a wound closure rate comparable to that of the full bilayered scaffold, as it independently creates an optimal healing environment. In contrast, the PLA layer functions as a protective, hydrophobic barrier that strengthens the scaffold and reduces moisture loss, rather than directly encouraging cell proliferation. Its dense, non-porous structure limits cellular interactions and nutrient transfer, resulting in a closure rate similar to that of the control, as it lacks the regenerative properties of the electrospun layer. Additionally, the differences in wound closure rate of both the layers was found to be statistically significant ($p < 0.01$) at initial time points (12 and 24 hrs) post-injury, and statistically highly significant ($p < 0.0001$) by the 48-hr time point, as represented in Figure 4.13 (b).

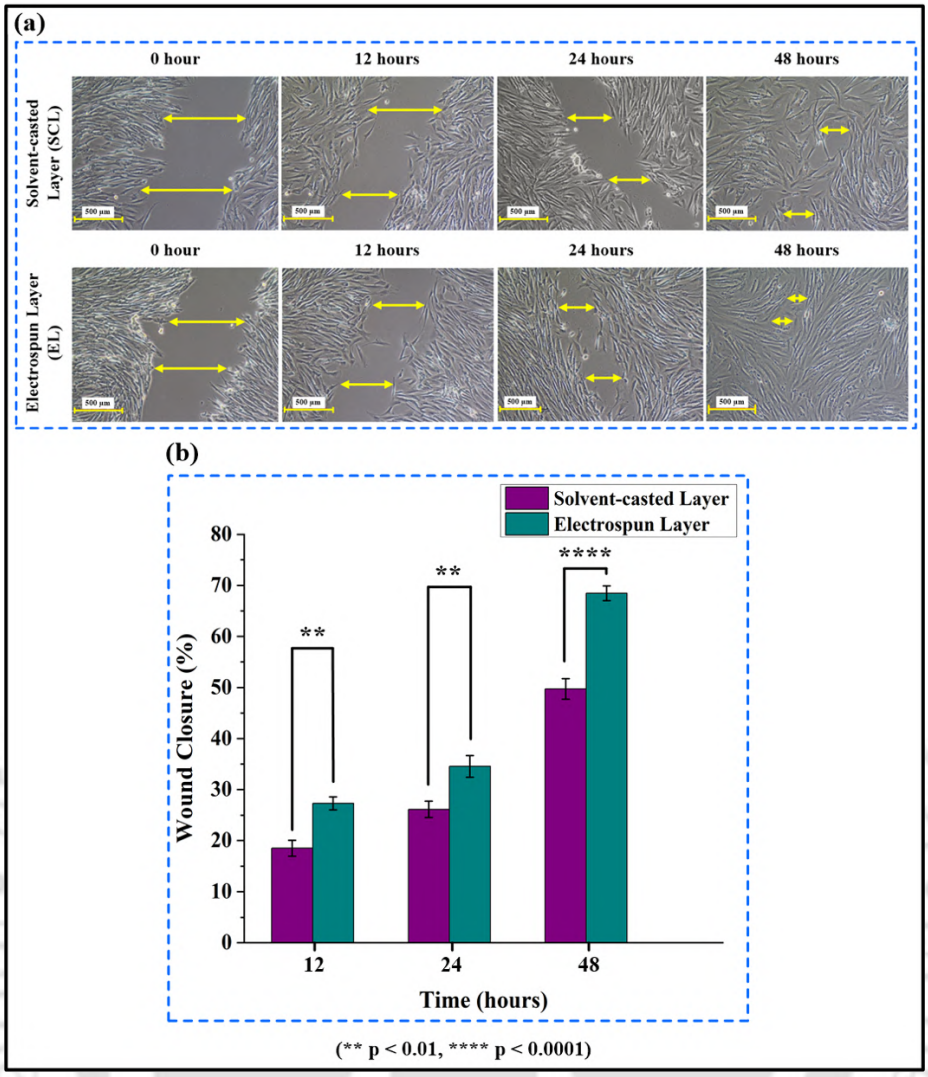

Figure 4.13 (a) Electrospun layer showing better wound healing activity compared to solvent-casted layer, and **(b)** Statistical analysis of wound closure rate of the layers. Results are shown as mean ± SD.

4.2.12 Confirmation of glutaraldehyde crosslinking of electrospun layer by FTIR

Figure 4.14 depicts the FTIR spectra of the pullulan/PVA/gum arabic nanofibrous layer before and after glutaraldehyde crosslinking. The peaks at around 3200–3500 cm^{-1} corresponds to the O–H stretching vibrations, from pullulan, PVA and gum arabic. This broad peak indicates hydrogen bonding, which is typically present in hydrophilic polymers. As depicted in Figure 4.14, after glutaraldehyde crosslinking, the intensity of this peak decreased due to the reduction of free hydroxyl (–OH) groups, as some –OH groups from pullulan, PVA and gum arabic participate in crosslinking with aldehyde (–CHO) groups of glutaraldehyde, forming acetal linkages [440–442].

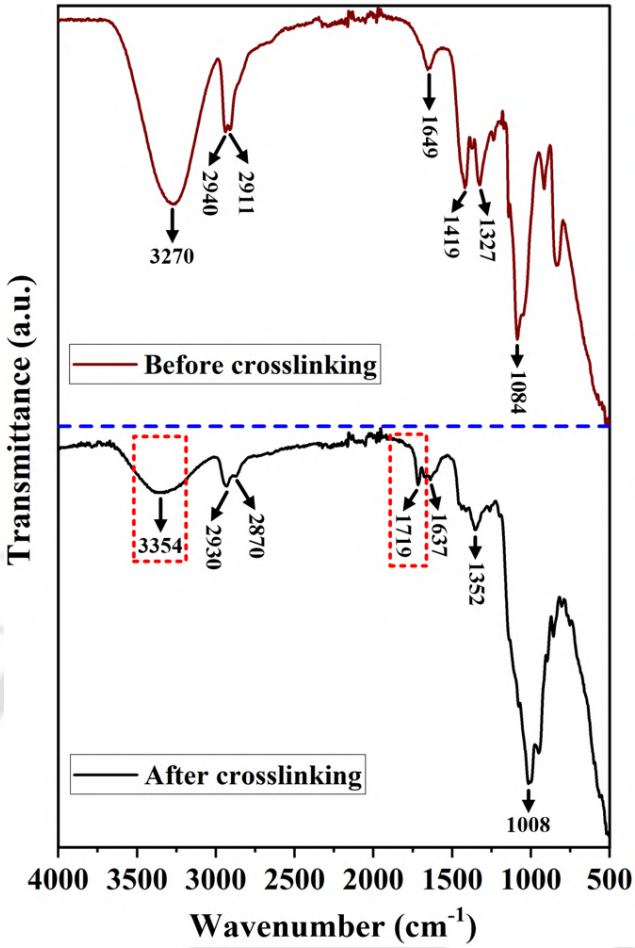

Figure 4.14 FTIR spectra of the pullulan/PVA/gum arabic electrospun nanofibrous layer before and after glutaraldehyde crosslinking.

Peaks in the 2800–3000 cm^{-1} range corresponds to the C–H stretching vibrations of aliphatic chains present in the polymers. Peaks at around 1649 and 1637 cm^{-1} may be attributed to O–H bending vibrations associated with bound or absorbed water within the hydrophilic polymers (pullulan, PVA and gum arabic). The peaks at 1416 cm^{-1}, 1352 cm^{-1}, and 1327 cm^{-1} are likely due to the vibrational CH_3 or CH_2 groups, while peaks at 1084 cm^{-1} and 1008 cm^{-1} correspond to the C–O stretching within C–O–C groups in pullulan and gum arabic. These finding are consistent with those reported in prior studies [434,442]. Additionally, the peak at 1719 cm^{-1} in the crosslinked sample spectrum may be attributed to the C=O stretching vibration. The introduction of carbonyl (C=O) groups by glutaraldehyde in this region confirms successful crosslinking, as reported in prior studies [440–442]. Therefore, the reduction in O–H stretching intensity alongside the introduction of carbonyl (C=O) group in the crosslinked sample indicates successful glutaraldehyde crosslinking. After crosslinking, slight shifts and changes

in peak intensities were observed which may be attributed to the alterations in molecular structure due to the formation of new bonds.

4.2.13 Impact of glutaraldehyde crosslinking on HDF cell viability

The cell viability on the electrospun layer before and after crosslinking was determined, and the results have been depicted in Figure 4.15. Prior to glutaraldehyde crosslinking, the viability percentage was found to be slightly higher than that observed after crosslinking. The slight decrease in cell viability after crosslinking may be attributed to the cell apoptosis caused by residual glutaraldehyde [443]. However, in both the cases, the viability was found to be more than 75 %, indicating the non-cytotoxic nature of the electrospun layer irrespective of crosslinking. Additionally, the differences in relative cell viability percentage before and after crosslinking were found to be statistically non-significant (ns). This indicates that although the presence of glutaraldehyde demonstrated slightly reduced viability, it maintained around 90.82 ± 2.77 % cell viability even after 72 hrs and hence could be regarded as non-cytotoxic according to the cytotoxicity grading criteria [433–437]. In this study, 25 % aqueous glutaraldehyde was used at a concentration of 2 % v/v in the 5 mL electrospinning solution. Prior studies have reported that this concentration is non-cytotoxic [444], thus confirming that the crosslinking process did not significantly affect cell viability or the overall non-cytotoxic nature of the electrospun layer.

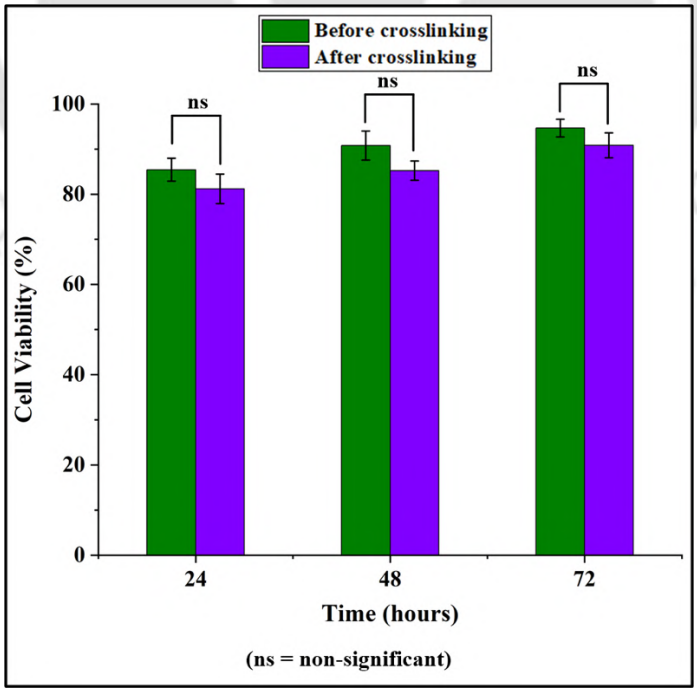

Figure 4.15 Relative viability percentage of the HDF cells on the electrospun layer before and after glutaraldehyde crosslinking.

4.2.14 In vitro release profile and kinetic analysis of gentamicin sulfate

As depicted in Figure 4.16 (a), the CDR percentage over time graph shows a steady and controlled release of gentamicin sulfate over 48 hrs, with approximately 93.09 ± 2.63 % of the drug released cumulatively by the end of this period. This observation is highly noteworthy as it corresponds to the established medical guideline of changing wound dressings every 1-2 days for optimal wound healing. The differences in CDR percentages were statistically significant ($p < 0.001$) throughout 48 hrs. Notably, there was no initial burst release, which indicates the uniform distribution of the polymeric matrix throughout the scaffold. This further reflects the controlled release behaviour attributed to the bilayered scaffold design. The hydrophilic pullulan/PVA/gum arabic nanofibrous sublayer likely provides a gradual and consistent drug diffusion rate, while the hydrophobic PLA top layer serves as a protective barrier against the external environment, reducing moisture loss and preventing external contamination. The controlled drug release pattern is particularly recommended when dealing with critical wounds, where continuous delivery of medication and prolonged antibacterial activity are essential for effective treatment. This release pattern would also help maintain therapeutic drug levels at the wound surface, thereby helping in better tissue regeneration and reducing the risk of infection. Additionally, this would also help in efficiently minimizing the side effects caused by the drug [445]. Notably, gentamicin sulfate has been reported as one of the most widely used antibiotic in controlled drug release systems, due to its solubility and stability at high temperature conditions [305].

Different release models were used to represent the *in vitro* release kinetics of gentamicin sulfate in PBS solution, as shown in Figure 4.16 (b–f). The regression coefficients obtained from each drug release kinetic model help to describe their release behaviour. Higher coefficient values (close to 1) indicate better fitting accuracy for a particular model. These coefficient values help to understand the release kinetics and to select the most appropriate model for further analysis and formulation optimisation. A tabular representation of the CDR kinetics mathematical modelling data is depicted in Table 4.2.

The Zero-Order model, which exhibited the highest R^2 value (0.9850), demonstrated that the release rate of gentamicin sulfate is independent of its concentration. This further indicates a steady release of the drug over time, which is suitable for maintaining consistent therapeutic levels. This observation aligns with the controlled release mechanism where the rate of drug release is constant and not influenced by the remaining drug concentration in the medium. The First-Order model plot (log (% remaining drug) vs. time) depicted a lower R^2 value of 0.8938, indicating a poorer fit compared to the Zero-Order model. This suggests that

the drug release is less influenced by the remaining drug concentration in the scaffold, further supporting the Zero-Order model conclusion of a controlled release mechanism. This is crucial for wound dressings to maintain a consistent drug level without rapid depletion. The Hixson-Crowell model, which accounts for changes in surface area and particle diameter during drug release, yielded a moderate fit (R^2 = 0.8666). This indicates that some level of surface erosion might have contributed to the drug release, likely due to gradual structural changes in the hydrophilic nanofiber layer as it absorbs PBS and releases gentamicin sulfate. However, the fit is not as strong as the Zero-Order or Higuchi models, suggesting that erosion is not the primary release mechanism. The Korsmeyer-Peppas model, with an R^2 of 0.9825, describes drug release behaviour and can indicate the release mechanism via the diffusion exponent (n value). In the present study, n = 1, which implies non-Fickian or anomalous transport, which typically indicates that the release mechanism is governed by polymer swelling and/or relaxation mechanisms [446,447]. This further supports the hypothesis that polymer swelling and/or relaxation could be influencing the release profile, as the drug release is not purely diffusion-controlled (Fickian) but instead aligns with a more complex, controlled release behaviour. The Higuchi model, with an R^2 of 0.959, is commonly associated with release from a porous matrix, where the drug release is proportional to the square root of time, indicating diffusion control. While the model provides a reasonably good fit, the slightly lower R^2 value compared to the Zero-Order and Korsmeyer-Peppas models suggest that the release is not influenced by simple diffusion alone.

Among all models, the Zero-Order model had the highest R^2 value, suggesting that the gentamicin sulfate release demonstrated a Zero-Order kinetic profile, which is indicative of concentration-independent release. This finding is further supported by the Korsmeyer-Peppas model results (n = 1), which indicate non-Fickian behaviour. This means the release mechanism involves both diffusion and polymer chain relaxation or swelling, aligning with a controlled-release system that can maintain steady drug levels over time. This release pattern is beneficial for wound healing applications, as it maintains a consistent antibacterial effect over time, avoids initial burst release, and minimizes the need for frequent dressing changes, thereby improving the healing outcomes.

Table 4.2 Cumulative gentamicin sulfate release kinetics mathematical modelling.

Time (hrs)	Cumulative gentamicin sulfate release %	% Remaining gentamicin sulfate	Square root of time	log (% Remaining gentamicin sulfate)	log (Time)	log (Cumulative gentamicin sulfate release %)	(Q_t)	($Q_0 - Q_t$)
2	1.98	98.02	1.414	1.991315	0.30103	0.297396	0.05	2.45
4	3.18	96.82	2	1.985965	0.60206	0.503564	0.08	2.42
6	4.72	95.28	2.449	1.979002	0.778151	0.673942	0.118	2.382
8	9.96	90.04	2.828	1.954435	0.90309	0.998477	0.249	2.251
10	14.85	85.15	3.162	1.930185	1	1.171873	0.371	2.129
12	19.75	80.25	3.464	1.904445	1.079181	1.295677	0.494	2.006
14	25.55	74.45	3.741	1.871865	1.146128	1.407504	0.639	1.861
16	31.82	68.18	4	1.833657	1.20412	1.502791	0.796	1.704
18	39.32	60.68	4.242	1.783046	1.255273	1.594706	0.983	1.517
24	47.29	52.71	4.898	1.721893	1.380211	1.674846	1.182	1.318
28	56.53	43.47	5.291	1.63819	1.447158	1.752343	1.413	1.087
32	66.25	33.75	5.656	1.528274	1.50515	1.821208	1.656	0.844
36	76.22	23.78	6	1.376212	1.556303	1.882116	1.906	0.594
38	86.01	13.99	6.164	1.145818	1.579784	1.934583	2.15	0.35
40	92.18	7.82	6.324	0.893207	1.60206	1.964676	2.305	0.195
48	93.09	6.91	6.928	0.839478	1.681241	1.968903	2.327	0.173

Note: Q_t - amount of drug released at the time *t* and, Q_0 - initial amount of the drug.

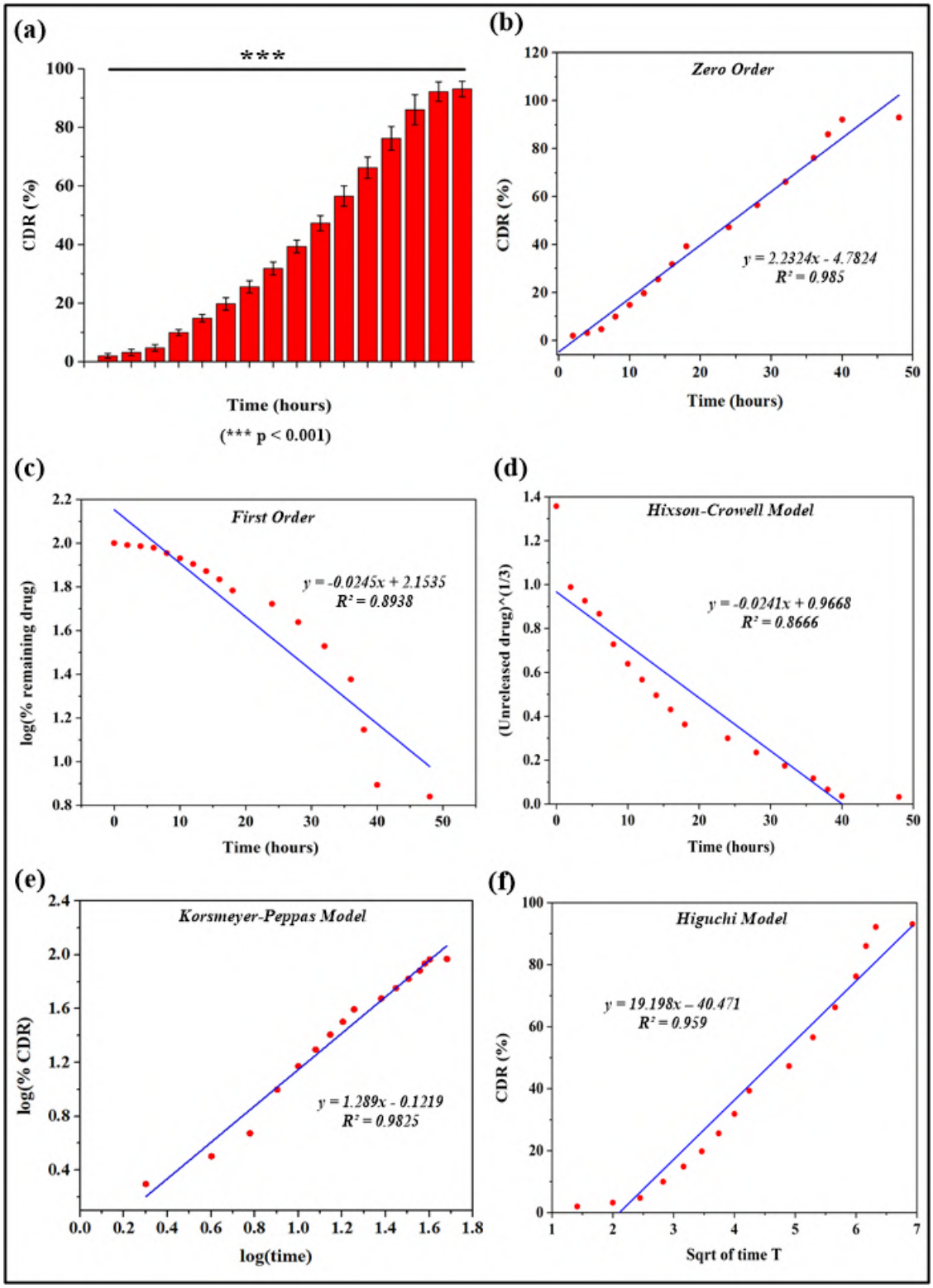

Figure 4.16 (a) Release pattern of gentamicin sulfate from the scaffold. Additionally, the release data are fitted into: **(b)** Zero-Order, **(c)** First-Order, **(d)** Hixson-Crowell, **(e)** Korsmeyer-Peppas, and **(f)** Higuchi models. Results are shown as mean ± SD.

4.3 Summary

The significance of wound dressings lies in their ability to provide multiple advantages, for example promoting tissue regeneration, lowering the risk of infection, and reducing the frequency of dressing replacements. The bilayered scaffold prepared in this study is designed to address the issues with conventional wound dressings that cause potential scarring and patient discomfort during removal from the wound surface. It would help in tissue repair by preventing scarring of wound surface. It showed significant antibacterial activity against *S. aureus* and *E. coli*, which confirms the successful incorporation of gentamicin sulfate. Ensuring homogeneous and controlled drug distribution within the electrospun layer is essential to maintain consistent antibacterial performance. The drug release profile followed a Zero-Order controlled mechanism, ensuring that the drug remains within therapeutic concentrations for a prolonged period, thereby improving efficacy and minimizing adverse effects. The scaffold exhibited a haemolytic index of 0.52 ± 0.30 %, which lies within the permissible limit of 2 %, thus confirming its haemocompatible nature towards human RBCs. Additionally, it was biocompatible and non-cytotoxic to HDF cells with 93.95 ± 2.67 % cell viability even after 72 hrs, facilitating cell adhesion and proliferation. Furthermore, the *in vitro* wound healing assay conducted on HDF cells demonstrated its enhanced wound healing properties. The scaffold exhibited a moisture content of 85.94 ± 1.86 % and swelling index of 611.85 ± 15.05 % up to 24 hrs immersion in distilled water, which indicates its excellent moisture retention and exudate absorbing capacity. The WVTR and porosity were measured as 94.20 ± 14.50 g/m^2/day and 70.56 ± 0.58 %, respectively, both falling within the permissible range for wound healing. This balance between porosity and barrier function ensured adequate permeability for air exchange and moisture regulation while maintaining effective wound protection. Additionally, the *in vitro* degradation study conducted in PBS solution showed favourable biodegradability, with 54.88 ± 2.00 % degradation over 7 days, indicating that the scaffold is a viable material for wound dressing applications.

CHAPTER 5

PREPARATION OF PULLULAN/PLGA DUAL DRUG-LOADED CORE/SHEATH NANOFIBERS BY COAXIAL ELECTRO-CENTRIFUGAL SPINNING AND THEIR *IN VITRO* CYTOTOXIC EFFICACY TOWARDS MELANOMA CELLS

Motivation

Melanoma is a highly aggressive skin cancer that often requires combination therapy to improve treatment outcomes. Delivering two drugs simultaneously in a controlled manner can enhance therapeutic effects and reduce drug resistance. However, producing nanofibers capable of efficiently encapsulating and releasing both hydrophilic and hydrophobic drugs remains challenging, especially using conventional coaxial electrospinning methods, which often face issues like nozzle clogging. This study was motivated by the need for a simple yet effective drug delivery system. By using an in-house developed coaxial electro-centrifugal spinning (ECS) technique, dual drug-loaded pullulan/PLGA core/sheath nanofibers were fabricated and tested for their basic cytotoxic effect against melanoma cells through an in vitro cytotoxicity assay. The results provide a foundation for further exploration of these nanofibers in cancer treatment applications.

The work in the chapter has received the scientific recognition as follows:

Das, K., *Xu, H., Gu, J., Sakurai, S., Tiwari, V., Banerjee, S.K. and Katiyar, V., 2025. Coaxially Electrocentrifugally Spun Ciprofloxacin/Paclitaxel-Loaded Pullulan/PLGA Core/Sheath Nanofibers and Their In Vitro Cytotoxic Efficacy Toward Melanoma Cells. Journal of Applied Polymer Science, p.e56759.*

Abstract

The study focuses on the fabrication and characterization of ciprofloxacin (CIP)/paclitaxel (PTX)-loaded pullulan/poly(lactic-co-glycolic acid) (PLGA) core/sheath nanofibers using the highly efficient coaxial electro-centrifugal spinning (ECS) technique. In contrast to conventional coaxial electrospinning, the in-house developed coaxial ECS setup used in this study effectively tackled the nozzle cleaning issue. In this study, core/sheath nanofibers with varying core-to-sheath ratio were fabricated, demonstrating suitable mechanical properties for use in biomedical applications. The primary objective was to determine the effect of core-to-sheath ratio on mechanical properties and dual drug release kinetics of the nanofibers. Additionally, the *in vitro* drug release study demonstrated simultaneous release profiles of CIP from the core and PTX from the sheath. The nanofibers exhibited initial burst release of 6 hrs, followed by controlled release, making them suitable for targeted therapeutic applications. Moreover, the *in vitro* cytotoxicity analysis demonstrated enhanced cytotoxic efficacy of the combination of CIP and PTX towards human melanoma A375 cells. The dual drug-loaded nanofibers with core-to-sheath ratios of 23G/1mm and 21G/1mm demonstrated melanoma cell viabilities of 65.37 ± 1.96 % and 67.82 ± 1.31 %, respectively, after 72 hrs, indicating significant cytotoxicity. This further highlights the possible potentiality of the nanofibers towards melanoma treatment and their application as dual drug delivery systems with tunable drug release properties.

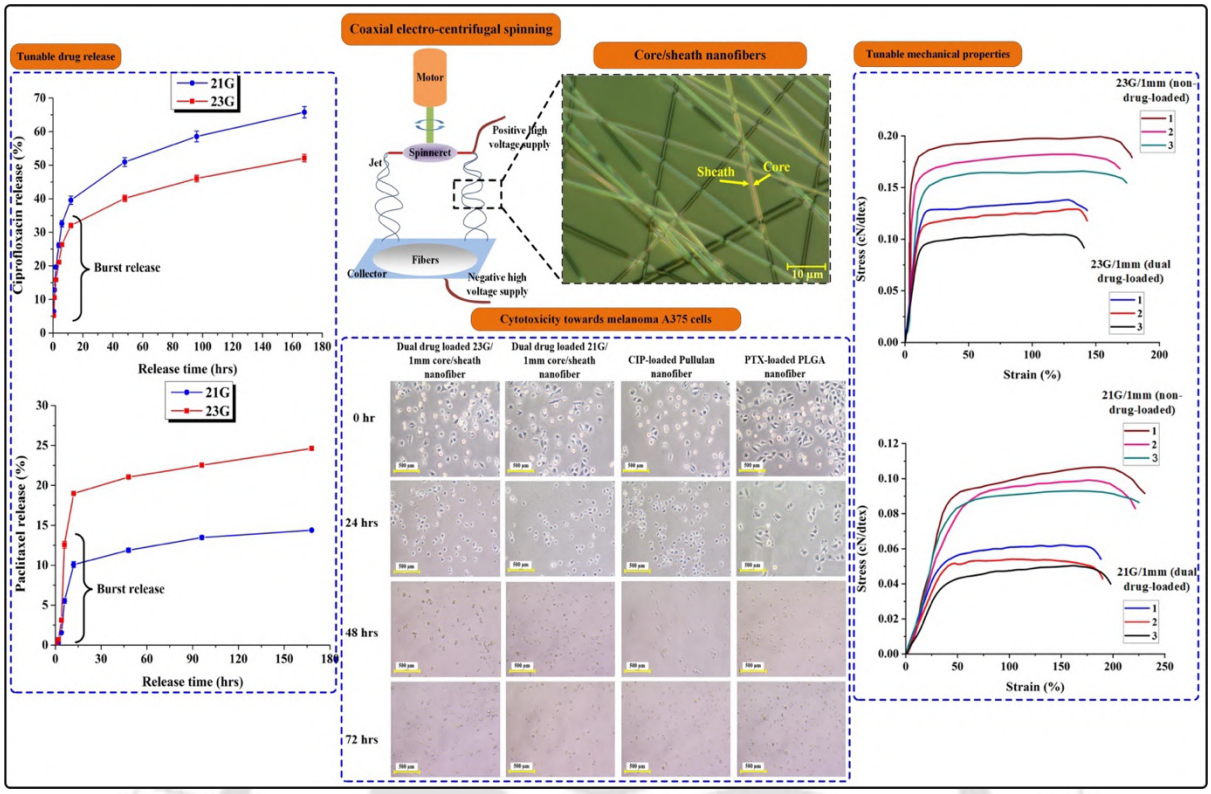

Figure 5.1 Scheme of chapter 5.

5.1 Introduction

Nanofiber fabrication techniques have gained much attention due to their applications across several domains, such as tissue engineering, drug delivery, wound healing and advanced filtration. Nanofiber-based drug delivery systems possess certain advantages, such as sustained drug release, improved bioavailability, and targeted therapy. Electro-centrifugal spinning (ECS) is an innovative hybrid technique, that effectively combines the principles of both electrospinning and centrifugal spinning, presenting numerous benefits that distinguish it from its precursor techniques [448–450]. It results in enhanced adaptability and efficiency in nanofiber production. The centrifugal spinning is known to achieve a production efficiency of at least ten times greater than that of electrospinning [451]. Nevertheless, the quality of fibers produced through centrifugal spinning is inferior to that of electrospinning, as factors like machine vibration and intense airflow around the spinneret can lead to the formation of beaded fibers [452–455]. Unlike traditional electrospinning, ECS naturally aligns nanofibers along the spinning axis, which is beneficial for fabrication of materials used in tissue engineering. Additionally, ECS accelerates the rate of fiber production due to high voltage along with added centrifugal force expelling polymer solutions [448,456–459]. This makes it suitable for industries requiring large quantities of nanofibers, like filtration, textiles and biomedical

applications. Moreover, the ECS technique reduces the likelihood of bead formation seen in electrospinning by combination of centrifugal force and electric fields [308,460]. This technique enables efficient regulation of the fiber structure, resulting in tunable mechanical and drug release properties for specific applications [461,462]. The coaxial ECS technique is a more advanced approach which combines ECS and coaxial spinning techniques for fabrication of core/sheath nanofibers with improved functionality [463,464].

Pullulan is a biodegradable and biocompatible exopolysaccharide obtained from the fungus *Aureobasidium pullulans* (*A. pullulans*). It is widely used in blends or composites along with other polymers for several biomedical applications, owing to its excellent potential for moisture retention and drug delivery [15,465,466]. It has also been reported to improve the spinnability of electrospinning solutions, by improving viscosity, reducing conductivity and surface tension [366]. Additionally, pullulan has been blended with hydroxypropyl-β-cyclodextrin (HP-β-CD) to create multi-functional fibers for drug delivery and encapsulation applications [467]. These studies demonstrate the versatility of pullulan in electrospinning for various biomedical applications.

Poly(lactic-co-glycolic acid) (PLGA) is another biodegradable polymer, extensively used for nanofiber fabrication by electrospinning. The PLGA-based nanofibers have been reported to possess suitable characteristics for use in biomedical applications, such as biodegradability, biocompatibility, good mechanical and thermal properties [468–470]. Electrospun PLGA nanofibers have large surface area, high porosity with small pore sizes, and can be tuned to possess suitable mechanical properties for use as drug delivery systems, wound dressing and tissue engineering scaffolds [469,470]. Additionally, PLGA has been used in blends along with other materials such as collagen to enhance its properties and promote cell adhesion and growth [471].

Ciprofloxacin (CIP) is an antibiotic that has been reported to show anticancer property in various studies, mainly due to its ability to induce DNA damage and apoptosis in cancer cells [472–478]. Paclitaxel (PTX), on the other hand, is a chemotherapeutic agent that inhibits cell division by stabilizing microtubules, leading to cell cycle arrest and apoptosis [479,480]. It has been reported in the literature [481,482] that the enhanced expression of ABC transporters within cancer cells has been found to accelerate the removal of chemotherapeutic drugs, leading to development of drug resistance, recurrence of cancer, and ultimately, the demise of cancer patients [481,482]. Notably, CIP has been reported by Gupta et al. [483] to enhance the responsiveness of ABCB1-overexpressing cells to PTX by preventing or delaying its removal from the cells. Thus, we hypothesized that a combination therapy of CIP and PTX

might contribute to the effectiveness of cancer treatment as a whole. However, to the best of our knowledge, there is no report thus far on Pullulan/PLGA core/sheath nanofibers demonstrating simultaneous release of CIP and PTX, coupled with enhanced cytotoxicity towards melanoma cells.

Hence, in the present work, we have demonstrated the fabrication of core/sheath nanofibers comprising CIP-loaded pullulan as the core material and PTX-loaded PLGA as the sheath material. The primary objective of this research was to determine the effect of varying core-to-sheath ratio of the nanofibers on the mechanical properties and the combined release profiles of CIP and PTX. Furthermore, the *in vitro* cytotoxicity analysis was conducted on human melanoma A375 cells, to determine the efficacy of the dual drug combination for possible melanoma treatment.

5.2 Results and discussion

5.2.1 Morphological analysis

The SEM images of the fabricated pullulan/PLGA core/sheath nanofibers with 21G/1mm and 23G/1mm needle sizes have been depicted in Figure 5.2 (a–d). The average diameter of nanofibers fabricated with 21G/1mm needle size was found to change from 775 ± 134 nm (Figure 5.2 (a)) to 539 ± 87 nm (Figure 5.2 (b)) after one week of dissolution in chloroform. Subsequently, that of the nanofibers fabricated with 23G/1mm needle size, changed from 765 ± 85 nm (Figure 5.2 (c)) to 404 ± 110 nm (Figure 5.2 (d)), under the same conditions of dissolution. This change in diameter upon dissolution in chloroform could be attributed to the core/sheath structure of nanofibers, since the sheath material (PLGA) is soluble in chloroform but the core material (pullulan) is not. After dipping into chloroform, the PLGA sheath gets dissolved, leaving behind only the core made of pullulan, and thus the reduction in nanofiber diameter. The main intention of dissolving the PLGA sheath component in chloroform was to validate the core/sheath structure and observe the core size of the nanofiber. Additionally, the spinnability of the monolithic pullulan and PLGA polymers were also examined prior to the fabrication of core/sheath pullulan/PLGA nanofibers.

The core/sheath structure of the nanofiber was further validated using an optical microscope. As depicted in Figure 5.2 (e), the core component was centrally positioned and surrounded by the sheath component, thereby confirming the fabrication of pullulan/PLGA core/sheath nanofibers using the coaxial ECS set-up discussed in this study. Unlike coaxial electrospinning, where the core needle must be slightly protruded from the outer needle to enhance spinnability; the tips of the core and sheath needles remain aligned on the same plane

in ECS, thereby facilitating the fabrication of uniform core/sheath nanofibers. Here, the core and the sheath diameters were found to be 581 ± 156 nm and 769 ± 114 nm, respectively (as measured by Image J 1.48), which was close to that depicted by the corresponding SEM images.

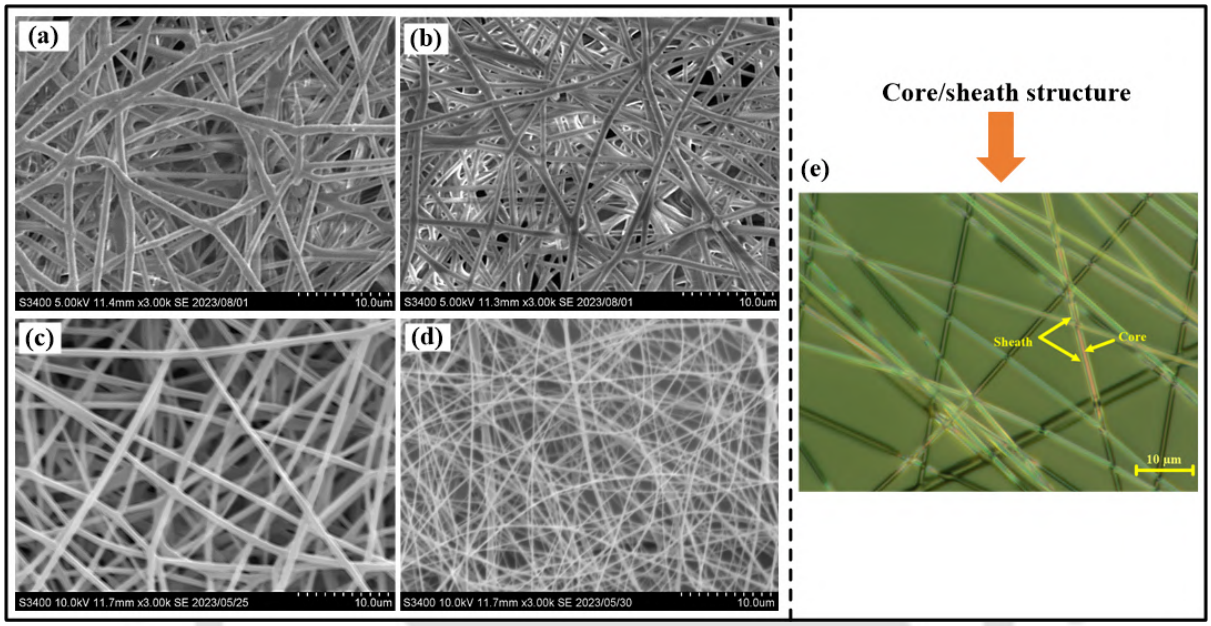

Figure 5.2 SEM images of pullulan/PLGA core/sheath nanofibers with **(a, b)** 21G/1mm and **(c, d)** 23G/1mm core-to-sheath ratio before and after dissolving in chloroform, respectively. Additionally, **(e)** optical microscopic image of nanofibers showing the core/sheath structure.

5.2.2 Mechanical testing

The interaction between the pullulan core and the PLGA sheath significantly influences the overall mechanical properties of the nanofiber. As depicted in Figure 5.3 (a–e), both the dual drug-loaded and non-drug-loaded core/sheath pullulan/PLGA nanofibers were tested for their mechanical properties. In both the cases, while dealing with a smaller core diameter, as in the case of 23G/1mm, the relative proportion of pullulan within the cross-sectional area is much less. Due to greater flexibility and higher elongation characteristics of pullulan as compared to PLGA, a reduced core diameter results in a lesser impact from the pullulan on the overall mechanical properties of the nanofiber. Consequently, the strength and rigidity of the comparatively less flexible PLGA sheath become more significant, leading to improved tensile strength (0.11 ± 0.01 cN/dtex and 0.18 ± 0.01 cN/dtex) and tensile modulus (1.13 ± 0.11 cN/dtex and 3.12 ± 0.15 cN/dtex) in the drug-loaded and non-drug-loaded 23G/1mm nanofibers, respectively. Moreover, the stress gets concentrated over a smaller area, thereby

resulting in higher stress and lower elongation at break of the nanofiber. Additionally, in the 23G/1mm nanofiber, the relatively stiffer and less deformable nature of PLGA becomes more significant due to the larger proportion of PLGA in the cross-sectional area, thereby resulting in higher tensile modulus (1.13 ± 0.11 cN/dtex and 3.12 ± 0.15 cN/dtex) and lower elongation at break (142.38 ± 1.37 % and 173.94 ± 4.78 %) in the drug-loaded and non-drug-loaded 23G/1mm nanofibers, respectively. On the other hand, in case of the 21G/1mm nanofiber with an increased core diameter, the proportion of pullulan within the cross-sectional area is much higher. The flexible nature of pullulan results in more effective distribution of load, thereby reducing the stress. This results in a relatively lower tensile strength (0.04 ± 0.005 cN/dtex and 0.09 ± 0.01 cN/dtex), lower tensile modulus (0.98 ± 0.14 cN/dtex and 1.21 ± 0.03 cN/dtex) and higher elongation at break (192.06 ± 5.02 % and 225.74 ± 4.67 %) of the drug-loaded and non-drug-loaded 21G/1mm nanofibers, respectively. Notably, the results demonstrated that the incorporation of CIP and PTX drugs led to a reduction in tensile strength by ~ 38.89 % and ~ 55.56 %, tensile modulus by ~ 63.78 % and ~ 19.01 %, and elongation at break by ~ 18.14 % and ~ 14.90 % in the 23G/1mm and 21G/1mm nanofibers, respectively. This is in line with reported literature where the incorporation of drug decreased the overall mechanical properties of the nanofibers [484–486]. Additionally, the mechanical properties of the as-spun nanofibers were consistent with those of other nonwoven nanofibers reported in the literature [308,487,488]. The stress-strain curves of the drug-loaded and non-drug-loaded nanofibers with 23G/1mm and 21G/1mm core/sheath needle size or core-to-sheath ratio are shown in Figure 5.3 (a, b), respectively. As shown in Figure 5.3 (c–e), the dual drug-loaded nanofibers exhibited statistically significant differences in tensile strength ($p < 0.01$, Figure 5.3 (c)) and elongation at break ($p < 0.0001$, Figure 5.3 (d)), but no significant difference in tensile modulus (ns, Figure 5.3 (e)) was observed when comparing the 21G/1mm nanofiber to the 23G/1mm nanofiber. In contrast, the non-drug-loaded nanofibers showed significant differences in all three properties: tensile strength ($p < 0.001$, Figure 5.3 (c)), elongation at break ($p < 0.0001$, Figure 5.3 (d)), and tensile modulus ($p < 0.0001$, Figure 5.3 (e)) between the 21G/1mm and 23G/1mm nanofibers. The incorporation of the drugs led to a significant decrease in tensile strength ($p < 0.01$ and $p < 0.001$, Figure 5.3 (c)), elongation at break ($p < 0.05$ and $p < 0.0001$, Figure 5.3 (d)), and tensile modulus ($p < 0.001$ for both, Figure 5.3 (e)) in the 21G/1mm and 23G/1mm nanofibers, respectively.

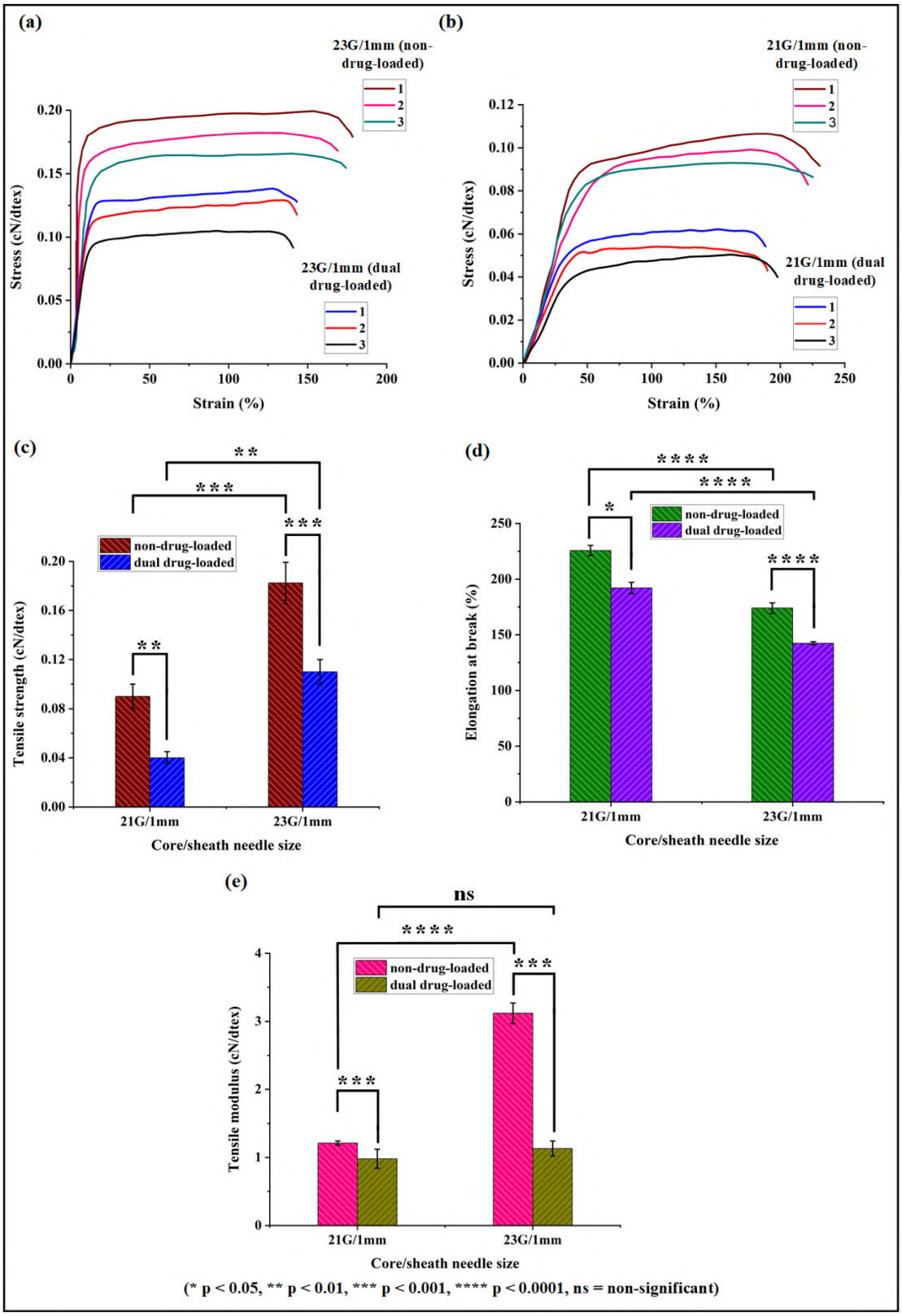

Figure 5.3 Stress-strain curves of the non-drug-loaded and dual drug-loaded core/sheath nanofibers with **(a)** 23G/1mm and **(b)** 21G/1mm core/sheath needle size. Additionally, statistical differences in **(c)** tensile strength, **(d)** elongation at break and **(e)** tensile modulus of the nanofibers with varying core/sheath needle size. Results are reported as mean ± SD.

5.2.3 FTIR analysis

The FTIR analysis revealed that there was no additional peak in the CIP-loaded pullulan (represented as pullulan + CIP) nanofiber spectrum when compared to that of pure pullulan nanofiber (Figure 5.4 (a)). Moreover, the characteristic peaks of pullulan remain unchanged even after CIP incorporation. This indicates that the incorporation of CIP did not induce any chemical interactions or alterations with the pullulan structure, and the CIP drug particles were dispersed within the pullulan matrix. Similarly, no additional peak was observed in the PTX-loaded PLGA (represented as PLGA + PTX) nanofiber spectrum when compared to that of pure PLGA nanofiber (Figure 5.4 (b)). This further indicates that the PTX drug particles were trapped inside the PLGA polymer matrix without undergoing any chemical alterations, interactions or bond formations. The absence of additional peaks in the drug-loaded nanofibers thus indicates the lack of significant chemical interactions or bond formation between the drugs and their respective polymers [308,489].

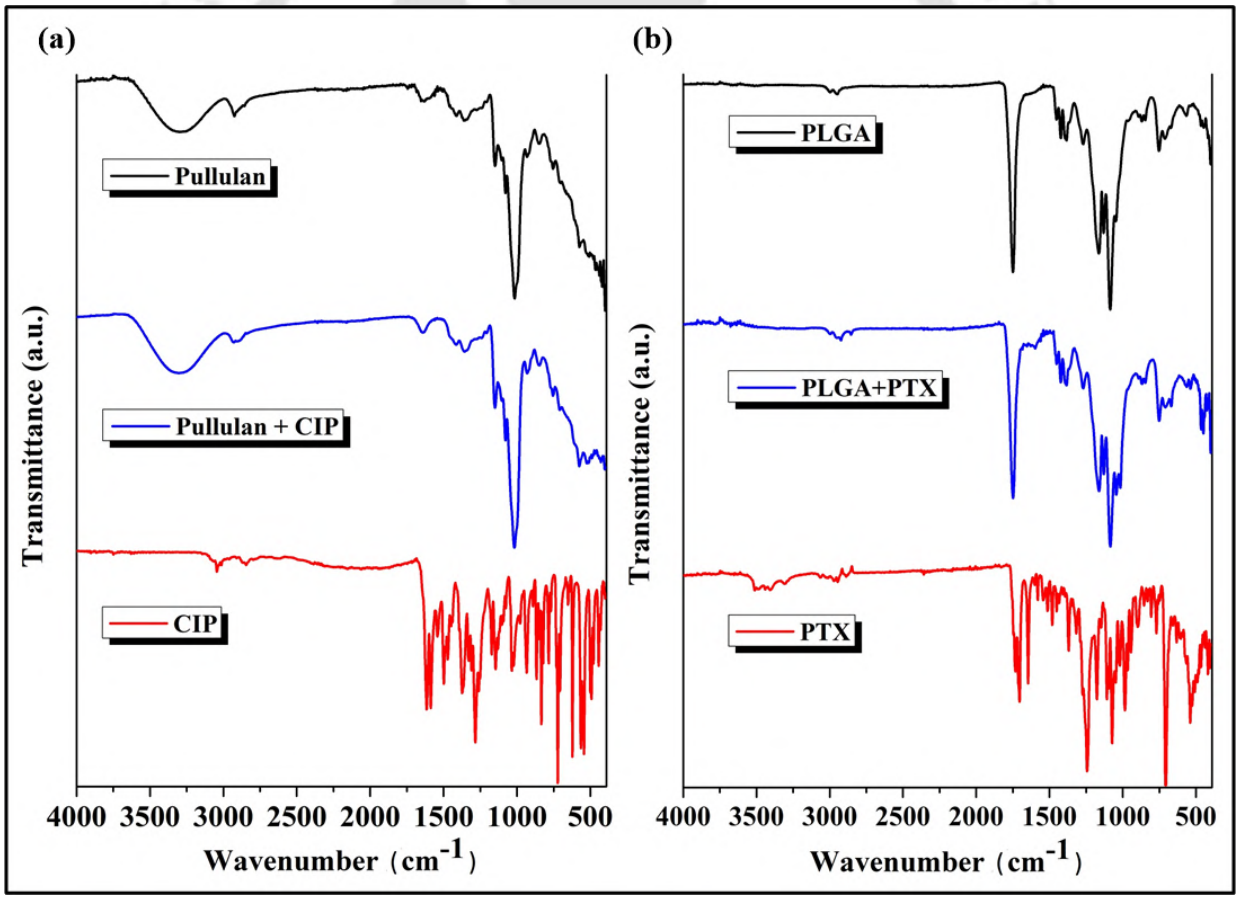

Figure 5.4 FTIR spectra of **(a)** pure pullulan nanofibers, CIP-loaded pullulan (represented as Pullulan + CIP) nanofibers and pure CIP powder, and **(b)** pure PLGA nanofibers, PTX-loaded PLGA (represented as PLGA + PTX) nanofibers and pure PTX powder.

5.2.4 Surface wettability

Hydrophilic materials like pullulan have a low contact angle with water, meaning they tend to readily wet and spread on the surface. On the other hand, hydrophobic materials like PLGA have a high contact angle with water, indicating their resistance to wetting. The observed behaviour of the water contact angle is due to the interactions between the hydrophilic pullulan core and the hydrophobic PLGA sheath.

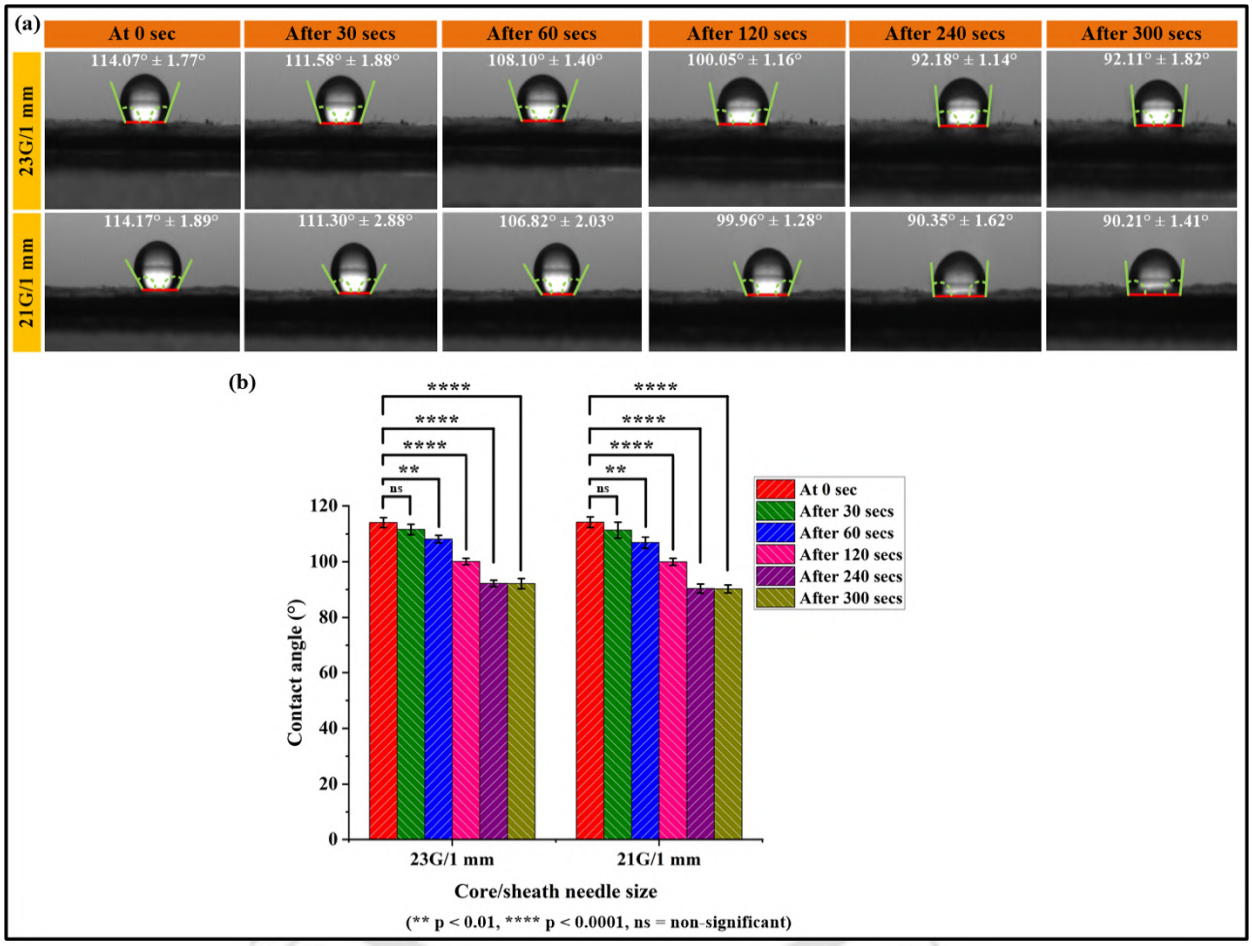

Figure 5.5 (a) Changes in water contact angle of core/sheath nanofibers of 23G/1mm and 21G/1mm core-to-sheath ratios and **(b)** Statistical analysis of the change in contact angle of the nanofibers, recorded over a period of 300 secs. Results are reported as mean ± SD.

As depicted in Figure 5.5 (a), the water contact angle of the dual drug-loaded core/sheath nanofiber changed from 114.07º ± 1.77º to 92.11º ± 1.82º when the core diameter is smaller (23G/1mm) and 114.17º ± 1.89º to 90.21º ± 1.41º when the core diameter is larger (21G/1mm), over a duration of 300 secs. Additionally, the contact angle of the nanofibers presented in this study was similar to other core/sheath nanofibers with PLGA sheath, as reported by Lee et al. [490]. The contact angle stabilized after 240 secs, as evidenced by the

nearly constant values recorded between 240 and 300 secs (Figure 5.5 (a)). The contact angle difference in both the 23G/1mm and 21G/1mm nanofibers was statistically non-significant (ns) when compared after 30 secs to that at 0 sec. However, it was statistically significant ($p < 0.01$) when compared after 60 secs to that at 0 sec, and statistically highly significant ($p < 0.0001$) when compared after 120, 240 and 300 secs to that at 0 sec (Figure 5.5 (b)). This indicates that the variations in core-to-sheath ratio have no significant effect on the overall surface wettability of the nanofibers.

5.2.5 In vitro drug release

The *in vitro* drug release of the nanofibers was studied over a period of 168 hrs. As depicted in Figure 5.6 (a, b), the drug release rate could be tuned by changing the core-to-sheath ratio of the core/sheath nanofiber. A similar study reported by Liu et al. [491] demonstrated tunable drug release by variations in core-to-sheath ratio of nanofibers. In the present study, the release rate of CIP is higher (up to 65.76 ± 1.66 %) in case of larger core diameter (21G/1mm) and comparatively lower (up to 52.10 ± 1.10 %) in case of smaller core diameter (23G/1mm) over a period of 168 hrs (Figure 5.6 (a)). Similarly, the release rate of PTX is lower (up to 14.38 ± 0.15 %) in 21G/1mm and comparatively higher (up to 24.62 ± 0.23 %) in 23G/1mm, over the same release period of 168 hrs (Figure 5.6 (b)). The reason behind such changes in the release rates may be attributed to the fact that larger core diameter (21G/1mm) accelerates the release rate of the core drug (CIP). Moreover, when the core diameter is smaller (23G/1mm), the sheath diameter being highly pronounced accelerates the release rate of the sheath drug (PTX).

As observed in Figure 5.6 (a, b), both the 23G/1mm and 21G/1mm nanofibers demonstrated a burst release during the initial 6 hrs, followed by controlled release up to 168 hrs. However, in both the 21G/1mm and 23G/1mm nanofibers, the overall *in vitro* dual drug release pattern demonstrated faster release rate of CIP as compared to PTX. The faster release of CIP and comparatively slower release of PTX can be attributed to their physicochemical properties. CIP is a smaller, hydrophilic molecule, while PTX is larger and hydrophobic. These differences affect their release rates. Smaller, hydrophilic molecules tend to diffuse more readily through the nanofiber matrix, leading to faster release. Similar results have been reported in prior studies where the hydrophilic CIP demonstrated faster release than the hydrophobic PTX [492]. CIP is an antibiotic that is prescribed to prevent or treat bacterial infections, especially if the immune system of the patient is compromised during cancer treatment [472,473]. Prior studies have reported that CIP possesses growth-inhibitory and apoptotic activities, demonstrates immunomodulatory effects, and can induce cell cycle arrest

in various cancer cell lines [474–477,493]. The fast release of CIP in the present study is expected to help reduce the risk of infection. On the other hand, for treatment of some cancerous condition, such as in malignant melanoma, slow-release formulations of chemotherapeutic drugs (such as PTX) might be preferred. PTX has been reported to stabilize microtubules which results in selective disruption of microtubule dynamics, that eventually cause mitotic arrest and cell death. It can also inhibit tumour angiogenesis and tumour cell proliferation, while promoting the expression of cytokines and genes that suppress cell growth and induce apoptosis [479,480,494–496].

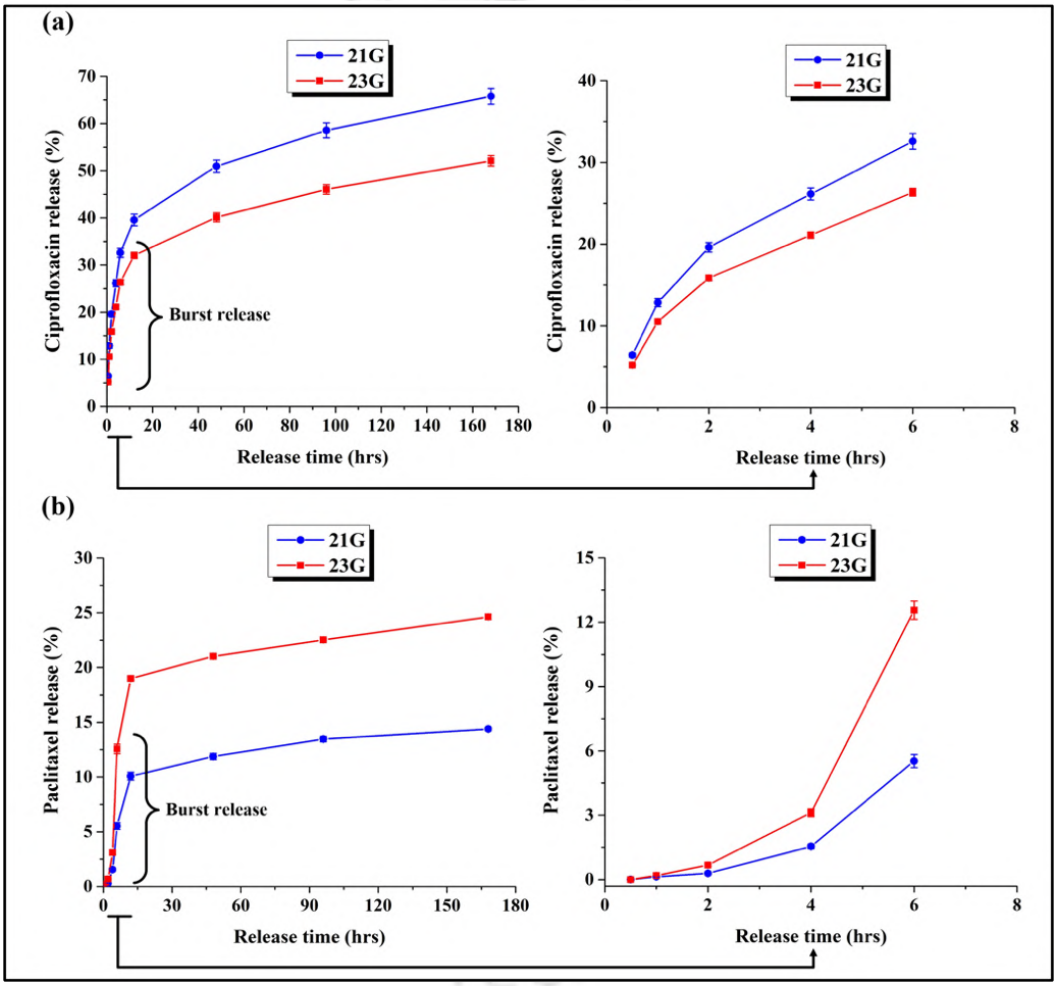

Figure 5.6 *In* vitro release profiles of **(a)** CIP and, **(b)** PTX from nanofibers with 21G/1mm and 23G/1mm core-to-sheath ratio. Results are reported as mean ± SD.

The relatively slower release of PTX in the present study would thus provide a more sustained and prolonged exposure of cancer cells to PTX, thereby destroying the cancer cells over time and enhance their sensitivity towards radiotherapy [497–500]. The slow release would potentially help in reducing certain side effects associated with PTX, such as

hypersensitivity reactions, by allowing for a more gradual and controlled delivery. Moreover, slow-release formulations require less frequent dosing, thereby offering convenience for patients who need fewer administration sessions [501,502]. Additionally, the slow-release can help maintain relatively steady levels of PTX in blood, which may be important for maintaining therapeutic effectiveness [503].

5.2.6 In vitro hydrolytic degradation

Analysis of the degradation behaviour of nanofibers is crucial for their applications in tissue engineering and drug delivery. As depicted in Figure 5.7 (a), the as-spun nanofibers showed a significant reduction in weight after immersion in PBS, which indicates the hydrolytic degradation of the nanofibers.

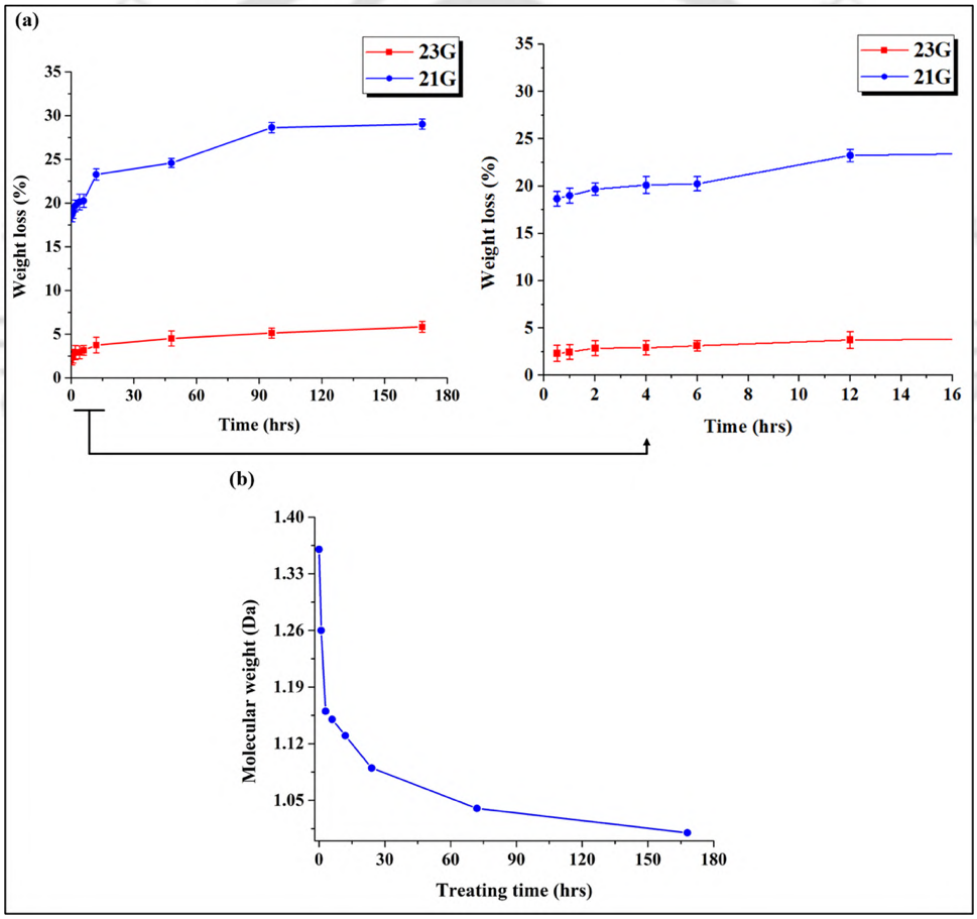

Figure 5.7 (a) Weight losses of the as-spun core/sheath nanofibers and, **(b)** GPC data showing molecular weight (M_w) reduction of PLGA, after immersion in PBS. Results are reported as mean ± SD.

Notably, the rate of weight loss of the 23G/1mm nanofiber was much slower as compared to the 21G/1mm nanofiber. The relatively higher rate of weight loss in the 21G/1mm

nanofiber may be attributed to its thicker core diameter, which comprises of a greater proportion of the hydrophilic core material (pullulan). The difference between rate of weight loss of the 23G/1mm and 21G/1mm nanofibers was statistically highly significant ($p < 0.0001$). Further confirmation of the nanofiber degradation was provided by the GPC analysis of the PLGA sheath. The GPC data (Figure 5.7 (b)) revealed a significant reduction in the molecular weight (M_w) of the PLGA from 136000 to 101000 Da, following a one-week immersion in PBS. The degradation results in the hydrolytic cleavage of ester bonds present within the PLGA polymer when exposed to PBS solution, thereby reducing the M_w. Additionally, the degradation products of PLGA, lactic acid and glycolic acid, are biocompatible and thus can be metabolized by the body, minimizing any potential adverse effects on human health [504].

5.2.7 Analysis of cytotoxicity

The *in vitro* cytotoxicity of the fabricated core/sheath nanofibers was determined using the MTT assay. Both the dual drug-loaded and non-drug-loaded core/sheath nanofibers were tested for cytotoxicity in order to determine the efficacy of the drugs (CIP and PTX) in inhibiting the human melanoma A375 cell proliferation. Additionally, the viability of melanoma cells in presence of the CIP-loaded pullulan and the PTX-loaded PLGA nanofibers were also examined in order to determine the cytotoxic efficacy of the individual drugs. As depicted in Figure 5.8 (a), the relative cell viability percentages in presence of the dual drug-loaded 23G/1mm core/sheath nanofibers after 24, 48 and 72 hrs were 70.56 ± 2.86 %, 67.77 ± 0.80 %, and 65.37 ± 1.96 %, respectively, and that in presence of the dual drug-loaded 21G/1mm core/sheath nanofibers were 70.85 ±1.12 %, 70.23 ± 2.52 %, and 67.82 ± 1.31 %, respectively. Similarly, the relative cell viability percentages in presence of the CIP-loaded pullulan nanofibers were 71.53 ± 2.60 %, 71.25 ± 1.90 %, and 70.87 ± 1.76 %, respectively, and those in presence of the PTX-loaded PLGA nanofibers were 71.03 ± 2.73 %, 70.93 ± 0.84 % and 68.72 ± 1.81 % after 24, 48 and 72 hrs, respectively. The results indicate significant reduction in melanoma cell viability in presence of all the drug-loaded nanofibers. Additionally, it was observed that the dual drug-loaded 23G/1mm and 21G/1mm nanofibers exhibited comparable cytotoxic effects on melanoma cells, with slightly lower cell viability observed for the 23G/1mm nanofiber, as shown in Figure 5.8 (a, b). This may be attributed to the relatively higher release rate of PTX from the 23G/1mm nanofiber (Figure 5.6 (a, b)), resulting in a more potent cytotoxic effect, as PTX is a highly effective chemotherapeutic agent that inhibits cancer cell proliferation [505]. All the drug-loaded nanofibers demonstrated less than 75 % cell viability, thus indicating their cytotoxic behaviour towards melanoma A375 cells, according to the percentage criteria for

cytotoxicity [432,506,507]. When compared to the control, the difference in relative cell viability percentage was statistically non-significant (ns) in presence of the non-drug-loaded nanofibers. This indicates that the non-drug-loaded nanofibers facilitated the cell growth and proliferation similar to that in the control, and hence has no cytotoxic effect on the A375 cells. However, in presence of the CIP-loaded pullulan, the PTX-loaded PLGA and the dual drug-loaded 23G/1mm and 21G/1mm core/sheath nanofibers, the reduction in cell viability percentage was statistically highly significant ($p < 0.0001$) with respect to that in the control (Figure 5.8 (a)).

Furthermore, as observed by the cell adhesion study (Figure 5.8 (b)), the A375 cells exhibited normal proliferation and adhesion in the control (or untreated A375 cells) as well as in presence of the non-drug-loaded core/sheath nanofibers. However, the A375 cells exposed to the drug-loaded nanofibers showed a marked reduction in cell adhesion and proliferation. Notably, the dual drug-loaded 23G/1mm core/sheath nanofibers demonstrated the lowest cell adhesion and hence the highest cytotoxicity towards the melanoma cells. Researchers have reported similar results on the cytotoxic effect of CIP [508] and PTX [505] on A375 cells. This significant reduction in cell viability indicates the efficacy of CIP and PTX in inducing cytotoxicity towards the melanoma cells. The enhanced cytotoxicity in presence of the dual drug-loaded nanofibers may be due to the ability of CIP to induce DNA damage, coupled with the inhibition of cell division by PTX, thereby resulting in a synergistic cytotoxic effect on the melanoma cells. This further indicates that the dual drug-loaded nanofibers presented in this study has the potential to inhibit the growth and proliferation of melanoma cells *in vitro*. The results of the cell adhesion study were found to be in line with that of the MTT assay (Figure 5.8 (a)), where the drug-loaded nanofibers effectively reduced the viability of the A375 cells.

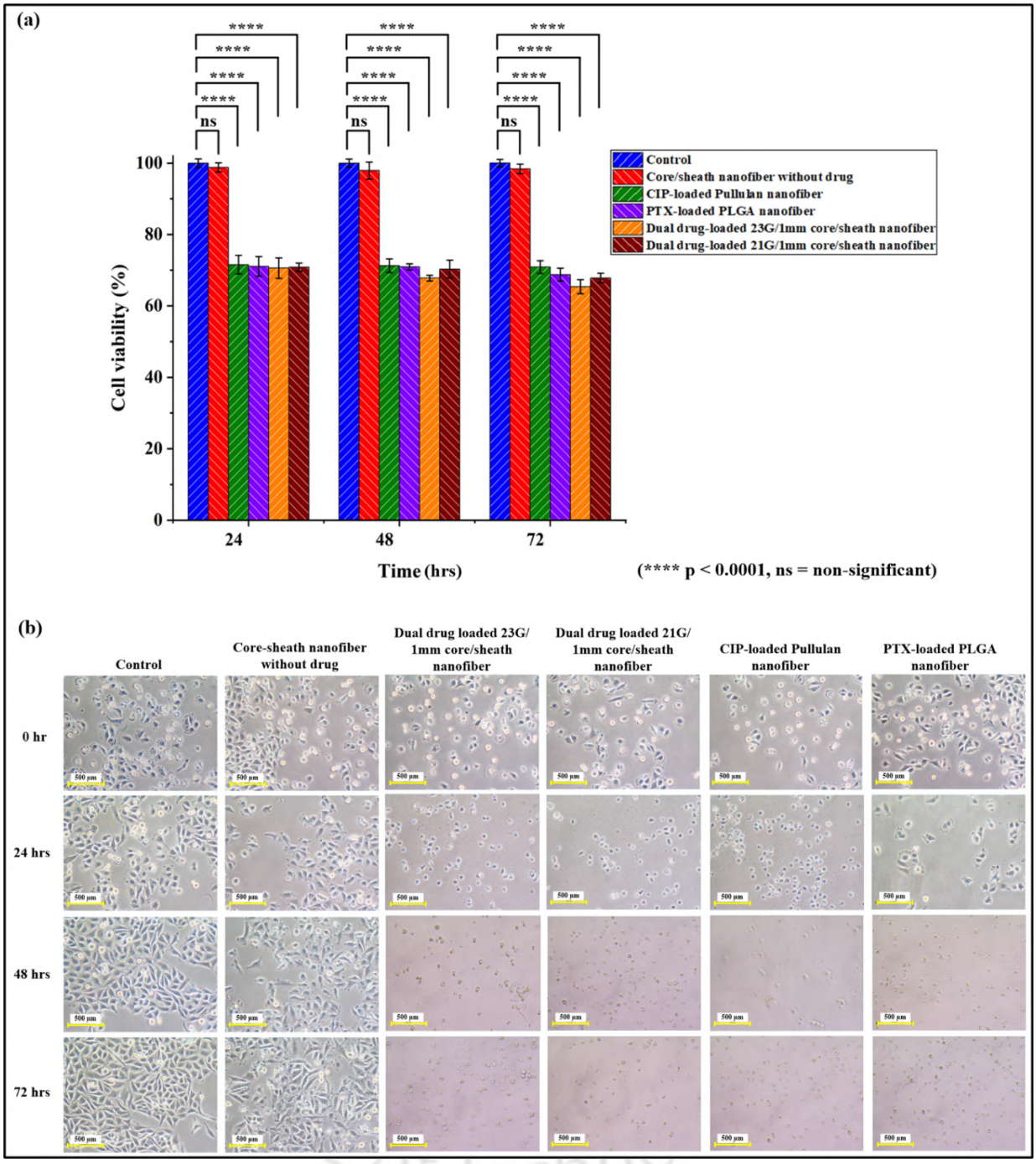

Figure 5.8 (a) Relative viability percentage of A375 cells in control, core/sheath nanofibers without drug, CIP-loaded pullulan nanofibers, PTX-loaded PLGA nanofibers and CIP/PTX or dual drug-loaded 23G/1mm and 21G/1mm core/sheath nanofibers, and **(b)** effect of fabricated nanofibers on A375 cell adhesion at 0 hr, and after 24, 48 and 72 hrs of cell seeding. Results are reported as mean ± SD.

5.3 Summary

The results of this study demonstrate the successful fabrication and characterization of CIP/PTX-loaded pullulan/PLGA core/sheath nanofibers using the coaxial ECS technique. The uniform morphology, suitable mechanical properties, and controlled drug release kinetics of the nanofibers highlight their potential for various biomedical applications, particularly in dual drug delivery systems. The ability to vary the core-to-sheath ratio allows for the tuning of mechanical properties and drug release profiles as per specific application needs. On varying the core-to-sheath ratio of the dual drug-loaded nanofibers from 21G/1mm to 23G/1mm, the tensile strength increased from 0.04 ± 0.005 cN/dtex to 0.11 ± 0.01 cN/dtex, the tensile modulus increased 0.98 ± 0.14 cN/dtex from to 1.13 ± 0.11 cN/dtex, but the elongation at break reduced from 192.06 ± 5.02 % to 142.38 ± 1.37 %. Additionally, the nanofiber with a larger core diameter (21G/1mm) facilitates a higher release rate of core drug (CIP), with up to 65.76 ± 1.66 % release over a period of 168 hrs. Conversely, the nanofiber with a smaller core diameter (23G/1mm) result in a higher release rate of sheath drug (PTX), with up to 24.62 ± 0.23 % release within the same time period. Both the nanofiber configurations exhibited a burst release during the initial 6 hrs, followed by a controlled release up to 168 hrs. However, the overall *in vitro* dual drug release pattern demonstrated that CIP is released more rapidly than PTX in both nanofiber configurations, owing to the smaller size and hydrophilic nature of CIP. This tunability enhances the versatility of the nanofibers for use in targeted drug delivery. Additionally, the *in vitro* cytotoxicity analysis of the 23G/1mm and 21G/1mm dual drug-loaded nanofibers conducted on A375 human melanoma cells demonstrated viabilities of only 65.37 ± 1.96 % and 67.82 ± 1.31 % respectively, after 72 hrs, indicating their potentiality for possible treatment of malignant melanoma. However, further research using *in vivo* animal models is necessary to confirm the efficacy of the fabricated nanofiber in delivering CIP and PTX for treatment of malignant melanoma. The effect of altering the core-to-sheath ratio on drug release profiles, mechanical properties, and therapeutic outcomes should also be investigated. Additionally, strategies should be explored to investigate the potential of combining CIP and PTX along with other therapeutic agents for more effective cancer treatment. Combination drug therapies should be widely explored to target multiple signalling pathways related to tumour progression and resistance. Furthermore, clinical trials should be conducted to determine the safety and efficacy of using the core/sheath nanofibers for localized treatment of cancer in human patients.

CHAPTER 6

FORMULATION AND CHARACTERIZATION OF ANTIBACTERIAL COSMETIC SKIN-CREAM INFUSED WITH PULLULAN AND TURKEY BERRY (*Solanum torvum*) LEAF EXTRACT

Motivation

The growing consumer demand for skin-friendly and sustainable cosmetic products has driven research toward biocompatible materials with multifunctional benefits. Conventional topical formulations often contain strong chemical preservatives including parabens, triclosan, and formaldehyde-releasing compounds that may cause irritation or raise environmental concerns. Pullulan, a natural polysaccharide with film-forming, moisturizing, and regenerative properties, presents a promising alternative for topical applications. Similarly, turkey berry (Solanum torvum) leaf extract is a rich source of bioactive compounds known for their antimicrobial, antioxidant, and anti-inflammatory effects. This study is motivated by the potential synergy between pullulan and turkey berry leaf extract to develop a safe and effective antibacterial skin-cream, incorporating natural bioactives while maintaining a partially synthetic formulation, in line with current trends in cosmeceuticals.

The work in the chapter has been filed as a patent (Patent application no.: 202531097797) under the title **"*Biopolymer based Cosmetic Skin Cream Formulation*".**

Abstract

The cosmetic industry is increasingly adopting biocompatible and sustainable materials to meet consumer demands for skin-friendly products. Pullulan, a water-soluble polysaccharide produced by *Aureobasidium pullulans* (*A. pullulans*), is known for its moisture retention, skin-regenerative, and oxygen-barrier properties, making it ideal for topical formulations. Its ability to form flexible, transparent films has led to its incorporation in several cosmetic skincare products. Additionally, turkey berry (*Solanum torvum, S. torvum*) has gained attention for its antimicrobial, anti-inflammatory, and wound-healing properties. This study investigated the formulation of an antibacterial skin-cream using pullulan and turkey berry leaf extract (TBLE). The leaf extract, rich in phenolics and flavonoids, exhibited significant antibacterial activity, determined by the disc diffusion method, with zones of inhibition of 11.51 ± 0.92 mm against *Staphylococcus aureus* (*S. aureus*) and 10.45 ± 0.50 mm against *Escherichia coli* (*E. coli*). The antibacterial activity of the cream formulation was also tested using the same method, which showed zones of inhibition of 16.67 ± 0.40 mm against *S. aureus* and 14.83 ± 0.12 mm against *E. coli*. The cream also exhibited good physical and thermal stability with a pH of 6.10 ± 0.20. Additionally, the cream was found to be free from harmful heavy metals, arsenic, and microbial contamination. It demonstrated a total fatty matter (TFM) of 8.5 % with 65 % moisture content, and shear-thinning behaviour, all within acceptable ranges for topical use. The results suggest that the combination of pullulan and TBLE produces a safe and effective antibacterial skin-cream, incorporating natural bioactives alongside some synthetic components.

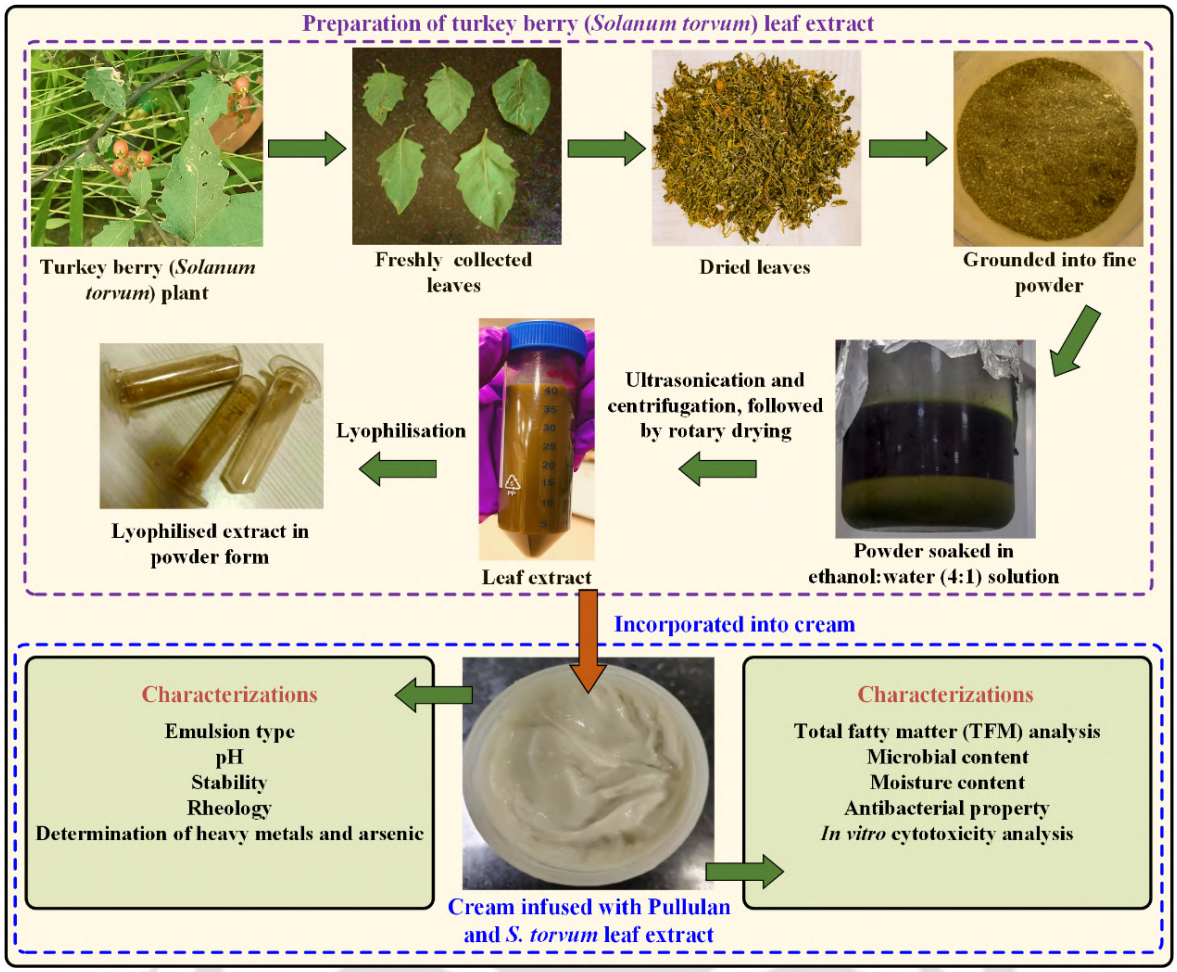

Figure 6.1 Scheme of chapter 6.

6.1 Introduction

The cosmetic industry is now aiming at utilization of biobased materials that are skin-compatible and can be used to generate more sustainable skincare products with enhanced properties. In case of skincare products, emulsions are the predominant form of product formulation, that are inherently thermodynamically unstable and tend to undergo rapid phase separation after formation. This occurs as the system tends to minimize the high-energy states caused by interfacial tension [509]. To counteract this, stabilizers such as surfactants, emulsifiers, or polymers are incorporated to improve the kinetic stability of the emulsion and prevent phase separation. Different cosmetic emulsions serve different functions such as oil control, whitening, and providing protection against Ultra-Violet (UV) rays. Cosmetic emulsions are mainly classified as oil-in-water (O/W) or water-in-oil (W/O) emulsions. In cosmetic formulations, both O/W and W/O emulsions must fulfil several essential criteria. These include possessing suitable rheological characteristics for skincare application, offering a pleasant sensory feel, while ensuring good spreadability, and maintaining long-term physical

stability under varying conditions. Additionally, the formulation components are required to be biocompatible, non-irritating, and free from harmful effects. Among the two types, O/W emulsions are most commonly used in the cosmetic industry [510].

Traditionally, polymers with good water solubility such as alginate, starch, hydroxyethyl cellulose, carboxymethyl cellulose, and methylcellulose have been used as carriers in cosmeceutical products. Pullulan, which is also a natural water-soluble polysaccharide, present a promising alternative as it is biodegradable, non-irritant, non-toxic, non-immunogenic, non-carcinogenic, and non-mutagenic [511,512]. It exhibits certain desirable properties like high moisture absorption and excellent water solubility, making it an effective binder, stabilizer, and carrier for active compounds, enabling site-specific skin delivery and enhancing product performance in cosmeceutical products [217,218]. Due to its Generally Recognized as Safe (GRAS) status, pullulan can be used without limitations in a wide range of cosmetic formulations, making it a versatile ingredient for skincare and personal care products [216].

The present study focuses on formulation of an antibacterial skin-cream using the biocompatible polymer pullulan, valued in cosmetics for its gas barrier, moisture retention, and skin-regenerative properties. In the formulation, pullulan was incorporated into the aqueous phase to serve as a texture enhancer and stabilizer, while the leaf extract of turkey berry (*S. torvum, S. torvum*) contributed to antibacterial activity. *S. torvum* is a medicinal plant widely used across Asia and Africa, traditionally applied for the treatment of infections and inflammation. Its leaves are known to be rich in bioactive phytochemicals such as flavonoids, saponins, tannins, and phenolic compounds, which contribute to antibacterial, anti-inflammatory, and antioxidant effects [513]. These properties make it a potential candidate for use in skincare applications, especially in formulations intended to prevent or treat minor skin infections and promote skin health. Recent studies have demonstrated its inhibitory activity against pathogenic microbes such as *Pseudomonas aeruginosa, Staphylococcus aureus*, and *Escherichia coli*, supporting its suitability for topical applications aimed at protecting the skin from microbial threats [513–516]. The findings of the present work aim to develop an antibacterial skin-cream that improves skin health and appearance while protecting against bacterial infections. The integration of traditional herbal extracts like *S. torvum* with biopolymers like pullulan supports the development of sustainable cosmetic formulations with both cosmetic and therapeutic benefits.

6.2 Results and discussion

6.2.1 Determination of the type of emulsion, pH and stability of cream

The formulated cream under consideration in this study was found to be of O/W emulsion type. The pH of the formulated cream was estimated to be 6.10 ± 0.20. The formulated cream was found to be thermally stable since there were no phase changes observed when kept at 4 °C, 37 °C and 45 °C for 24 hrs.

6.2.2 Rheological analyses

6.2.2.1 Viscosity

The rheological properties of the cream formulation were assessed to evaluate its stability and applicability as a topical product. The flow curve of the developed cream formulation (shown in Figure 6.2 (a)) revealed a typical non-Newtonian shear-thinning behaviour, characteristic of complex fluids such as ketchup, paint, blood, polymeric solutions, etc. and semi-solid formulations like toothpastes, cosmetic creams, ointments and others. At low shear rates, the cream exhibited high viscosity values (> 6000 cP), indicative of a strong internal structure likely supported by emulsifiers, thickeners, or polymeric agents such as pullulan and could be due to long polymeric chain entanglements or intermolecular interactions. This high viscosity at rest is advantageous for physical stability, reducing the risk of phase separation or settling during storage.

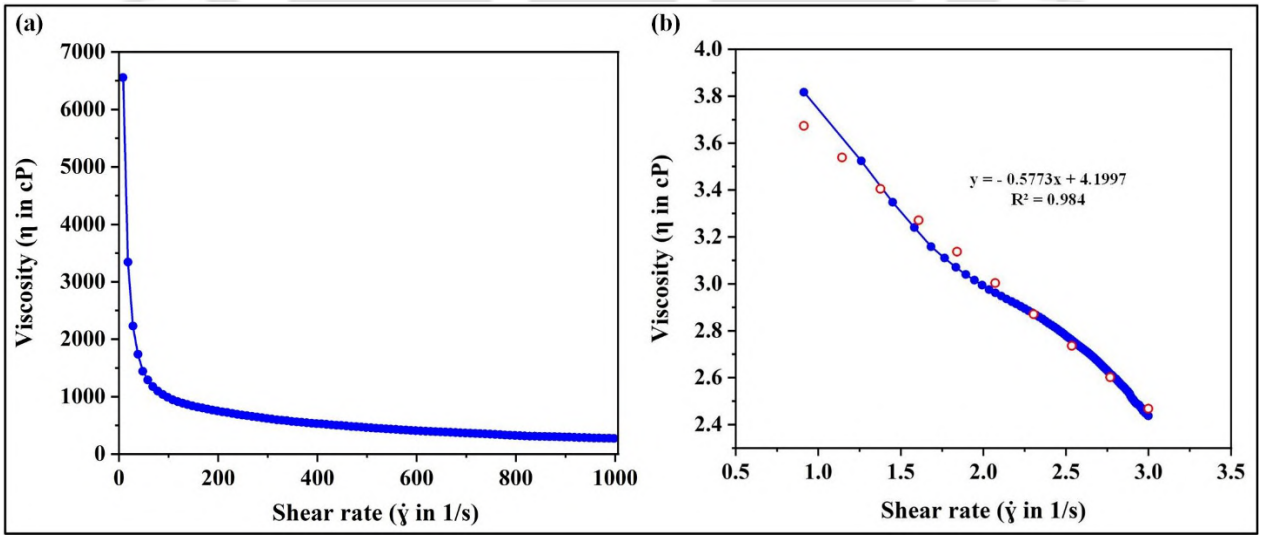

Figure 6.2 (a) Flow curve and **(b)** logarithmic flow curve of the formulated cream.

As the shear rate increased, viscosity decreased sharply, falling below 1000 cP at approximately 100 s^{-1}, and continued to decline before reaching a plateau at higher shear rates (> 600–800 s^{-1}). The sharp decrease in viscosity could be because of alignment of polymeric

chain when stress was applied. The power-law model equation for the prepared non-Newtonian shear-thinning cream formulation is given as:

$\eta = K(\dot{\gamma})^{n-1}$, which in logarithmic form is, $\log\eta = (n-1)\log(\dot{\gamma}) + \log K$,

where η is the viscosity, $\dot{\gamma}$ is the shear rate, K is the consistency index and n is the flow behaviour index, (equation (21) as discussed in chapter 2).

When fitted to a straight-line equation ($y = mx + c$), it was represented as: $y = -0.5773x + 4.1997$, and has $R^2 = 0.984$, (shown in Figure 6.2 (b)). Here, the flow behaviour index (n) was calculated as: $n = (-0.5773 + 1) = 0.4227$.

Since $0 < n < 1$, the cream formulation was said to exhibit shear-thinning behaviour. This behaviour suggested efficient structural breakdown under stress, facilitating ease of spreading during application. The final plateau indicated a transition to a stable, fluid-like state, ensuring the cream remained consistent without becoming excessively runny during use. These findings confirmed that the formulation exhibited desirable features, such as high viscosity at rest for stability, and pronounced shear-thinning for user-friendly application, both essential for effective topical delivery.

6.2.2.2 Amplitude sweep measurements

Amplitude sweep measurements were conducted at 25 ℃ to identify the Linear Viscoelastic Region (LVR) of the prepared cream formulation. During this analysis, both the storage modulus (G′) and the loss modulus (G″) remained almost constant in LVR which means that below critical strain (γ_L) of 0.25 %, G′ and G″ were 781.06 and 308.46 Pa, respectively. These measurements also provide insights into the material's structural strength; typically, a stable formulation remains within the LVR. A representative curve illustrating the G′ and G″ moduli of the formulation plotted against the applied shear strain (%), has been depicted in Figure 6.3. The curve clearly shows that G′ is greater than G″, suggesting that the formulation exhibited solid-like behaviour or an elastic nature of cream within the LVR and before crossover point (shear strain = 4.67 %). Additionally, both G′ and G″ values decreased with the increase in shear strain %. After application of high shear strain or beyond the cross-over point, G″ was found to be greater than G′ which indicated that the elasticity of the formulation decreased as the shear strain increased and it showed a liquid-like characteristic or improved flowability for easy usage as a topical product. In oscillatory rheology experiments, the loss factor, tan δ, the ratio of loss modulus (G″) to storage modulus (G′), is a key parameter to characterize the

behaviour of the material. When tan δ exceeds 1, it indicates a predominantly viscous behaviour, with the loss modulus (G″) surpassing the storage modulus (G′). On the other hand, a tan δ less than 1 signifies an elastic material, where the storage modulus (G′) takes precedence. Furthermore, when tan δ > 0.1, the material is not considered to be a true gel and is said to have a structure between that of a highly concentrated polymer solution and a true gel. In the present study, the tan δ value of the cream was found to be 0.39, which ranges between 0.1 and 1, illustrating its characteristics as a weak gel like an emulsion. This means the cream had temporary chain entanglements and macromolecules interactions which could be disrupted due to application of high shear strain, therefore, the cream did not exhibit the structure of real gel.

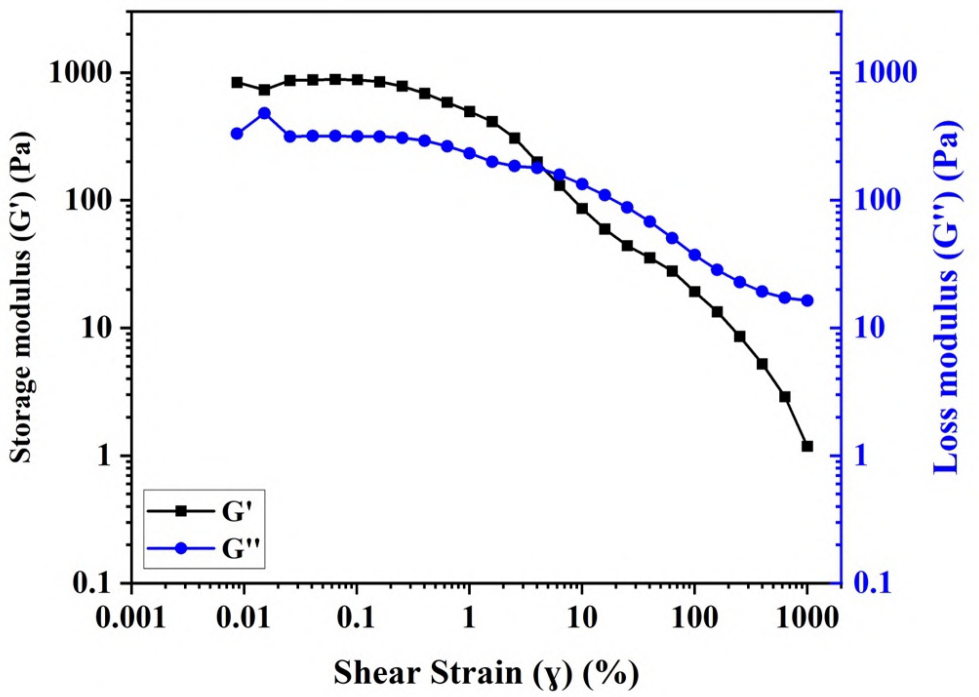

Figure 6.3 Amplitude sweep measurements of the formulated cream.

6.2.2.3 Frequency sweep measurements

Frequency sweep measurements provide valuable insights into the structural characteristics of materials when they are subjected to a range of angular frequency while measuring storage and loss modulus values as a function of angular frequency. This test, as illustrated in Figure 6.4, categorize materials as either gel, concentrated, or dilute solutions, based on the behaviour of G′ and G″ across the frequency range at 25 °C. If G′ > G″ holds true across the entire frequency range, the materials are classified as gels where elastic behaviour dominates viscous nature. For materials where G″ > G′ at higher frequencies, the storage and loss moduli are nearer to

one another, then these materials are classified as dilute solutions. Additionally, in case of G″ > G′ along with the intersection of moduli within the frequency range, the material is classified as concentrated. In the present study, it is clear from Figure 6.4, that the formulated cream can be considered as a gel since G′ > G″ across the entire frequency range which is in line with the observation made in amplitude sweep measurement (discussed in Section 6.2.2.2) where tan δ <1, in particular tan δ = 0.39, indicated a weak gel. Also, there was no crossover point noticed in the observed angular frequency range.

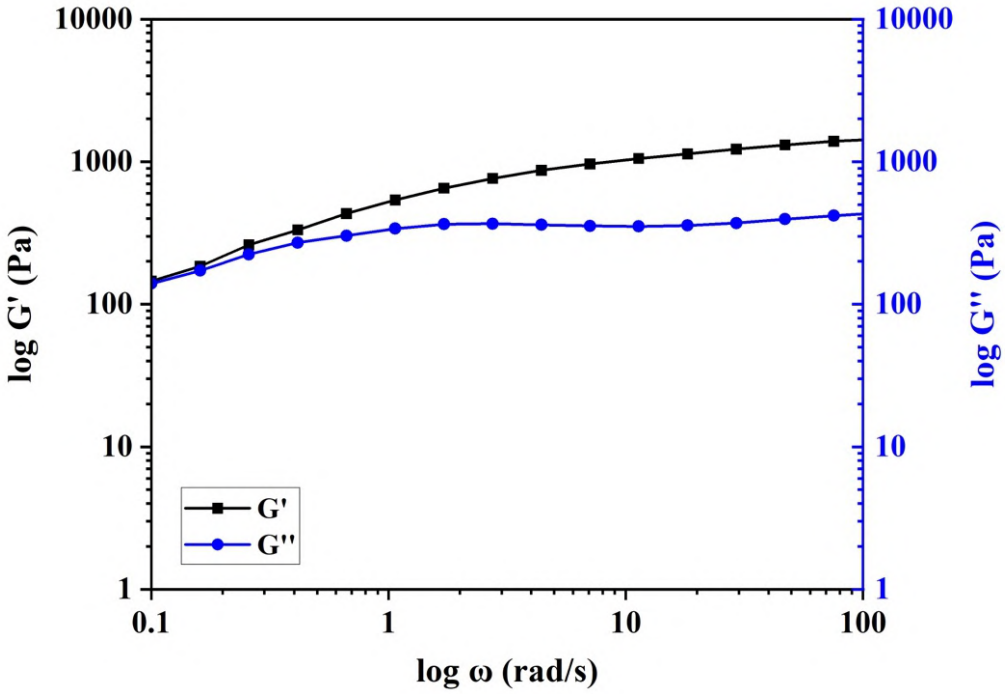

Figure 6.4 Frequency sweep measurements of the formulated cream.

6.2.3 Determination of heavy metals, arsenic and TFM

The cream sample was found to have passed the tests for heavy metals and arsenic, as the colour developed in the sample cream solution was less than that in the standard solutions in both the cases. For the determination of TFM, the mass of residue (M_1) was found to be 0.17 g, with respect to the mass of cream taken for the test (M_2) which was 2 g. Therefore, the total fatty substance (% by mass) was calculated using the following equation (16), discussed in chapter 2:

$$\text{Total fatty substance (\% by mass)} = \frac{M_1}{M_2} \times 100 = \frac{0.17}{2} \times 100 = 8.5\ \%$$

Note: Minimum 5 % TFM is required to pass the test as per Indian Standard for Skin Creams (IS 6608: 2004).

6.2.4 Determination of moisture content

The moisture content in the formulated cream was determined to be around 65 %, as calculated using the following equation (17), discussed in chapter 2:

$$\text{Moisture content } (\%) = \left(\frac{\text{Volume of water extracted}}{\text{Amount of cream sample taken}} \right) \times 100 = \frac{0.65}{1} \times 100 = 65\ \%$$

This result demonstrated that approximately 65 % of the cream's weight was attributable to water content. Such a moisture level is typical and desirable for oil-in-water (O/W) emulsion-type creams, as it enhances the hydrating properties of the cream and facilitates better absorption into the skin. Additionally, the water phase acts as a carrier for hydrophilic active compounds, including pullulan and bioactive phytoconstituents from *S. torvum* leaf extract. In the present study, the observed moisture content also suggested that the cream is unlikely to be excessively greasy and hence would support user comfort upon application. However, moisture content must be balanced with appropriate preservative systems and formulation stability considerations, as higher water content can increase susceptibility to microbial contamination and phase separation if not properly stabilized. Thus, the 65 % moisture content in the formulated cream was found to align with standard cosmetic emulsion requirements.

6.2.5 Determination of microbial content

The formulated cream demonstrated the absence of microbial load, thereby indicating its suitability for use as a cosmetic skin-cream. Ensuring that a topical cream is free from microbial contamination is essential for its safety and effectiveness. In this study, a simple microbial load test was conducted to check whether the cream formulation contained any unwanted microbial growth. As expected, the negative control plates, which were prepared under sterile conditions, showed no signs of microbial growth. This confirmed that the experimental setup was clean and contamination-free. The test plates containing the cream also showed no visible growth, indicating that the formulation did not carry any microbial contamination. This suggests that the preparation process was carried out under hygienic conditions and that the final product is microbiologically safe for use. On the other hand, the positive control plates showed clear microbial growth, as these were intentionally exposed to air, allowing naturally present

airborne microbes to settle and grow. The presence of colonies in the positive control confirmed that the test environment was suitable for microbial growth, and that if the cream had been contaminated, similar growth would have appeared in the test plates as well. The absence of growth in both the cream sample and the negative control, along with the expected growth in the positive control, as depicted in Figure 6.5 (a–e), provides strong evidence that the cream formulation was free from microbial load. These results reflect good manufacturing practices and reinforce the safety and quality of the product, making it suitable for topical application.

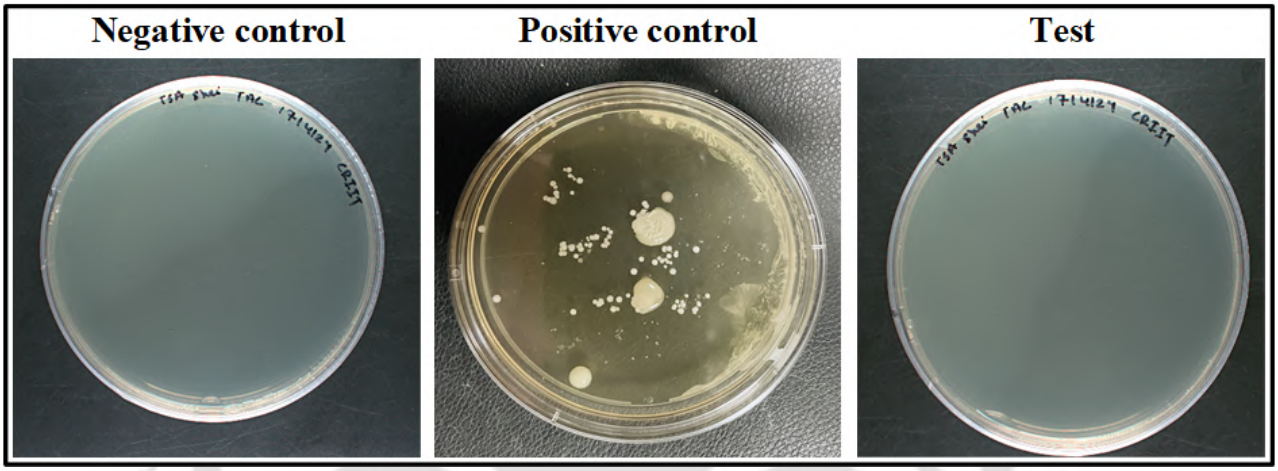

Figure 6.5 (a) Soyabean casein agar for determination of different bacterial colonies.

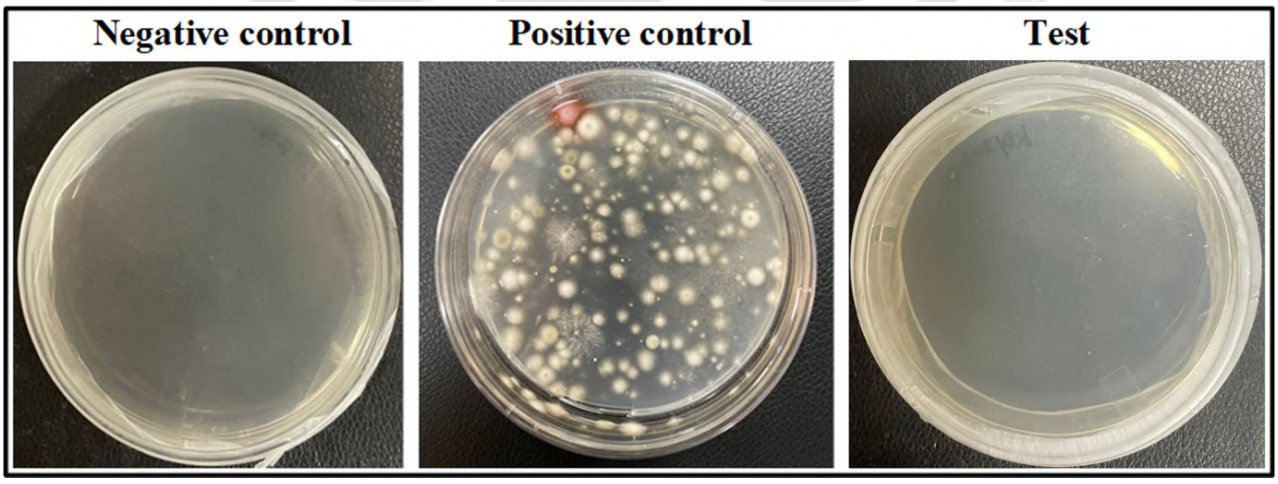

Figure 6.5 (b) Potato dextrose agar for determination of fungal colonies.

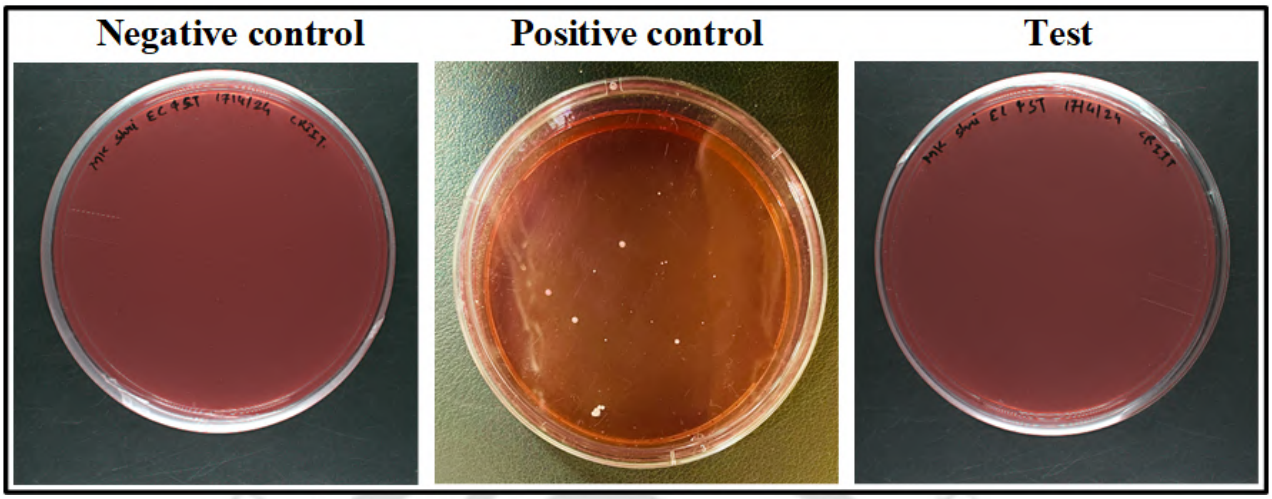

Figure 6.5 (c) MacConkey agar for determination of *Escherichia coli* (pink coloured colonies) and *Salmonella spp.* (colourless or pale colonies).

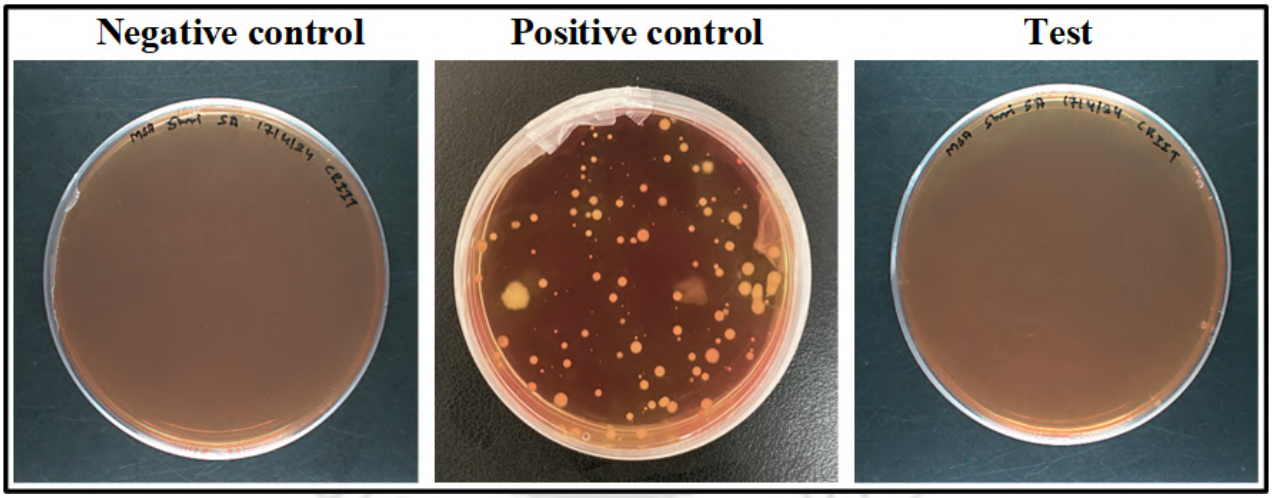

Figure 6.5 (d) Mannitol salt agar for determination of *Staphylococcus aureus* (yellow coloured colonies).

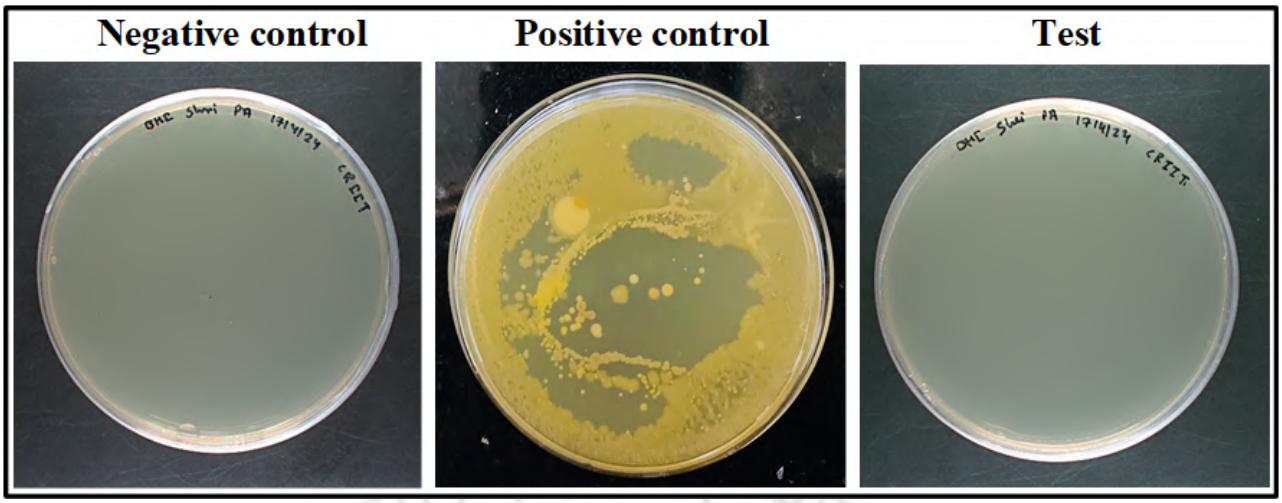

Figure 6.5 (e) Brain heart infusion agar for determination of *Pseudomonas aeruginosa* (green or yellowish-green coloured colonies).

The microbial parameters along with their corresponding results have been represented in Table 6.1.

Table 6.1 Summary of microbial load in the cream.

Sr. No.	Parameters	Result
1	Total Viable Count	0 CFU/g
2	Total Fungal Count	0 CFU/g
3	*Escherichia coli*	Absent
4	*Staphylococcus aureus*	Absent
5	*Pseudomonas aeruginosa*	Absent
6	*Salmonella sp.*	Absent

6.2.6 Antibacterial property of TBLE and the formulated cream

The antibacterial activity of TBLE and the prepared TBLE-infused cream formulation was determined using the disc diffusion method, with the zones of inhibition shown by dotted circles in Figure 6.6 (a, b). The TBLE alone exhibited activity against both *S. aureus* and *E. coli*, producing inhibition zones of 11.51 ± 0.92 mm and 10.45 ± 0.50 mm, respectively (Figure 6.6 (a)). Incorporation into a cream formulation relatively enhanced the antibacterial effect against both *S. aureus* (16.67 ± 0.40 mm), and *E. coli* (14.83 ± 0.12 mm), as depicted in Figure 6.6 (b).

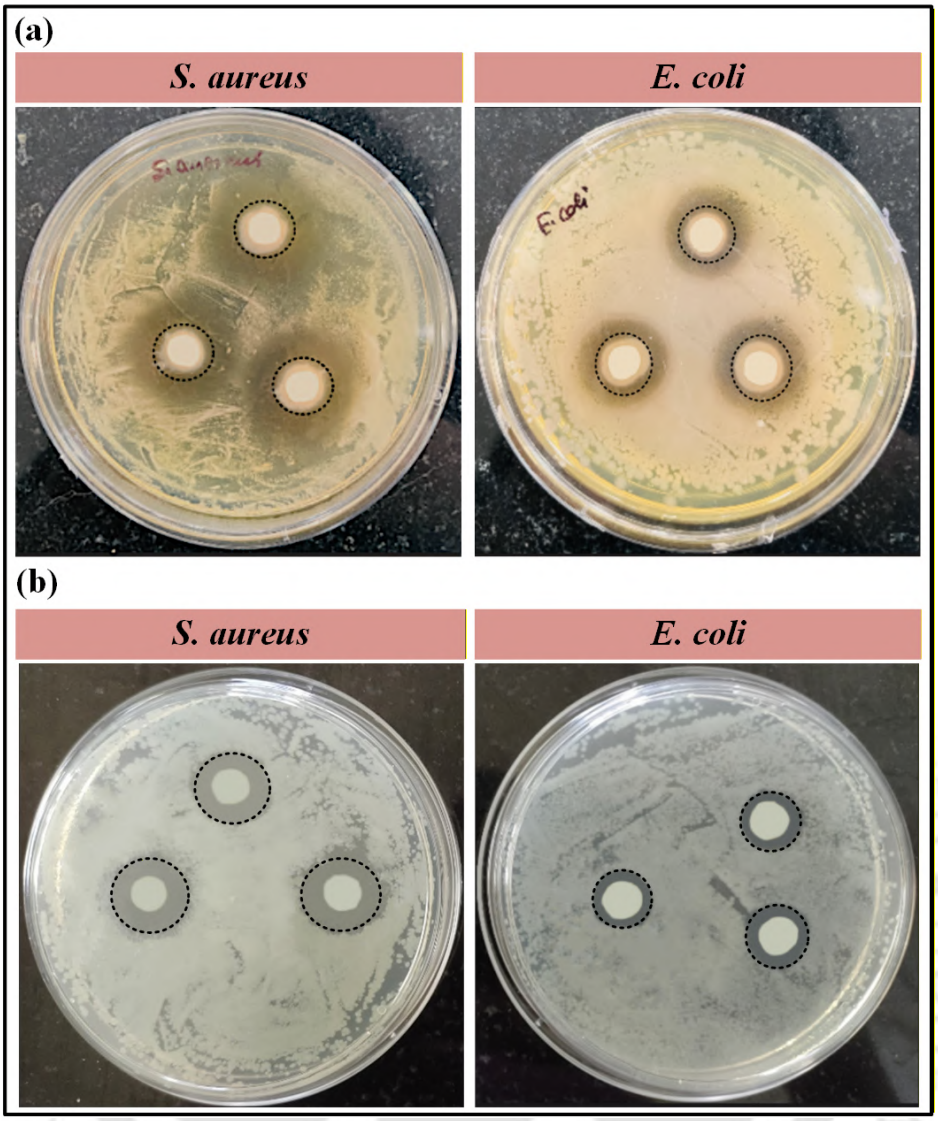

Figure 6.6 Antibacterial activity of **(a)** TBLE and **(b)** the cream formulation, against *S. aureus* and *E. coli.*

Moreover, the differences in the zones of inhibition between TBLE and the cream were statistically significant ($p < 0.05$) against both *S. aureus* and *E. coli*, as shown in Table 6.2. This enhancement may be attributed to the cream matrix improving solubility, stability, and diffusion of bioactive constituents present in the TBLE, thereby increasing the overall antibacterial efficacy of the cream. Importantly, the antibacterial activity of the cream formulation was solely due to the incorporation of TBLE, as the base cream alone did not exhibit any inhibition zones. However, the excipients in the formulation supported the action of TBLE by facilitating better delivery and potency, resulting in a relatively stronger antibacterial effect compared to TBLE alone. Excipients such as propylene glycol and glycerol likely facilitated greater diffusion or solubilisation [517], while EDTA, despite lacking intrinsic

antibacterial activity at the tested concentration in the cream formulation, may have indirectly enhanced bacterial susceptibility through chelation [518]. Furthermore, ZnO and phenoxyethanol, though inactive in the base cream alone, are known antimicrobials and may have synergistically contributed to enhanced antibacterial activity of the TBLE-infused cream [519–521]. However, the relatively lower antibacterial property observed against *E. coli* can be explained by the structural barrier of its outer membrane, which restricts the penetration of antimicrobial agents [522].

Table 6.2 Zones of inhibition showing antibacterial activity of TBLE and the cream formulation.

Samples	Zone of Inhibition (mm)	
	S. aureus	***E. coli***
TBLE	11.51 ± 0.92^{a}	10.45 ± 0.50^{a}
Cream formulation	16.67 ± 0.40^{b}	14.83 ± 0.12^{b}

Results are represented as mean ± SD, N = 3. Different letters in the superscript represent statistically significant ($p < 0.05$) differences and the same letters represent statistically non-significant ($p > 0.05$) differences for each column.

6.2.7 In vitro cytotoxicity analysis (MTT assay) of TBLE and the formulated cream

The viability of human dermal fibroblast (HDF) cells in the presence of TBLE was tested at concentrations ranging from 0.005–0.05 mg/mL over incubation periods of 24, 48, and 72 hrs (Figure 6.7 (a)). According to ISO 10993-5:2009 standards, cell viability above 75 % indicates a non-cytotoxic material [434–437]. As depicted in Figure 6.7 (a), a mild decrease in cell viability with increasing TBLE concentration and exposure time was observed. Notably, the reduction in relative cell viability was statistically non-significant ($p > 0.05$) in the control (0 mg/mL), whereas it was statistically significant ($p < 0.05$) at all tested extract concentrations over the incubation periods of 24, 48, and 72 hours. This slight reduction may be attributed to the dose- and time-dependent cellular response to phytochemicals (flavonoids, phenolics, and saponins) present in the extract. While these compounds contribute to antioxidant and antibacterial properties at lower concentrations, their higher concentrations or prolonged exposure may lead to mild cellular stress. Consequently, such effects may slightly reduce mitochondrial activity (measured by MTT), even without inducing actual cytotoxicity or

apoptosis. This is in line with reported literature where cell viability reduced with increasing concentrations of bioactive extracts [523,524]. In the present study, the extract maintained 77.20 ± 0.89 % cell viability at 0.03 mg/mL concentration, even after 72 hrs of incubation.

Additionally, as depicted in Figure 6.7 (b), the MTT assay of the formulated cream containing 0.5 % w/w of the TBLE demonstrated a dose- and time-dependent reduction in HDF cell viability over 24, 48, and 72 hrs. Although the cream is composed entirely of non-toxic ingredients and the extract itself has been previously reported as non-cytotoxic, a gradual decrease in cell viability was observed with increasing cream concentrations (from 0.1–3 mg/mL) and longer exposure durations. In the control (0 mg/mL), the reduction in cell viability was statistically non-significant ($p > 0.05$), whereas, all the tested cream concentrations exhibited statistically significant ($p < 0.05$) reduction in cell viability over the incubation period of 24, 48 and 72 hrs. This reduction in viability may be attributed to the cumulative cellular stress at higher doses and prolonged exposure, which can interfere with metabolic activity without necessarily indicating true cytotoxicity. This may also be attributed to the fact that cream formulations, especially those containing oils, emulsifiers, and thickeners, can introduce turbidity or physical interference in cell culture systems. This turbidity may hinder the proper uptake or metabolism of the MTT reagent, leading to an underestimation of viable cells. This is in line with reported literature where topical formulations demonstrated reduced cell viability at higher concentrations [523,525]. However, in the present study, the cell viability remained above 75 % even after 72 hrs of incubation, for concentrations up to 1 mg/mL, confirming the overall safety of the formulation at and above expected real-use concentrations. Since the cream formulation is prepared as a ready-to-use emulsion with standardized ingredient levels, end users are not required to dilute or measure concentrations. The amount of cream typically applied during routine usage is significantly lower than the test concentrations used for the *in vitro* MTT assay, ensuring that consumer exposure remains within the safe, non-cytotoxic range.

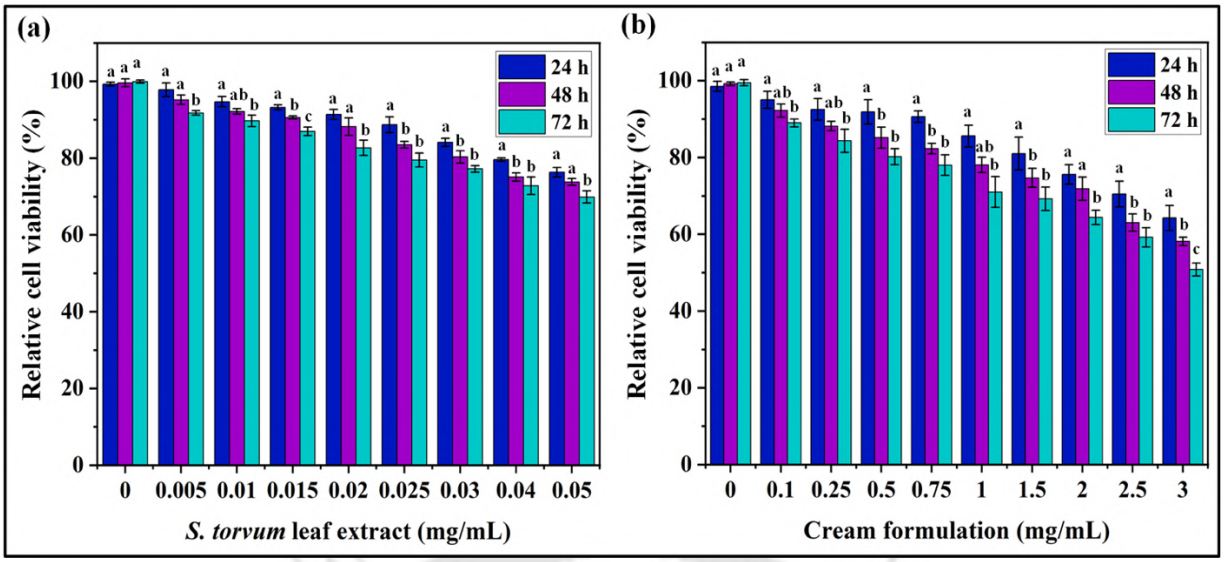

Figure 6.7 Relative viability percentage of HDF cells in presence of different concentrations of **(a)** TBLE and **(b)** the formulated cream, over a period of 24, 48 and 72 hrs. Results are represented as mean ± SD, N = 3. Different letters in the superscript represent statistically significant ($p < 0.05$) differences and the same letters represent statistically non-significant ($p > 0.05$) differences for each column.

6.3 Summary

This study demonstrated the formulation of a skin-friendly antibacterial cream using pullulan and *S. torvum* leaf extract, highlighting how the combination of a bioactive plant leaf extract with a biopolymer can be formulated into a cosmetic skincare product. The formulated cream exhibited a stable texture, maintained a skin-friendly pH of 6.10 ± 0.20, and was confirmed to be free from harmful heavy metals, arsenic, or microbial contamination, ensuring its safety for topical use. It also demonstrated a total fatty matter (TFM) of 8.5 %, moisture content of 65 %, and shear-thinning behaviour, which are within acceptable ranges for topical skincare formulations. The incorporation of *S. torvum* leaf extract (TBLE) contributed to its antibacterial property, effectively protecting against common pathogens such as *S. aureus* and *E. coli*. Pullulan further enhanced the formulation by providing moisturizing and film-forming properties, which would support skin hydration and prolonged activity of the extract. Additionally, *in vitro* cytotoxicity analysis conducted on HDF cells confirmed the non-cytotoxic nature of the cream formulation. Thus, the prepared cream formulation provides a safer alternative by avoiding commonly used preservatives such as parabens, triclosan, and formaldehyde-releasing compounds, which are often incorporated in many conventional topical formulations.

CHAPTER 7

PREPARATION OF CHITOSAN NANOPARTICLES AND NEEM ESSENTIAL OIL-FUNCTIONALIZED PULLULAN/GUM ARABIC BIOCOMPOSITES FOR EDIBLE FOOD PACKAGING

Motivation

The growing demand for sustainable and safe food packaging has intensified the search for biodegradable, edible materials that can effectively extend shelf life while minimizing environmental impact. However, many natural biopolymers suffer from poor mechanical strength, high water sensitivity, and limited barrier properties, restricting their real-world applicability. This research was motivated by the need to overcome these limitations through the strategic integration of chitosan nanoparticles (NCS) and neem essential oil (NEO) into a pullulan/gum arabic matrix. By enhancing its packaging-related characteristics, this work aims to develop an eco-friendly biocomposite film with improved hydrophobicity, mechanical strength, and antimicrobial activity to enhance the shelf-life of fresh-cut fruits.

The work in the chapter has received the scientific recognition as follows:

Das, K., *Sharma, S., Kumar, S., Mahajan, S., Banerjee, S.K. and Katiyar, V., 2024. Chitosan nanoparticles and neem essential oil functionalized pullulan/gum arabic active edible biocomposites for fresh-cut guava preservation. International Journal of Biological Macromolecules, 283, p.136936.*

Abstract

This study presents the development of active edible biocomposite films based on pullulan (PUL) and gum arabic (GA), incorporating chitosan nanoparticles (NCS) and neem essential oil (NEO). The formulation aimed to address the limitations of conventional biopolymer-based packaging, particularly high hydrophilicity and poor barrier properties. To achieve this, the effects of different NCS concentrations (1 %, 2 %, and 3 %) were systematically investigated, while PUL, GA, and NEO concentrations maintaining constant. Among the formulations studied, the biocomposite containing 3 % NCS and 1 % NEO (PUL/GA/NCS3/NEO) exhibited the most significant enhancements in physicochemical and functional properties. The incorporation of NCS and NEO effectively modified the surface characteristics of the film, transitioning it from hydrophilic (water contact angle: 55.49 ± 2.31°) to hydrophobic (115.01 ± 1.86°). Additionally, tensile strength increased by ~ 12.77 MPa, elongation at break by ~ 6.26 %, thermal stability (T_{offset}) by ~ 22.49 °C, and water vapour barrier by ~ 45.95 %, alongside enhanced UV-shielding, antimicrobial and antioxidant properties. Energy-dispersive X-ray (EDX) spectroscopy confirmed the elemental composition of the biocomposite, with 55.7 % carbon (C), 3.6 % nitrogen (N), and 40.8 % oxygen (O), ensuring the safety of the material. To assess biocompatibility, *in vitro* cytotoxicity studies were conducted on human embryonic kidney (HEK-293) cells. The results indicated excellent biocompatibility, with a cell viability of 86.82 ± 2.28 % after 72 hrs of exposure, affirming the non-cytotoxic nature of the biocomposite. The practical utility of the PUL/GA/NCS3/NEO biocomposite was further evaluated by applying it as an edible coating for extending shelf-life of fresh-cut guava. The coated guava samples exhibited prolonged shelf-life and superior storage quality compared to uncoated samples. The edible coating effectively preserved essential parameters such as colour, firmness, and weight retention, while significantly reducing microbial spoilage. Moreover, the antioxidant activity of the coated guava remained higher throughout storage, under both ambient and refrigerated conditions, demonstrating the potential of PUL/GA/NCS3/NEO as a sustainable edible coating material.

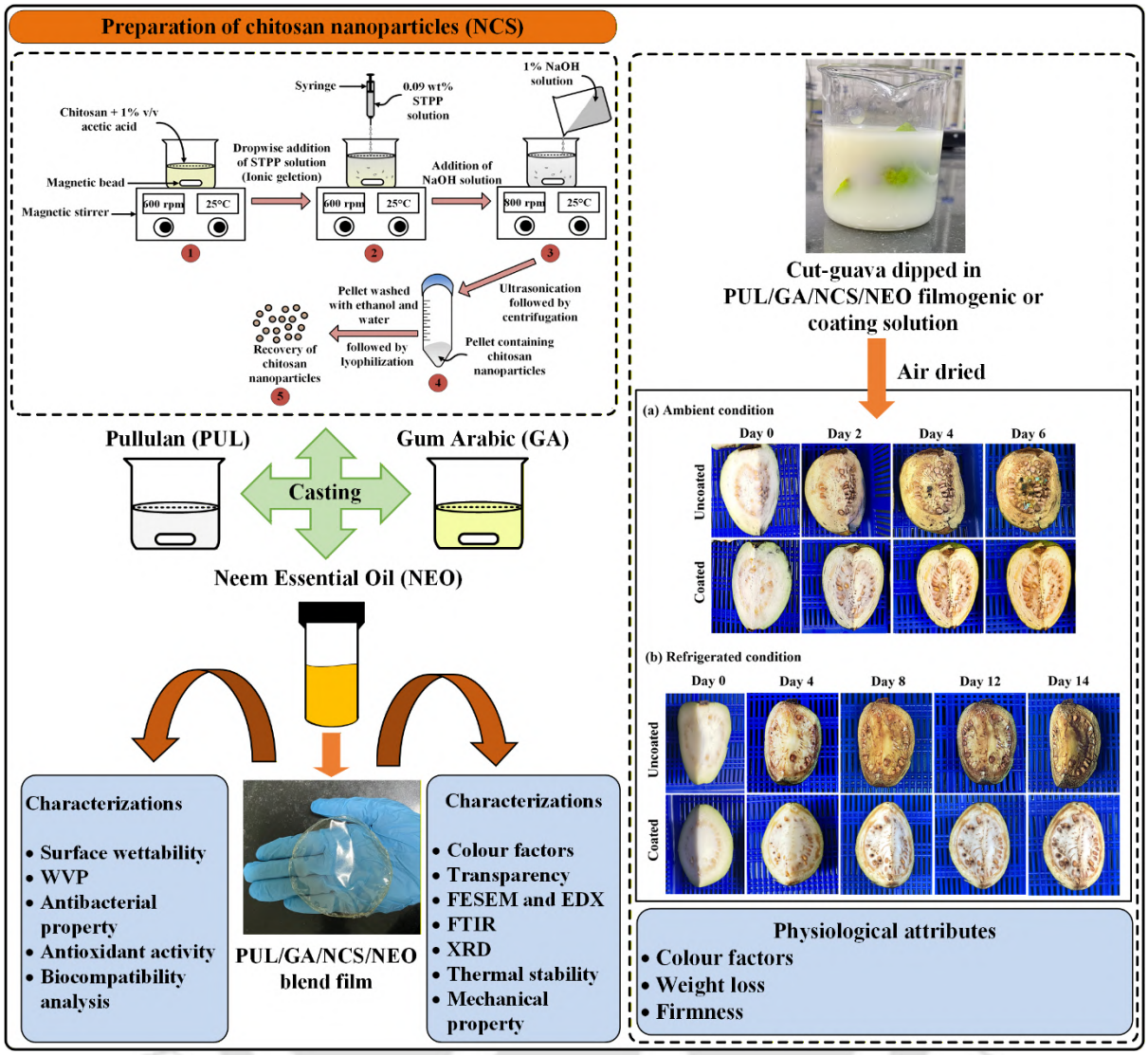

Figure 7.1 Scheme of Chapter 7.

7.1 Introduction

The need for sustainable food packaging to extend the shelf-life of fruits and vegetables has increased in recent years, driven by the demand for fresh products and reduced food waste. Active biodegradable edible packaging offers a solution by enhancing food safety and quality while addressing environmental concerns from conventional non-biodegradable materials [526,527]. Generally, such active packaging systems include antioxidants, antimicrobial agents, and possess other beneficial characteristics such as UV-shielding capability, which are absent in conventional packaging. Researchers are now developing active edible packaging from biodegradable biopolymers and natural resources, preparing active edible films and coating solutions that extend shelf-life of fresh produce, owing to their biodegradability, safety, and bioactive properties.

Pullulan (PUL) is a water-soluble exopolysaccharide derived from the fungus *Aureobasidium pullulans* (*A. pullulans*), widely used in food packaging due to its biodegradability and film-forming property. PUL-based films are transparent, tasteless, colourless, odourless, heat-sealable and possess excellent impermeability to oil and oxygen, making them suitable for food packaging [528]. Despite these advantages, there are certain limitations associated with pure PUL-based films such as hydrophilicity and high production costs [529]. To overcome these limitations and enhance its packaging-related property, different crosslinking agents or plasticizers such as propylene glycol, sorbitol, glycerol, etc could be used. Another effective strategy involves blending PUL with other polymers or proteins to prepare composite films with enhanced properties. PUL has been blended with several other polymers such as alginate [530], gellan gum [238], cassava starch [314], polyvinyl alcohol [531,532], pectin [246], chitosan [533,534], carboxymethylcellulose [535], etc. for use in various food-grade applications.

Gum Arabic (GA) is another biodegradable polymer that is obtained from *Acacia senegal* and *Acacia seyal*. It is composed of glucuronic acid, galactose, arabinose, rhamnose, and proteins [536]. It finds widespread applications in the food sector owing to its binding, thickening, stabilizing, and film-forming properties. It is also frequently utilized as an emulsifier in the food industry, as GA forms an interfacial membrane around emulsion droplets when absorbed, contributing to the stabilization of the emulsion [537]. These attributes make it an useful ingredient in various food products like ice creams, beverages, jellies, candies, chewing gums, syrups and soft drinks. Additionally, it is used as edible coating material to enhance the shelf-life of food items [538,539].

Chitosan (CS), a cationic biopolymer derived from deacetylated chitin, consists of β (1–4)-2-amino-2-deoxy d-glucopyranose units. It is biodegradable, non-toxic, biocompatible, and has antioxidant, antimicrobial, and film-forming properties, along with low oxygen permeability and strong mechanical properties, making it suitable for food packaging [540,541]. When processed into chitosan nanoparticles (NCS), it has increased surface area and enhanced properties, exhibiting higher antioxidant and antimicrobial properties compared to CS, thus protecting packaged foods from microbial spoilage [542]. It has been used in edible coatings for various foods like apple [543], mandarin [544], etc. Additionally, its combination with essential oils in edible coatings further enhances the firmness of food products [545,546].

Food spoilage caused by microorganisms is one of the major reasons of food deterioration and wastage. Essential oils, known for their antibacterial, antifungal, and insecticidal properties, are extracted via solvent extraction or steam distillation and are

considered environmentally safe [545]. Neem essential oil (NEO), extracted from *Azadirachta indica*, contains phytochemicals like nimbidin, nimbin, nimbolide, azadirachtin, gedunin, salannin, margolone, margolonone and isomargolonone; providing antimicrobial, antioxidant, plasticizing, and insecticidal properties [547]. Inclusion of NEO to the composite films enhances their antimicrobial activity, preventing food spoilage, extending shelf life, and delaying oxidative deterioration, preserving the nutritional value of packaged foods.

Previous studies have reported improved mechanical properties of PUL films with incorporation of active substances [531,533]. On the other hand, GA has been shown to improve essential oil retention and facilitate the stabilization of emulsions in edible coating formulations [537]. Additionally, inclusion of NCS in edible films can effectively promote the retention and controlled release of essential oils, thereby resulting in enhanced antimicrobial efficacy [548]. Furthermore, NEO, well-known for its antimicrobial and antioxidant properties, has been widely explored for preparation of edible films and coatings, but not extensively combined with PUL in the studies reported. While the effectiveness of the individual components have been well-documented in the literature for different food packaging applications, the novelty of this work lies in the unique combination of these components. To the best of the authors' knowledge, no prior studies have explored the synergistic use of PUL, GA, NCS and NEO, particularly for the preservation of fresh-cut guava.

Based on these findings, we prepared NCS from CS using the ionotropic gelation method, and developed a novel active edible PUL/GA biocomposite functionalized with NCS and NEO. The prepared biocomposites were characterized for their mechanical, optical, thermal, antimicrobial and antioxidant properties, and *in vitro* biocompatibility. The study aimed to address the issues of high hydrophilicity and poor water vapour barrier properties related with PUL-based biocomposites. Additionally, it emphasized on the efficacy of the prepared filmogenic or coating solution in shelf-life enhancement of fresh-cut guava.

7.2 Results and discussion

7.2.1 Characterization of NCS

The preparation of NCS by the ionic gelation technique using STPP as the cross-linking agent is shown in Figure 7.2 (a). The chemical structure of CS and STPP contain the cationic amino and the anionic phosphate groups, respectively, which interact to form intermolecular and intramolecular bonds, thereby reducing the overall size of CS. The average particle size of the prepared NCS, as depicted by FETEM image (Figure 7.2 (b)), was found to be 46 ± 6 nm.

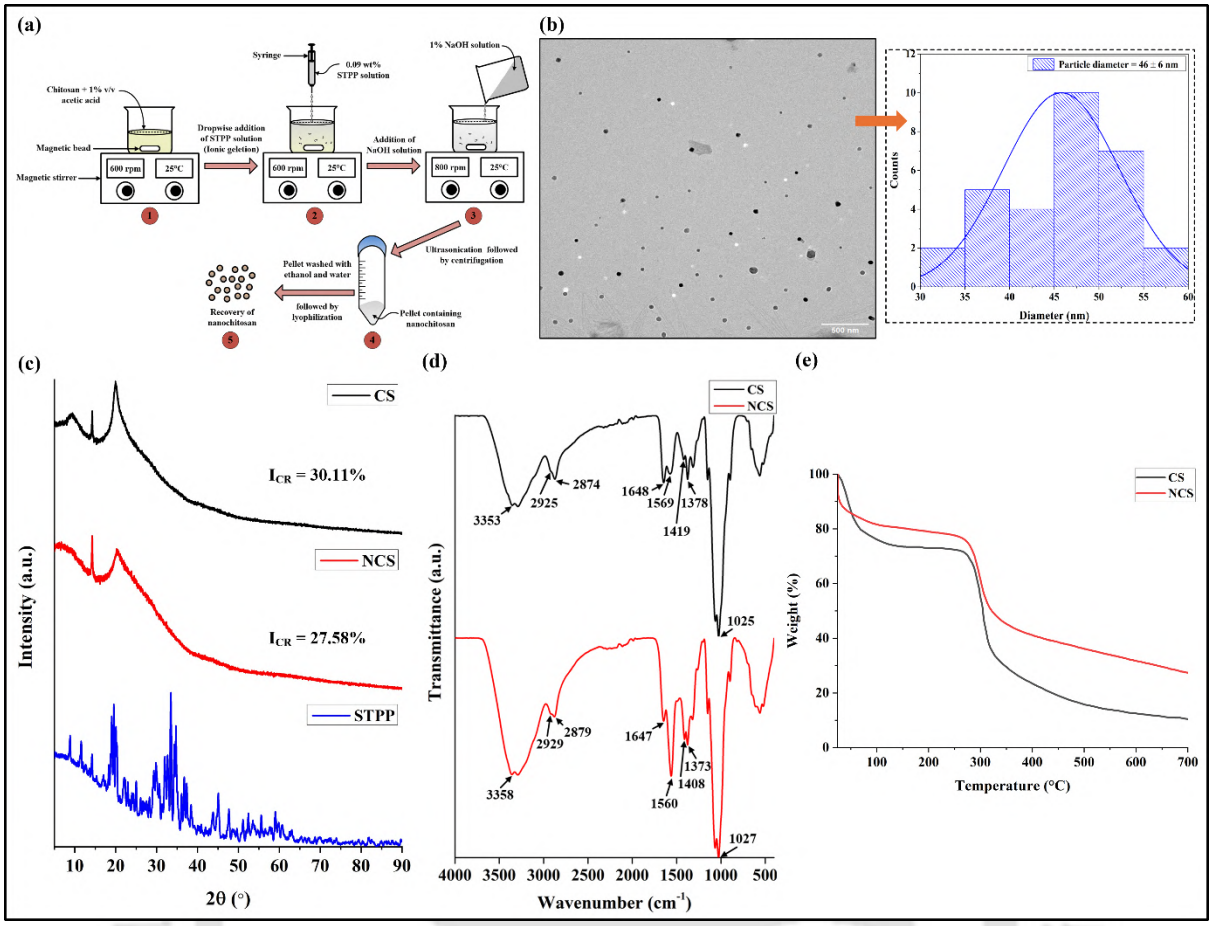

Figure 7.2 (a) Overview of preparation process of NCS, **(b)** TEM image and particle size distribution of prepared NCS, **(c)** XRD pattern of CS, NCS and STPP, **(d)** FTIR spectra of CS and NCS, and **(e)** TGA curves of CS and NCS.

As shown in Figure 7.2 (c), the XRD pattern of CS depicts three characteristic peaks at 2θ values of 9.28°, 14.22° and 20°. Interestingly, a reduced crystallinity was observed in case of NCS (I_{CR} = 27.58 %) as compared to CS (I_{CR} = 30.11 %), which may be attributed to the cross-linking formed between CS and STPP upon formation of NCS. This further confirms the presence of a dense structural network formed within the oppositely charged CS and STPP. The decreased crystallinity of the prepared NCS has certain advantages such as increased surface area, which facilitates faster rate of dissolution, enhanced physical, chemical and dimensional stability, and increased exposure to bioactive components.

The FTIR analysis of CS and NCS was conducted to determine their functional groups (Figure 7.2 (d)). As observed in the FTIR spectrum of CS, peaks at 1569 and 1648 cm^{-1} correspond to –NH bending in the secondary amides, and –C=O stretching in the primary amides, respectively. Furthermore, the peak observed at 3353 cm^{-1} correspond to –NH_2 and –OH stretching in CS [312]. Peaks at 2925 and 2874 cm^{-1} are attributed to –CH symmetric

stretching and –CH asymmetric stretching, respectively [549]. Peaks at 1419 and 1378 cm^{-1} correspond to the –NH stretching in amide bonds and the –NH stretching of the amide III band [254]. Additionally, the peak at 1025 cm^{-1} is attributed to the –CO based IR-band [550]. In the case of NCS, there is a shift in peaks to 1647 and 1560 cm^{-1} from 1648 and 1569 cm^{-1} (in CS), which is attributed to the interaction between the cationic group in CS and the phosphate group in STPP. The FTIR peak at 3353 cm^{-1} in CS shifts to 3358 cm^{-1} in NCS and become more sharpened due to increased hydrogen bonding.

The TGA curves of NCS and CS depict the weight loss due to thermal treatment between 28 to 700 °C, as shown in Figure 7.2 (e). Two steps of degradation were observed for the prepared NCS. The first step of degradation could be attributed to the loss of moisture content. The second step of degradation corresponds to the actual thermal degradation of the prepared NCS. The first and the second steps of degradation were observed within the temperature ranges of 45 to 150 °C and 240 to 385 °C, respectively. It was observed that the NCS retained significantly higher percentage of its initial weight (~ 27.35 %) at 700 °C, as compared to CS (~ 10.46 %) , which is in line with reported literature [312,551,552].

7.2.2 Characterization of the biocomposites

7.2.2.1 Optical properties

The optical properties of PUL-based biocomposites were analyzed based on their transparency and colour factors, as many foods are light-sensitive, especially to Ultraviolet-Visible (UV-Vis) light. As depicted in the visual images (Figure 7.3 (a)), all the biocomposite films possess a uniform transparent or translucent appearance. The film transparency depends on molecular weight, dispersion, homogeneity and use of plasticizers. The neat PUL film had the highest transparency and a white transparent appearance, while the inclusion of GA added a yellowish colour and reduced transparency. Interestingly, the inclusion of NCS enhanced the transparency (Figure 7.3 (b)), which increased with increase in NCS concentrations (PUL/GA/NCS3> PUL/GA/NCS2> PUL/GA/NCS1 and PUL/GA/NCS3/NEO> PUL/GA/NCS2/NEO> PUL/GA/NCS1/NEO). The enhancement of transparency due to inclusion of NCS may be attributed to its enhanced compatibility and distribution within the biocomposite matrix. This is in line with reported literature where NCS enhanced film transparency [312].

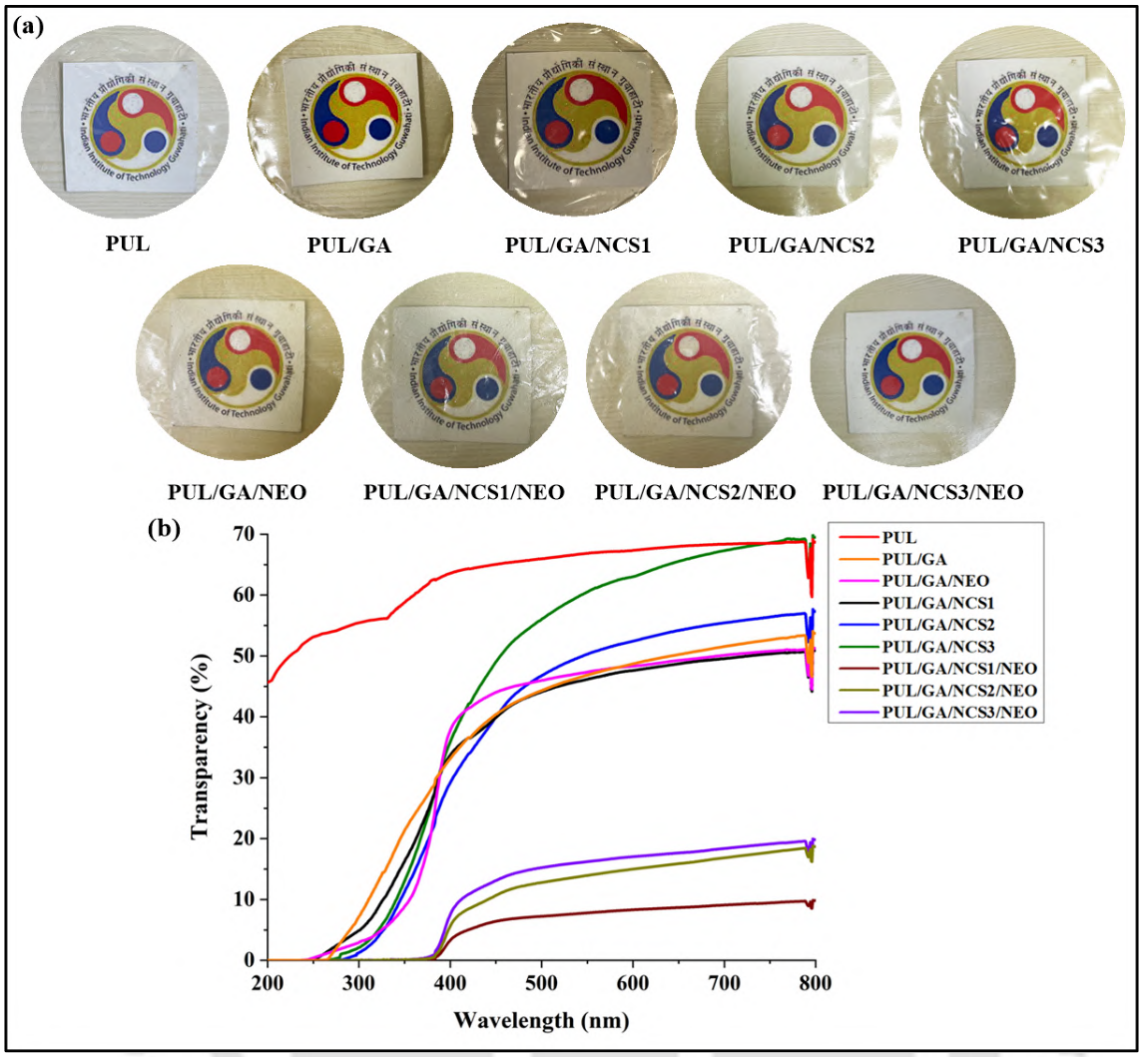

Figure 7.3 (a) Visual images and **(b)** UV-Vis light transparency of the prepared films.

Additionally, the NEO-containing biocomposites were found to exhibit significant reduction in the transmittance values and hence reduced transparency in comparison to those without NEO. This is comparable to reported literature where inclusion of essential oils reduced film transparency [553–555]. The reduction in transparency of the biocomposites in turn corresponds to their enhanced UV-shielding property, and vice-versa. Thus, the NEO-containing biocomposites PUL/GA/NCS1/NEO, PUL/GA/NCS2/NEO and PUL/GA/NCS3/NEO with reduced transparency were found to exhibit effective light transmission blocking property in the UV (< 400) and the visible light (400–800) region. The neat PUL film, being the most transparent, showed no blocking property (Figure 7.3 (b)).

The optical properties of the biocomposites were further determined using the colour factors (L*, a*, b*, Chroma and hue), as shown in Table 7.1. The L* value, which is an indicative of brightness, varied from 78.80 ± 0.80 to 59.94 ± 0.77. The a* value varied from

2.33 ± 0.66 to 11.78 ± 0.31 (indicating redness), b* value ranges from 10.21 ± 0.44 to 39.31 ± 0.40 (indicating yellowness), the Chroma value varied from 10.46 ± 0.58 to 40.55 ± 0.75, and the hue angle varied from 78.78 ± 0.96 to 71.29 ± 0.54, indicating yellow colouration effect. As depicted in Table 7.1, the L* and the h values were found to be highest for the neat PUL film, which slightly reduce upon inclusion of GA and NCS (as in PUL/GA, PUL/GA/NCS1, PUL/GA/NCS2 and PUL/GA/NCS3) and further reduce in case of the NEO-containing films (as in PUL/GA/NEO, PUL/GA/NCS1/NEO, PUL/GA/NCS2/NEO and PUL/GA/NCS3/NEO).

Table 7.1 Colour factors of the prepared film samples.

Film samples	L*	a*	b*	Chroma	hue
PUL	78.80 ± 0.80^{a}	2.33 ± 0.66^{a}	10.21 ± 0.44^{a}	10.46 ± 0.58^{a}	78.78 ± 0.96^{a}
PUL/GA	73.38 ± 0.43^{b}	4.66 ± 0.59^{b}	23.48 ± 0.52^{b}	23.94 ± 0.49^{b}	77.64 ± 0.49^{a}
PUL/GA/NEO	68.81 ± 0.63^{c}	7.62 ± 0.68^{c}	34.78 ± 0.49^{c}	35.52 ± 0.76^{c}	77.19 ± 0.53^{ab}
PUL/GA/NCS1	68.12 ± 0.42^{c}	8.25 ± 0.41^{cd}	37.58 ± 0.39^{d}	38.23 ± 0.35^{e}	78.26 ± 0.49^{a}
PUL/GA/NCS1/NEO	65.95 ± 0.53^{d}	9.26 ± 0.53^{de}	38.63 ± 0.41^{de}	40.11 ± 0.39^{f}	75.46 ± 0.82^{b}
PUL/GA/NCS2	69.75 ± 0.59^{c}	8.76 ± 0.40^{cde}	38.80 ± 0.47^{de}	39.77 ± 0.54^{f}	77.29 ± 0.36^{ab}
PUL/GA/NCS2/NEO	59.94 ± 0.77^{f}	11.72 ± 0.46^{f}	34.57 ± 0.50^{c}	36.56 ± 0.41^{cd}	71.29 ± 0.54^{b}
PUL/GA/NCS3	64.49 ± 0.57^{de}	11.78 ± 0.31^{f}	35.33 ± 0.43^{c}	37.25 ± 0.35^{de}	75.70 ± 0.80^{b}
PUL/GA/NCS3/NEO	63.97 ± 0.98^{e}	10.02 ± 0.36^{e}	39.31 ± 0.40^{e}	40.55 ± 0.75^{f}	71.57 ± 0.79^{a}

Results are represented as mean ± SD, N = 3. Different letters in the superscript represent statistically significant ($p < 0.05$) differences and the same letters represent statistically non-significant ($p > 0.05$) differences for each column.

7.2.2.2 Morphological and compositional analysis

The surface morphology, fractured and overview cross-sections of the PUL, PUL/GA, PUL/GA/NEO, PUL/GA/NCS3 and PUL/GA/NCS3/NEO biocomposites were studied using FESEM, as shown in Figure 7.4 (a–e").

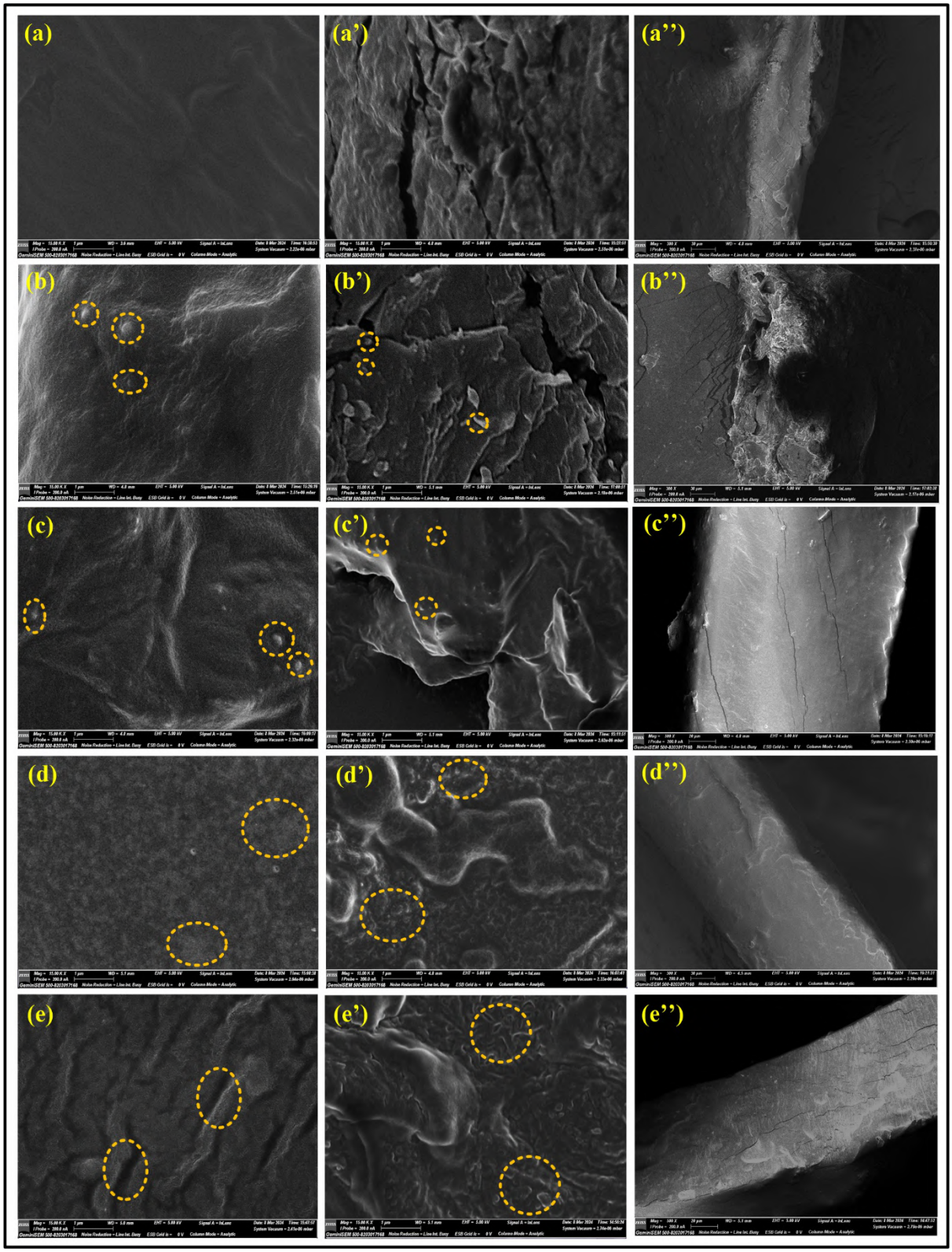
(a)
(a')
(a'')
(b)
(b')
(b'')
(c)
(c')
(c'')
(d)
(d')
(d'')
(e)
(e')
(e'')

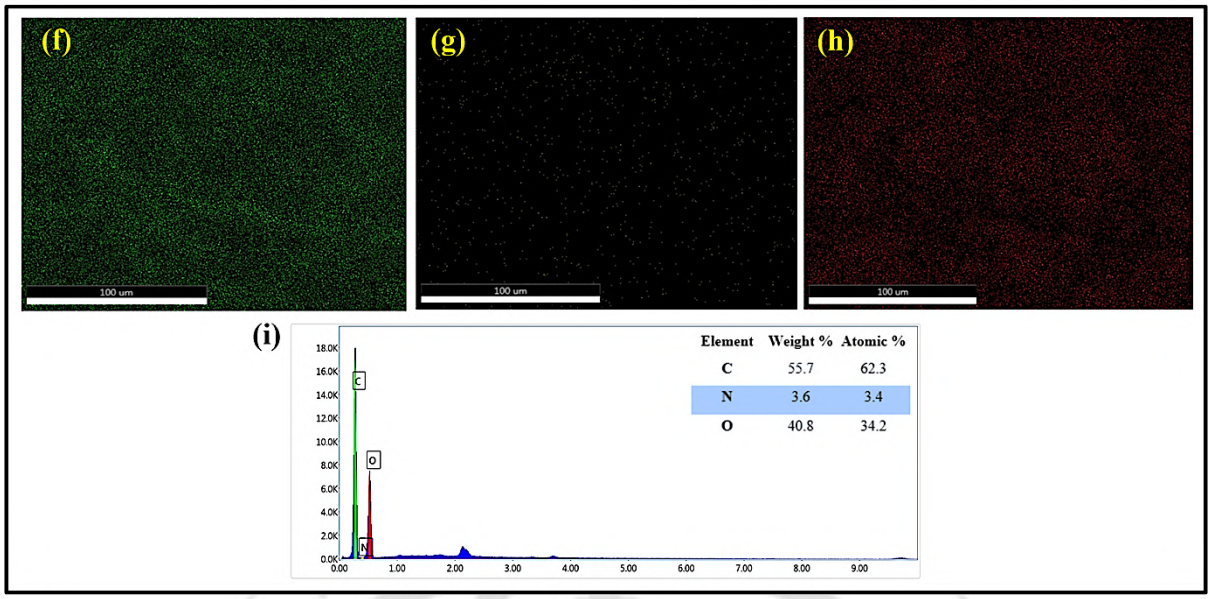

Figure 7.4 FESEM images representing surface, fractured cross-section, and cross-sectional overview of **(a–a'')** PUL, **(b–b'')** PUL/GA, **(c–c'')** PUL/GA/NEO, **(d–d'')** PUL/GA/NCS3, and **(e–e'')** PUL/GA/NCS3/NEO. Additionally, EDX analysis of PUL/GA/NCS3/NEO showing elemental mapping of **(f)** C, **(g)** N, **(h)** O, and **(i)** the corresponding spectrum with elemental weight percentages.

The characteristics of the biocomposites were mainly influenced by the interactions between the film components. The neat PUL film was found to have a smooth texture and uniform morphology, as observed in its surface (Figure 7.4 (a)) and cross-sectional FESEM image (Figure 7.4 (a')). However, the inclusion of GA resulted in appearance of small granular or spherical structures on the surface (Figure 7.4 (b)) and the fractured cross-section (Figure 7.4 (b')) of the PUL/GA biocomposite. These spherical structures (shown by dotted circles) may be attributed to the inclusion of GA, that is uniformly distributed all over the biocomposite surface. Moreover, the inclusion of NCS resulted in alteration of the morphology of GA, thereby resulting in its more uniform dispersion in the resultant biocomposite. This is evident from the surface (Figure 7.4 (d)) and the fractured cross-section (Figure 7.4 (d')) morphology of the PUL/GA/NCS3 biocomposite. Additionally, in the NEO containing biocomposites, there were appearance of wrinkled structures both in surface (Figure 7.4 (c, e)) and fractured cross-section (Figure 7.4 (c', e')) of PUL/GA/NEO and PUL/GA/NCS3/NEO, respectively. These wrinkled structures (shown by dotted circles) may be attributed to the internal phase separation caused upon inclusion of the hydrophobic NEO in the biocomposite matrix. This is in line with reported literature, where inclusion of essential oils results in wrinkled and rougher morphology of the film surface [556,557]. Furthermore, Figure 7.4 (a", b", c", d", e") represent

the cross-sectional overviews of PUL, PUL/GA, PUL/GA/NEO, PUL/GA/NCS3 and PUL/GA/NCS3/NEO, respectively.

For the compositional analysis and to determine the elemental mapping of C, N and O, the biocomposite containing the highest concentration of NCS (PUL/GA/NCS3/NEO) was selected. The EDX mapping and spectra are as shown in Figure 7.4 (f–i). Additionally, the results depict the weight percentages of C, N and O to be ~ 55.7%, ~ 3.6% and ~ 40.8%, respectively. The compositional analysis of the biocomposite revealed that there were no metallic components or other minerals present, thereby confirming the safety of materials [312,328,329]. Moreover, the uniform distribution of N further validates the presence of NCS within the biocomposite, as CS comprises of N in its amine ((1 → 4)-linked 2-amino-2-deoxy-β-D-glucan) structure.

7.2.2.3 FTIR and XRD

The chemical interactions between PUL, GA, NCS, and NEO were analyzed using FTIR (Figure 7.5 (a)), where the peaks represent the functional groups in the film samples. Peaks at 3293 cm^{-1} and 2929 cm^{-1} correspond to –OH and –CH stretching, respectively. The 1647 cm^{-1} peak indicates hydrogen bonds along with bound water, while 1416 cm^{-1} and 850 cm^{-1} are attributed to the vibrational CH_2 groups. Peaks at 1150 cm^{-1} and 1000 cm^{-1} correspond to -CO stretching in C-O-C groups of the anhydroglucose ring. These results are in line with reported literature [312,558]. Distinct FTIR peaks were observed in the PUL-based biocomposites with varying intensities, indicating some shifts in the FTIR peaks. Two additional peaks at 2855 cm^{-1} and 1744 cm^{-1} in NEO-containing biocomposites indicate aliphatic C-H and C=O stretching present in neem oil, confirming interactions between NEO and the biocomposite matrix components, as reported by Das et al. [559].

The XRD patterns of the prepared PUL-based biocomposites or films are shown in Figure 7.5 (b). Within the biocomposites, the peak at 19.74° indicates the amorphous nature of PUL, which may be due to the presence of tightly packed PUL molecules connected by hydrogen bonds [535,560]. Furthermore, in the diffraction patterns of the biocomposites, the characteristic peaks were observed with varying intensities. As observed in Figure 7.5 (b), the crystallinity index (I_{CR}) of neat PUL film was found to be 46.24 %. It is important to note that the inclusion of GA increased the crystallinity to 51.14 %. Additionally, the inclusion of NCS demonstrated effectiveness across different levels due to varying proportions of NCS in the composite materials. The I_{CR} of PUL/GA/NCS3 and PUL/GA/NCS3/NEO was found to be 55.11 % and 58.83 %, respectively; indicating significantly increased crystallinity upon

inclusion of NCS at 3 % w/v along with NEO. This enhanced crystallinity of the biocomposites is possibly due to interfacial interactions within the functional groups of the biocomposite components.

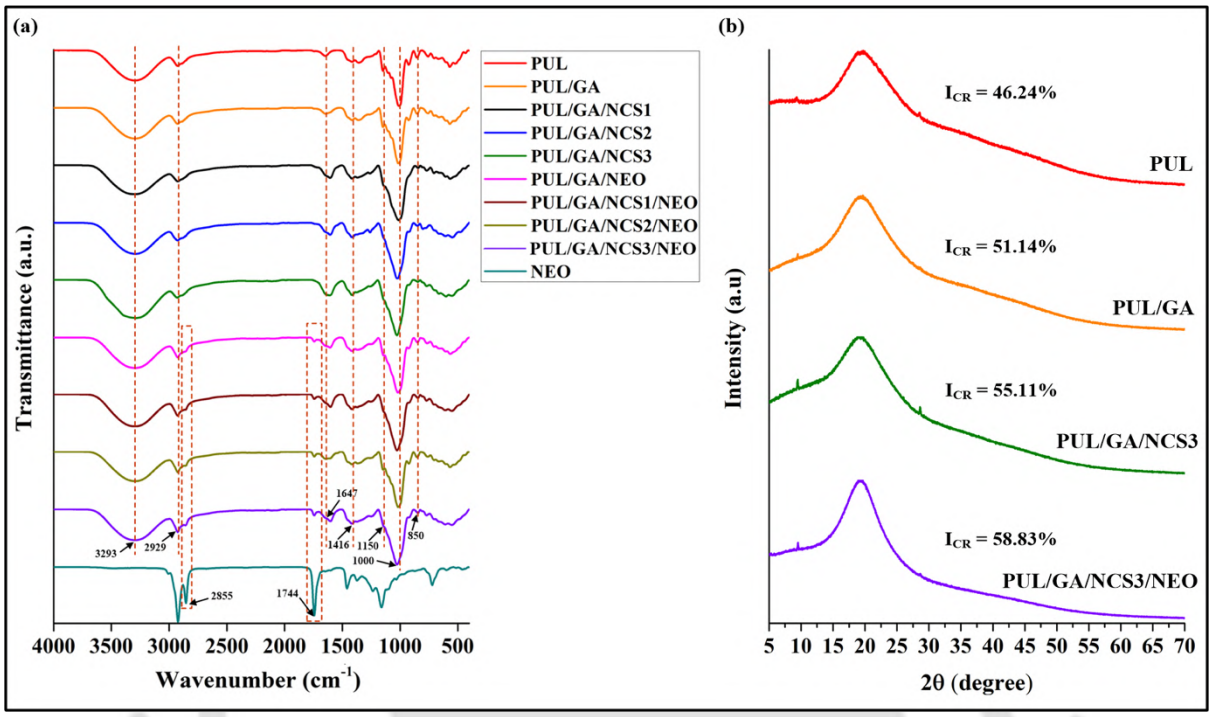

Figure 7.5 (a) FTIR spectra and **(b)** XRD patterns of the PUL film and PUL-based biocomposites.

7.2.2.4 Analysis of thermal stability

The thermal stability of the prepared films was determined using TGA, (as shown in Figure 7.6 and Table 7.2). The TGA curves of the different PUL-based biocomposites provide information about the efficacy of the GA, NCS and NEO against different temperature conditions. Different parameters such as the temperature at which 10% and 50% of the biocomposite sample had thermally degraded, indicated as T_{10} and T_{50}, respectively were determined. Additionally, the offset temperature (T_{offset}) for thermal degradation of the biocomposite was determined. The initial step of degradation ranging between 40 to 195 ºC corresponds to the loss of moisture present in the edible biocomposite samples. The final step of degradation may be attributed to the actual degradation (depolymerization and breakdown) of the components of the biocomposite matrix. As observed in Table 7.2, the neat PUL film has the highest T_{10} value (201.81 ºC), but the lowest T_{50} (291.48 ºC) and T_{offset} (318.78 ºC) values as compared to the other film samples. This may be attributed to the rapid mass loss or

highest degradation rate (least difference between T_{10} and T_{50}) of the neat PUL film, thus corresponding to its least thermal stability.

Table 7.2 Thermal degradation of the prepared film samples.

Film samples	T_{10} (ºC)	T_{50} (ºC)	T_{offset} (ºC)	W_{res} (%)
PUL	201.81	291.48	318.78	16.96
PUL/GA	141.56	300.73	347.87	13.68
PUL/GA/NEO	145.41	302.16	336.18	17.32
PUL/GA/NCS1	148.34	303.77	339.78	17.57
PUL/GA/NCS1/NEO	131.83	298.73	331.23	15.55
PUL/GA/NCS2	134.91	301.30	333.93	18.78
PUL/GA/NCS2/NEO	176.65	299.34	341.42	12.16
PUL/GA/NCS3	168.12	303.53	329.73	21.43
PUL/GA/NCS3/NEO	132.47	301.76	341.27	17.78

Moreover, the observed T_{50} values of the biocomposites PUL/GA, PUL/GA/NEO, PUL/GA/NCS1, PUL/GA/NCS1/NEO, PUL/GA/NCS2, PUL/GA/NCS2/NEO, PUL/GA/NCS3 and PUL/GA/NCS3/NEO, were found to be ~ 300.73, ~ 302.16, ~ 303.77, ~ 298.73, ~ 301.30, ~ 299.34, ~ 303.53 and ~ 301.76 ºC, respectively (Table 7.2). Thus, the incorporation of GA in the PUL-based biocomposite enhanced its thermal stability by ~ 9.25 ºC, considering the T_{50} values of the biocomposites. Similarly, the incorporation of NCS in proportions of 1% (NCS1), 2% (NCS2), 3% (NCS3) in the biocomposites significantly enhanced the thermal stability by ~ 12.29, ~ 9.82 and ~ 12.05 ºC, respectively. Moreover, the T_{offset} value of the PUL/GA/NCS3/NEO biocomposite increased by ~ 22.49 °C compared to the neat PUL film, indicating enhanced thermal stability. This is in line with reported literature where incorporation of NCS enhanced the thermal stability of biocomposites [312]. Additionally, the NEO containing films also exhibited higher T_{50} and T_{offset} values than neat PUL film, hence suggesting improvement in thermal stability. The T_{offset} values of the prepared films indicate the enhanced thermal stability of the PUL-based biocomposites upon incorporation of GA, NCS and NEO. The enhanced thermal stability may be attributed to the

effective interactions between the PUL, GA, NCS and NEO. The T_{10}, T_{50}, T_{offset} values and the weight residue (W_{res}) % of the prepared film samples are shown in Table 7.2.

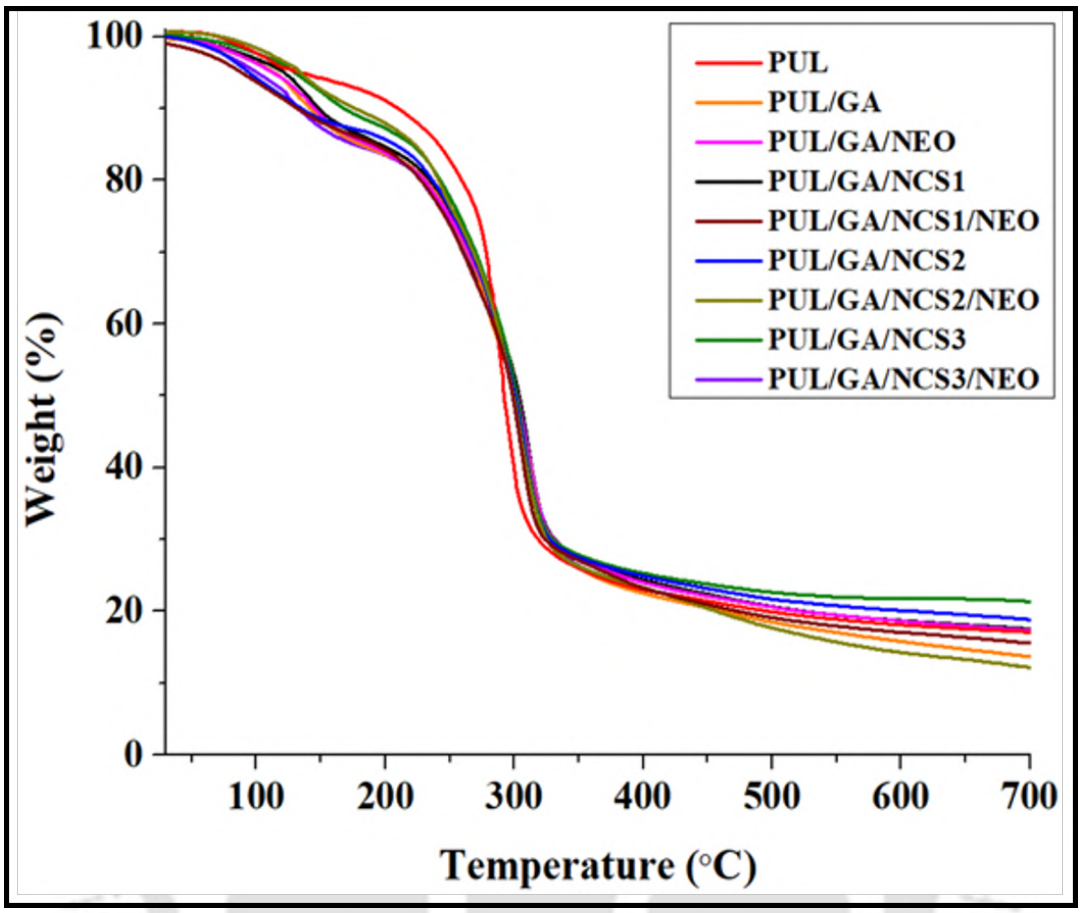

Figure 7.6 TGA curves of the PUL film and PUL-based biocomposites.

7.2.2.5 Mechanical properties

The tensile strength and the elongation at break of the composite films have been depicted in Figure 7.7 (a, b). The neat PUL film demonstrated the lowest tensile strength (54.73 ± 1.63 MPa) and elongation at break (12.48 ± 0.96 %), which is comparable to that reported in literature [561,562]. However, incorporation of GA in the PUL/GA biocomposite, increased the tensile strength and the elongation at break to 56.14 ± 3.21 MPa and 14.14 ± 2.49 %, respectively. It is noteworthy, that the films containing NEO showed higher tensile strength and elongation at break compared to those without NEO. Interestingly, in the PUL/GA/NCS2/NEO biocomposite, the incorporation of NEO did not have significant effect on the elongation at break. The increased tensile strength and elongation at break with NEO incorporation could be related to its plasticizing effect, improving flexibility and reducing brittleness [563]. The increased tensile strength upon NEO incorporation may be attributed to the chemical interaction between bioactive groups in NEO and the polymer functional groups

in the PUL-based biocomposite matrix, as described earlier in the FTIR spectrum (Figure 7.5 (a)). Moreover, many other studies have reported that the inclusion of essential oils enhanced the overall mechanical properties of the film, which is a very important criteria for its use as packaging material [564]. According to Romani et al. [565], polyphenols present in essential oil have a tendency to make hydrogen bonds with hydroxyls present in the carbohydrate polymer, thereby increasing the interfacial interaction between essential oil and the carbohydrate polymer, which in turn increases the resistance of the material.

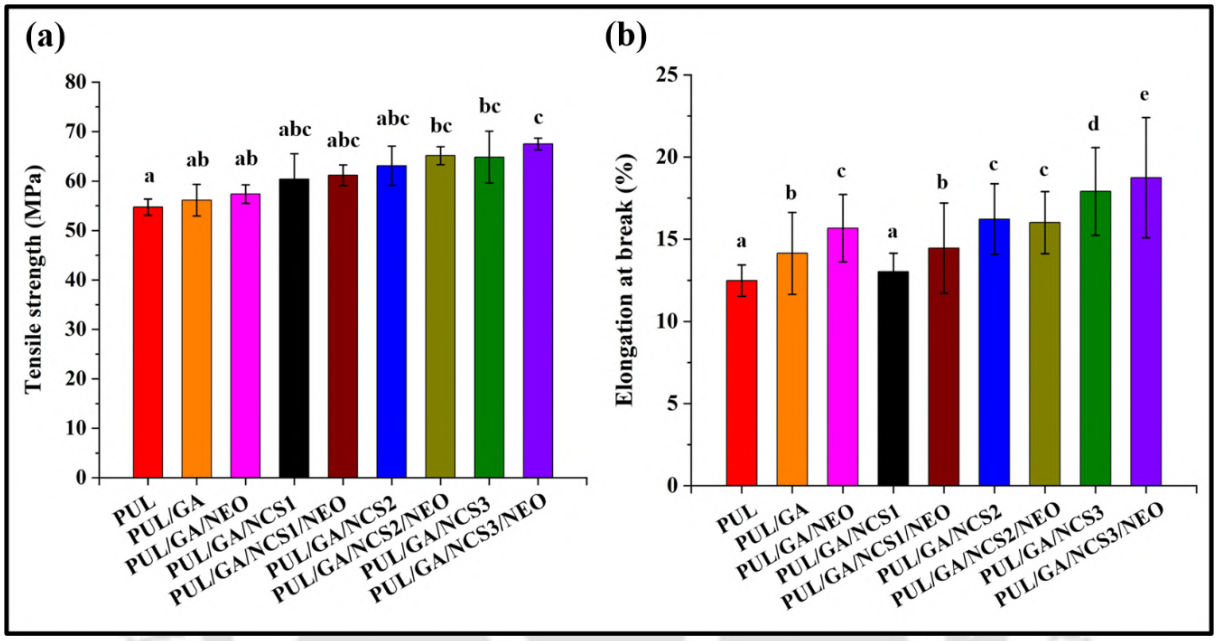

Figure 7.7 (a) Tensile strength and **(b)** elongation at break of the PUL film and PUL-based biocomposites. Results are represented as mean ± SD, N = 3. Different letters in the superscript represent statistically significant ($p < 0.05$) differences and the same letters represent statistically non-significant ($p > 0.05$) differences.

Additionally, as reported by Romani et al. [565], strong interactions between essential oil and carbohydrate polymer create a crosslinking effect that enhances tensile strength by reducing chain mobility. Moreover, the incorporation of lipids or essential oils in polysaccharide-based or protein-based films can influence the chain-to-chain interactions within the polymer, increasing cohesiveness and flexibility of the resultant films [566]. Additionally, increasing the proportion of NCS increased both tensile strength and elongation at break due to increased ductility. This is in line with reported literature where NCS enhanced the elongation at break and ductile nature of the films [312]. In this study, the PUL/GA/NCS3/NEO biocomposite demonstrated the highest tensile strength (67.50 ± 1.18 MPa) and elongation at break (18.74 ± 3.66 %), with ~ 12.77 MPa increase in tensile strength

and ~ 6.26 % increase in elongation at break as compared to neat PUL film. Thus, the results indicate that the incorporation of GA, NCS and NEO increased the tensile strength and the elongation at break of the PUL-based biocomposites. The differences in tensile strength (Figure 7.7 (a)) and the elongation at break (Figure 7.7 (b)) of the prepared films were statistically significant ($p < 0.05$).

7.2.2.6 Surface wettability and WVP

The surface wettability of the prepared films was determined by water contact angle measurement as represented in Figure 7.8 (a, b). The wettability of the biocomposites was significantly influenced by the inclusion of NCS and NEO. The water contact angle of neat PUL film was found to be 55.49 ± 2.31°, which is close to that reported by Priyadarshi et al. [567]. On the other hand, the inclusion of GA was found to increase the hydrophilicity of the biocomposite, resulting in a decreased contact angle of 48.49 ± 1.25°, which is not suitable for food packaging materials. However, the incorporation of NCS and NEO significantly increased the water contact angle to 115.01 ± 1.86° (as in case of PUL/GA/NCS3/NEO), directing towards improved hydrophobicity of the film biocomposites. As depicted in Figure 7.8 (b), the differences in contact angle of the biocomposites with respect to that of neat PUL, were statistically significant ($p < 0.05$). Additionally, the water contact angle data were found to be in line with the WVP data (Figure 7.8 (c)), in which the inclusion of GA was found to significantly increase the WVP (due to increased hydrophilicity). On the other hand, and the inclusion of NCS and NEO decreased the WVP (due to increased hydrophobicity).

Water vapour barrier property of food packaging material is a very crucial factor to prevent spoilage and degradation of food products. The WVP of film is highly influenced by its microstructure. The WVP of neat PUL film was estimated to be 1.98 ± 0.21 g/m/day/Pa ($\times 10^{-6}$), which is close to that reported in literature [568]. Additionally, the incorporation of GA significantly increased the WVP value to 2.94 ± 0.95 g/m/day/Pa ($\times 10^{-6}$), thereby reducing the barrier property (Figure 7.8 (c)). This is in line with reported literature where GA significantly increased the WVP of the films [569]. However, the incorporation of NCS and NEO in the biocomposite film (PUL/GA/NCS3/NEO) was found to reduce its WVP to 1.07 ± 0.14 g/m/day/Pa ($\times 10^{-6}$), thereby enhancing the barrier property by ~ 45.95 %. Additionally, it has been reported that NCS efficiently helps in reduction of WVTR (and hence the WVP) value of film, as nanoparticles can more efficiently occupy the void spaces present in the film [312]. The incorporation of essential oils also enhances the surface hydrophobicity of edible films, thereby reducing their water vapour permeability, as reported by Roshandel-Hesari et al. [570].

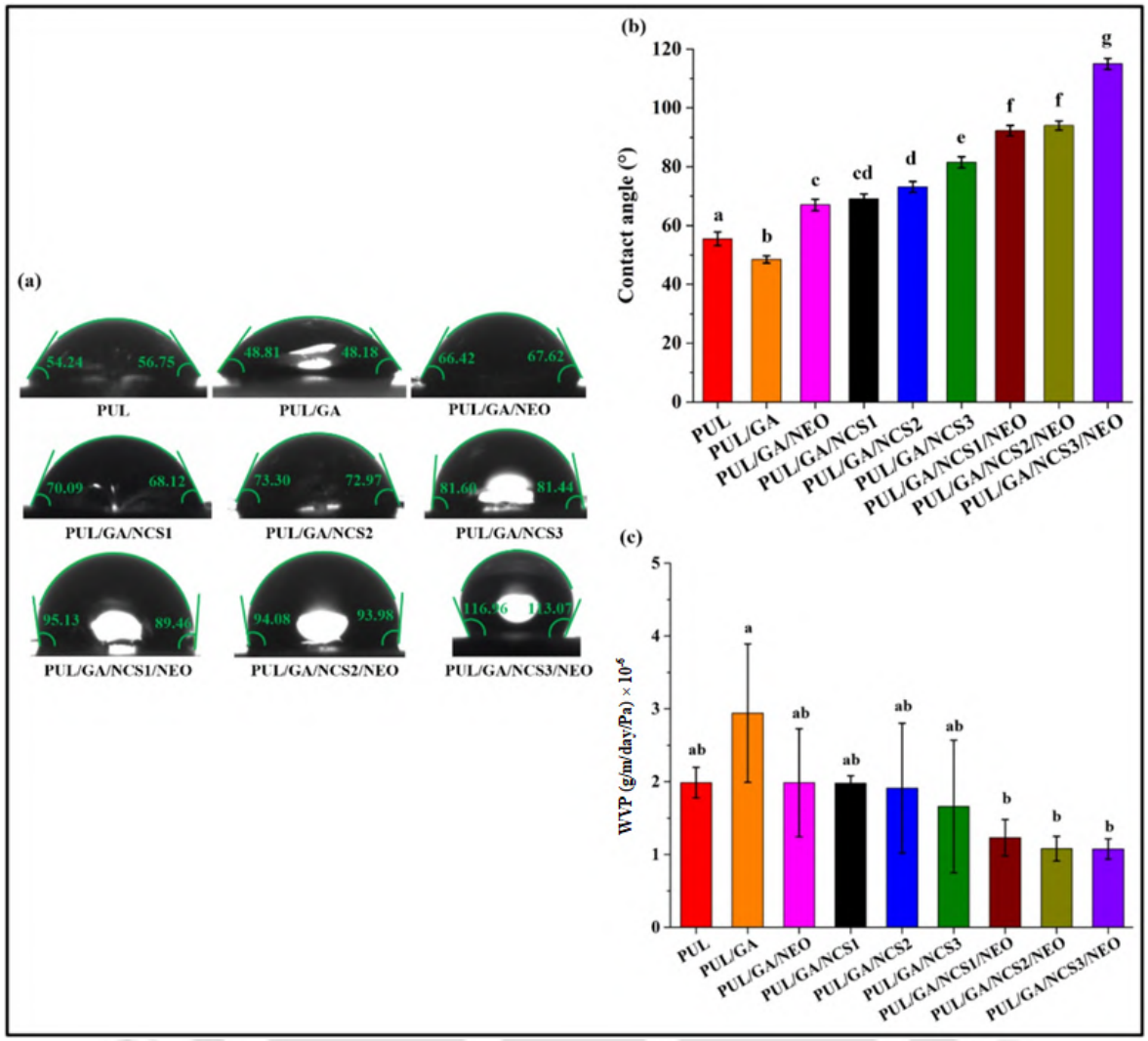

Figure 7.8 (a, b) Static water contact angles and **(c)** WVP of the PUL film and PUL-based biocomposites. Results are represented as mean ± SD, N = 3. Different letters in the superscript represent statistically significant ($p < 0.05$) differences and the same letters represent statistically non-significant ($p > 0.05$) differences.

7.2.2.7 Antimicrobial property of filmogenic/ coating solutions

The biocomposites PUL/GA/NEO, PUL/GA/NCS1, PUL/GA/NCS2, PUL/GA/NCS3, PUL/GA/NCS1/NEO, PUL/GA/NCS2/NEO and PUL/GA/NCS3/NEO showed antimicrobial property due to the presence of NCS and NEO. The zones of inhibition (shown by dotted circles) surrounding the biocomposite samples indicate their antibacterial property against *S. aureus* (Figure 7.9 (a)) and *E. coli* (Figure 7.9 (b)), and antifungal property against *A. niger* (Figure 7.9 (c)). On the other hand, the composites PUL and PUL/GA do not show any antimicrobial property and hence no zone of inhibition, due to lack of antimicrobial property in PUL and GA. The lack of antimicrobial activity in neat PUL film is in line with reported

literature [571]. As depicted in Table 7.3, amongst all the filmogenic solutions, the antimicrobial efficacy was highest in case of PUL/GA/NCS3/NEO, (12.57 ± 0.13 mm against *S. aureus,* 11.88 ± 0.23 mm against *E. coli* and 19.64 ± 0.71 mm against *A. niger*).

Table 7.3 Zones of inhibition showing antimicrobial activity of the prepared films.

Films	Zone of Inhibition (mm)		
	S. aureus	***E. coli***	***A. niger***
PUL	0.00 ± 0.00^{a}	0.00 ± 0.00^{a}	0.00 ± 0.00^{a}
PUL/GA	0.00 ± 0.00^{a}	0.00 ± 0.00^{a}	0.00 ± 0.00^{a}
PUL/GA/NEO	9.12 ± 0.44^{b}	8.88 ± 0.35^{b}	11.89 ± 1.02^{b}
PUL/GA/NCS1	10.01 ± 0.33^{bc}	9.27 ± 0.28^{b}	15.35 ± 0.33^{c}
PUL/GA/NCS1/NEO	10.36 ± 0.72^{bc}	9.58 ± 1.03^{b}	16.14 ± 0.20^{cd}
PUL/GA/NCS2	10.90 ± 1.03^{cd}	9.86 ± 1.45^{bc}	16.97 ± 0.66^{d}
PUL/GA/NCS2/NEO	11.26 ± 0.87^{cde}	10.59 ± 0.44^{bc}	17.65 ± 1.01^{d}
PUL/GA/NCS3	11.92 ± 0.56^{de}	11.05 ± 0.58^{bcd}	19.21 ± 0.58^{e}
PUL/GA/NCS3/NEO	12.57 ± 0.13^{e}	11.88 ± 0.23^{d}	19.64 ± 0.71^{e}
Chloramphenicol	28.51 ± 0.23^{f}	28.32 ± 0.74^{e}	-
Voriconazole	-	-	41.56 ± 0.51^{f}

Results are represented as mean ± SD, N = 3. Different letters in the superscript represent statistically significant ($p < 0.05$) differences and the same letters represent statistically non-significant ($p > 0.05$) differences for each column.

This indicates that the antimicrobial efficacy not only increases with the increase in concentration of NCS, but also with the incorporation of NEO in the composites. The antimicrobial properties of NCS have been extensively documented in prior studies [572,573], with its mechanism of action primarily attributed to the interaction between polycationic CS molecules and the anionic membranes of microbial cells, leading to cell membrane disruption and subsequent molecular leakage. The presence of amino (NH_2) groups in NCS cause microbial cell death by disruption of cell membrane, leading to the leakage of intracellular contents and negatively charging the cytoplasmic membrane [574]. Furthermore, the CS molecules are capable of penetrating the microbial cell nucleus, thereby inhibiting the synthesis of mRNA and proteins. They also function as metal chelators, contributing to the inhibition of microbial growth [318]. Neem essential oil (NEO), on the other hand, is also well-known for

its antimicrobial properties due to the presence of various bioactive compounds, as documented in prior studies [547,575,576]. Additionally, the hydrophobic nature of essential oils allow them to interact with the lipids in the bacterial cell membrane and mitochondria, disrupting their structure and increasing membrane permeability. This disruption affects the proton motive force, leading to changes in the pH gradient and electron flow across the membrane, eventually resulting in cell death [577,578]. It is also evident from the results that show higher antimicrobial property in the composites containing NEO, than that in the ones without NEO. This is in line with reported literature where incorporation of NEO enhanced antimicrobial efficacy of the films [579].

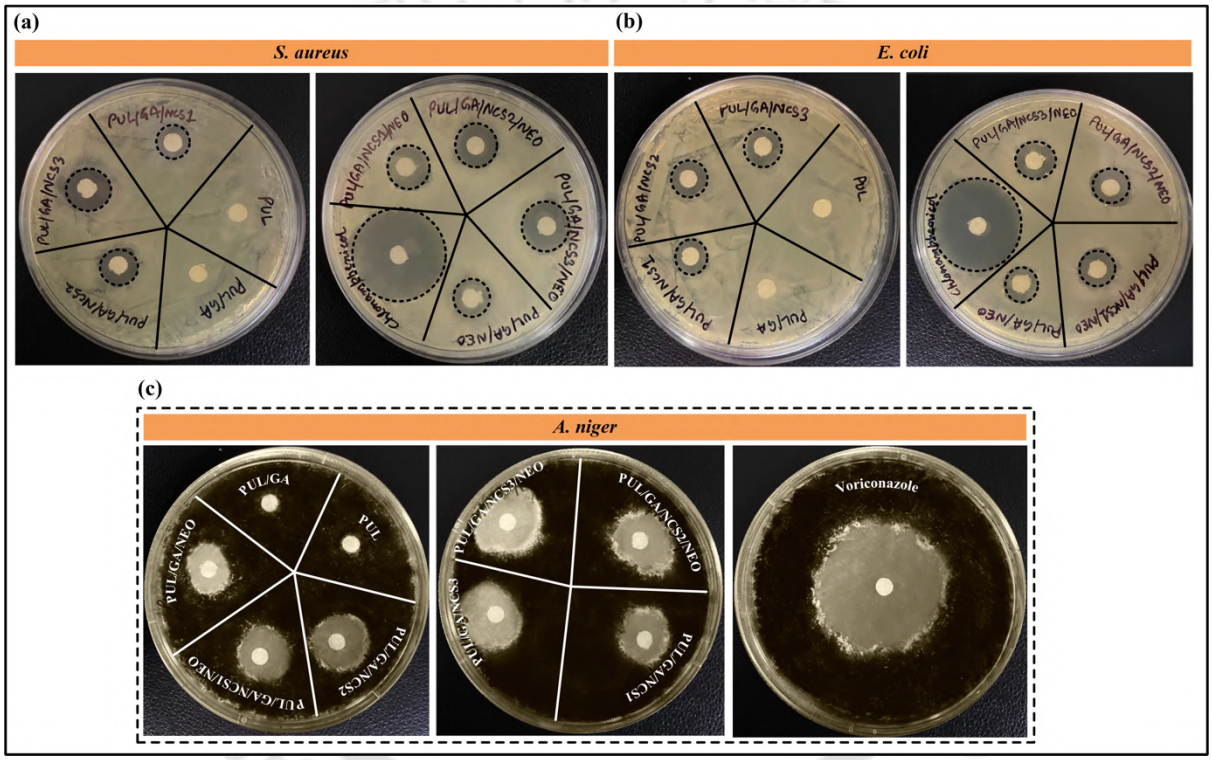

Figure 7.9 Antimicrobial activity of the filmogenic solutions against **(a)** *S. aureus*, **(b)** *E. coli* and **(c)** *A. niger*.

7.2.2.8 Antioxidant property of the prepared biocomposites

The presence of antioxidant activity in the biocomposites could be attributed to the presence of GA, NCS and NEO (Table 7.4). The neat PUL film did not exhibit any antioxidant or radical scavenging activity, which is in line with reported literature [571]. However, the PUL/GA biocomposite exhibited antioxidant activity of 2.89 ± 0.35 % by DPPH and 6.05 ± 0.88 % by ABTS assay (Table 7.4). The antioxidant activity of PUL/GA may be attributed to the fact that GA comprises of various amino acid residues, such as tyrosine, lysine and histidine, that are usually regarded as antioxidants [580]. Additionally, the DPPH and ABTS radical-scavenging

activity of the biocomposites increased with the increasing concentration of NCS from 1 to 3 wt. % and incorporation of NEO. The antioxidant activity of the PUL/GA/NCS3/NEO biocomposite was found to be 52.69 ± 0.46 % by DPPH and 73.98 ± 0.91 % by ABTS assay, which was highest in comparison to the other PUL-based biocomposites.

Table 7.4 Percentage of DPPH and ABTS radical scavenging activity of the prepared films.

Films	DPPH scavenging activity (%)	ABTS scavenging activity (%)
PUL	0.00 ± 0.00^{a}	0.00 ± 0.00^{a}
PUL/GA	2.89 ± 0.35^{b}	6.05 ± 0.88^{b}
PUL/GA/NEO	7.66 ± 0.40^{c}	13.21 ± 0.77^{c}
PUL/GA/NCS1	7.98 ± 0.35^{c}	16.11 ± 1.15^{d}
PUL/GA/NCS2	9.25 ± 0.45^{d}	17.89 ± 0.53^{d}
PUL/GA/NCS3	12.41 ± 0.47^{e}	20.55 ± 0.79^{e}
PUL/GA/NCS1/NEO	29.07 ± 0.66^{f}	37.13 ± 0.53^{f}
PUL/GA/NCS2/NEO	34.02 ± 0.37^{g}	45.78 ± 0.53^{g}
PUL/GA/NCS3/NEO	52.69 ± 0.46^{h}	73.98 ± 0.91^{h}

Results are represented as mean ± SD, N = 3. Different letters in the superscript represent statistically significant ($p < 0.05$) differences and the same letters represent statistically non-significant ($p > 0.05$) differences for each column.

The increase in antioxidant activity with increase in NCS concentration may be attributed to the fact that the CS structure contains free amino (NH_2) groups that can scavenge free radicals. These groups interact with the reactive oxygen species, neutralizing them and reducing oxidative stress. Additionally, the increase in antioxidant activity upon incorporation of NEO may be attributed to the presence of several bioactive phytochemicals in NEO, such as azadirachtin, nimbolide, and nimbin, as reported by [581]. These phytochemicals help to neutralize free radicals and inhibit or delay the oxidative deterioration responsible for food spoilage and nutrient loss, thereby contributing to the preservation of freshness and the extension of food shelf-life. This is in line with reported literature where incorporation of NCS and essential oils improved the antioxidant property of films [545,548]. Thus, in the present

study, the combination of NCS and NEO significantly enhanced the overall antioxidant activity of the film. Furthermore, the antioxidant activity was found to significantly increase for each of the samples, when tested using the ABTS assay compared to that using the DPPH assay. This may be attributed to the better solubility of the PUL-based films in ABTS solution, as reported in prior studies [582–584].

7.2.2.9 Biocompatibility analysis

The biocompatibility of the filmogenic solutions was assessed by MTT assay conducted on HEK-293 cells. As shown in Figure 7.10 (a–c), the results demonstrated that the filmogenic solutions supported the proliferation of HEK-293 cells, with cell viability progressively increasing over a 72-hr incubation period. Interestingly, the NEO-containing films exhibited slightly lower percentage of cell viability in comparison to the other films. As depicted in Figure 7.10 (a–c), the difference in cell viability percentages in case of the neat PUL and all the PUL-based biocomposites or filmogenic solutions were statistically significant ($p < 0.05$), when compared to that of the control. According to the cytotoxicity grading criteria, cell viability above 75 % indicates non-cytotoxicity, while values between 50 % and 74 % are considered slightly toxic. Moderately toxic effects are observed with viability ranging from 25 % to 49 %, and viability below 24 % indicates extreme toxicity [433]. Moreover, according to ISO10993-5:2009 standards, the substances with cell viability of atleast 75 % of that of the control group, are considered non-cytotoxic [435–437]. In the present study, the cell viability percentages of all the filmogenic solutions (the neat PUL and the PUL-based biocomposites) were found to be more than 80 % even after 72 hrs. Thus, the PUL/GA/NCS3/NEO solution with cell viability of 86.82 ± 2.28 %, could be regarded as non-cytotoxic or biocompatible for use as edible coating material.

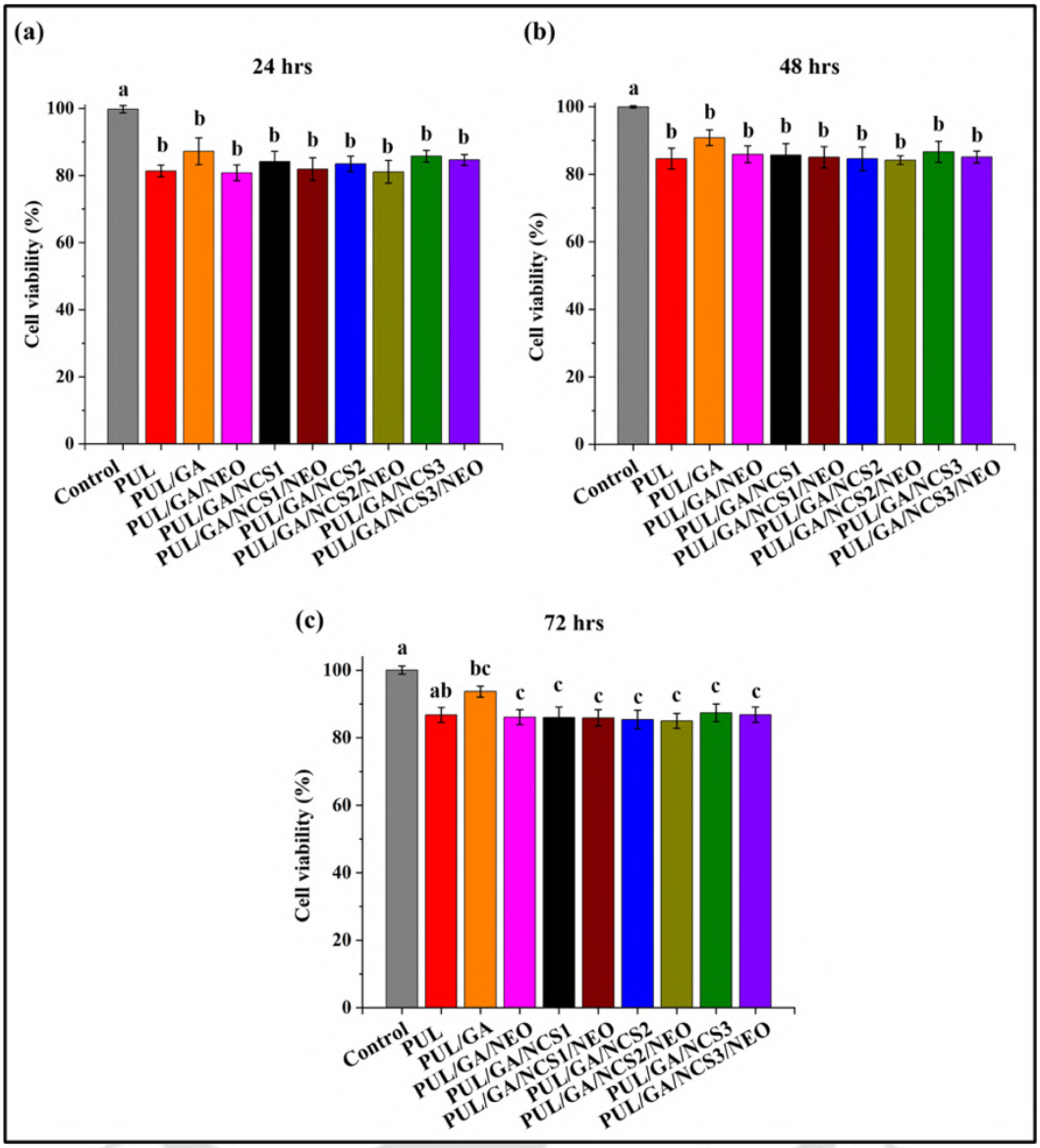

Figure 7.10 Relative viability percentage of HEK-293 cells in presence of the prepared films after **(a)** 24, **(b)** 48 and **(c)** 72 hrs of cell seeding. Results are represented as mean ± SD, N = 3. Different letters in the superscript represent statistically significant ($p < 0.05$) differences and the same letters represent statistically non-significant ($p > 0.05$) differences.

7.3 Application of edible coating and analysis of shelf-life

The application of edible coating have been reported to significantly enhance the shelf-life of various perishable food products [573]. The filmogenic solution of the PUL/GA/NCS3/NEO biocomposite was selected for application of edible coating on fresh-cut guava. The efficacy of the coating solution was determined in terms of retention of colour attributes, initial weight, firmness, visual appearance, microbiological shelf-life and antioxidant activity of the coated cut guava fruits.

7.3.1 Colour factors

Determination of optical properties is essential for edible coating applications as they significantly influence the visual appearance of coated food products. The optical properties of uncoated and coated cut guava were determined using colour factors such as L*, a*, b*, Chroma, and hue values, as shown in Table 7.5 (a–d). The L* values, representing brightness, decreased very slowly in the coated fruit (Table 7.5 (a, c)), but rapidly in the uncoated fruit (Table 7.5 (b, d)), both under ambient and refrigerated conditions. The rapid decline in L* for uncoated fruit may be attributed to its quicker browning along with initiation of fungal growth. Moreover, the browning effect of cut fruits could be attributed to the enzymatic activity of polyphenol oxidase upon coming in direct contact with the atmospheric oxygen [585]. Furthermore, the positive a* (redness) and b* (yellowness) values increased rapidly in the uncoated fruits due to faster oxidative deterioration compared to the coated ones. The observed hue angle further validates the yellowness of the cut fruits. The Chroma values indicate the efficacy of the hue colour during storage. With respect to storage duration, the coated guava fruit showed significantly ($p < 0.05$) lower variation in colour features than the uncoated one, both under ambient and refrigerated conditions (Table 7.5 (a–d)). Thus, the obtained results suggest that the edible coating formulation helped to retain the natural appearance and colour attributes of the cut guava fruits, both under ambient and refrigerated conditions. Similar findings were reported by Nur Hanani et al. [318], who observed better retention of natural colour parameters on cut guava by application of chitosan and cinnamon essential oil based edible coating formulation.

Table 7.5 (a) Colour factors of coated guava under ambient condition.

Day	L*	a*	b*	Chroma	hue
0	71.35±2.55^{a}	5.35±1.46^{a}	14.10±3.01^{a}	15.08±3.32^{a}	69.39±1.48^{a}
2	69.99±0.19^{a}	6.93±1.39^{ab}	21.91±2.26^{b}	22.72±4.01^{ab}	68.01±3.11^{a}
4	66.42±3.40^{a}	8.73±1.82^{ab}	21.81±3.46^{b}	23.51±3.72^{ab}	68.18±3.01^{a}
6	61.35±6.42^{a}	10.60±2.47^{b}	22.36±2.67^{b}	25.44 ±3.39^{b}	66.03±3.56^{a}

Table 7.5 (b) Colour factors of uncoated guava under ambient condition.

Day	L*	a*	b*	Chroma	hue
0	69.35±5.62^{a}	4.35±1.08^{a}	11.72±3.20^{a}	12.89±3.13^{a}	74.03±0.70^{a}
2	50.05±2.71^{b}	7.33±1.29^{b}	12.91±3.34^{a}	14.85±3.52^{a}	63.81±1.32^{b}
4	38.66±2.41^{c}	6.30±0.76^{ab}	14.10±1.81^{ab}	15.77±3.77^{ab}	60.10±2.20^{bc}
6	33.69±1.33^{c}	10.84±0.87^{c}	21.37±1.92^{b}	25.24±2.38^{b}	57.03±3.68^{c}

Table 7.5 (c) Colour factors of coated guava under refrigerated condition.

Day	L*	a*	b*	Chroma	hue
0	76.34±0.21^{a}	1.47±0.33^{a}	10.86±1.13^{a}	10.29±1.06^{a}	80.21±0.39^{a}
2	75.14±0.60^{ab}	6.34±1.47^{b}	15.29±2.63^{ab}	16.65±2.92^{ab}	67.14±1.88^{a}
4	73.67±0.55^{bc}	6.71±1.19^{bc}	18.67±2.45^{ab}	20.25±6.87^{b}	66.72±3.42^{a}
6	72.60±0.50^{c}	6.78±1.57^{bc}	19.03±6.89^{b}	20.76±3.07^{b}	66.40±3.90^{a}
8	69.81±0.33^{d}	9.05±1.99^{bcd}	21.64±3.27^{bc}	22.62±2.61^{b}	65.72±0.94^{a}
10	67.14±1.17^{e}	10.06±0.17^{cd}	21.19±0.40^{bc}	23.29±0.52^{bc}	65.76±0.85^{a}
12	61.67±1.16^{f}	11.23±0.81^{de}	22.01±1.76^{bc}	25.12±2.24^{bc}	64.23±2.78^{a}
14	57.79±0.50^{g}	13.92±1.36^{e}	30.50±5.04^{c}	33.10±4.26^{c}	63.29±0.60^{a}

Table 7.5 (d) Colour factors of uncoated guava under refrigerated condition.

Day	L*	a*	b*	Chroma	hue
0	73.79±1.55^{a}	1.74±0.29^{a}	10.30±1.39^{a}	9.11±1.28^{a}	80.64±1.59^{a}
2	60.25±0.29^{b}	11.11±0.29^{b}	24.39±1.60^{b}	27.86±0.61^{b}	72.46±5.81^{b}
4	57.65±0.38^{bc}	12.64±1.22^{b}	28.73±2.91^{b}	31.63±2.33^{b}	69.70±4.39^{bc}
6	55.59±0.50^{c}	12.32±1.77^{b}	28.96±4.05^{b}	31.65±4.09^{b}	66.82±0.54^{bc}
8	53.36±0.84^{cd}	12.68±3.87^{b}	29.12±1.83^{b}	32.28±4.69^{b}	66.02±2.00^{bc}
10	49.21±3.22^{d}	13.76±3.17^{b}	29.73±1.12^{b}	33.03±1.63^{b}	64.33±2.04^{c}
12	38.36±2.14^{e}	14.65±1.17^{b}	30.52±4.48^{b}	34.11±5.50^{b}	64.28±0.36^{c}
14	34.97±1.13^{e}	15.30±3.22^{b}	32.87±2.03^{b}	34.66±4.68^{b}	62.97±0.19^{c}

Results are represented as mean ± SD, N = 3. Different letters in the superscript represent statistically significant ($p < 0.05$) differences and the same letters represent statistically non-significant ($p > 0.05$) differences for each column.

7.3.2 Weight loss and firmness

The degree of weight loss is an indicative of decline in freshness of food products, mainly due to moisture evaporation causing shrinkage on their surface [586]. However, the weight loss could be significantly delayed by using biopolymer based edible films and coating materials, such as pullulan, chitosan, gum arabic, starch, alginate, etc [587,588]. In the present study, the coated cut guava fruit showed significantly lesser amount of weight loss as compared to that in the uncoated fruit (Figure 7.11 (a, b)), demonstrating the efficient moisture barrier properties of the edible coating material. Additionally, a statistically significant ($p < 0.05$) difference in weight loss between the coated and uncoated guava fruits was observed both under ambient and refrigerated conditions, as shown in Table 7.6 (a, b). This significantly lower reduction in weight in the coated fruit may be attributed to the excellent water vapour barrier property of the PUL/GA/NCS3/NEO active edible biocomposite. The rapid weight loss in the uncoated fruit during storage may be attributed to the natural process of respiration and trans-evaporation, whereas the coating material effectively minimized the rate of weight loss in the coated fruit. Importantly, the weight of a fruit or vegetable gets reduced due to loss of a carbon molecule during the respiration process [311].

Table 7.6 (a) Weight loss of coated and uncoated guava under ambient condition.

Storage Time (Days)	Weight Loss (%)	
	Coated	Uncoated
0	0.00 ± 0.00^{a}	0.00 ± 0.00^{a}
1	5.22 ± 0.43^{b}	14.64 ± 0.42^{b}
2	8.11 ± 2.22^{c}	19.23 ± 1.27^{c}
3	10.84 ± 1.07^{d}	23.43 ± 2.18^{d}
4	15.35 ± 0.53^{e}	27.35 ± 1.43^{e}
5	16.83 ± 2.14^{e}	30.35 ± 0.83^{f}
6	19.76 ± 0.69^{f}	32.93 ± 0.74^{g}

Table 7.6 (b) Weight loss of coated and uncoated guava under refrigerated condition.

Storage Time (Days)	Weight Loss (%)	
	Coated	Uncoated
0	0.00 ± 0.00^{a}	0.00 ± 0.00^{a}
1	2.62 ± 0.53^{ab}	3.77 ± 0.99^{a}
2	6.74 ± 1.34^{bc}	10.12 ± 0.44^{b}
3	8.04 ± 1.02^{cd}	14.60 ± 1.02^{bc}
4	10.53 ± 2.55^{de}	17.18 ± 2.42^{c}
5	12.90 ± 2.88^{de}	19.59 ± 0.44^{cd}
6	15.55 ± 0.96^{ef}	24.78 ± 0.67^{de}
7	19.35 ± 2.69^{fg}	29.28 ± 2.45^{ef}
8	22.39 ± 1.56^{g}	33.49 ± 1.21^{fg}
9	25.17 ± 2.4^{gh}	36.62 ± 0.88^{g}
10	28.59 ± 2.75^{hi}	43.88 ± 2.02^{h}
11	30.32 ± 0.29^{ij}	46.40 ± 3.40^{hi}
12	33.79 ± 0.36^{jk}	49.31 ± 1.83^{hij}
13	35.89 ± 1.23^{k}	51.85 ± 2.78^{ij}
14	38.67 ± 0.4^{k}	53.84 ± 2.58^{j}

Results are represented as mean ± SD, N = 3. Different letters in the superscript represent statistically significant ($p < 0.05$) differences and the same letters represent statistically non-significant ($p > 0.05$) differences for each column.

Reduction in firmness of fresh produce is an indicative of its quality deterioration, mainly caused by respiration. In the present study, both coated and uncoated fruits showed firmness reduction over time, attributed to various factors like microbial contamination, moisture loss and mechanical damage [311]. However, the rate of reduction in firmness was found to be much slower in the coated fruit as compared to the uncoated one, where a rapid reduction was observed in Figure 7.11 (c, d). The difference in firmness reduction of coated and uncoated guava fruits, was statistically significant ($p < 0.05$) under both ambient and refrigerated conditions, as shown in Table 7.7 (a, b).

Table 7.7 (a) Firmness of coated and uncoated guava under ambient condition.

Storage Time (Days)	Firmness (N)	
	Coated	Uncoated
0	41.89±1.62[a]	41.42±1.34[a]
2	38.60±1.08[a]	34.86±1.93[b]
4	30.58±0.73[b]	24.15±1.44[c]
6	22.50±1.70[c]	10.87±2.28[d]

Table 7.7 (b) Firmness of coated and uncoated guava under refrigerated condition.

Storage Time (Days)	Firmness (N)	
	Coated	Uncoated
0	42.50±1.27[a]	41.50±1.30[a]
2	41.73±0.75[a]	31.50±1.65[b]
4	39.76±1.02[a]	29.22±0.89[b]
6	35.78±0.84[b]	23.20±0.75[c]
8	29.65±1.17[c]	21.00±1.09[c]
10	27.63±1.50[c]	17.34±1.66[d]
12	24.12±1.20[d]	12.26±1.39[e]
14	20.20±1.24[e]	9.85±1.57[e]

Results are represented as mean ± SD, N = 3. Different letters in the superscript represent statistically significant ($p < 0.05$) differences and same letters represent statistically non-significant ($p > 0.05$) differences for each column.

Thus, the coating material demonstrated effective retention of firmness by creating a modified atmosphere around the exterior surface of the coated fruit. Moreover, during storage of fresh fruits and vegetables they undergo the process of aerobic respiration, which leads to the formation of superoxide radicals. These radicals in turn can result in disruption of cell wall and enable the pectinase enzyme to degrade pectin (a polysaccharide present in cell wall) and cause quality deterioration by reduction in firmness and post-harvest life [589].

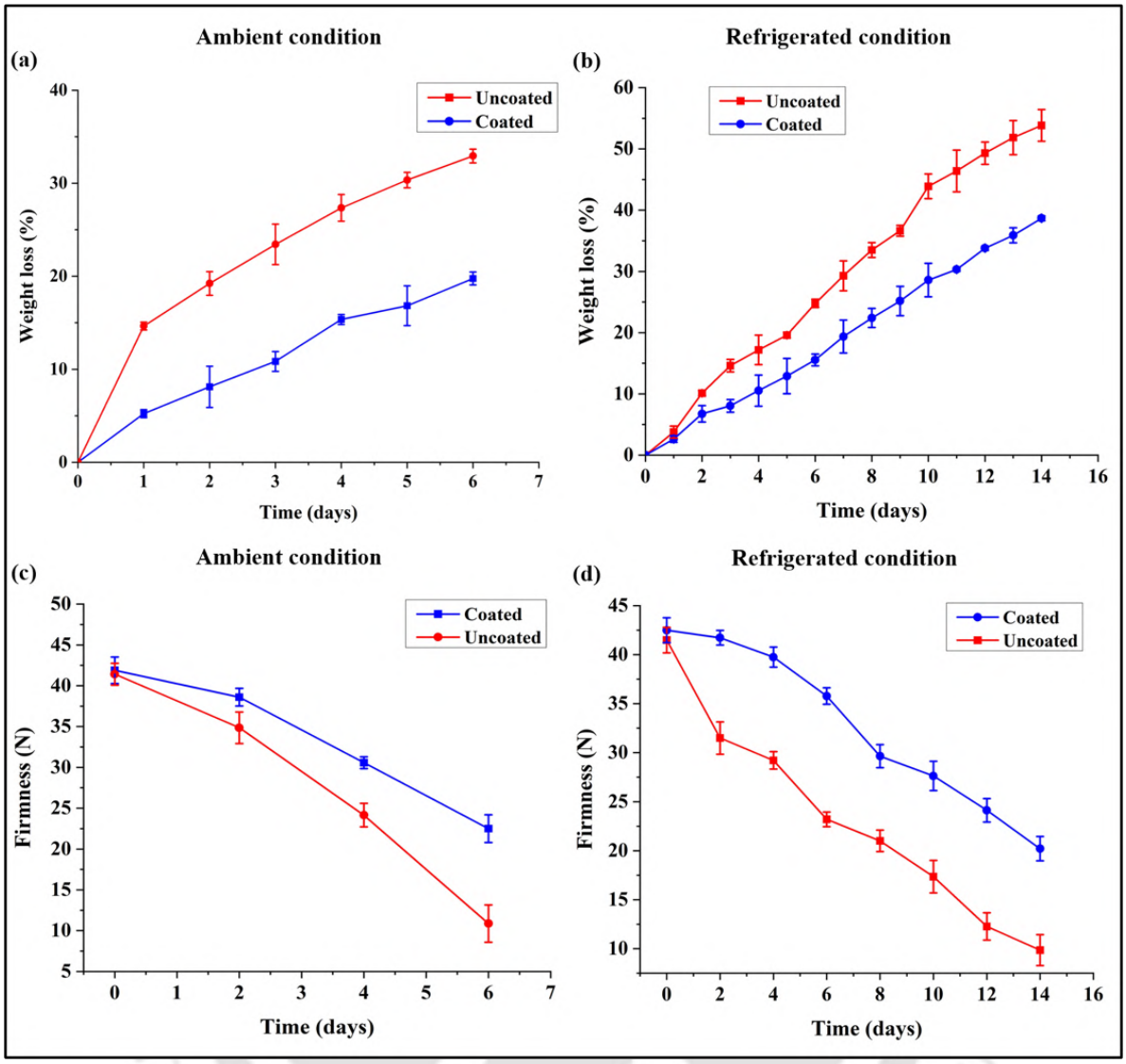

Figure 7.11 Weight loss of coated and uncoated cut guava under **(a)** ambient and **(b)** refrigerated conditions, and firmness of coated and uncoated cut guava under **(c)** ambient and **(d)** refrigerated conditions. Results are represented as mean ± SD, N = 3.

7.3.3 Visual appearance

Figure 7.12 (a, b) depicts the effect of the formulated edible coating solution (PUL/GA/NCS3/NEO) on the visual quality and appearance of cut guava fruits over storage durations of 6 and 14 days under ambient and refrigerated conditions, respectively. The uncoated cut guava stored under ambient condition exhibited signs of degradation, such as browning and shrinkage, starting from the 2nd day, with fungal growth appearing on the surface by the 4th day. However, the coated cut guava under ambient condition showed only slight browning starting from the 4th day, with almost no shrinkage or fungal growth observed up to the 6th day (Figure 7.12 (a)). Similarly, under refrigerated conditions, the uncoated cut guava

began to show browning and shrinkage from the 4th day, and appearance of fungal growth by the 8th day. In contrast, the coated cut guava stored under refrigeration demonstrated significantly reduced browning and shrinkage, with no fungal growth observed up to the 14th day (Figure 7.12 (b)). These effects in the coated guava may be attributed to the excellent weight and firmness retention and antimicrobial properties of the edible coating solution, due to the presence of NCS and NEO. The results indicate that the PUL/GA/NCS3/NEO coating solution help in maintaining the visual appearance and quality of the coated cut guava fruit, thereby significantly extending its shelf-life.

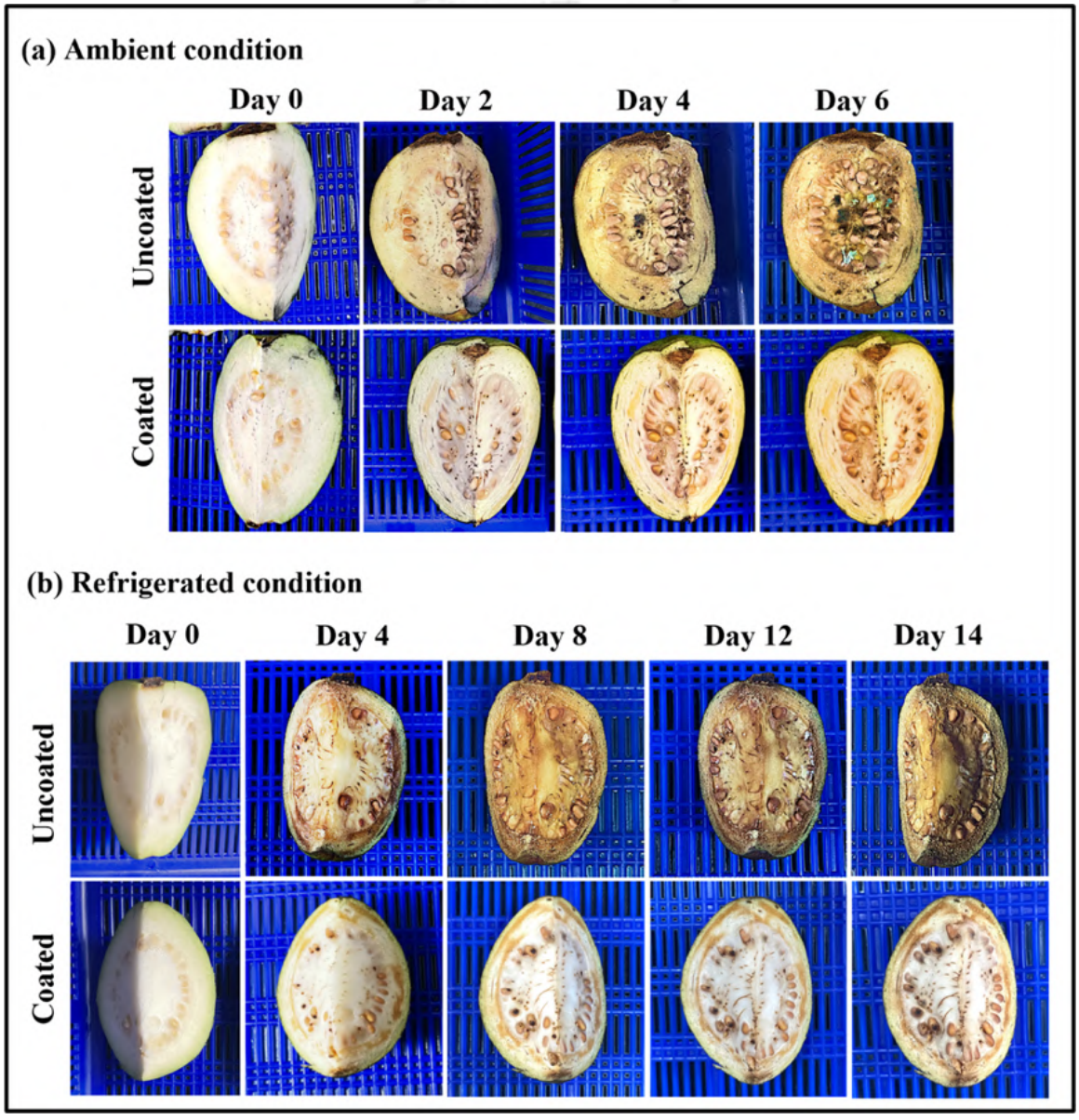

Figure 7.12 Visual appearance of uncoated and coated cut guava under **(a)** ambient and **(b)** refrigerated conditions, over storage period of 6 and 14 days respectively.

7.3.4 Microbiological shelf-life analysis

As depicted in Table 7.8, the TVC of all guava samples on the 0^{th} day ranged from 4.02 ± 0.03 to 3.96 ± 0.01 log_{10} CFU/mL under ambient condition, and from 3.93 ± 0.06 to 3.87 ± 0.04 log_{10} CFU/mL under refrigeration. Similarly, the YMC ranged from 4.45 ± 0.06 to 4.28 ± 0.05 log_{10} CFU/mL under ambient condition, and from 4.33 ± 0.04 to 4.17 ± 0.01 log_{10} CFU/mL under refrigeration. Over time, microbial counts (TVC and YMC) increased significantly ($p < 0.05$), with the uncoated guava having a relatively higher count than the coated one. It was observed that on the 4th day under ambient condition, the YMC in the uncoated guava exceeded the acceptable limit of 6 log_{10} CFU/mL [590], while the coated one remained below this limit. Additionally, under refrigeration, the TVC and YMC in the uncoated guava exceeded the acceptable limit on the 14^{th} and 12^{th} days, respectively (Table 7.8). However, both the TVC and YMC in the coated guava did not exceed this limit even up to 14^{th} days of storage under refrigeration. In general, the microbial resistance of the coated guava was found to be higher than that of the uncoated one. This may be attributed to the presence of antimicrobial components such as NCS and NEO in the coating material, as discussed earlier in Section 7.2.2.7. Thus, the edible coating material comprising both NCS and NEO was found to be very effective in significantly reducing the microbial count in the coated cut guava fruits.

Table 7.8 Microbial count of uncoated and coated guava samples under ambient and refrigerated conditions.

Storage conditions	Cut guava samples	Storage time (days)	TVC (log_{10} CFU/ml)	YMC (log_{10} CFU/ml)
Ambient	Uncoated	0	4.02±0.03^{a}	4.45±0.06^{a}
		2	4.57±0.01^{b}	5.74±0.02^{b}
		4	5.14±0.05^{c}	6.12±0.04^{c}
		6	5.72±0.03^{d}	6.44±0.01^{d}
	Coated	0	3.96±0.01^{a}	4.28±0.05^{a}
		2	4.11±0.02^{b}	4.88±0.01^{b}
		4	4.28±0.01^{c}	5.43±0.05^{c}
		6	4.80±0.04^{d}	5.87±0.01^{d}
Refrigeration	Uncoated	0	3.93±0.06^{a}	4.33±0.04^{a}
		4	4.41±0.02^{b}	5.02±0.01^{b}
		8	5.05±0.01^{c}	5.65±0.05^{c}
		12	5.77±0.01^{d}	6.23±0.12^{d}
		14	6.11±0.04^{e}	6.72±0.02^{e}
	Coated	0	3.87±0.04^{a}	4.17±0.01^{a}
		4	4.18±0.03^{b}	4.48±0.03^{b}
		8	4.35±0.06^{c}	4.76±0.01^{c}
		12	4.88±0.02^{d}	5.24±0.01^{d}
		14	5.14±0.02^{e}	5.65±0.03^{e}

Results are represented as mean ± SD, N = 3. Different letters in the superscript represent statistically significant ($p < 0.05$) differences and the same letters represent statistically non-significant ($p > 0.05$) differences for each column.

7.3.5 Antioxidant property of the uncoated and coated cut guava fruits

As depicted in Table 7.9, the initial antioxidant activity (on the 0th day) was found to be ~ 74–79 % under both ambient and refrigerated conditions. This high antioxidant value may be attributed to the presence of natural antioxidant compounds, such as vitamin C, phenols and flavonoids, found in freshly harvested guava [591]. The antioxidant activity demonstrated an overall decreasing trend with respect to storage time in both uncoated and coated guava fruits. Interestingly, there was an increase in antioxidant activity up to the 2nd day, irrespective of application of edible coating material and storage conditions (Table 7.9). This may be because the guava underwent physiological or wound stress during the initial days after cutting, resulting in an increase in antioxidant compounds such as phenolics, flavonoids and ascorbic acid. This stress response induced the biosynthesis of these compounds, which explains the significant rise in antioxidant activity up to the 2nd day. However, as the fruit underwent chemical and enzymatic degradation, the oxidative processes took over, causing breakdown of antioxidant compounds and resulting in decreased antioxidant activity from the 4th day onwards. This is in line with reported literature which demonstrate that cut fruits initially exhibit an increase in antioxidant capacity due to wounding stress. However, as degradation progresses, the breakdown of cellular structures leads to the loss of antioxidants, resulting in decreased antioxidant activity over time [592,593].

The antioxidant activity was found to significantly decrease ($p < 0.05$) with respect to time from the 4th day onwards. However, it remained relatively higher and better maintained in the coated guava fruit compared to the uncoated one. The coated guava maintained ~ 67–69 % of its antioxidant activity up to the 6th day under ambient conditions and ~ 54–57 % up to the 14th day under refrigeration. In contrast, the uncoated guava exhibited a retention of only ~ 55–58 % of its antioxidant activity up to the 6th day at ambient conditions, which further decreased to ~ 40–42 % up to the 14th day under refrigeration (Table 7.9). The increased antioxidant activity in the coated guava may be attributed to their delayed ripening process due to the reduced production of ethylene, as reported by [594]. This may also be related to the modification of the internal atmosphere by application of edible coating, thereby lowering the risk of oxidative damage in the coated guava. On the other hand, in the uncoated guava, the phenolic compounds undergo rapid degradation due to senescence and higher respiration rates, thereby resulting in relatively faster decrease in antioxidant activity.

Table 7.9 Antioxidant activity of the uncoated and coated guava fruit samples.

Storage conditions	Cut guava samples	Storage time (days)	DPPH scavenging activity (%)	ABTS scavenging activity (%)
Ambient	Uncoated	0	75.03±1.22^{b}	78.68±0.65^{b}
		2	82.72±0.35^{a}	84.04±1.46^{a}
		4	69.59±0.28^{c}	73.11±1.33^{c}
		6	55.84±1.11^{d}	58.25±0.24^{d}
	Coated	0	74.68±0.75^{b}	79.25±1.03^{a}
		2	78.29±1.55^{a}	81.21±0.84^{a}
		4	70.03±0.22^{c}	72.68±1.36^{b}
		6	67.73±1.45^{c}	69.68±0.85^{c}
Refrigeration	Uncoated	0	75.54±0.68^{b}	78.16±1.25^{b}
		2	80.31±0.56^{a}	82.59±1.43^{a}
		4	68.46±0.11^{c}	71.24±0.87^{c}
		6	61.87±1.64^{d}	65.05±0.42^{d}
		8	55.23±0.44^{e}	58.56±1.29^{e}
		10	47.35±1.38^{f}	49.64±0.78^{f}
		12	42.73±0.72^{g}	45.42±1.13^{g}
		14	40.28±0.57^{h}	42.34±0.88^{h}
	Coated	0	74.88±1.63^{b}	78.65±1.47^{a}
		2	77.55±1.41^{a}	80.53±0.88^{a}
		4	72.14±0.22^{c}	74.78±1.62^{b}
		6	68.58±0.36^{d}	70.59±0.77^{c}
		8	63.73±0.68^{e}	65.11±1.24^{d}
		10	59.65±0.31^{f}	62.16±1.06^{e}
		12	56.68±1.07^{g}	59.31±0.23^{f}
		14	54.26±0.44^{h}	57.43±0.18^{f}

Results are represented as mean ± SD, N = 3. Different letters in the superscript represent statistically significant ($p < 0.05$) differences and the same letters represent statistically non-significant ($p > 0.05$) differences for each column.

Additionally, the observed antioxidant activity assessed by ABTS assay was slightly higher than that of DPPH assay. This variation in antioxidant activity percentages assessed by the DPPH and ABTS assays may be attributed to the relative differences in the ability of the antioxidant constituents in the extracts to reduce the DPPH and ABTS free radicals. Moreover, the ABTS assay generates a blue/green ABTS·+ radical, making it suitable for both hydrophilic and lipophilic antioxidant systems. In contrast, the DPPH assay involves a radical dissolved in organic solvents, limiting its application primarily to hydrophobic systems [595]. As guava contains both hydrophilic (vitamin C, phenolics) and lipophilic (carotenoids) antioxidants, so the antioxidant activity assessed by ABTS is relatively higher than that assessed by DPPH.

7.4 Summary

The study demonstrated the preparation of NCS by the ionic gelation technique. The prepared NCS was further used along with NEO to enhance the packaging-related property of PUL/GA based biocomposites for use in edible food packaging. The inclusion of NCS and NEO significantly transformed the biocomposite surface from hydrophilic to hydrophobic, which is an essential characteristic for packaging materials. Moreover, the barrier performance (WVP), and other properties such as mechanical, thermal, UV-shielding and antioxidant properties were also improved. Additionally, the filmogenic solutions showed antimicrobial properties against *S. aureus*, *E. coli* and *A. niger*, and hence could be used as edible coating material for enhancing the shelf-life of food products. Furthermore, the *in vitro* biocompatibility analysis of the filmogenic solutions conducted on HEK-293 cells demonstrated their non-cytotoxic nature. In the present study, the filmogenic solution with the most optimum attributes (PUL/GA/NCS3/NEO) was selected for edible coating application on fresh-cut guava. The edible coating solution was found to prolong the shelf-life of fresh-cut guava by significantly delaying its oxidative deterioration and microbial attack, preventing rapid moisture loss and maintaining firmness, during storage period (up to 6 days under ambient condition and 14 days under refrigerated condition). The prepared biocomposite/ filmogenic solution could also be explored for shelf-life extension of other food products, especially those that are sensitive to UV light.

CHAPTER 8

CONCLUSION

This doctoral research was motivated by the growing need for sustainable, biocompatible, and multifunctional biomaterials that can serve as alternatives to conventional synthetic polymers across various areas, including healthcare, cosmetics, and food preservation. Pullulan, a natural polysaccharide produced by *Aureobasidium pullulans* (*A. pullulans*), was selected as the central material of study due to its remarkable properties, such as water solubility, film-forming ability, non-toxicity, and compatibility with biological systems. The aim was to optimize its production and explore its versatility across diverse real-world applications. The first part of this work focused on shake-flask fermentation of *A. pullulans* NCIM 1049, where pullulan production was optimized using statistical experimental design. Plackett–Burman Design (PBD) identified jaggery, yeast extract, and NaCl as significant factors, which were further optimized using Box–Behnken Design (BBD). The BBD was used to optimize the concentrations of the significant media components to maximize pullulan production. The optimized conditions (jaggery 49.09 g/L, yeast extract 2.15 g/L, NaCl 1.28 g/L) resulted in a predicted pullulan yield of 5.106 g/L, closely matching the experimentally obtained yield of 4.923 ± 0.14 g/L, confirming the reliability of the model. To explore the biomedical potential of pullulan, a bilayered wound dressing scaffold was developed. The hydrophilic sublayer composed of pullulan/polyvinyl alcohol (PVA)/gum arabic nanofibers was prepared via electrospinning and loaded with the antibiotic gentamicin sulfate to promote wound healing and prevent infection. On the other hand, the hydrophobic top layer made of solvent-casted polylactic acid (PLA) provided structural integrity and protection against environmental contaminants. The scaffold demonstrated controlled antibiotic release (93.09 ± 2.63 % over 48 hrs), excellent swelling index of 611.85 ± 15.05 %, porosity of 70.56 ± 0.58 %, appropriate water vapour transmission rate (WVTR) of 94.20 ± 14.50 g/m²/day, and significant antibacterial activity against *S. aureus* and *E. coli*. Importantly, *in vitro* biocompatibility tests conducted on human dermal fibroblast (HDF) cells confirmed its safety and efficacy, making it a potential candidate for advanced wound healing applications. Additionally, recognizing the growing demand for targeted cancer therapies, the study also focussed on fabrication of coaxially electro-centrifugally spun pullulan/poly(lactic-co-glycolic acid) (PLGA) core/sheath

nanofibers containing ciprofloxacin (CIP) and paclitaxel (PTX). The dual drug-loaded nanofibers fabricated using 23G/1mm and 21G/1mm core-sheath configurations demonstrated a drug release pattern characterized by an initial burst release followed by sustained delivery. Furthermore, these nanofibers significantly reduced the viability of melanoma A375 cells *in vitro* to 65.37 ± 1.96 % and 67.82 ± 1.31 %, respectively, after 72 hrs of incubation. This highlights the utility of pullulan in developing drug delivery systems for localized cancer treatment. In another application-based study, pullulan was incorporated into an antibacterial skin-cream infused with turkey berry leaf extract (TBLE), known for its antibacterial properties. The cream formulation containing the extract demonstrated zone of inhibition of 16.67 ± 0.40 mm (against *S. aureus*) and 14.83 ± 0.12 mm (against *E. coli*). It also successfully passed all safety and quality evaluations, showing a stable texture, skin-compatible pH (6.10 ± 0.20), and compliance with heavy metal, arsenic, and microbial safety standards. Its physicochemical parameters, including total fatty matter (TFM, 8.5 %), moisture content (65 %), and shear-thinning behaviour, were found to be within acceptable ranges for skincare formulations, confirming the feasibility of using pullulan in cosmetic applications. Further exploring the applications of pullulan, edible biocomposite films were developed for food preservation using pullulan combined with gum arabic, chitosan nanoparticles (NCS), and neem essential oil (NEO). The incorporation of 3 % NCS and 1 % NEO significantly enhanced the packaging-related properties of pullulan/gum arabic films, with enhanced antimicrobial activity against *S. aureus*, *E. coli* and *A. niger*. Surface hydrophobicity improved from 55.49 ± 2.31° to 115.01 ± 1.86°, tensile strength increased by ~ 12.77 MPa, elongation at break improved by ~ 6.26 %, and barrier performance improved by ~ 45.95 %. The active biocomposite coating effectively reduced weight loss, delayed microbial growth, and preserved firmness and antioxidant activity of fresh-cut guava under both ambient and refrigerated storage conditions, thereby extending shelf life. To place these findings in the broader context of natural polymer research, Table 8.1 presents a comparative overview of widely studied biopolymers alongside the pullulan-based materials developed in this thesis. Several biopolymers such as chitosan, alginate, collagen, starch, and cellulose derivatives are widely recognized for their biomedical or implantable applications, film-forming properties, edibility, barrier properties, biocompatibility, and antimicrobial properties.

Table 8.1 Comparative analysis of pullulan-based materials developed in this thesis with chitosan, alginate, collagen, starch, and cellulose derivatives based on their functional properties.

Property	Pullulan-based composites (This Thesis)	Chitosan	Alginate	Collagen	Starch	Cellulose Derivatives
Biomedical/ Implantable Applicability	Demonstrated in wound scaffold and dual drug-loaded nanofibers with confirmed cytocompatibility	Widely used in wound dressings and tissue engineering; charge-influenced behaviour	Used in hydrogels and wound systems; requires ionic crosslinking	Extensively used due to ECM similarity; limited standalone stability	Limited direct implantable use, due to poor mechanical stability	Used in selected biomedical films and scaffolds
Film-Forming Ability	Excellent transparency, smooth and uniform films without chemical crosslinking	Good film formation; relatively opaque	Moderate; brittle without crosslinking	Weak standalone film formation	Good but brittle and opaque	Good film formation; moderate transparency
Edibility	GRAS status; demonstrated edible coating with shelf-life extension	GRAS; edible films reported	GRAS; edible coatings widely studied	Edible but primarily used in biomedical field	Widely edible	Some derivatives approved for edible use
Barrier Performance	Excellent oxygen barrier; enhanced moisture resistance through functionalization	Moderate barrier performance	Poor moisture barrier; high permeability	Poor barrier properties	Poor moisture resistance	Moderate barrier performance
Biocompatibility	Confirmed cytocompatibility (HDF, HEK-293); neutral polymer reduces charge-related interactions	Generally biocompatible; cationic nature may influence cell response	Biocompatible	Excellent biocompatibility	Biocompatible	Biocompatible
Antimicrobial Activity	Achieved through incorporation of gentamicin, NCS, NEO, and plant extracts	Intrinsic antimicrobial activity due to cationic nature	Requires antimicrobial additives	Requires antimicrobial additives	Requires antimicrobial additives	Requires antimicrobial additives

In this context, the pullulan-based materials presented in this work demonstrated exceptionally good properties in terms of forming highly transparent and uniform films, maintaining stable cytocompatibility, and performing well as edible coatings with proven shelf-life extension. Moreover, this work validates that pullulan can be functionalized to have antimicrobial

properties while retaining its biocompatibility. Thus, this work demonstrates that through fermentation media optimization pullulan can be efficiently produced and further highlights its potential in biomedical, cosmetic and food preservation applications.

REFERENCES

[1] V. Rishi, A.K. Sandhu, A. Kaur, J. Kaur, S. Sharma, S.K. Soni, Utilization of kitchen waste for production of pullulan to develop biodegradable plastic, Appl. Microbiol. Biotechnol. 104 (2020) 1307–1317. https://doi.org/10.1007/s00253-019-10167-9.

[2] A. Rafey, F.Z. Siddiqui, A review of plastic waste management in India–challenges and opportunities, Int. J. Environ. Anal. Chem. 103 (2023) 3971–3987. https://doi.org/10.1080/03067319.2021.1917560.

[3] R. V. Gadhave, A. Das, P.A. Mahanwar, P.T. Gadekar, Starch Based Bio-Plastics: The Future of Sustainable Packaging, Open J. Polym. Chem. 08 (2018) 21–33. https://doi.org/10.4236/ojpchem.2018.82003.

[4] V.D. Prajapati, G.K. Jani, S.M. Khanda, Pullulan: An exopolysaccharide and its various applications, Carbohydr. Polym. 95 (2013) 540–549. https://doi.org/10.1016/j.carbpol.2013.02.082.

[5] L. Yu, K. Dean, L. Li, Polymer blends and composites from renewable resources, Prog. Polym. Sci. 31 (2006) 576–602. https://doi.org/10.1016/j.progpolymsci.2006.03.002.

[6] S.V.N. Vijayendra, T.R. Shamala, Film forming microbial biopolymers for commercial applications-A review, Crit. Rev. Biotechnol. 34 (2014) 338–357. https://doi.org/10.3109/07388551.2013.798254.

[7] Z. Wang, K. Li, Q. Xu, G. Fu, H. Li, W. Yang, Preparation and evaluation of chitosan- and hyaluronic acid-grafted pullulan succinate films for skin wound healing, Int. J. Biol. Macromol. 223 (2022) 1432–1442. https://doi.org/10.1016/j.ijbiomac.2022.11.100.

[8] K. Sharma, N. Sharma, S. Handa, S. Pathania, Purification and characterization of novel exopolysaccharides produced from Lactobacillus paraplantarum KM1 isolated from human milk and its cytotoxicity, J. Genet. Eng. Biotechnol. 18 (2020). https://doi.org/10.1186/s43141-020-00063-5.

[9] M. Moscovici, Present and future medical applications of microbial exopolysaccharides, Front. Microbiol. 6 (2015) 1–11. https://doi.org/10.3389/fmicb.2015.01012.

[10] A. Tabernero, S. Cardea, Microbial exopolysaccharides as drug carriers, Polymers (Basel). 12 (2020). https://doi.org/10.3390/POLYM12092142.

[11] A. Kaith, U. Garg, N. Jain, M. Pandey, S. Kaul, B. Gorain, M.C.I.M. Amin, Pullulan as a sustained release carrier for ocular drug delivery: a review, Int. J. Biol. Macromol. 309 (2025) 143146. https://doi.org/10.1016/j.ijbiomac.2025.143146.

[12] W. Gao, Y. Liu, S. Wu, Properties of pullulan and its effects on starch gelatinization, retrogradation, and protein interaction: A review, Food Chem. 483 (2025) 144337. https://doi.org/10.1016/j.foodchem.2025.144337.

[13] R. Singh, R. Gaur, S. Bansal, P. Biswas, P.K. Pandey, F. Jamal, S. Tiwari, M.K. Gaur, Aureobasidium pullulans - An Industrially Important Pullulan Producing Black Yeast, Int. J. Curr. Microbiol. Appl. Sci. 4 (2015) 605–622.

[14] M.K. Singh, R., Gaur, R., Tiwari, S. and Gaur, PRODUCTION OF PULLULAN BY A THERMOTOLERANT AUREOBASIDIUM PULLULANS STRAIN IN NON-STIRRED FED BATCH FERMENTATION PROCESS, Brazilian J. Microbiol. 43 (2012) 1042–1050.

[15] R.S. Singh, G.K. Saini, J.F. Kennedy, Pullulan: Microbial sources, production and applications, Carbohydr. Polym. 73 (2008) 515–531. https://doi.org/10.1016/j.carbpol.2008.01.003.

[16] N. Aquinas, C.H. Chithra, M.R. Bhat, Progress in bioproduction, characterization and applications of pullulan: a review, Springer Berlin Heidelberg, 2024.

https://doi.org/10.1007/s00289-024-05300-2.
[17] J.S. Webb, M. Nixon, I.M. Eastwood, M. Greenhalgh, G.D. Robson, P.S. Handley, Fungal colonization and biodeterioration of plasticized polyvinyl chloride, Appl. Environ. Microbiol. 66 (2000) 3194–3200. https://doi.org/10.1128/AEM.66.8.3194-3200.2000.
[18] P. Kremnický, L., Slavikova, E., Mislovičová, D. and Biely, Production of extracellular β-mannanases by yeasts and yeast-like microorganisms, Folia Microbiol. (Praha). 41 (1996) 43–47.
[19] P. Kremnický, L. and Biely, β-Mannanolytic system of Aureobasidium pullulans, Arch. Microbiol. 167 (1997) 350–355.
[20] S. and A. Ramos, A vegetative cycle of Pullularia pullulans, Trans. Br. Mycol. Soc. 64 (1975) 129-IN9.
[21] J.M. Deshpande, M.S., Rale, V.B. and Lynch, Aureobasidium pullulans in applied microbiology: a status report, Enzyme Microb. Technol. 14 (1992) 514–527.
[22] K.C. Cheng, A. Demirci, J.M. Catchmark, Pullulan: Biosynthesis, production, and applications, Appl. Microbiol. Biotechnol. 92 (2011) 29–44. https://doi.org/10.1007/s00253-011-3477-y.
[23] Z. Chi, S. Zhao, Optimization of medium and cultivation conditions for pullulan production by a new pullulan-producing yeast strain, Enzyme Microb. Technol. 33 (2003) 206–211. https://doi.org/10.1016/S0141-0229(03)00119-4.
[24] Y. Li, Z. Chi, G.Y. Wang, Z.P. Wang, G.L. Liu, C.F. Lee, Z.C. Ma, Z.M. Chi, Taxonomy of Aureobasidium spp. and biosynthesis and regulation of their extracellular polymers, Crit. Rev. Microbiol. 41 (2015) 228–237. https://doi.org/10.3109/1040841X.2013.826176.
[25] R. Taguchi, Y. Sakano, Y. Kikuchi, M. Sakuma, T. Kobayashi, Synthesis of pullulan by acetone-dried cells and cell-free enzyme from pullularia pullulans, and the participation of lipid intermediate, Agric. Biol. Chem. 37 (1973) 1635–1641. https://doi.org/10.1080/00021369.1973.10860882.
[26] G.K. Singh, R.S. and Saini, Biosynthesis of pullulan and its applications in food and pharmaceutical industry, in: Microorg. Sustain. Agric. Biotechnol., 2012: pp. 509–553.
[27] J. Guo, S. Huang, Y. Chen, X. Guo, D. Xiao, Discovering the role of the apolipoprotein gene and the genes in the putative pullulan biosynthesis pathway on the synthesis of pullulan, heavy oil and melanin in Aureobasidium pullulans, World J. Microbiol. Biotechnol. 34 (2018) 1–8. https://doi.org/10.1007/s11274-017-2398-z.
[28] X. Duan, Z. Chi, L. Wang, X. Wang, Influence of different sugars on pullulan production and activities of α-phosphoglucose mutase, UDPG-pyrophosphorylase and glucosyltransferase involved in pullulan synthesis in Aureobasidium pullulans Y68, Carbohydr. Polym. 73 (2008) 587–593. https://doi.org/10.1016/j.carbpol.2007.12.028.
[29] K.I. Shingel, Current knowledge on biosynthesis, biological activity, and chemical modification of the exopolysaccharide, pullulan, Carbohydr. Res. 339 (2004) 447–460. https://doi.org/10.1016/j.carres.2003.10.034.
[30] I. Widyastuti, S. Wikarsa, S.N. Soewandhi, Elfahmi, Production, optimisation and characterisation of exopolysaccharides from Aureobasidium pullulans Y428 using Melinjo seeds (Gnetum gnemon Linn.) as substrate, Nat. Prod. Res. 0 (2025) 1–10. https://doi.org/10.1080/14786419.2025.2509880.
[31] R.F.T. Tagne, M.M. Cruz-Santos, F.A.F. Antunes, V.P. Shibukawa, S.B. Miano, J.A.A. Kenfack, S.S. da Silva, S.B.L. Ngomade, J.C. Santos, Pullulan Production from Sugarcane Bagasse Hemicellulosic Hydrolysate by Aureobasidium pullulans ATCC 42023 inBubble Column Reactor, Fermentation 10 (2024) 1–14. https://doi.org/10.3390/fermentation10060322.

[32] G.N. Mujdeci, M.T. Bozdemir, Z.Y. Ozbas, Experimental modeling and optimization of pullulan production by Aureobasidium pullulans AZ-6, Springer Berlin Heidelberg, 2024. https://doi.org/10.1007/s00289-024-05146-8.
[33] V. Dsouza, G. Thoidingjam, A. Saleh, M. Zavrel, An iterative approach to statistical optimization of exopolysaccharide produced by fermentation of Aureobasidium pullulans, Biotechnol. Reports 47 (2025) e00914. https://doi.org/10.1016/j.btre.2025.e00914.
[34] J. Chen, Y. Lu, L. Liu, R. Bai, S. Zhang, Y. Hao, F. Xu, B. Wei, H. Zhao, Characteristic analysis and fermentation optimization of a novel Aureobasidium pullulans RM1603 with high pullulan yield, J. Biosci. Bioeng. 137 (2024) 335–343. https://doi.org/10.1016/j.jbiosc.2023.12.018.
[35] S. Chen, H. Zheng, J. Gao, H. Song, W. Bai, High-level production of pullulan and its biosynthesis regulation in Aureobasidium pullulans BL06, Front. Bioeng. Biotechnol. 11 (2023) 1–10. https://doi.org/10.3389/fbioe.2023.1131875.
[36] V. Ganduri, U. Mangamuri, R. Babu, Response surface optimization of fermentation parameters for pullulan elaboration from jaggery by Aureobasidium pullulans MTCC 2195, J. Chem. Pharm. Sci. 10 (2017) 457–461.
[37] S.V.N. Vijayendra, D. Bansal, M.S. Prasad, K. Nand, Jaggery: A novel substrate for pullulan production by Aureobasidium pullulans CFR-77, Process Biochem. 37 (2001) 359–364. https://doi.org/10.1016/S0032-9592(01)00214-X.
[38] B. Akdeniz Oktay, M.T. Bozdemir, Z.Y. Ozbas, Optimization of hazelnut husk medium for pullulan production by a domestic A. pullulans strain, Prep. Biochem. Biotechnol. 53 (2023) 317–330. https://doi.org/10.1080/10826068.2022.2084625.
[39] K. Zhang, L. Yue, J. Cong, J. Zhang, Z. Feng, Q. Yang, X. Lu, Increased production of pullulan in Aureobasidium pullulans YQ65 through reduction of intracellular glycogen content, Carbohydr. Polym. 352 (2025) 123196. https://doi.org/10.1016/j.carbpol.2024.123196.
[40] R.S. Singh, N. Kaur, A. Pandey, J.F. Kennedy, Hyper-production of pullulan from de-oiled rice bran by Aureobasidium pullulans in a stirred tank reactor and its characterization, Bioresour. Technol. Reports 11 (2020). https://doi.org/10.1016/j.biteb.2020.100494.
[41] R. Viveka, S. Varjani, N. Ekambaram, Valorization of cassava waste for pullulan production by Aureobasidium pullulans MTCC 1991, Energy Environ. 32 (2021) 1086–1102. https://doi.org/10.1177/0958305X20908065.
[42] H. Mirzaee, F. Khodaiyan, J.F. Kennedy, S.S. Hosseini, Production, optimization and characterization of pullulan from sesame seed oil cake as a new substrate by Aureobasidium pullulans, Carbohydr. Polym. Technol. Appl. 1 (2020) 0–7. https://doi.org/10.1016/j.carpta.2020.100004.
[43] R. Terán Hilares, J. Resende, C.A. Orsi, M.A. Ahmed, T.M. Lacerda, S.S. da Silva, J.C. Santos, Exopolysaccharide (pullulan) production from sugarcane bagasse hydrolysate aiming to favor the development of biorefineries, Int. J. Biol. Macromol. 127 (2019) 169–177. https://doi.org/10.1016/j.ijbiomac.2019.01.038.
[44] N. Sharma, G.S. Prasad, A.R. Choudhury, Utilization of corn steep liquor for biosynthesis of pullulan, an important exopolysaccharide, Carbohydr. Polym. 93 (2013) 95–101. https://doi.org/10.1016/j.carbpol.2012.06.059.
[45] S. Srikanth, M. Swathi, M. Tejaswini, G. Sharmila, C. Muthukumaran, M.K. Jaganathan, K. Tamilarasan, Statistical optimization of molasses based exopolysaccharide and biomass production by Aureobasidium pullulans MTCC 2195, Biocatal. Agric. Biotechnol. 3 (2014) 7–12. https://doi.org/10.1016/j.bcab.2013.11.011.
[46] A. Mehta, G.S. Prasad, A.R. Choudhury, Cost effective production of pullulan from

agri-industrial residues using response surface methodology, Int. J. Biol. Macromol. 64 (2014) 252–256. https://doi.org/10.1016/j.ijbiomac.2013.12.011.
[47] G. Sharmila, C. Muthukumaran, G. Nayan, B. Nidhi, Extracellular Biopolymer Production by Aureobasidium pullulans MTCC 2195 Using Jackfruit Seed Powder, J. Polym. Environ. 21 (2013) 487–494. https://doi.org/10.1007/s10924-012-0459-9.
[48] Y. Chen, J. Guo, F. Li, M. Liu, X. Zhang, X. Guo, D. Xiao, Production of pullulan from xylose and hemicellulose hydrolysate by Aureobasidium pullulans AY82 with pH control and DL-dithiothreitol addition, Biotechnol. Bioprocess Eng. 19 (2014) 282–288. https://doi.org/10.1007/s12257-013-0715-4.
[49] C. An, S. jian Ma, F. Chang, W. jiao Xue, Efficient production of pullulan by Aureobasidium pullulans grown on mixtures of potato starch hydrolysate and sucrose, Brazilian J. Microbiol. 48 (2017) 180–185. https://doi.org/10.1016/j.bjm.2016.11.001.
[50] S. K.R., V. Ponnusami, Review on production, downstream processing and characterization of microbial pullulan, Carbohydr. Polym. 173 (2017) 573–591. https://doi.org/10.1016/j.carbpol.2017.06.022.
[51] K. Thirumavalavan, T.R. Manikkadan, R. Dhanasekar, Pullulan production from coconut by-products by Aureobasidium pullulans, African J. Biotechnol. 8 (2009) 254–258.
[52] R.S. Singh, N. Kaur, J.F. Kennedy, Pullulan production from agro-industrial waste and its applications in food industry: A review, Carbohydr. Polym. 217 (2019) 46–57. https://doi.org/10.1016/j.carbpol.2019.04.050.
[53] K.R. Sugumaran, E. Gowthami, B. Swathi, S. Elakkiya, S.N. Srivastava, R. Ravikumar, D. Gowdhaman, V. Ponnusami, Production of pullulan by Aureobasidium pullulans from Asian palm kernel: A novel substrate, Carbohydr. Polym. 92 (2013) 697–703. https://doi.org/10.1016/j.carbpol.2012.09.062.
[54] S.K. Sheoran, K.K. Dubey, D.P. Tiwari, B.P. Singh, Directive Production of Pullulan by Altering Cheap Source of Carbons and Nitrogen at 5 L Bioreactor Level, ISRN Chem. Eng. 2012 (2012) 1–5. https://doi.org/10.5402/2012/867198.
[55] S. Wu, Z. Jin, Q. Tong, H. Chen, Sweet potato: A novel substrate for pullulan production by Aureobasidium pullulans, Carbohydr. Polym. 76 (2009) 645–649. https://doi.org/10.1016/j.carbpol.2008.11.034.
[56] A. Hafez, H. Abdelhady, M. Sharaf, T.E.-T.-J.A.S. Res, undefined 2007, Bioconversion of various industrial by-products and agricultural wastes into pullulan, Citeseer 3 (2007) 1416–1425. https://citeseerx.ist.psu.edu/document?repid=rep1&type=pdf&doi=7698b233081f12cd38ed7054b474796bdea0a1d0.
[57] J. Yang, Y. Zhang, S. Zhao, Q. Zhou, X. Xin, L. Chen, Statistical optimization of medium for pullulan production by aureobasidium pullulans NCPS2016 using fructose and soybean meal hydrolysates, Molecules 23 (2018). https://doi.org/10.3390/molecules23061334.
[58] K.R. Sugumaran, V. Ponnusami, Conventional optimization of aqueous extraction of pullulan in solid-state fermentation of cassava bagasse and Asian palm kernel, Biocatal. Agric. Biotechnol. 10 (2017) 204–208. https://doi.org/10.1016/j.bcab.2017.03.010.
[59] K.R. Sugumaran, V. Ponnusami, Statistical modeling of pullulan production and its application in pullulan acetate nanoparticles synthesis, Int. J. Biol. Macromol. 81 (2015) 867–876. https://doi.org/10.1016/j.ijbiomac.2015.09.025.
[60] K.R. Sugumaran, P. Jothi, V. Ponnusami, Bioconversion of industrial solid waste - Cassava bagasse for pullulan production in solid state fermentation, Carbohydr. Polym. 99 (2014) 22–30. https://doi.org/10.1016/j.carbpol.2013.08.039.
[61] S.S. Haghighatpanah, N., Khodaiyan, F., Kennedy, J. F., & Hosseini, Optimization and

characterization of pullulan obtained from corn bran hydrolysates by Aerobasidiom pullulan KY767024, 33 (2021).
[62] R.S. Singh, N. Kaur, Understanding response surface optimization of medium composition for pullulan production from de-oiled rice bran by Aureobasidium pullulans, Food Sci. Biotechnol. 28 (2019) 1507–1520. https://doi.org/10.1007/s10068-019-00585-w.
[63] R. Terán Hilares, J. Resende, C.A. Orsi, M.A. Ahmed, T.M. Lacerda, S.S. da Silva, J.C. Santos, Exopolysaccharide (pullulan) production from sugarcane bagasse hydrolysate aiming to favor the development of biorefineries, Int. J. Biol. Macromol. 127 (2019) 169–177. https://doi.org/10.1016/j.ijbiomac.2019.01.038.
[64] D. Wang, X. Ju, D. Zhou, G. Wei, Efficient production of pullulan using rice hull hydrolysate by adaptive laboratory evolution of Aureobasidium pullulans, Bioresour. Technol. 164 (2014) 12–19. https://doi.org/10.1016/j.biortech.2014.04.036.
[65] H. Jiang, S.J. Xue, Y.F. Li, G.L. Liu, Z.M. Chi, Z. Hu, Z. Chi, Efficient transformation of sucrose into high pullulan concentrations by Aureobasidium melanogenum TN1-2 isolated from a natural honey, Food Chem. 257 (2018) 29–35. https://doi.org/10.1016/j.foodchem.2018.03.003.
[66] L. Sheng, Q. Tong, M. Ma, Why sucrose is the most suitable substrate for pullulan fermentation by Aureobasidium pullulans CGMCC1234?, Enzyme Microb. Technol. 92 (2016) 49–55. https://doi.org/10.1016/j.enzmictec.2016.06.016.
[67] K.C. Cheng, A. Demirci, J. Catchmark, Effect of temperature, carbon source, yeast extract, and pH on pullulan production by aureobasidium pullulans, Am. Soc. Agric. Biol. Eng. Annu. Int. Meet. 2009, ASABE 2009 4 (2009) 2394–2407. https://doi.org/10.13031/2013.27038.
[68] G. Chen, J. Wang, Y. Su, Y. Zhu, G. Zhang, H. Zhao, H. Liu, Y. Yang, R. Nian, H. Zhang, Y. Wei, M. Xian, Pullulan production from synthetic medium by a new mutant of Aureobasidium pullulans, Prep. Biochem. Biotechnol. 47 (2017) 963–969. https://doi.org/10.1080/10826068.2017.1350979.
[69] Y. Göksungur, P. Uzunoullari, S. Dağbağli, Optimization of pullulan production from hydrolysed potato starch waste by response surface methodology, Carbohydr. Polym. 83 (2011) 1330–1337. https://doi.org/10.1016/j.carbpol.2010.09.047.
[70] J.H. Lee, J.H. Kim, I.H. Zhu, X.B. Zhan, J.W. Lee, D.H. Shin, S.K. Kim, Optimization of conditions for the production of pullulan and high molecular weight pullulan by Aureobasidium pullulans, Biotechnol. Lett. 23 (2001) 817–820. https://doi.org/10.1023/A:1010365706691.
[71] L. Sheng, G. Zhu, Q. Tong, Comparative proteomic analysis of Aureobasidium pullulans in the presence of high and low levels of nitrogen source, J. Agric. Food Chem. 62 (2014) 10529–10534. https://doi.org/10.1021/jf503390f.
[72] L. Jiang, S. Wu, J.M. Kim, Effect of different nitrogen sources on activities of UDPG-pyrophosphorylase involved in pullulan synthesis and pullulan production by Aureobasidium pullulans, Carbohydr. Polym. 86 (2011) 1085–1088. https://doi.org/10.1016/j.carbpol.2011.05.016.
[73] Y. Wang, J. Wen, D. Jia, C. Piao, J. Liu, H. Yu, J. Liu, Response surface optimization of the nitrogen source for pullulan production by Aureobasidium pullulans CGMCC3945 with corn steep liquor, (2016). https://doi.org/10.2991/ifeesd-16.2016.153.
[74] S.M. Wani, S.A. Mir, F.A. Khanday, F.A. Masoodi, Advances in pullulan production from agro-based wastes by Aureobasidium pullulans and its applications, Innov. Food Sci. Emerg. Technol. 74 (2021). https://doi.org/10.1016/j.ifset.2021.102846.
[75] B.S. Campbell, A.B.M. Siddique, B.M. McDougall, R.J. Seviour, Which morphological

forms of the fungus Aureobasidium pullulans are responsible for pullulan production?, FEMS Microbiol. Lett. 232 (2004) 225–228. https://doi.org/10.1016/S0378-1097(04)00076-X.

[76] P. Badhwar, A. Kumar, A. Yadav, P. Kumar, R. Siwach, D. Chhabra, K.K. Dubey, Improved pullulan production and process optimization using novel GA–ANN and GA–ANFIS hybrid statistical tools, Biomolecules 10 (2020). https://doi.org/10.3390/biom10010124.

[77] G. Chen, Y. Zhu, G. Zhang, H. Liu, Y. Wei, P. Wang, F. Wang, M. Xian, H. Xiang, H. Zhang, Optimization and characterization of pullulan production by a newly isolated high-yielding strain Aureobasidium melanogenum, Prep. Biochem. Biotechnol. 49 (2019) 557–566. https://doi.org/10.1080/10826068.2019.1591988.

[78] L. Sheng, G. Tang, P. Su, J. Zhang, Q. Xiao, Q. Tong, M. Ma, Understanding the influence of Tween 80 on pullulan fermentation by Aureobasidium pullulans CGMCC1234, Carbohydr. Polym. 136 (2016) 1332–1337. https://doi.org/10.1016/j.carbpol.2015.10.058.

[79] L. Sheng, G. Zhu, Q. Tong, Mechanism study of Tween 80 enhancing the pullulan production by Aureobasidium pullulans, Carbohydr. Polym. 97 (2013) 121–123. https://doi.org/10.1016/j.carbpol.2013.04.058.

[80] L. Sheng, G. Zhu, Q. Tong, Effect of uracil on pullulan production by Aureobasidium pullulans CGMCC1234, Carbohydr. Polym. 101 (2014) 435–437. https://doi.org/10.1016/j.carbpol.2013.09.063.

[81] A. Forabosco, G. Bruno, L. Sparapano, G. Liut, D. Marino, F. Delben, Pullulans produced by strains of Cryphonectria parasitica - I. Production and characterisation of the exopolysaccharides, Carbohydr. Polym. 63 (2006) 535–544. https://doi.org/10.1016/j.carbpol.2005.10.005.

[82] B. and Duy, Medium Optimization for Pullulan Production, 48 (1984) 26–30.

[83] R.F. Sena, M.C. Costelli, L.H. Gibson, R.W. Coughlin, Enhanced production of pullulan by two strains of A. pullulans with different concentrations of soybean oil in sucrose solution in batch fermentations, Brazilian J. Chem. Eng. 23 (2006) 507–515. https://doi.org/10.1590/S0104-66322006000400008.

[84] R.S. Singh, G.K. Saini, J.F. Kennedy, Downstream processing and characterization of pullulan from a novel colour variant strain of Aureobasidium pullulans FB-1, Carbohydr. Polym. 78 (2009) 89–94. https://doi.org/10.1016/j.carbpol.2009.03.040.

[85] Y.C. Shin, Y.H. Kim, H.S. Lee, S.J. Cho, S.M. Byun, Production of Exopolysaccharide pullulan from inulin by a mixed culture of Aureobasidium pullulans and Kluyveromyces fragilis, Biotechnol. Bioeng. 33 (1989) 129–133. https://doi.org/10.1002/bit.260330117.

[86] D.K. Kachhawa, P. Bhattacharjee, R.S. Singhal, Studies on downstream processing of pullulan, Carbohydr. Polym. 52 (2003) 25–28. https://doi.org/10.1016/S0144-8617(02)00261-8.

[87] R. Srikanth, C.H.S.S.S. Reddy, G. Siddartha, M.J. Ramaiah, K.B. Uppuluri, Review on production, characterization and applications of microbial levan, Carbohydr. Polym. 120 (2015) 102–114. https://doi.org/10.1016/j.carbpol.2014.12.003.

[88] J. Schmitt, H.C. Flemming, FTIR-spectroscopy in microbial and material analysis, Int. Biodeterior. Biodegrad. 41 (1998) 1–11. https://doi.org/10.1016/S0964-8305(98)80002-4.

[89] R.S. Singh, H. Singh, G.K. Saini, Response surface optimization of the critical medium components for pullulan production by Aureobasidium pullulans FB-1, Appl. Biochem. Biotechnol. 152 (2009) 42–53. https://doi.org/10.1007/s12010-008-8180-9.

[90] H. zhu Zhang, F. ping Gao, L. rong Liu, X. min Li, Z. min Zhou, X. du Yang, Q. qing Zhang, Pullulan acetate nanoparticles prepared by solvent diffusion method for

epirubicin chemotherapy, Colloids Surfaces B Biointerfaces 71 (2009) 19–26. https://doi.org/10.1016/j.colsurfb.2008.12.039.
[91] M. Tako, Y. Dobashi, Y. Tamaki, T. Konishi, M. Yamada, H. Ishida, M. Kiso, Identification of rare 6-deoxy-d-altrose from an edible mushroom (Lactarius lividatus), Carbohydr. Res. 350 (2012) 25–30. https://doi.org/10.1016/j.carres.2011.12.016.
[92] S.E. Bulman, C.M. Coleman, J.M. Murphy, N. Medcalf, A.E. Ryan, F. Barry, Pullulan: A new cytoadhesive for cell-mediated cartilage repair, Stem Cell Res. Ther. 6 (2015) 1–12. https://doi.org/10.1186/s13287-015-0011-7.
[93] R.S. Singh, N. Kaur, V. Rana, J.F. Kennedy, Recent insights on applications of pullulan in tissue engineering, Carbohydr. Polym. 153 (2016) 455–462. https://doi.org/10.1016/j.carbpol.2016.07.118.
[94] Amrita, A. Arora, P. Sharma, D.S. Katti, Pullulan-based composite scaffolds for bone tissue engineering: Improved osteoconductivity by pore wall mineralization, Carbohydr. Polym. 123 (2015) 180–189. https://doi.org/10.1016/j.carbpol.2015.01.038.
[95] M. Kang, M. Koosha, T. Li, X. Geng, The favorable role of oxidized pullulan as a multipurpose crosslinker in polyvinyl alcohol (PVA)/chitosan/collagen films for promoting human skin fibroblast viability, antibacterial activity and healing of methicillin-resistant Staphylococcus aureus (MRSA, Int. J. Biol. Macromol. 311 (2025) 143435. https://doi.org/10.1016/j.ijbiomac.2025.143435.
[96] T. Liu, H. Lei, L. Qu, C. Zhu, X. Ma, D. Fan, Algae-inspired chitosan-pullulan-based multifunctional hydrogel for enhanced wound healing, Carbohydr. Polym. 347 (2025) 122751. https://doi.org/10.1016/j.carbpol.2024.122751.
[97] Q. Li, X. Lai, Y. Duan, F. Jiang, Y. Li, Z. Huang, S. Liu, Y. Wang, C. Jiang, C. Zhang, X. Pan, 3D nanofiber sponge based on natural insect quaternized chitosan/pullulan/citric acid for accelerating wound healing, Carbohydr. Polym. 348 (2025) 122827. https://doi.org/10.1016/j.carbpol.2024.122827.
[98] J. Li, Y., Xiang, Y., Chen, Y., Wang, Y., Dong, W., Liu, Y., Qi, X. and Shen, A natural eumelanin-assisted pullulan/chitosan hydrogel for the management of diabetic oral ulcers, (2025) 2400526.
[99] J. Reinoza, R. Tiwari, I. Morales, L. Sotelo, D. Sengupta, J.P. Hernandez, V. Padilla, M.M. Yallapu, K. Lozano, Fabrication of pullulan-chitosan fiber membranes for enhanced hemostatic applications, Int. J. Biol. Macromol. 308 (2025) 142552. https://doi.org/10.1016/j.ijbiomac.2025.142552.
[100] I.A. Plugariu, M. Bercea, L.M. Gradinaru, D. Rusu, A. Lupu, Poly(vinyl alcohol)/Pullulan Composite Hydrogels as a Potential Platform for Wound Dressing Applications, Gels 9 (2023). https://doi.org/10.3390/gels9070580.
[101] F. Jiang, Y. Duan, Q. Li, X. Li, Y. Li, Y. Wang, S. Liu, M. Liu, C. Zhang, X. Pan, Insect chitosan/pullulan/gallium photo-crosslinking hydrogels with multiple bioactivities promote MRSA-infected wound healing, Carbohydr. Polym. 334 (2024) 122045. https://doi.org/10.1016/j.carbpol.2024.122045.
[102] Z. Wang, K. Li, Q. Xu, G. Fu, H. Li, W. Yang, Preparation and evaluation of chitosan- and hyaluronic acid-grafted pullulan succinate films for skin wound healing, Int. J. Biol. Macromol. 223 (2022) 1432–1442. https://doi.org/10.1016/j.ijbiomac.2022.11.100.
[103] M. Shahriari-Khalaji, G. Hu, L. Chen, Z. Cao, T. Andreeva, X. Xiong, R. Krastev, F.F. Hong, Functionalization of Aminoalkylsilane-Grafted Bacterial Nanocellulose with ZnO-NPs-Doped Pullulan Electrospun Nanofibers for Multifunctional Wound Dressing, ACS Biomater. Sci. Eng. 7 (2021) 3933–3946. https://doi.org/10.1021/acsbiomaterials.1c00444.
[104] Y. Duan, K. Li, H. Wang, T. Wu, Y. Zhao, H. Li, H. Tang, W. Yang, Preparation and evaluation of curcumin grafted hyaluronic acid modified pullulan polymers as a

functional wound dressing material, Carbohydr. Polym. 238 (2020) 116195. https://doi.org/10.1016/j.carbpol.2020.116195.
[105] V.S. Priya, K. Iyappan, V.S. Gayathri, S. William, L. Suguna, Influence of pullulan hydrogel on sutureless wound healing in rats, Wound Med. 14 (2016) 1–5. https://doi.org/10.1016/j.wndm.2016.05.003.
[106] G. Mao, Z. Wang, S. Tian, H. Li, W. Yang, A novel chitosan-hyaluronic acid-pullulan composite film wound dressing for effectively inhibiting bacteria and accelerating wound healing, Mater. Today Commun. 33 (2022) 104801. https://doi.org/10.1016/j.mtcomm.2022.104801.
[107] J. Chen, K., Sivaraj, D., Davitt, M.F., Leeolou, M.C., Henn, D., Steele, S.R., Huskins, S.L., Trotsyuk, A.A., Kussie, H.C., Greco, A.H. and Padmanabhan, Pullulan-Collagen hydrogel wound dressing promotes dermal remodelling and wound healing compared to commercially available collagen dressings, Wound Repair Regen. 30 (2022) 397–408.
[108] H. Li, Y. Xue, B. Jia, Y. Bai, Y. Zuo, S. Wang, Y. Zhao, W. Yang, H. Tang, The preparation of hyaluronic acid grafted pullulan polymers and their use in the formation of novel biocompatible wound healing film, Carbohydr. Polym. 188 (2018) 92–100. https://doi.org/10.1016/j.carbpol.2018.01.102.
[109] H. Mert, B. Özkahraman, H. Damar, A novel wound dressing material: Pullulan grafted copolymer hydrogel via UV copolymerization and crosslinking, J. Drug Deliv. Sci. Technol. 60 (2020). https://doi.org/10.1016/j.jddst.2020.101962.
[110] D. Atila, A. Karataş, D. Keskin, A. Tezcaner, Pullulan hydrogel-immobilized bacterial cellulose membranes with dual-release of vitamin C and E for wound dressing applications, Int. J. Biol. Macromol. 218 (2022) 760–774. https://doi.org/10.1016/j.ijbiomac.2022.07.160.
[111] N. Khandan-Nasab, E. Mahdipour, S. Askarian, M.R. Kalantari, N. Ramezanian, R. Kazemi Oskuee, Design and characterization of adipose-derived mesenchymal stem cell loaded alginate/pullulan/hyaluronic acid hydrogel scaffold for wound healing applications, Int. J. Biol. Macromol. 241 (2023) 124556. https://doi.org/10.1016/j.ijbiomac.2023.124556.
[112] C.N. Elangwe, S.N. Morozkina, A. V. Podshivalov, M. V. Uspenskaya, Evaluation of composition effects on the tissue-adhesive, mechanical and physical properties of physically crosslinked hydrogels based on chitosan and pullulan for wound healing applications, Int. J. Biol. Macromol. 276 (2024) 133857. https://doi.org/10.1016/j.ijbiomac.2024.133857.
[113] P. Thangavel, S.P. Vilvanathan, I. Kuttalam, S. Lonchin, Topical administration of pullulan gel accelerates skin tissue regeneration by enhancing collagen synthesis and wound contraction in rats, Int. J. Biol. Macromol. 149 (2020) 395–403. https://doi.org/10.1016/j.ijbiomac.2020.01.187.
[114] A.S. Soubhagya, K. Balagangadharan, N. Selvamurugan, D. Sathya Seeli, M. Prabaharan, Preparation and characterization of chitosan/carboxymethyl pullulan/bioglass composite films for wound healing, J. Biomater. Appl. 36 (2022) 1151–1163. https://doi.org/10.1177/08853282211050161.
[115] A. Bal-Öztürk, G. Torkay, N. İdil, R.O. Akar, Z. Özbaş, B. Özkahraman, Propolis-loaded photocurable methacrylated pullulan films: Evaluation of mechanical, antibacterial, biocompatibility, wound healing and pro-angiogenic abilities, Int. J. Biol. Macromol. 282 (2024). https://doi.org/10.1016/j.ijbiomac.2024.137071.
[116] A.D. Dalgic, E. Koman, A. Karatas, A. Tezcaner, D. Keskin, Natural origin bilayer pullulan-PHBV scaffold for wound healing applications, Biomater. Adv. 134 (2022) 112554. https://doi.org/10.1016/j.msec.2021.112554.
[117] G. Selvakumar, S. Lonchin, Bioactive functional collagen-oxidized pullulan scaffold

loaded with polydatin for treating chronic wounds, Biomater. Adv. 140 (2022) 213078. https://doi.org/10.1016/j.bioadv.2022.213078.
[118] J. Su, W. Yu, X. Guo, C. Wang, Q. Wang, B. Chen, Y. Hu, H. Dai, Development and Evaluation of a Novel Antibacterial Wound Dressing: A Powder Preparation Based on Cross-Linked Pullulan with Polyhexamethylene Biguanide for Hydrogel-Transition in Advanced Wound Management and Infection Control, Polymers (Basel). 16 (2024). https://doi.org/10.3390/polym16101352.
[119] W. Cui, C. Gong, Y. Liu, Y. Yue, J. Wang, Z. Yang, J. Yang, Composite antibacterial hydrogels based on two natural products pullulan and ε-poly-L-lysine for burn wound healing, Int. J. Biol. Macromol. 277 (2024) 134208. https://doi.org/10.1016/j.ijbiomac.2024.134208.
[120] S. Roy, P. Haloi, R. Choudhary, S. Chawla, M. Kumari, V.B. Konkimalla, A. Jaiswal, Quaternary Pullulan-Functionalized 2D MoS2Glycosheets: A Potent Bactericidal Nanoplatform for Efficient Wound Disinfection and Healing, ACS Appl. Mater. Interfaces 15 (2023) 24209–24227. https://doi.org/10.1021/acsami.3c04390.
[121] A. Younas, Z. Dong, Z. Hou, M. Asad, M. Li, N. Zhang, A chitosan/fucoidan nanoparticle-loaded pullulan microneedle patch for differential drug release to promote wound healing, Carbohydr. Polym. 306 (2023) 120593. https://doi.org/10.1016/j.carbpol.2023.120593.
[122] T.H. Park, S. Lee, R. Amatya, P. Maharjan, H.J. Kim, W.S. Park, M.J. Ahn, S.Y. Kim, C. Moon, H. Cheong, K.A. Min, M.C. Shin, Development and characterization of a superabsorbing hydrogel film containing Ulmus davidiana var. Japonica root bark and pullulan for skin wound healing, Saudi Pharm. J. 28 (2020) 791–802. https://doi.org/10.1016/j.jsps.2020.05.007.
[123] P. Nonsuwan, P.P. Phiboonchaiyanan, N. Hirun, P. Kraisit, Curcumin-loaded methacrylate pullulan with grafted carboxymethyl-β-cyclodextrin to form hydrogels for wound healing: In vitro evaluation, Carbohydr. Polym. 321 (2023). https://doi.org/10.1016/j.carbpol.2023.121294.
[124] Y. Zhao, R. Li, Y. Liu, L. Song, Z. Gao, Z. Li, X. Peng, P. Wang, An injectable, self-healable, antibacterial, and pro-healing oxidized pullulan polysaccharide/carboxymethyl chitosan hydrogel for early protection of open abdominal wounds, Int. J. Biol. Macromol. 250 (2023). https://doi.org/10.1016/j.ijbiomac.2023.126282.
[125] F. Ajalloueian, S. Asgari, P.R. Guerra, C.I. Chamorro, O. Ilchenco, S. Piqueras, M. Fossum, A. Boisen, Amoxicillin-loaded multilayer pullulan-based nanofibers maintain long-term antibacterial properties with tunable release profile for topical skin delivery applications, Int. J. Biol. Macromol. 215 (2022) 413–423. https://doi.org/10.1016/j.ijbiomac.2022.06.054.
[126] H. Aydogdu, D. Keskin, E.T. Baran, A. Tezcaner, Pullulan microcarriers for bone tissue regeneration, Mater. Sci. Eng. C 63 (2016) 439–449. https://doi.org/10.1016/j.msec.2016.03.002.
[127] S.A. Ganie, L.J. Rather, Q. Li, A review on anticancer applications of pullulan and pullulan derivative nanoparticles, Carbohydr. Polym. Technol. Appl. 2 (2021) 100115. https://doi.org/10.1016/j.carpta.2021.100115.
[128] S. Laksee, S. Puthong, T. Teerawatananond, T. Palaga, N. Muangsin, Highly efficient and facile fabrication of monodispersed Au nanoparticles using pullulan and their application as anticancer drug carriers, Carbohydr. Polym. 173 (2017) 178–191. https://doi.org/10.1016/j.carbpol.2017.05.101.
[129] F. Xu, B. Weng, R. Gilkerson, L.A. Materon, K. Lozano, Development of tannic acid/chitosan/pullulan composite nanofibers from aqueous solution for potential

applications as wound dressing, Carbohydr. Polym. 115 (2015) 16–24. https://doi.org/10.1016/j.carbpol.2014.08.081.
[130] L. Yuan, B. Guo, W. Zhong, Y. Nie, X. Yao, X. Peng, R. Wang, H. Yu, S. Yang, C. He, X. Tao, Q. Zhang, Interaction of mitoxantrone-loaded cholesterol modified pullulan nanoparticles with human serum albumin and effect on drug release, J. Nanomater. 2019 (2019). https://doi.org/10.1155/2019/8036863.
[131] G. Mocanu, M. Nichifor, L. Picton, E. About-Jaudet, D. Le Cerf, Preparation and characterization of anionic pullulan thermoassociative nanoparticles for drug delivery, Carbohydr. Polym. 111 (2014) 892–900. https://doi.org/10.1016/j.carbpol.2014.05.037.
[132] L. Vora, M. Tyagi, K. Patel, S. Gupta, P. Vavia, Self-assembled nanocomplexes of anionic pullulan and polyallylamine for DNA and pH-sensitive intracellular drug delivery, J. Nanoparticle Res. 16 (2014). https://doi.org/10.1007/s11051-014-2781-8.
[133] A. Balasso, S. Salmaso, P. Pontisso, A. Rosato, S. Quarta, A. Malfanti, F. Mastrotto, P. Caliceti, Re-programming pullulan for targeting and controlled release of doxorubicin to the hepatocellular carcinoma cells, Eur. J. Pharm. Sci. 103 (2017) 104–115. https://doi.org/10.1016/j.ejps.2017.02.016.
[134] Y. Liang, X. Zhao, P.X. Ma, B. Guo, Y. Du, X. Han, pH-responsive injectable hydrogels with mucosal adhesiveness based on chitosan-grafted-dihydrocaffeic acid and oxidized pullulan for localized drug delivery, J. Colloid Interface Sci. 536 (2019) 224–234. https://doi.org/10.1016/j.jcis.2018.10.056.
[135] X. Chen, Q.Q. Wang, N.N. Liu, G.L. Liu, Z. Chi, Z.M. Chi, A glycosyltransferase gene responsible for pullulan biosynthesis in Aureobasidium melanogenum P16, Int. J. Biol. Macromol. 95 (2017) 539–549. https://doi.org/10.1016/j.ijbiomac.2016.11.081.
[136] S.S. Priya, M.R. Rekha, Redox sensitive cationic pullulan for efficient gene transfection and drug retention in C6 glioma cells, Int. J. Pharm. 530 (2017) 401–414. https://doi.org/10.1016/j.ijpharm.2017.08.004.
[137] L. Huang, Y. Wang, X. Ling, B. Chaurasiya, C. Yang, Y. Du, J. Tu, Y. Xiong, C. Sun, Efficient delivery of paclitaxel into ASGPR over-expressed cancer cells using reversibly stabilized multifunctional pullulan nanoparticles, Carbohydr. Polym. 159 (2017) 178–187. https://doi.org/10.1016/j.carbpol.2016.11.094.
[138] J.M. Choi, B. Lee, D. Jeong, K.H. Park, E.J. Choi, Y.J. Jeon, S.D. Dindulkar, E. Cho, S.H. Do, K. Lee, I.S. Lee, S. Park, B.H. Jun, J.H. Yu, S. Jung, Characterization and regulated naproxen release of hydroxypropyl cyclosophoraose-pullulan microspheres, J. Ind. Eng. Chem. 48 (2017) 108–118. https://doi.org/10.1016/j.jiec.2016.12.026.
[139] M. Constantin, S. Bucătariu, I. Stoica, G. Fundueanu, Smart nanoparticles based on pullulan-g-poly(N-isopropylacrylamide) for controlled delivery of indomethacin: Paper dedicated to the 150th anniversary of the Romanian Academy, Int. J. Biol. Macromol. 94 (2017) 698–708. https://doi.org/10.1016/j.ijbiomac.2016.10.064.
[140] Bibeklaha, S. Maiti, Design of core-shell stearyl pullulan nanostructures for drug delivery, Mater. Today Proc. 11 (2019) 620–627. https://doi.org/10.1016/j.matpr.2019.03.019.
[141] H. Li, C. Yu, J. Zhang, Q. Li, H. Qiao, Z. Wang, D. Zeng, pH-sensitive pullulan-doxorubicin nanoparticles loaded with 1,1,2-trichlorotrifluoroethane as a novel synergist for high intensity focused ultrasound mediated tumor ablation, Int. J. Pharm. 556 (2019) 226–235. https://doi.org/10.1016/j.ijpharm.2018.12.006.
[142] S. Li, W. Dai, Z.Z. Yin, J. Gao, D. Wu, Y. Kong, Synthesis of oxidized pullulan coated mesoporous silica for pH-sensitive drug delivery, Eur. Polym. J. 122 (2020) 109399. https://doi.org/10.1016/j.eurpolymj.2019.109399.
[143] K. Lin, J. Yi, X. Mao, H. Wu, L.M. Zhang, L. Yang, Glucose-sensitive hydrogels from covalently modified carboxylated pullulan and concanavalin A for smart controlled

release of insulin, React. Funct. Polym. 139 (2019) 112–119. https://doi.org/10.1016/j.reactfunctpolym.2019.01.016.
[144] Y. Pawara, H. Mahajan, Surface-functionalized pullulan-based polymeric nanoparticles containing resveratrol: a green approach for lung cancer targeted delivery, Part. Sci. Technol. 43 (2025) 416–432. https://doi.org/10.1080/02726351.2025.2463114.
[145] T. Nakatsukasa, D. Muraoka, S. Deng, K. Yasui, S.I. Sawada, A. Shimoda, H. Matsushita, K. Matsumoto, T. Nagayasu, N. Harada, K. Akiyoshi, H. Ikeda, Antitumor immune response elicited by M2 TAM-specific DDS via C-type lectin CD209b using cholesteryl pullulan nanogel as a protein drug carrier, Biomater. Sci. 13 (2025) 2340–2350. https://doi.org/10.1039/d5bm00342c.
[146] A. Sheikhi, S. Hamedi, G. Sodeifian, F. Razmimanesh, Improvement of the dissolution of the antineoplastic drug regorafenib through impregnation into pullulan polysaccharide using supercritical fluid technology: Optimization of the process, J. CO2 Util. 93 (2025) 103040. https://doi.org/10.1016/j.jcou.2025.103040.
[147] E. Lopez-Vince, T. Simon-Yarza, C. Wilhelm, A polysaccharide-based hydrogel platform for tumor spheroid production and anticancer drug screening, Sci. Rep. 15 (2025) 1–13. https://doi.org/10.1038/s41598-025-87896-7.
[148] N. Thomas, L.E. Puluhulawa, F.R. Cindana Mo'o, A. Rusdin, A.M. Gazzali, A. Budiman, Potential of Pullulan-Based Polymeric Nanoparticles for Improving Drug Physicochemical Properties and Effectiveness, Polymers (Basel). 16 (2024) 1–20. https://doi.org/10.3390/polym16152151.
[149] P. Varadhan, M. Jayaraman, Hyalgan-decorated-ferulic acid-loaded pullulan acetate nanoparticles against gastrointestinal cancer cell lines, Emergent Mater. 7 (2024) 1115–1127. https://doi.org/10.1007/s42247-024-00634-z.
[150] R. Solanki, B. Parmar, M. Jadav, D. Pooja, H. Kulhari, S. Patel, Berberine encapsulated phenylboronic acid-conjugated pullulan nanoparticles: Synthesis, characterization and anticancer activity validated in A431 skin cancer cells and 3D spheroids, Int. J. Biol. Macromol. 273 (2024) 132737. https://doi.org/10.1016/j.ijbiomac.2024.132737.
[151] N. Barer, B. Tunc, B. Yilmaz, Y.Y. Ng, A.D. Dalgic, Using embossing ice particulate method to prepare polyvinyl alcohol/pullulan hydrogels with surface open pores loaded with microspheres for breast cancer treatment, J. Drug Deliv. Sci. Technol. 92 (2024). https://doi.org/10.1016/j.jddst.2024.105351.
[152] G.H. Fard, Z. Moinipoor, S. Anastasova-Ivanova, H.M.N. Iqbal, M. V. Dwek, S.J. Getting, T. Keshavarz, Development of chitosan, pullulan, and alginate based drug-loaded nano-emulsions as a potential malignant melanoma delivery platform, Carbohydr. Polym. Technol. Appl. 4 (2022). https://doi.org/10.1016/j.carpta.2022.100250.
[153] F. Asgari, S., Pourjavadi, A., Setayeshmehr, M., Boisen, A. and Ajalloueian, Encapsulation of drug-loaded graphene oxide-based nanocarrier into electrospun pullulan nanofibers for potential local chemotherapy of breast cancer, (2021) 2100096.
[154] H.E. Emam, H.B. Ahmed, Antitumor/antiviral carbon quantum dots based on carrageenan and pullulan, Int. J. Biol. Macromol. 170 (2021) 688–700. https://doi.org/10.1016/j.ijbiomac.2020.12.151.
[155] L. Chen, M. Qian, L. Zhang, J. Xia, Y. Bao, J. Wang, L. Guo, Y. Li, Co-delivery of doxorubicin and shRNA of Beclin1 by folate receptor targeted pullulan-based multifunctional nanomicelles for combinational cancer therapy, RSC Adv. 8 (2018) 17710–17722. https://doi.org/10.1039/c8ra01679h.
[156] D. Wang, S. Zhang, T. Zhang, G. Wan, B. Chen, Q. Xiong, J. Zhang, W. Zhang, Y. Wang, Pullulan-coated phospholipid and Pluronic F68 complex nanoparticles for carrying IR780 and paclitaxel to treat hepatocellular carcinoma by combining

photothermal therapy/photodynamic therapy and chemotherapy, Int. J. Nanomedicine 12 (2017) 8649–8670. https://doi.org/10.2147/IJN.S147591.
[157] H. Li, Y. Cui, J. Sui, S. Bian, Y. Sun, J. Liang, Y. Fan, X. Zhang, Efficient Delivery of DOX to Nuclei of Hepatic Carcinoma Cells in the Subcutaneous Tumor Model Using pH-Sensitive Pullulan-DOX Conjugates, ACS Appl. Mater. Interfaces 7 (2015) 15855–15865. https://doi.org/10.1021/acsami.5b03150.
[158] M. Lavergne, M. Derkaoui, C. Delmau, D. Letourneur, G. Uzan, C. Le Visage, Porous Polysaccharide-Based Scaffolds for Human Endothelial Progenitor Cells, Macromol. Biosci. 12 (2012) 901–910. https://doi.org/10.1002/mabi.201100431.
[159] R. Tamura, S. Uemoto, Y. Tabata, Augmented liver targeting of exosomes by surface modification with cationized pullulan, Acta Biomater. 57 (2017) 274–284. https://doi.org/10.1016/j.actbio.2017.05.013.
[160] T. Li, X. Song, C. Weng, X. Wang, J. Wu, L. Sun, X. Gong, W.N. Zeng, L. Yang, C. Chen, Enzymatically crosslinked and mechanically tunable silk fibroin/pullulan hydrogels for mesenchymal stem cells delivery, Int. J. Biol. Macromol. 115 (2018) 300–307. https://doi.org/10.1016/j.ijbiomac.2018.04.046.
[161] H. Ishikawa, J.I. Jo, Y. Tabata, Liver anti-fibrosis therapy with mesenchymal stem cells secreting hepatocyte growth factor, J. Biomater. Sci. Polym. Ed. 23 (2012) 2259–2272. https://doi.org/10.1163/156856211X614761.
[162] T.Y. Zhang, B. Huang, Z.Y. Yuan, Y.L. Hu, Y. Tabata, J.Q. Gao, Gene recombinant bone marrow mesenchymal stem cells as a tumor-targeted suicide gene delivery vehicle in pulmonary metastasis therapy using non-viral transfection, Nanomedicine Nanotechnology, Biol. Med. 10 (2014) 257–267. https://doi.org/10.1016/j.nano.2013.06.003.
[163] C.F. Seeding, A.S.C. Delivery, T ISSUE E NGINEERING AND R EGENERATIVE M EDICINE Capillary Force Seeding of Hydrogels for Adipose-Derived Stem Cell Delivery in Wounds, (2014) 1079–1089.
[164] L.S. Reichel, A. Kemmer, T. Heinze, A. Traeger, Design of pH-responsive and amphiphilic pullulan-based biological macromolecule for gene delivery, Int. J. Biol. Macromol. 301 (2025). https://doi.org/10.1016/j.ijbiomac.2025.140014.
[165] M.C.D. Sherly, R. MR, H. V.S., Cationised dextran and pullulan modified with diethyl aminoethyl methacrylate for gene delivery in cancer cells, Carbohydr. Polym. 242 (2020) 116426. https://doi.org/10.1016/j.carbpol.2020.116426.
[166] F.C. Moraes, J.C. Antunes, L.M. Forero Ramirez, P. Aprile, G. Franck, C. Chauvierre, F. Chaubet, D. Letourneur, Synthesis of cationic quaternized pullulan derivatives for miRNA delivery, Int. J. Pharm. 577 (2020) 119041. https://doi.org/10.1016/j.ijpharm.2020.119041.
[167] D.S.M. Caroline, M.R. Rekha, Exploring the efficacy of ethylene glycol dimethacrylate crosslinked cationised pullulan for gene delivery in cancer cells, J. Drug Deliv. Sci. Technol. 68 (2022) 103067. https://doi.org/10.1016/j.jddst.2021.103067.
[168] A. Farahpour, N. Ramezanian, L. Gholami, S. Askarian, A. Banisadr, R. Kazemi Oskuee, Synthesis and characterization of polyethyleneimine-terminated poly(β-amino esters) conjugated with pullulan for gene delivery, Pharm. Dev. Technol. 27 (2022) 606–614. https://doi.org/10.1080/10837450.2022.2096069.
[169] J. Zhou, A.R. Mohamed Wali, S. Ma, Y. He, D. Yue, J.Z. Tang, Z. Gu, Tailoring the Supramolecular Structure of Guanidinylated Pullulan toward Enhanced Genetic Photodynamic Therapy, Biomacromolecules 19 (2018) 2214–2226. https://doi.org/10.1021/acs.biomac.8b00273.
[170] S. Priya, M. Rekha, Disulphide cross linked pullulan based cationic polymer for improved gene delivery and efflux pump inhibition, Colloids Surfaces B Biointerfaces

146 (2016) 879–887. https://doi.org/10.1016/j.colsurfb.2016.07.013.
[171] L.T. de Carvalho, M.B. da Silva, T.A. Vieira, L.S. Maia, E.F. de Macedo, D.B. Tada, D.S. Rosa, D.R. Mulinari, S.F. Medeiros, Unveiling the potential of pullulan in enhancing ketoprofen release from PHBV filaments, Int. J. Biol. Macromol. 294 (2025) 139421. https://doi.org/10.1016/j.ijbiomac.2024.139421.
[172] X. Qin, R. He, H. Chen, D. Fu, Y. Peng, S. Meng, C. Chen, L. Yang, Methacrylated pullulan/polyethylene (glycol) diacrylate composite hydrogel for cartilage tissue engineering, J. Biomater. Sci. Polym. Ed. 32 (2021) 1057–1071. https://doi.org/10.1080/09205063.2021.1899888.
[173] N. Chauhan, P. Gupta, L. Arora, D. Pal, Y. Singh, Dexamethasone-loaded, injectable pullulan-poly(ethylene glycol) hydrogels for bone tissue regeneration in chronic inflammatory conditions, Mater. Sci. Eng. C 130 (2021) 112463. https://doi.org/10.1016/j.msec.2021.112463.
[174] N.M.N. Le, B. Le-Vinh, J.D. Friedl, A. Jalil, G. Kali, A. Bernkop-Schnürch, Polyaminated pullulan, a new biodegradable and cationic pullulan derivative for mucosal drug delivery, Carbohydr. Polym. 282 (2022) 119143. https://doi.org/10.1016/j.carbpol.2022.119143.
[175] H. Moris, A. Ghaee, M. Karimi, M. Nouri-Felekori, A. Mashak, Preparation and characterization of Pullulan-based nanocomposite scaffold incorporating Ag-Silica Janus particles for bone tissue engineering, Biomater. Adv. 135 (2022) 212733. https://doi.org/10.1016/j.bioadv.2022.212733.
[176] T. Su, W. Zhao, L. Wu, W. Dong, X. Qi, Facile fabrication of functional hydrogels consisting of pullulan and polydopamine fibers for drug delivery, Int. J. Biol. Macromol. 163 (2020) 366–374. https://doi.org/10.1016/j.ijbiomac.2020.06.283.
[177] E.J. Ribot, C. Tournier, R. Aid-Launais, N. Koonjoo, H. Oliveira, A.J. Trotier, S. Rey, D. Wecker, D. Letourneur, J. Amedee Vilamitjana, S. Miraux, 3D anatomical and perfusion MRI for longitudinal evaluation of biomaterials for bone regeneration of femoral bone defect in rats, Sci. Rep. 7 (2017) 1–11. https://doi.org/10.1038/s41598-017-06258-0.
[178] M.Z. Tamayo, L. Choudat, R. Aid-Launais, O. Thibaudeau, L. Louedec, D. Letourneur, V. Gueguen, A. Meddahi-Pellé, A. Couvelard, G. Pavon-Djavid, Astaxanthin complexes to attenuate muscle damage after in vivo femoral ischemia-reperfusion, Mar. Drugs 17 (2019) 1–17. https://doi.org/10.3390/md17060354.
[179] S. Schlaubitz, S.M. Derkaoui, L. Marosa, S. Miraux, M. Renard, S. Catros, C. Le Visage, D. Letourneur, J. Amédée, J.C. Fricain, Pullulan/dextran/nHA macroporous composite beads for bone repair in a femoral condyle defect in rats, PLoS One 9 (2014) 1–11. https://doi.org/10.1371/journal.pone.0110251.
[180] A. P. Alivisatos, Published by : American Association for the Advancement of Science Semiconductor Clusters , Nanocrystals , and Quantum Dots, Science (80-.). 271 (1996) 933–937.
[181] H. Arya, Z. Kaul, R. Wadhwa, K. Taira, T. Hirano, S.C. Kaul, Quantum dots in bio-imaging: Revolution by the small, Biochem. Biophys. Res. Commun. 329 (2005) 1173–1177. https://doi.org/10.1016/j.bbrc.2005.02.043.
[182] W.C.W. Chan, D.J. Maxwell, X. Gao, R.E. Bailey, M. Han, S. Nie, Luminescent quantum dots for multiplexed biological detection and imaging, Curr. Opin. Biotechnol. 13 (2002) 40–46. https://doi.org/10.1016/S0958-1669(02)00282-3.
[183] A.M. Derfus, W.C.W. Chan, S.N. Bhatia, Intracellular delivery of quantum dots for live cell labeling and organelle tracking, Adv. Mater. 16 (2004) 961–966. https://doi.org/10.1002/adma.200306111.
[184] E.B. Voura, J.K. Jaiswal, H. Mattoussi, S.M. Simon, Tracking metastatic tumor cell

extravasation with quantum dot nanocrystals and fluorescence emission-scanning microscopy, Nat. Med. 10 (2004) 993–998. https://doi.org/10.1038/nm1096.

[185] U. Hasegawa, S.I.M. Nomura, S.C. Kaul, T. Hirano, K. Akiyoshi, Nanogel-quantum dot hybrid nanoparticles for live cell imaging, Biochem. Biophys. Res. Commun. 331 (2005) 917–921. https://doi.org/10.1016/j.bbrc.2005.03.228.

[186] G. Biliuta, L. Sacarescu, V. Socoliuc, M. Iacob, L. Gheorghe, D. Negru, S. Coseri, Carboxylated Polysaccharides Decorated with Ultrasmall Magnetic Nanoparticles with Antibacterial and MRI Properties, Macromol. Chem. Phys. 218 (2017) 1–9. https://doi.org/10.1002/macp.201700062.

[187] S.H. Kong, Y.W. Noh, Y.S. Suh, H.S. Park, H.J. Lee, K.W. Kang, H.C. Kim, Y.T. Lim, H.K. Yang, Evaluation of the novel near-infrared fluorescence tracers pullulan polymer nanogel and indocyanine green/γ-glutamic acid complex for sentinel lymph node navigation surgery in large animal models, Gastric Cancer 18 (2015) 55–64. https://doi.org/10.1007/s10120-014-0345-3.

[188] R. Jenjob, N. Kun, J.Y. Ghee, Z. Shen, X. Wu, S.K. Cho, D.H. Lee, S.G. Yang, Enhanced conjugation stability and blood circulation time of macromolecular gadolinium-DTPA contrast agent, Mater. Sci. Eng. C 61 (2016) 659–664. https://doi.org/10.1016/j.msec.2016.01.008.

[189] S. Chen, X.L. Xu, B. Zhou, J. Tian, B.M. Luo, L.M. Zhang, Acidic pH-Activated Gas-Generating Nanoparticles with Pullulan Decorating for Hepatoma-Targeted Ultrasound Imaging, ACS Appl. Mater. Interfaces (2019). https://doi.org/10.1021/acsami.9b06745.

[190] Y. Huang, H. Hu, R.Q. Li, B. Yu, F.J. Xu, Versatile Types of MRI-Visible Cationic Nanoparticles Involving Pullulan Polysaccharides for Multifunctional Gene Carriers, ACS Appl. Mater. Interfaces 8 (2016) 3919–3927. https://doi.org/10.1021/acsami.5b11016.

[191] A. Naman, S., Sharma, S., Dwivedi, J. and Baldi, Pullulan in drug delivery system for the treatment of lung disorders, 2023.

[192] K. Akiyoshi, Y. Sasaki, J. Sunamoto, Molecular chaperone-like activity of hydrogel nanoparticles of hydrophobized pullulan: Thermal stabilization with refolding of carbonic anhydrase B, Bioconjug. Chem. 10 (1999) 321–324. https://doi.org/10.1021/bc9801272.

[193] D.H. Donabedian, S.P. McCarthy, Acylation of pullulan by ring-opening of lactones, Macromolecules 31 (1998) 1032–1039. https://doi.org/10.1021/ma961741g.

[194] K.I. Shingel, P.T. Petrov, Behavior of γ-ray-irradiated pullulan in aqueous solutions of cationic (cetyltrimethylammonium hydroxide) and anionic (sodium dodecyl sulfate) surfactants, Colloid Polym. Sci. 280 (2002) 176–182. https://doi.org/10.1007/s00396-001-0599-2.

[195] W.M. Kulicke, T. Heinze, Improvements in polysaccharides for use as blood plasma expanders, Macromol. Symp. 231 (2005) 47–59. https://doi.org/10.1002/masy.200590024.

[196] J.F. Singh, R.S., Kaur, N., Rana, V. and Kennedy, Pullulan: A novel molecule for biomedical applications, Carbohydr. Polym. 171 (2017) 102–121.

[197] V.I. Gapanovich, V.N., Petrov, P.T., Ivanov, E.P., Tsarenkov, V.M., Lapkovski, M.P. and Tyurin, Blood plasma substituting preparation, the corrector of hemodynamical disfunctions—Neorondex, 1992.

[198] T. Kikuchi, Y., Taguchi, R., Sakano, Y. and Kobayashi, Comparison of extracellular polysaccharide produced by Pullularia pullulans with polysaccharides in the cells and cell wall, (1973).

[199] M. Tsianou, P. Alexandridis, Control of the rheological properties in solutions of a polyelectrolyte and an oppositely charged surfactant by the addition of cyclodextrins,

Langmuir 15 (1999) 8105–8112. https://doi.org/10.1021/la990701d.
[200] C. Catley, B.J., Ramsay, A. and Servis, Observations on the structure of the fungal extracellular polysaccharide, pullulan, Carbohydr. Res. 153 (1986) 79–86.
[201] T. Hirakura, Y. Nomura, Y. Aoyama, K. Akiyoshi, Photoresponsive nanogels formed by the self-assembly of spiropyrane-bearing pullulan that act as artificial molecular chaperones, Biomacromolecules 5 (2004) 1804–1809. https://doi.org/10.1021/bm049860o.
[202] 1994 Nishikawa et al., Supramolecular Assembly between Nanoparticles of Hydrophobized Polysaccharide and Soluble Protein Complexation between the Self-Aggregate of Cholesterol-Bearing Pullulan and a-Chymotrypsin, Dict. Genomics, Transcr. Proteomics (1994) 1–1. https://doi.org/10.1002/9783527678679.dg12721.
[203] Y. Li, D. Maciel, J. Rodrigues, X. Shi, H. Tomás, Biodegradable polymer nanogels for drug/nucleic acid delivery, Chem. Rev. 115 (2015) 8564–8608. https://doi.org/10.1021/cr500131f.
[204] M.B. Coltelli, S. Danti, K. de Clerk, A. Lazzeri, P. Morganti, Pullulan for advanced sustainable body- And skin-contact applications, J. Funct. Biomater. 11 (2020) 1–17. https://doi.org/10.3390/jfb11010020.
[205] S. Heo, H.S. Hwang, Y. Jeong, K. Na, Skin protection efficacy from UV irradiation and skin penetration property of polysaccharide-benzophenone conjugates as a sunscreen agent, Carbohydr. Polym. 195 (2018) 534–541. https://doi.org/10.1016/j.carbpol.2018.05.010.
[206] H.. Hijiya, M. Shiosaka, US3784390A; Shaped Bodies of Pullulan Esters and Their Use, (1975) Patent 3,871,892.
[207] T. Saito, B. Laboratories, P.E. Foelak, F. Application, P. Data, United States Patent (19), (1976).
[208] T. Saito, P.E.M. Woodberry, United States Patent (19), (1977).
[209] P.E.A. Pitlick, United States Patent (19), (1976).
[210] R. Jiang, M.S. Roberts, D.M. Collins, H.A.E. Benson, Absorption of sunscreens across human skin: An evaluation of commercial products for children and adults, Br. J. Clin. Pharmacol. 48 (1999) 635–637. https://doi.org/10.1046/j.1365-2125.1999.00056.x.
[211] C.G.J. Hayden, M.S. Roberts, H.A.E. Benson, Systemic absorption of sunscreen after topical application [4], Lancet 350 (1997) 863–864. https://doi.org/10.1016/S0140-6736(05)62032-6.
[212] M. Xiao, M. Tan, C. Peng, F. Jiang, K. Wu, N. Liu, D. Li, X. Yao, Soft and flexible polyvinyl alcohol/pullulan aerogels with fast and high water absorption capacity for facial mask substrates, Int. J. Biol. Macromol. 264 (2024). https://doi.org/10.1016/j.ijbiomac.2024.130469.
[213] P. Morganti, M. Palombo, G. Tishchenko, V.E. Yudin, F. Guarneri, M. Cardillo, P. Del Ciotto, F. Carezzi, G. Morganti, G. Fabrizi, Chitin-hyaluronan nanoparticles: A multifunctional carrier to deliver anti-aging active ingredients through the skin, Cosmetics 1 (2014) 140–158. https://doi.org/10.3390/cosmetics1030140.
[214] L. Hong, W.S. Kim, S.M. Lee, S.K. Kang, Y.J. Choi, C.S. Cho, Pullulan nanoparticles as prebiotics enhance the antibacterial properties of lactobacillus plantarum through the induction of mild stress in probiotics, Front. Microbiol. 10 (2019) 1–12. https://doi.org/10.3389/fmicb.2019.00142.
[215] L.K. Vora, A.J. Courtenay, I.A. Tekko, E. Larrañeta, R.F. Donnelly, Pullulan-based dissolving microneedle arrays for enhanced transdermal delivery of small and large biomolecules, Int. J. Biol. Macromol. 146 (2020) 290–298. https://doi.org/10.1016/j.ijbiomac.2019.12.184.
[216] C. Corinaldesi, G. Barone, F. Marcellini, A. Dell'Anno, R. Danovaro, Marine microbial-

derived molecules and their potential use in cosmeceutical and cosmetic products, Mar. Drugs 15 (2017) 1–21. https://doi.org/10.3390/md15040118.
[217] S. Nakashio, K. Tsuji, N. Toyota, F. Fujita, Novel cosmetics containing pullulan, 1976.
[218] H.S.K.K.K. Ozaki, Y., Nomura, T. and Miyake, T., PULLULAN BINDER AND ITS USES, 1995.
[219] P. Agredo, M.C. Rave, J.D. Echeverri, D. Romero, C.H. Salamanca, An evaluation of the physicochemical properties of stabilized oil-in-water emulsions using different cationic surfactant blends for potential use in the cosmetic industry, Cosmetics 6 (2019). https://doi.org/10.3390/cosmetics6010010.
[220] P. Morganti, M. Coltelli, S. Danti, Biobased Tissues for Innovative Cosmetic Products: Polybioskin as an EU Research Project, Glob. J. Nanomedicine 3 (2018) 1–6. https://doi.org/10.19080/GJN.2018.03.555620.
[221] A. Shukla, K. Mehta, J. Parmar, J. Pandya, M. Saraf, Depicting the exemplary knowledge of microbial exopolysaccharides in a nutshell, Eur. Polym. J. 119 (2019) 298–310. https://doi.org/10.1016/j.eurpolymj.2019.07.044.
[222] S. Danti, L. Trombi, A. Fusco, B. Azimi, A. Lazzeri, P. Morganti, M.B. Coltelli, G. Donnarumma, Chitin nanofibrils and nanolignin as functional agents in skin regeneration, Int. J. Mol. Sci. 20 (2019). https://doi.org/10.3390/ijms20112669.
[223] A. Martins, H. Vieira, H. Gaspar, S. Santos, Marketed marine natural products in the pharmaceutical and cosmeceutical industries: Tips for success, Mar. Drugs 12 (2014) 1066–1101. https://doi.org/10.3390/md12021066.
[224] T. Sato, United States Patent : 5861366 United States Patent : 5861366, New York 2 (2020) 1–29. https://patentimages.storage.googleapis.com/30/f4/62/e9b75605352fb0/US10679987.pdf.
[225] T. Ghosh, S.M. Bhasney, V. Katiyar, Blown films fabrication of poly lactic acid based biocomposites: Thermomechanical and migration studies, Mater. Today Commun. 22 (2020). https://doi.org/10.1016/j.mtcomm.2019.100737.
[226] S.S. Borkotoky, T. Ghosh, P. Bhagabati, V. Katiyar, Poly (lactic acid)/modified gum arabic (MG)based microcellular composite foam: Effect of MG on foam properties, thermal and crystallization behavior, Int. J. Biol. Macromol. 125 (2019) 159–170. https://doi.org/10.1016/j.ijbiomac.2018.11.257.
[227] O. Pınar, F. Yangılar, P. Oğuzhan, F. Yangılar, Pullulan : Production and usage in food ındustry, African J. Food Sci. Technol. 4 (2013) 57–63.
[228] E. Yatmaz, I. Turhan, Carob as a carbon source for fermentation technology, Biocatal. Agric. Biotechnol. 16 (2018) 200–208. https://doi.org/10.1016/j.bcab.2018.08.006.
[229] S. Barak, D. Mudgil, Locust bean gum: Processing, properties and food applications-A review, Int. J. Biol. Macromol. 66 (2014) 74–80. https://doi.org/10.1016/j.ijbiomac.2014.02.017.
[230] S. Roy, J.W. Rhim, Effect of chitosan modified halloysite on the physical and functional properties of pullulan/chitosan biofilm integrated with rutin, Appl. Clay Sci. 211 (2021). https://doi.org/10.1016/j.clay.2021.106205.
[231] R. Priyadarshi, S.M. Kim, J.W. Rhim, Pectin/pullulan blend films for food packaging: Effect of blending ratio, Food Chem. 347 (2021). https://doi.org/10.1016/j.foodchem.2021.129022.
[232] J. Kim, Y. Choi, S. Ron, B. Kim, S. Lim, Food Hydrocolloids Humidity stability of tapioca starch e pullulan composite fi lms, 41 (2014) 140–145.
[233] K. Kraśniewska, M. Gniewosz, Active Packaging Based on a PET/PP Food-Grade Film Coated with Pullulan and Clove Essential Oil: Physicochemical and Antimicrobial Properties, Molecules 30 (2025). https://doi.org/10.3390/molecules30102118.

[234] J. Liu, A. Cao, Y. Liu, X. Zheng, K. Tang, Development and characterization of soluble soybean polysaccharide/pullulan blend films enriched with essential oils, Int. J. Biol. Macromol. 309 (2025) 143092. https://doi.org/10.1016/j.ijbiomac.2025.143092.
[235] V. Mayakrishnan, R. Venkatesan, M.M. Alrashed, R. Vaidhyanathan, A.A. Madhavan, Effect of Silicon Carbide Nanoparticles on the Mechanical, Barrier, Antibacterial and Biodegradable Properties of Pullulan/Lignin Bio Nanocomposite Blends for Food Packaging Applications, Silicon 17 (2025) 1059–1075. https://doi.org/10.1007/s12633-025-03265-z.
[236] N. Afzia, S. Bora, T. Ghosh, Utilization of cassava peel based cellulose nanofiber for developing functionalized pectin/pullulan/olive oil nanocomposite film for cling wrapping of chicken meat, Int. J. Biol. Macromol. 305 (2025) 140879. https://doi.org/10.1016/j.ijbiomac.2025.140879.
[237] Y. Sul, A. Khan, J.T. Kim, J.W. Rhim, Tangerine peel-derived nitrogen-doped carbon dots incorporated chitosan/pullulan-based active packaging film for bread packaging, Colloids Surfaces B Biointerfaces 245 (2025) 114339. https://doi.org/10.1016/j.colsurfb.2024.114339.
[238] Z. Bian, X. Wu, X. Sun, X. Huang, X. Zhuo, H. Wang, S. Komarneni, K. Zhang, Z. Ni, G. Hu, Gellan gum and pullulan-based films with triple functionalities of antioxidant, antibacterial and freshness indication properties for food packaging, Int. J. Biol. Macromol. 278 (2024). https://doi.org/10.1016/j.ijbiomac.2024.134825.
[239] S. Madihalli, S.P. Masti, M.P. Eelager, R.B. Chougale, L.K. Kurabetta, A.A. Hunashyal, N.P. Dalbanjan, S.K. Praveen Kumar, Quinic acid and montmorillonite integrated chitosan/pullulan active films with potent antimicrobial and barrier properties to prolong the shelf life of tofu, Food Biosci. 62 (2024). https://doi.org/10.1016/j.fbio.2024.105492.
[240] Y. Dong, T. Lan, L. Wang, X. Wang, Z. Xu, L. Jiang, Y. Zhang, X. Sui, Development of composite electrospun films utilizing soy protein amyloid fibrils and pullulan for food packaging applications, Food Chem. X 20 (2023) 0–7. https://doi.org/10.1016/j.fochx.2023.100995.
[241] L. Gan, G. Jiang, Y. Yang, B. Zheng, S. Zhang, X. Li, Y. Tian, B. Peng, Development and characterization of levan/pullulan/chitosan edible films enriched with ε-polylysine for active food packaging, Food Chem. 388 (2022) 132989. https://doi.org/10.1016/j.foodchem.2022.132989.
[242] T. Gasti, S. Dixit, V.D. Hiremani, R.B. Chougale, S.P. Masti, S.K. Vootla, B.S. Mudigoudra, Chitosan/pullulan based films incorporated with clove essential oil loaded chitosan-ZnO hybrid nanoparticles for active food packaging, Carbohydr. Polym. 277 (2022). https://doi.org/10.1016/j.carbpol.2021.118866.
[243] N. Kumar, Neeraj, Pratibha, M. Singla, Enhancement of Storage Life and Quality Maintenance of Litchi (Litchi Chinensis Sonn.) Fruit Using Chitosan:pullulan Blend Antimicrobial Edible Coating, Int. J. Fruit Sci. 20 (2020) S1662–S1680. https://doi.org/10.1080/15538362.2020.1828224.
[244] N.H.C.S. Silva, C. Vilela, A. Almeida, I.M. Marrucho, C.S.R. Freire, Pullulan-based nanocomposite films for functional food packaging: Exploiting lysozyme nanofibers as antibacterial and antioxidant reinforcing additives, Food Hydrocoll. 77 (2018) 921–930. https://doi.org/10.1016/j.foodhyd.2017.11.039.
[245] K. Ertan, A. Celebioglu, R. Chowdhury, G. Sumnu, S. Sahin, C. Altier, T. Uyar, Carvacrol/cyclodextrin inclusion complex loaded gelatin/pullulan nanofibers for active food packaging applications, Food Hydrocoll. 142 (2023) 108864. https://doi.org/10.1016/j.foodhyd.2023.108864.
[246] R. Priyadarshi, Z. Riahi, J.W. Rhim, Antioxidant pectin/pullulan edible coating

incorporated with Vitis vinifera grape seed extract for extending the shelf life of peanuts, Postharvest Biol. Technol. 183 (2022) 111740. https://doi.org/10.1016/j.postharvbio.2021.111740.

[247] M. Duan, S. Yu, J. Sun, H. Jiang, J. Zhao, C. Tong, Y. Hu, J. Pang, C. Wu, Development and characterization of electrospun nanofibers based on pullulan/chitin nanofibers containing curcumin and anthocyanins for active-intelligent food packaging, Int. J. Biol. Macromol. 187 (2021) 332–340. https://doi.org/10.1016/j.ijbiomac.2021.07.140.

[248] W. Zhou, Y. He, F. Liu, L. Liao, X. Huang, R. Li, Y. Zou, L. Zhou, L. Zou, Y. Liu, R. Ruan, J. Li, Carboxymethyl chitosan-pullulan edible films enriched with galangal essential oil: Characterization and application in mango preservation, Carbohydr. Polym. 256 (2021) 117579. https://doi.org/10.1016/j.carbpol.2020.117579.

[249] M. Omar-Aziz, M. Gharaghani, S.S. Hosseini, F. Khodaiyan, M. Mousavi, G. Askari, J.F. Kennedy, Effect of octenylsuccination of pullulan on mechanical and barrier properties of pullulan-chickpea protein isolate composite film, Food Hydrocoll. 121 (2021). https://doi.org/10.1016/j.foodhyd.2021.107047.

[250] N. Kumar, N. Neeraj, N. Pratibha, A. Trajkovska Petkoska, Improved Shelf Life and Quality of Tomato (Solanum lycopersicum L.) by Using Chitosan-Pullulan Composite Edible Coating Enriched with Pomegranate Peel Extract, ACS Food Sci. Technol. 1 (2021) 500–510. https://doi.org/10.1021/acsfoodscitech.0c00076.

[251] N. Kumar, Pratibha, Neeraj, A. Ojha, A. Upadhyay, R. Singh, S. Kumar, Effect of active chitosan-pullulan composite edible coating enrich with pomegranate peel extract on the storage quality of green bell pepper, Lwt 138 (2021) 110435. https://doi.org/10.1016/j.lwt.2020.110435.

[252] N. Kumar, Pratibha, Neeraj, A.T. Petkoska, S.A. Al-Hilifi, O.A. Fawole, Effect of chitosan–pullulan composite edible coating functionalized with pomegranate peel extract on the shelf life of mango (Mangifera indica), Coatings 11 (2021) 25–40. https://doi.org/10.3390/coatings11070764.

[253] X. wen Jia, Z. yu Qin, J. xin Xu, B. hua Kong, Q. Liu, H. Wang, Preparation and characterization of pea protein isolate-pullulan blend electrospun nanofiber films, Int. J. Biol. Macromol. 157 (2020) 641–647. https://doi.org/10.1016/j.ijbiomac.2019.11.216.

[254] J. Wu, F. Zhong, Y. Li, C.F. Shoemaker, W. Xia, Preparation and characterization of pullulan-chitosan and pullulan-carboxymethyl chitosan blended films, Food Hydrocoll. 30 (2013) 82–91. https://doi.org/10.1016/j.foodhyd.2012.04.002.

[255] G. Zhu, L. Sheng, Q. Tong, Preparation and characterization of carboxymethyl-gellan and pullulan blend films, Food Hydrocoll. 35 (2014) 341–347. https://doi.org/10.1016/j.foodhyd.2013.06.009.

[256] P.M. Tomasula, A.M.M. Sousa, S.C. Liou, R. Li, L.M. Bonnaillie, L.S. Liu, Short communication: Electrospinning of casein/pullulan blends for food-grade applications, J. Dairy Sci. 99 (2016) 1837–1845. https://doi.org/10.3168/jds.2015-10374.

[257] B. Çabuk, Ş. Harsa, Whey Protein-Pullulan (WP/Pullulan) Polymer Blend for Preservation of Viability of Lactobacillus acidophilus, Dry. Technol. 33 (2015) 1223–1233. https://doi.org/10.1080/07373937.2015.1021008.

[258] M. Aceituno-Medina, S. Mendoza, J.M. Lagaron, A. López-Rubio, Development and characterization of food-grade electrospun fibers from amaranth protein and pullulan blends, Food Res. Int. 54 (2013) 667–674. https://doi.org/10.1016/j.foodres.2013.07.055.

[259] E. Trovatti, S.C.M. Fernandes, L. Rubatat, D. da S. Perez, C.S.R. Freire, A.J.D. Silvestre, C.P. Neto, Pullulan-nanofibrillated cellulose composite films with improved thermal and mechanical properties, Compos. Sci. Technol. 72 (2012) 1556–1561. https://doi.org/10.1016/j.compscitech.2012.06.003.

[260] M. Hassannia-Kolaee, F. Khodaiyan, R. Pourahmad, I. Shahabi-Ghahfarrokhi, Development of ecofriendly bionanocomposite: Whey protein isolate/pullulan films with nano-SiO2, Int. J. Biol. Macromol. 86 (2016) 139–144. https://doi.org/10.1016/j.ijbiomac.2016.01.032.
[261] Q. Xiao, Q. Tong, L.T. Lim, Pullulan-sodium alginate based edible films: Rheological properties of film forming solutions, Carbohydr. Polym. 87 (2012) 1689–1695. https://doi.org/10.1016/j.carbpol.2011.09.077.
[262] S. Zhang, F. Wei, X. Han, An edible film of sodium alginate/pullulan incorporated with capsaicin, New J. Chem. 42 (2018) 17756–17761. https://doi.org/10.1039/C8NJ04249G.
[263] N.N. Shah, C. Vishwasrao, R.S. Singhal, L. Ananthanarayan, N-Octenyl succinylation of pullulan: Effect on its physico-mechanical and thermal properties and application as an edible coating on fruits, Food Hydrocoll. 55 (2016) 179–188. https://doi.org/10.1016/j.foodhyd.2015.11.026.
[264] T. Diab, C.G. Biliaderis, D. Gerasopoulos, E. Sfakiotakis, Physicochemical properties and application of pullulan edible films and coatings in fruit preservation, J. Sci. Food Agric. 81 (2001) 988–1000. https://doi.org/10.1002/jsfa.883.
[265] M.E. Gounga, S.Y. Xu, Z. Wang, W.G. Yang, Effect of whey protein isolate-pullulan edible coatings on the quality and shelf life of freshly roasted and freeze-dried Chinese chestnut, J. Food Sci. 73 (2008) 155–161. https://doi.org/10.1111/j.1750-3841.2008.00694.x.
[266] S. Wu, J. Chen, Using pullulan-based edible coatings to extend shelf-life of fresh-cut "Fuji" apples, Int. J. Biol. Macromol. 55 (2013) 254–257. https://doi.org/10.1016/j.ijbiomac.2013.01.012.
[267] S. Wu, M. Lu, S. Wang, Effect of oligosaccharides derived from Laminaria japonica-incorporated pullulan coatings on preservation of cherry tomatoes, Food Chem. 199 (2016) 296–300. https://doi.org/10.1016/j.foodchem.2015.12.029.
[268] S. Ye, Z. Ma, Z. Liu, Y. Liu, M. Zhang, J. Wang, Effects of carbohydrate sources on biosorption properties of the novel exopolysaccharides produced by Arthrobacter ps-5, Carbohydr. Polym. 112 (2014) 615–621. https://doi.org/10.1016/j.carbpol.2014.05.076.
[269] Y. Shuhong, Z. Meiping, Y. Hong, W. Han, X. Shan, L. Yan, W. Jihui, Biosorption of Cu2+, Pb2+ and Cr6+ by a novel exopolysaccharide from Arthrobacter ps-5, Carbohydr. Polym. 101 (2014) 50–56. https://doi.org/10.1016/j.carbpol.2013.09.021.
[270] S.Y. Kim, J.H. Kim, C.J. Kim, D.K. Oh, Metal adsorption of the polysaccharide produced from Methylobacterium organophilum, Biotechnol. Lett. 18 (1996) 1161–1164. https://doi.org/10.1007/BF00128585.
[271] W.W. Li, W.Z. Zhou, Y.Z. Zhang, J. Wang, X.B. Zhu, Flocculation behavior and mechanism of an exopolysaccharide from the deep-sea psychrophilic bacterium Pseudoalteromonas sp. SM9913, Bioresour. Technol. 99 (2008) 6893–6899. https://doi.org/10.1016/j.biortech.2008.01.050.
[272] M. Constantin, I. Asmarandei, V. Harabagiu, L. Ghimici, P. Ascenzi, G. Fundueanu, Removal of anionic dyes from aqueous solutions by an ion-exchanger based on pullulan microspheres, Carbohydr. Polym. 91 (2013) 74–84. https://doi.org/10.1016/j.carbpol.2012.08.005.
[273] G. McKay, M.S. Otterburn, J.A. Aga, Fuller's earth and fired clay as adsorbents for dyestuffs - Equilibrium and rate studies, Water. Air. Soil Pollut. 24 (1985) 307–322. https://doi.org/10.1007/BF00161790.
[274] G. Crini, Non-conventional low-cost adsorbents for dye removal: A review, Bioresour. Technol. 97 (2006) 1061–1085. https://doi.org/10.1016/j.biortech.2005.05.001.
[275] D. Pokhrel, T. Viraraghavan, Treatment of pulp and paper mill wastewater - A review,

Sci. Total Environ. 333 (2004) 37–58. https://doi.org/10.1016/j.scitotenv.2004.05.017.
[276] V.K. Gupta, Suhas, Application of low-cost adsorbents for dye removal - A review, J. Environ. Manage. 90 (2009) 2313–2342. https://doi.org/10.1016/j.jenvman.2008.11.017.
[277] E. Forgacs, T. Cserháti, G. Oros, Removal of synthetic dyes from wastewaters: A review, Environ. Int. 30 (2004) 953–971. https://doi.org/10.1016/j.envint.2004.02.001.
[278] T. Su, L. Wu, X. Pan, C. Zhang, M. Shi, R. Gao, X. Qi, W. Dong, Pullulan-derived nanocomposite hydrogels for wastewater remediation: Synthesis and characterization, J. Colloid Interface Sci. 542 (2019) 253–262. https://doi.org/10.1016/j.jcis.2019.02.025.
[279] X. Qi, Q. Zeng, X. Tong, T. Su, L. Xie, K. Yuan, J. Xu, J. Shen, Polydopamine/montmorillonite-embedded pullulan hydrogels as efficient adsorbents for removing crystal violet, J. Hazard. Mater. 402 (2021) 123359. https://doi.org/10.1016/j.jhazmat.2020.123359.
[280] Richa, A. Roy Choudhury, Synthesis of a novel gellan-pullulan nanogel and its application in adsorption of cationic dye from aqueous medium, Carbohydr. Polym. 227 (2020) 115291. https://doi.org/10.1016/j.carbpol.2019.115291.
[281] L. Ghimici, M. Constantin, G. Fundueanu, Novel biodegradable flocculanting agents based on pullulan, J. Hazard. Mater. 181 (2010) 351–358. https://doi.org/10.1016/j.jhazmat.2010.05.017.
[282] L. Ghimici, M. Constantin, The separation of the pyrethroid insecticide Fastac 10 EC by cationic pullulan derivatives, React. Funct. Polym. 95 (2015) 12–18. https://doi.org/10.1016/j.reactfunctpolym.2015.08.001.
[283] A. Abbas, M.A. Hussain, M. Amin, M. Sher, M.N. Tahir, W. Tremel, Succinate-bonded pullulan: An efficient and reusable super-sorbent for cadmium-uptake from spiked high-hardness groundwater, J. Environ. Sci. (China) 37 (2015) 51–58. https://doi.org/10.1016/j.jes.2015.04.013.
[284] M.D. Radulović, O.G. Cvetković, S.D. Nikolić, D.S. Dordević, D.M. Jakovljević, M.M. Vrvić, Simultaneous production of pullulan and biosorption of metals by Aureobasidium pullulans strain CH-1 on peat hydrolysate, Bioresour. Technol. 99 (2008) 6673–6677. https://doi.org/10.1016/j.biortech.2007.11.053.
[285] C.K. de Souza, T. Ghosh, N. Lukhmana, S. Tahiliani, R. Priyadarshi, T.G. Hoffmann, S.D. Purohit, S.S. Han, Pullulan as a sustainable biopolymer for versatile applications: A review, Mater. Today Commun. 36 (2023) 106477. https://doi.org/10.1016/j.mtcomm.2023.106477.
[286] E.D.M. Isa, K. Shameli, N.W.C. Jusoh, R. Hazan, Rapid photodecolorization of methyl orange and rhodamine B using zinc oxide nanoparticles mediated by pullulan at different calcination conditions, J. Nanostructure Chem. 11 (2021) 187–202. https://doi.org/10.1007/s40097-020-00358-6.
[287] E.D. Mohamed Isa, N.W. Che Jusoh, R. Hazan, K. Shameli, Photocatalytic degradation of methyl orange using pullulan-mediated porous zinc oxide microflowers, Environ. Sci. Pollut. Res. 28 (2021) 5774–5785. https://doi.org/10.1007/s11356-020-10939-1.
[288] B. Sonmez, A.N. Celikkol, Pullulan based hydrogels for the removal of various metal ions from aqueous solutions, J. Environ. Chem. Eng. 9 (2021) 106188. https://doi.org/10.1016/j.jece.2021.106188.
[289] G. Lopinski, N. Du, G. Dubey, J. Lefebvre, Z. Li, S. Zou, P. Malenfant, Cyanoethylated pullulan as a high-k solution processable polymer gate dielectric for SWCNT TFTs, Org. Electron. 42 (2017) 329–336. https://doi.org/10.1016/j.orgel.2016.12.045.
[290] S.H. Al-Araimi, A. Elshafie, S.N. Al-Bahry, Y.M. Al-Wahaibi, A.S. Al-Bemani, Biopolymer production by Aureobasidium mangrovei SARA-138H and its potential for oil recovery enhancement, Appl. Microbiol. Biotechnol. 105 (2021) 105–117.

https://doi.org/10.1007/s00253-020-11015-x.
[291] L. Ghimici, M.M. Nafureanu, M. Constantin, Cationic Pullulan Derivatives Based Flocculants for Removal of Some Metal Oxides from Simulated Wastewater, Int. J. Mol. Sci. 24 (2023). https://doi.org/10.3390/ijms24054383.
[292] C.A. Farris, S., Unalan, I.U., Introzzi, L., Fuentes-Alventosa, J.M. and Cozzolino, Pullulan-Based Films and Coatings for Food Packaging: Present Applications, Emerging Opportunities, and Future Challenges, J. Appl. Polym. Sci. 131 (2014).
[293] M. Dubois, K.A. Gilles, J.K. Hamilton, P.A. Rebers, F. Smith, Colorimetric Method for Determination of Sugars and Related Substances, Anal. Chem. 28 (1956) 350–356. https://doi.org/10.1021/ac60111a017.
[294] H.P.D.T. Hewa Pathirana, L.L.W.C. Yalegama, W.L.I. Wijesekara, M.A. Jayasinghe, D.L.C.N. Hitigedara, Effects of Harvesting Techniques and Value Addition on the Nutritional and Physicochemical Properties of Coconut (Cocos nucifera L.) Jaggery, Sugar Tech 27 (2025) 1409–1417. https://doi.org/10.1007/s12355-025-01589-z.
[295] L. Jiang, Optimization of fermentation conditions for pullulan production by Aureobasidium pullulan using response surface methodology, Carbohydr. Polym. 79 (2010) 414–417. https://doi.org/10.1016/j.carbpol.2009.08.027.
[296] L. Liu, J. Zhang, X. Zou, M. Arslan, J. Shi, X. Zhai, J. Xiao, X. Wang, X. Huang, Z. Li, Y. Li, A high-stable and sensitive colorimetric nanofiber sensor based on PCL incorporating anthocyanins for shrimp freshness, Food Chem. 377 (2022) 131909. https://doi.org/10.1016/j.foodchem.2021.131909.
[297] A. Kefayat, R. Hamidi Farahani, M. Rafienia, E. Hazrati, N. Hosseini Yekta, Synthesis and characterization of cellulose nanofibers/chitosan/cinnamon extract wound dressing with significant antibacterial and wound healing properties, J. Iran. Chem. Soc. 19 (2022) 1191–1202. https://doi.org/10.1007/s13738-021-02374-x.
[298] M. Kokabi, M. Sirousazar, Z.M. Hassan, PVA-clay nanocomposite hydrogels for wound dressing, Eur. Polym. J. 43 (2007) 773–781. https://doi.org/10.1016/j.eurpolymj.2006.11.030.
[299] H. Yong, J. Liu, Recent advances in the preparation, physical and functional properties, and applications of anthocyanins-based active and intelligent packaging films, Food Packag. Shelf Life 26 (2020) 100550. https://doi.org/10.1016/j.fpsl.2020.100550.
[300] S. Gist, I. Tio-Matos, S. Falzgraf, S. Cameron, M. Beebe, Wound care in the geriatric client., Clin. Interv. Aging 4 (2009) 269–287. https://doi.org/10.2147/cia.s4726.
[301] Y. Hussein, E.M. El-Fakharany, E.A. Kamoun, S.A. Loutfy, R. Amin, T.H. Taha, S.A. Salim, M. Amer, Electrospun PVA/hyaluronic acid/L-arginine nanofibers for wound healing applications: Nanofibers optimization and in vitro bioevaluation, Int. J. Biol. Macromol. 164 (2020) 667–676. https://doi.org/10.1016/j.ijbiomac.2020.07.126.
[302] R. Khan, M.U. Aslam Khan, G.M. Stojanović, A. Javed, S. Haider, S.I. Abd Razak, Fabrication of Bilayer Nanofibrous-Hydrogel Scaffold from Bacterial Cellulose, PVA, and Gelatin as Advanced Dressing for Wound Healing and Soft Tissue Engineering, ACS Omega 9 (2024) 6527–6536. https://doi.org/10.1021/acsomega.3c06613.
[303] G. Pandey, P. Pandey, D.K. Arya, S. Kanaujiya, D. Deepak Kapoor, R.K. Gupta, S. Ranjan, K. Chidambaram, B. Manickam, P.S. Rajinikanth, Multilayered nanofibrous scaffold of Polyvinyl alcohol/gelatin/poly (lactic-co-glycolic acid) enriched with hemostatic/antibacterial agents for rapid acute hemostatic wound healing, Int. J. Pharm. 638 (2023) 122918. https://doi.org/10.1016/j.ijpharm.2023.122918.
[304] J. Qi, H. Zhang, Y. Wang, M.P. Mani, S.K. Jaganathan, Development and blood compatibility assessment of electrospun polyvinyl alcohol blended with metallocene polyethylene and plectranthus amboinicus (PVA/mPE/PA) for bone tissue engineering, Int. J. Nanomedicine 13 (2018) 2777–2788. https://doi.org/10.2147/IJN.S151242.

[305] J.L.P. Gemeinder, N.R. de Barros, G.S. Pegorin, J. de L. Singulani, F.A. Borges, M.C.G. Del Arco, M.J.S.M. Giannini, A.M.F. Almeida, S.L. de S. Salvador, R.D. Herculano, Gentamicin encapsulated within a biopolymer for the treatment of Staphylococcus aureus and Escherichia coli infected skin ulcers, J. Biomater. Sci. Polym. Ed. 32 (2021) 93–111. https://doi.org/10.1080/09205063.2020.1817667.

[306] S.K. Karuppannan, J. Bushion, R. Ramalingam, S. Swaminathan, K.D. Arunachalam, A.A. Kadam, R. Rajagopal, R. Sathya, S. Chinnappan, Fabrication, characterization and in vitro evaluation of Melia dubia extract infused nanofibers for wound dressing, J. King Saud Univ. - Sci. 34 (2022) 101931. https://doi.org/10.1016/j.jksus.2022.101931.

[307] M. Das, O. Zandraa, C. Mudenur, N. Saha, P. Sáha, B. Mandal, V. Katiyar, Composite Scaffolds Based on Bacterial Cellulose for Wound Dressing Application, ACS Appl. Bio Mater. 5 (2022) 3722–3733. https://doi.org/10.1021/acsabm.2c00226.

[308] J. Gu, S. Yagi, J. Meng, Y. Dong, C. Qian, D. Zhao, A. Kumar, T. Xu, A. Lucchetti, H. Xu, High-efficiency production of core-sheath nanofiber membrane via co-axial electro-centrifugal spinning for controlled drug release, J. Memb. Sci. 654 (2022) 120571. https://doi.org/10.1016/j.memsci.2022.120571.

[309] Y. Wu, W. Chen, F. Meng, Z. Wang, R. Cheng, C. Deng, H. Liu, Z. Zhong, Core-crosslinked pH-sensitive degradable micelles: A promising approach to resolve the extracellular stability versus intracellular drug release dilemma, J. Control. Release 164 (2012) 338–345. https://doi.org/10.1016/j.jconrel.2012.07.011.

[310] S. Kumar, P. Shukla, K. Das, V. Katiyar, Chitosan/water caltrop pericarp extract reinforced active edible film and its efficacy as strawberry coating for prolonging shelf life, Int. J. Biol. Macromol. 307 (2025) 142115. https://doi.org/10.1016/j.ijbiomac.2025.142115.

[311] K. Mondal, S.K. Bhattacharjee, C. Mudenur, T. Ghosh, V. V. Goud, V. Katiyar, Development of antioxidant-rich edible active films and coatings incorporated with de-oiled ethanolic green algae extract: a candidate for prolonging the shelf life of fresh produce, RSC Adv. 12 (2022) 13295–13313. https://doi.org/10.1039/d2ra00949h.

[312] T. Ghosh, V. Katiyar, Nanochitosan functionalized hydrophobic starch/guar gum biocomposite for edible coating application with improved optical, thermal, mechanical, and surface property, Int. J. Biol. Macromol. 211 (2022) 116–127. https://doi.org/10.1016/j.ijbiomac.2022.05.079.

[313] E. Ruggeri, D. Kim, Y. Cao, S. Farè, L. De Nardo, B. Marelli, A Multilayered Edible Coating to Extend Produce Shelf Life, ACS Sustain. Chem. Eng. 8 (2020) 14312–14321. https://doi.org/10.1021/acssuschemeng.0c03365.

[314] M.Y. Adame, Y. Wang, C. Shi, T. Aziz, F. Al-Asmari, M.Y. Sameeh, H. Cui, L. Lin, Fortification of pullulan/cassava starch-based edible films incorporated with LC-EO nanoparticles and the application for beef meat preservation, Int. J. Biol. Macromol. 279 (2024) 135629. https://doi.org/10.1016/j.ijbiomac.2024.135629.

[315] S. Roy, J.W. Rhim, Agar-based antioxidant composite films incorporated with melanin nanoparticles, Food Hydrocoll. 94 (2019) 391–398. https://doi.org/10.1016/j.foodhyd.2019.03.038.

[316] M. Ma, A. Li, J. Feng, Z. Wang, Y. Jia, X. Ma, Y. Ning, Antifungal mechanism of Lactiplantibacillus plantarum P10 against Aspergillus niger and its in-situ biopreservative application in Chinese steamed bread, Food Chem. 449 (2024). https://doi.org/10.1016/j.foodchem.2024.139181.

[317] F.N. Eze, R.C. Eze, K.E. Okpara, A.E. Adekoya, H.N. Kalu, Design and development of locust bean gum-endowed/Phyllanthus reticulatus anthocyanin- functionalized biogenic gold nanosystem for enhanced antioxidative and anticancer chemotherapy, Int. J. Biol. Macromol. 275 (2024) 133687. https://doi.org/10.1016/j.ijbiomac.2024.133687.

[318] Z.A. Nur Hanani, K.L. Soo, W.I.W. Zunairah, S. Radhiah, Prolonging the shelf life of fresh-cut guava (Psidium guajaya L.) by coating with chitosan and cinnamon essential oil, Heliyon 9 (2023) e22419. https://doi.org/10.1016/j.heliyon.2023.e22419.
[319] K. Venkatachalam, S. Lekjing, P. Noonim, N. Charoenphun, Extension of Quality and Shelf Life of Tomatoes Using Chitosan Coating Incorporated with Cinnamon Oil, Foods 13 (2024). https://doi.org/10.3390/foods13071000.
[320] K.A. Shiekh, T. Luanglaor, N. Hanprerakriengkrai, S. Jafari, I. Kijpatanasilp, N. Asadatorn, R.W. Worobo, A.E.A. Bekhit, K. Assatarakul, Purple Corn (Zea mays L .) Milk Fortified with Low Sucrose Content during Cold Storage, Foods 12 (2023) 277.
[321] G. Liu, X. Zhao, C. Chen, Z. Chi, Y. Zhang, Q. Cui, Z. Chi, Y.J. Liu, Robust production of pigment-free pullulan from lignocellulosic hydrolysate by a new fungus co-utilizing glucose and xylose, Carbohydr. Polym. 241 (2020) 116400. https://doi.org/10.1016/j.carbpol.2020.116400.
[322] Ž. Mitić, G.M. Nikolić, M. Cakić, G.S. Nikolić, S. Živanović, S. Mitić, S. Najman, Synthesis, spectroscopic and structural characterization of Co(II)-pullulan complexes by UV-Vis, ATR-FTIR, MALDI-TOF/TOF MS and XRD, Carbohydr. Polym. 200 (2018) 25–34. https://doi.org/10.1016/j.carbpol.2018.07.032.
[323] S.M. Wani, F.A. Khanday, F.A. Masoodi, Optimization of pullulan production from apple pomace in solid-state and submerged fermentation conditions: structural, thermal and rheological characterization, J. Food Sci. Technol. (2025). https://doi.org/10.1007/s13197-025-06258-3.
[324] K. Mondal, S.K. Bhattacharjee, V. V. Goud, V. Katiyar, Effect of waste Dunaliella tertiolecta biomass ethanolic extract and turmeric essential oil on properties of guar gum-based active films, Food Hydrocoll. 146 (2024) 109199. https://doi.org/10.1016/j.foodhyd.2023.109199.
[325] B. Sun, F. Xu, D. Chen, J. Liu, Quaternary ammonium chitosan-based active packaging films incorporated with dialdehyde guar gum-proanthocyanidins conjugates: Characterization and application in the edible coating of pork, Food Hydrocoll. 158 (2025) 110597. https://doi.org/10.1016/j.foodhyd.2024.110597.
[326] K. Mondal, N. Soundararajan, V. V. Goud, V. Katiyar, Cellulose Nanocrystals Modulate Curcumin Migration in PLA-Based Active Films and Its Application as Secondary Packaging, ACS Sustain. Chem. Eng. 12 (2024) 9642–9657. https://doi.org/10.1021/acssuschemeng.4c00518.
[327] H. Guo, P. Prempree, S. Chen, Y. Yamashige, N. Kondo, Y. Ogawa, Crystallinity determination of amylose-fatty acid complex in gelatinized rice starch-fatty acid mixtures using Terahertz spectroscopy, Food Hydrocoll. 146 (2024) 109279. https://doi.org/10.1016/j.foodhyd.2023.109279.
[328] R. Thakur, V. Gupta, T. Ghosh, A.B. Das, Effect of anthocyanin-natural deep eutectic solvent (lactic acid/fructose) on mechanical, thermal, barrier, and pH-sensitive properties of polyvinyl alcohol based edible films, Food Packag. Shelf Life 33 (2022) 100914. https://doi.org/10.1016/j.fpsl.2022.100914.
[329] T. Ghosh, K. Mondal, B.S. Giri, V. Katiyar, Silk nanodisc based edible chitosan nanocomposite coating for fresh produces: A candidate with superior thermal, hydrophobic, optical, mechanical and food properties, Food Chem. 360 (2021) 130048. https://doi.org/10.1016/j.foodchem.2021.130048.
[330] G. Yi, M. Tavassoli, M. Taghizadeh, W. Zhang, E. Assadpour, S.M. Jafari, Pullulan electrospun nanofibers; from food packaging to encapsulation and delivery of bioactive compounds, Int. J. Biol. Macromol. 322 (2025) 146936. https://doi.org/10.1016/j.ijbiomac.2025.146936.
[331] V.S.R.K. Ganduri, K.R.S.S. Rao, U.K. Mangamuri, V.L. M, S. Poda, Production of

Pullulan using Jaggery as substrate by Aureobasidium pullulans MTCC 2195, Curr. Trends Biotechnol. Pharm. 10 (2016) 153–160.
[332] K.R. Sugumaran, R. V. Sindhu, S. Sukanya, N. Aiswarya, V. Ponnusami, Statistical studies on high molecular weight pullulan production in solid state fermentation using jack fruit seed, Carbohydr. Polym. 98 (2013) 854–860. https://doi.org/10.1016/j.carbpol.2013.06.071.
[333] R. Pratibha, P. Malar, T. Rajapriya, S. Balapoornima, V. Ponnusami, Statistical and equilibrium studies on enhancing biosorption capacity of Saccharomyces cerevisiae through acid treatment, Desalination 264 (2010) 102–107. https://doi.org/10.1016/j.desal.2010.07.011.
[334] B.H. Hameed, I.A.W. Tan, A.L. Ahmad, Optimization of basic dye removal by oil palm fibre-based activated carbon using response surface methodology, J. Hazard. Mater. 158 (2008) 324–332. https://doi.org/10.1016/j.jhazmat.2008.01.088.
[335] V. Ponnusami, V. Krithika, R. Madhuram, S.N. Srivastava, Biosorption of reactive dye using acid-treated rice husk: Factorial design analysis, J. Hazard. Mater. 142 (2007) 397–403. https://doi.org/10.1016/j.jhazmat.2006.08.040.
[336] K. Ravikumar, S.H. Kim, Y.A. Son, Design of experiments for the optimization and statistical analysis of Berberine finishing of polyamide substrates, Dye. Pigment. 75 (2007) 401–407. https://doi.org/10.1016/j.dyepig.2006.06.020.
[337] Y. Göksungur, S. Dăgbağli, A. Uçan, U. Güvenç, Optimization of pullulan production from synthetic medium by Aureobasidium pullulans in a stirred tank reactor by response surface methodology, J. Chem. Technol. Biotechnol. 80 (2005) 819–827. https://doi.org/10.1002/jctb.1254.
[338] Y.C. Shin, Y.H. Kim, S.M. Byun, I.S.L. I, Y.N. Kim, Production of pullulan by a fed-batch fermentation, Biotechnol. Lett. 9 (1987) 621–624.
[339] A. Lazaridou, C.G. Biliaderis, T. Roukas, M. Izydorczyk, Production and characterization of pullulan from beet molasses using a nonpigmented strain of Aureobasidium pullulans in batch culture, Appl. Biochem. Biotechnol. - Part A Enzym. Eng. Biotechnol. 97 (2002) 1–22. https://doi.org/10.1385/ABAB:97:1:01.
[340] J.H. Kim, M.R. Kim, J.H. Lee, J.W. Lee, S.K. Kim, Production of high molecular weight pullulan by Aureobasidium pullulans using glucosamine, Biotechnol. Lett. 22 (2000) 987–990. https://doi.org/10.1023/A:1005681019573.
[341] L.B. Rothman, E. Cabib, Regulation of glycogen synthesis in the intact yeast cell, Biochemistry 8 (1969) 3332–3341. https://doi.org/10.1021/bi00836a030.
[342] S.M. Wani, F.A. Masoodi, S.A. Mir, F.A. Khanday, Pullulan production by Aureobasidium pullulans MTCC 1991 from apple pomace and its characterization, Food Biosci. 51 (2023) 102254. https://doi.org/10.1016/j.fbio.2022.102254.
[343] K.C. Cheng, A. Demirci, J.M. Catchmark, V.M. Puri, Effects of initial ammonium ion concentration on pullulan production by Aureobasidium pullulans and its modeling, J. Food Eng. 103 (2011) 115–122. https://doi.org/10.1016/j.jfoodeng.2010.10.004.
[344] P.T. Nguyen, T.T. Nguyen, T.N.T. Vo, T.T.X. Nguyen, Q.K. Hoang, H.T. Nguyen, Response of Lactobacillus plantarum VAL6 to challenges of pH and sodium chloride stresses, Sci. Rep. 11 (2021) 1–9. https://doi.org/10.1038/s41598-020-80634-1.
[345] N. Sahu, B. Mahanty, D. Haldar, Response surface methodology and artificial neural network based media optimization for pullulan production in Aureobasidium pullulans, Int. J. Biol. Macromol. 284 (2025) 138045. https://doi.org/10.1016/j.ijbiomac.2024.138045.
[346] S. Prasongsuk, M.A. Berhow, C.A. Dunlap, D. Weisleder, T.D. Leathers, D.E. Eveleigh, H. Punnapayak, Pullulan production by tropical isolates of Aureobasidium pullulans, J. Ind. Microbiol. Biotechnol. 34 (2007) 55–61. https://doi.org/10.1007/s10295-006-0163-

7.
[347] M. Kacuráková, P. Capek, V. Sasinková, N. Wellner, A. Ebringerová, FT-IR study of plant cell wall model compounds: Pectic polysaccharides and hemicelluloses, Carbohydr. Polym. 43 (2000) 195–203. https://doi.org/10.1016/S0144-8617(00)00151-X.
[348] R.S. Singh, G.K. Saini, Production, purification and characterization of pullulan from a novel strain of Aureobasidium pullulans FB-1, J. Biotechnol. 136 (2008) S506–S507. https://doi.org/10.1016/j.jbiotec.2008.07.625.
[349] S. Yang, X. Li, P. Liu, M. Zhang, C. Wang, B. Zhang, Multifunctional Chitosan/Polycaprolactone Nanofiber Scaffolds with Varied Dual-Drug Release for Wound-Healing Applications, ACS Biomater. Sci. Eng. 6 (2020) 4666–4676. https://doi.org/10.1021/acsbiomaterials.0c00674.
[350] B.S. Kim, Y.W. Kwon, J.S. Kong, G.T. Park, G. Gao, W. Han, M.B. Kim, H. Lee, J.H. Kim, D.W. Cho, 3D cell printing of in vitro stabilized skin model and in vivo pre-vascularized skin patch using tissue-specific extracellular matrix bioink: A step towards advanced skin tissue engineering, Biomaterials 168 (2018) 38–53. https://doi.org/10.1016/j.biomaterials.2018.03.040.
[351] M.E. Okur, I.D. Karantas, Z. Şenyiğit, N. Üstündağ Okur, P.I. Siafaka, Recent trends on wound management: New therapeutic choices based on polymeric carriers, Asian J. Pharm. Sci. 15 (2020) 661–684. https://doi.org/10.1016/j.ajps.2019.11.008.
[352] K.A. Rieger, N.P. Birch, J.D. Schiffman, Designing electrospun nanofiber mats to promote wound healing-a review, J. Mater. Chem. B 1 (2013) 4531–4541. https://doi.org/10.1039/c3tb20795a.
[353] Y. Liu, T. Li, Y. Han, F. Li, Y. Liu, Recent development of electrospun wound dressing, Curr. Opin. Biomed. Eng. 17 (2021) 100247. https://doi.org/10.1016/j.cobme.2020.100247.
[354] F. Amini, D. Semnani, S. Karbasi, S.N. Banitaba, A novel bilayer drug-loaded wound dressing of PVDF and PHB/Chitosan nanofibers applicable for post-surgical ulcers, Int. J. Polym. Mater. Polym. Biomater. 68 (2019) 772–777. https://doi.org/10.1080/00914037.2018.1506982.
[355] P.S. Murphy, G.R.D. Evans, Advances in Wound Healing: A Review of Current Wound Healing Products, Plast. Surg. Int. 2012 (2012) 1–8. https://doi.org/10.1155/2012/190436.
[356] A. Memic, T. Abudula, H.S. Mohammed, K. Joshi Navare, T. Colombani, S.A. Bencherif, Latest Progress in Electrospun Nanofibers for Wound Healing Applications, ACS Appl. Bio Mater. 2 (2019) 952–969. https://doi.org/10.1021/acsabm.8b00637.
[357] J.X. Liu, W.H. Dong, X.J. Mou, G.S. Liu, X.W. Huang, X. Yan, C.F. Zhou, S. Jiang, Y.Z. Long, In Situ Electrospun Zein/Thyme Essential Oil-Based Membranes as an Effective Antibacterial Wound Dressing, ACS Appl. Bio Mater. 3 (2020) 302–307. https://doi.org/10.1021/acsabm.9b00823.
[358] X. Zhang, Y. Wang, Z. Gao, X. Mao, J. Cheng, L. Huang, J. Tang, Advances in wound dressing based on electrospinning nanofibers, J. Appl. Polym. Sci. 141 (2024) 1–28. https://doi.org/10.1002/app.54746.
[359] S.P. Miguel, M.P. Ribeiro, P. Coutinho, I.J. Correia, Electrospun polycaprolactone/Aloe Vera_chitosan nanofibrous asymmetric membranes aimed for wound healing applications, Polymers (Basel). 9 (2017). https://doi.org/10.3390/polym9050183.
[360] S. Alven, X. Nqoro, B.A. Aderibigbe, Polymer-based materials loaded with curcumin for wound healing applications, Polymers (Basel). 12 (2020) 1–25. https://doi.org/10.3390/polym12102286.
[361] C.T.B. Paula, S. Saraiva, P. Pereira, J.F.J. Coelho, A.C. Fonseca, A.C. Serra, ROS-

responsive electrospun poly(amide thioketal) mats for wound dressing applications, Polymer (Guildf). 294 (2024). https://doi.org/10.1016/j.polymer.2024.126697.
[362] M.H.A. Kalijaga, A. Nurrochman, D. Annur, W.R. Sari, A. Sumboja, E. Prajatelistia, CeO2-loaded PVA/GelMA core-shell nanofiber membrane to promote wound healing, Polymer (Guildf). 307 (2024) 127320. https://doi.org/10.1016/j.polymer.2024.127320.
[363] H. Orhan, B. Yilmaz, In Vitro Properties of Electrospun Composite Fibers Containing Boric Acid and Enhanced with Epidermal Growth Factor for Wound Dressing Applications, Fibers Polym. 25 (2024) 485–500. https://doi.org/10.1007/s12221-023-00454-8.
[364] S. Agarwal, J.H. Wendorff, A. Greiner, Use of electrospinning technique for biomedical applications, Polymer (Guildf). 49 (2008) 5603–5621. https://doi.org/10.1016/j.polymer.2008.09.014.
[365] M. Hamidi, J.F. Kennedy, F. Khodaiyan, Z. Mousavi, S.S. Hosseini, Production optimization, characterization and gene expression of pullulan from a new strain of Aureobasidium pullulans, Int. J. Biol. Macromol. 138 (2019) 725–735. https://doi.org/10.1016/j.ijbiomac.2019.07.123.
[366] M.R. Karim, H.W. Lee, R. Kim, B.C. Ji, J.W. Cho, T.W. Son, W. Oh, J.H. Yeum, Preparation and characterization of electrospun pullulan/montmorillonite nanofiber mats in aqueous solution, Carbohydr. Polym. 78 (2009) 336–342. https://doi.org/10.1016/j.carbpol.2009.04.024.
[367] S. Kalia, A. Roy Choudhury, Synthesis and rheological studies of a novel composite hydrogel of xanthan, gellan and pullulan, Int. J. Biol. Macromol. 137 (2019) 475–482. https://doi.org/10.1016/j.ijbiomac.2019.06.212.
[368] Y. Han, S. Lv, Synthesis of chemically crosslinked pullulan/gelatin-based extracellular matrix-mimetic gels, Int. J. Biol. Macromol. 122 (2019) 1262–1270. https://doi.org/10.1016/j.ijbiomac.2018.09.080.
[369] R. Ahmed, M. Tariq, I. Ali, R. Asghar, P. Noorunnisa Khanam, R. Augustine, A. Hasan, Novel electrospun chitosan/polyvinyl alcohol/zinc oxide nanofibrous mats with antibacterial and antioxidant properties for diabetic wound healing, Int. J. Biol. Macromol. 120 (2018) 385–393. https://doi.org/10.1016/j.ijbiomac.2018.08.057.
[370] K.T. Shalumon, K.H. Anulekha, S. V. Nair, S. V. Nair, K.P. Chennazhi, R. Jayakumar, Sodium alginate/poly(vinyl alcohol)/nano ZnO composite nanofibers for antibacterial wound dressings, Int. J. Biol. Macromol. 49 (2011) 247–254. https://doi.org/10.1016/j.ijbiomac.2011.04.005.
[371] M.R. Safaee-Ardakani, A. Hatamian-Zarmi, S.M. Sadat, Z.B. Mokhtari-Hosseini, B. Ebrahimi-Hosseinzadeh, H. Kooshki, J. Rashidiani, In situ Preparation of PVA/Schizophyllan-AgNPs Nanofiber as Potential of Wound Healing: Characterization and Cytotoxicity, Fibers Polym. 20 (2019) 2493–2502. https://doi.org/10.1007/s12221-019-9388-8.
[372] M. Ranjbar Mohammadi, S. Kargozar, S.H. Bahrami, S. Rabbani, An excellent nanofibrous matrix based on gum tragacanth-poly (Ɛ-caprolactone)-poly (vinyl alcohol) for application in diabetic wound healing, Polym. Degrad. Stab. 174 (2020) 109105. https://doi.org/10.1016/j.polymdegradstab.2020.109105.
[373] F. Chogan, T. Mirmajidi, A.H. Rezayan, A.M. Sharifi, A. Ghahary, J. Nourmohammadi, A. Kamali, M. Rahaie, Design, fabrication, and optimization of a dual function three-layer scaffold for controlled release of metformin hydrochloride to alleviate fibrosis and accelerate wound healing, Acta Biomater. 113 (2020) 144–163. https://doi.org/10.1016/j.actbio.2020.06.031.
[374] M.S. Islam, M.M. Rabbani, S.B. Yang, W.S. Choi, J.H. Choi, W. Oh, J.C. Shin, J.T. Lee, J.H. Yeum, Poly(vinyl alcohol)/pullulan blend nanofibres prepared from aqueous

solutions using electrospinning method, Polym. Polym. Compos. 22 (2014) 779–786. https://doi.org/10.1177/096739111402200904.
[375] A. Koyyada, P. Orsu, Natural gum polysaccharides as efficient tissue engineering and drug delivery biopolymers, J. Drug Deliv. Sci. Technol. 63 (2021) 102431. https://doi.org/10.1016/j.jddst.2021.102431.
[376] Z. Pedram Rad, J. Mokhtari, M. Abbasi, Fabrication and characterization of PCL/zein/gum arabic electrospun nanocomposite scaffold for skin tissue engineering, Mater. Sci. Eng. C 93 (2018) 356–366. https://doi.org/10.1016/j.msec.2018.08.010.
[377] M. Keykhaee, M. Rahimifard, A. Najafi, M. Baeeri, M. Abdollahi, F. Mottaghitalab, M. Farokhi, M. Khoobi, Alginate/gum arabic-based biomimetic hydrogel enriched with immobilized nerve growth factor and carnosine improves diabetic wound regeneration, Carbohydr. Polym. 321 (2023) 121179. https://doi.org/10.1016/j.carbpol.2023.121179.
[378] M. Hadavi, S. Hasannia, S. Faghihi, F. Mashayekhi, H.H. Zadeh, S.B. Mostofi, Novel calcified gum Arabic porous nano-composite scaffold for bone tissue regeneration, Biochem. Biophys. Res. Commun. 488 (2017) 671–678. https://doi.org/10.1016/j.bbrc.2017.03.046.
[379] W. Li, J. Wang, Z. Cheng, G. Yang, C. Zhao, F. Gao, Z. Zhang, Y. Qian, Sandwich structure Aloin-PVP/Aloin-PVP-PLA/PLA as a wound dressing to accelerate wound healing, RSC Adv. 12 (2022) 27300–27308. https://doi.org/10.1039/d2ra02320b.
[380] M. Hajikhani, Z. Emam-Djomeh, G. Askari, Fabrication and characterization of mucoadhesive bioplastic patch via coaxial polylactic acid (PLA) based electrospun nanofibers with antimicrobial and wound healing application, Int. J. Biol. Macromol. 172 (2021) 143–153. https://doi.org/10.1016/j.ijbiomac.2021.01.051.
[381] D. Bose, V. Prasannavenkadesan, V. Katiyar, Tailored material for bioresorbable internal fixation devices: a novel approach using nanohydroxyapatite and chitosan in polylactic acid, J. Mater. Sci. 59 (2024) 215–227. https://doi.org/10.1007/s10853-023-09110-1.
[382] A. Prasad, S.M. Bhasney, V. Prasannavenkadesan, M.R. Sankar, V. Katiyar, Polylactic acid reinforced with nano-hydroxyapatite bioabsorbable cortical screws for bone fracture treatment, J. Polym. Res. 30 (2023) 1–12. https://doi.org/10.1007/s10965-023-03542-8.
[383] A. Kwong, J. Cogan, Y. Hou, R. Antaya, M. Hao, G. Kim, V. Lincoln, Q. Chen, D.T. Woodley, M. Chen, Gentamicin Induces Laminin 332 and Improves Wound Healing in Junctional Epidermolysis Bullosa Patients with Nonsense Mutations, Mol. Ther. 28 (2020) 1327–1338. https://doi.org/10.1016/j.ymthe.2020.03.006.
[384] S. Wang, Y. Xiong, J. Chen, A. Ghanem, Y. Wang, J. Yang, B. Sun, Three Dimensional Printing Bilayer Membrane Scaffold Promotes Wound Healing, Front. Bioeng. Biotechnol. 7 (2019) 1–11. https://doi.org/10.3389/fbioe.2019.00348.
[385] S. Zhou, Q. Wang, W. Yang, L. Wang, J. Wang, R. You, Z. Luo, Q. Zhang, S. Yan, Development of a bioactive silk fibroin bilayer scaffold for wound healing and scar inhibition, Int. J. Biol. Macromol. 255 (2024) 128350. https://doi.org/10.1016/j.ijbiomac.2023.128350.
[386] A. Hajati Ziabari, S. Ebrahimi, K. Jafari, S.M. Doodmani, O. Natouri, A. Nobakht, S. Mouseli, Bilayer nanofibers loaded with Malva sylvestris extract for enhanced wound healing applications, J. Drug Deliv. Sci. Technol. 93 (2024) 105373. https://doi.org/10.1016/j.jddst.2024.105373.
[387] Z. Song, J. Wang, S. Tan, J. Gao, L. Wang, Conductive biomimetic bilayer fibrous scaffold for skin regeneration, Colloids Surfaces A Physicochem. Eng. Asp. 656 (2023) 130211. https://doi.org/10.1016/j.colsurfa.2022.130211.
[388] A. Pissarenko, C.J. Ruestes, M.A. Meyers, Constitutive description of skin dermis:

Through analytical continuum and coarse-grained approaches for multi-scale understanding, Acta Biomater. 106 (2020) 208–224. https://doi.org/10.1016/j.actbio.2020.01.026.

[389] N. Asadi, A. Mehdipour, M. Ghorbani, M. Mesgari-Abbasi, A. Akbarzadeh, S. Davaran, A novel multifunctional bilayer scaffold based on chitosan nanofiber/alginate-gelatin methacrylate hydrogel for full-thickness wound healing, Int. J. Biol. Macromol. 193 (2021) 734–747. https://doi.org/10.1016/j.ijbiomac.2021.10.180.

[390] A. Eskandarinia, A. Kefayat, M. Agheb, M. Rafienia, M. Amini Baghbadorani, S. Navid, K. Ebrahimpour, D. Khodabakhshi, F. Ghahremani, A Novel Bilayer Wound Dressing Composed of a Dense Polyurethane/Propolis Membrane and a Biodegradable Polycaprolactone/Gelatin Nanofibrous Scaffold, Sci. Rep. 10 (2020) 1–15. https://doi.org/10.1038/s41598-020-59931-2.

[391] B. Yu, C. He, W. Wang, Y. Ren, J. Yang, S. Guo, Y. Zheng, X. Shi, Asymmetric Wettable Composite Wound Dressing Prepared by Electrospinning with Bioinspired Micropatterning Enhances Diabetic Wound Healing, ACS Appl. Bio Mater. 3 (2020) 5383–5394. https://doi.org/10.1021/acsabm.0c00695.

[392] C. Su, H. Zhao, H. Yang, R. Chen, Stearic Acid-Modified Starch/Chitosan Composite Sponge with Asymmetric and Gradient Wettability for Wound Dressing, ACS Appl. Bio Mater. 2 (2019) 171–181. https://doi.org/10.1021/acsabm.8b00508.

[393] A. Chanda, J. Adhikari, A. Ghosh, S.R. Chowdhury, S. Thomas, P. Datta, P. Saha, Electrospun chitosan/polycaprolactone-hyaluronic acid bilayered scaffold for potential wound healing applications, Int. J. Biol. Macromol. 116 (2018) 774–785. https://doi.org/10.1016/j.ijbiomac.2018.05.099.

[394] Z. Lu, J. Gao, Q. He, J. Wu, D. Liang, H. Yang, R. Chen, Enhanced antibacterial and wound healing activities of microporous chitosan-Ag/ZnO composite dressing, Carbohydr. Polym. 156 (2017) 460–469. https://doi.org/10.1016/j.carbpol.2016.09.051.

[395] Q. Li, F. Lu, G. Zhou, K. Yu, B. Lu, Y. Xiao, F. Dai, D. Wu, G. Lan, Silver Inlaid with Gold Nanoparticle/Chitosan Wound Dressing Enhances Antibacterial Activity and Porosity, and Promotes Wound Healing, Biomacromolecules 18 (2017) 3766–3775. https://doi.org/10.1021/acs.biomac.7b01180.

[396] G. Ramanathan, L.S. Seleenmary Sobhanadhas, G.F. Sekar Jeyakumar, V. Devi, U.T. Sivagnanam, P. Fardim, Fabrication of Biohybrid Cellulose Acetate-Collagen Bilayer Matrices as Nanofibrous Spongy Dressing Material for Wound-Healing Application, Biomacromolecules 21 (2020) 2512–2524. https://doi.org/10.1021/acs.biomac.0c00516.

[397] J.P.E. Junker, R.A. Kamel, E.J. Caterson, E. Eriksson, Clinical Impact Upon Wound Healing and Inflammation in Moist, Wet, and Dry Environments, Adv. Wound Care 2 (2013) 348–356. https://doi.org/10.1089/wound.2012.0412.

[398] J. Zhang, X. Huang, J. Zhang, L. Liu, J. Shi, A. Muhammad, X. Zhai, X. Zou, J. Xiao, Z. Li, Y. Li, T. Shen, Development of nanofiber indicator with high sensitivity for pork preservation and freshness monitoring, Food Chem. 381 (2022) 132224. https://doi.org/10.1016/j.foodchem.2022.132224.

[399] M.M. Delavari, I. Stiharu, Preparing and Characterizing Novel Biodegradable Starch/PVA-Based Films with Nano-Sized Zinc-Oxide Particles for Wound-Dressing Applications, Appl. Sci. 12 (2022). https://doi.org/10.3390/app12084001.

[400] M.M. Delavari, I. Ocampo, I. Stiharu, Optimizing Biodegradable Starch-Based Composite Films Formulation for Wound-Dressing Applications, Micromachines 13 (2022). https://doi.org/10.3390/mi13122146.

[401] A.S. Ahmed, U.K. Mandal, M. Taher, D. Susanti, J.M. Jaffri, PVA-PEG physically cross-linked hydrogel film as a wound dressing: experimental design and optimization,

Pharm. Dev. Technol. 23 (2018) 751–760. https://doi.org/10.1080/10837450.2017.1295067.
[402] K. Pal, A.K. Banthia, D.K. Majumdar, Preparation and characterization of polyvinyl alcohol-gelatin hydrogel membranes for biomedical applications, AAPS PharmSciTech 8 (2007). https://doi.org/10.1208/pt080121.
[403] C. Echeverría, I. Limón, A. Muñoz-Bonilla, M. Fernández-García, D. López, Development of highly crystalline polylactic acid with β-crystalline phase from the induced alignment of electrospun fibers, Polymers (Basel). 13 (2021). https://doi.org/10.3390/polym13172860.
[404] R. Fu, L. Tu, Y. Zhou, L. Fan, F. Zhang, Z. Wang, J. Xing, D. Chen, C. Deng, G. Tan, P. Yu, L. Zhou, C. Ning, A Tough and Self-Powered Hydrogel for Artificial Skin, Chem. Mater. 31 (2019) 9850–9860. https://doi.org/10.1021/acs.chemmater.9b04041.
[405] A. Ní Annaidh, K. Bruyère, M. Destrade, M.D. Gilchrist, M. Otténio, Characterization of the anisotropic mechanical properties of excised human skin, J. Mech. Behav. Biomed. Mater. 5 (2012) 139–148. https://doi.org/10.1016/j.jmbbm.2011.08.016.
[406] T. Zhang, H. Xu, Y. Zhang, S. Zhang, X. Yang, Y. Wei, D. Huang, X. Lian, Fabrication and characterization of double-layer asymmetric dressing through electrostatic spinning and 3D printing for skin wound repair, Mater. Des. 218 (2022) 110711. https://doi.org/10.1016/j.matdes.2022.110711.
[407] H. Chen, G. Lan, L. Ran, Y. Xiao, K. Yu, B. Lu, F. Dai, D. Wu, F. Lu, A novel wound dressing based on a Konjac glucomannan/silver nanoparticle composite sponge effectively kills bacteria and accelerates wound healing, Carbohydr. Polym. 183 (2018) 70–80. https://doi.org/10.1016/j.carbpol.2017.11.029.
[408] M. Shie Karizmeh, S.A. Poursamar, A. Kefayat, Z. Farahbakhsh, M. Rafienia, An in vitro and in vivo study of PCL/chitosan electrospun mat on polyurethane/propolis foam as a bilayer wound dressing, Biomater. Adv. 135 (2022). https://doi.org/10.1016/j.msec.2022.112667.
[409] T.T. Paterlini, L.F.B. Nogueira, C.B. Tovani, M.A.E. Cruz, R. Derradi, A.P. Ramos, The role played by modified bioinspired surfaces in interfacial properties of biomaterials, Biophys. Rev. 9 (2017) 683–698. https://doi.org/10.1007/s12551-017-0306-2.
[410] J.I. Kim, H.R. Pant, H.J. Sim, K.M. Lee, C.S. Kim, Electrospun propolis/polyurethane composite nanofibers for biomedical applications, Mater. Sci. Eng. C 44 (2014) 52–57. https://doi.org/10.1016/j.msec.2014.07.062.
[411] S. Amjadi, M. Nazari, S.A. Alizadeh, H. Hamishehkar, Multifunctional betanin nanoliposomes-incorporated gelatin/chitosan nanofiber/ZnO nanoparticles nanocomposite film for fresh beef preservation, Meat Sci. 167 (2020) 108161. https://doi.org/10.1016/j.meatsci.2020.108161.
[412] N. Yasrebi, A.H. Zarmi, M. Larypoor, M. Zeynali, B. Ebrahimi-Hosseinzadeh, Z.B. Mokhtari-Hosseini, H. Alvandi, In vivo and in vitro evaluation of the wound healing properties of chitosan extracted from Trametes versicolor, J. Polym. Res. 28 (2021). https://doi.org/10.1007/s10965-021-02773-x.
[413] A. V. Janorkar, A.T. Metters, D.E. Hirt, Modification of poly(lactic acid) films: Enhanced wettability from surface-confined photografting and increased degradation rate due to an artifact of the photografting process, Macromolecules 37 (2004) 9151–9159. https://doi.org/10.1021/ma049056u.
[414] S. Sousa, A. Costa, A. Silva, R. Simões, Poly(lactic acid)/Cellulose films produced from composite spheres prepared by emulsion-solvent evaporation method, Polymers (Basel). 11 (2019) 1–19. https://doi.org/10.3390/polym11010066.
[415] N. Masood, R. Ahmed, M. Tariq, Z. Ahmed, M.S. Masoud, I. Ali, R. Asghar, A.

Andleeb, A. Hasan, Silver Nanoparticle Impregnated Chitosan-PEG Hydrogel Enhances Wound Healing in Department of Biotechnology , Faculty of Science , Mirpur University of Science and Department of Chemistry , Faculty of Science , Mirpur University of Science and Department , Int. J. Pharm. (2019). https://doi.org/10.1016/j.ijpharm.2019.01.019.

[416] R. Xu, H. Xia, W. He, Z. Li, J. Zhao, B. Liu, Y. Wang, Q. Lei, Y. Kong, Y. Bai, Z. Yao, R. Yan, H. Li, R. Zhan, S. Yang, G. Luo, J. Wu, Controlled water vapor transmission rate promotes wound-healing via wound re-epithelialization and contraction enhancement, Sci. Rep. 6 (2016) 1–12. https://doi.org/10.1038/srep24596.

[417] G. Xia, D. Zhai, Y. Sun, L. Hou, X. Guo, L. Wang, Z. Li, F. Wang, Preparation of a novel asymmetric wettable chitosan-based sponge and its role in promoting chronic wound healing, Carbohydr. Polym. 227 (2020) 115296. https://doi.org/10.1016/j.carbpol.2019.115296.

[418] A.E. Giannakas, C.E. Salmas, A. Leontiou, M. Baikousi, D. Moschovas, G. Asimakopoulos, N.E. Zafeiropoulos, A. Avgeropoulos, Synthesis of a novel chitosan/basil oil blend and development of novel low density poly ethylene/chitosan/basil oil active packaging films following a melt-extrusion process for enhancing chicken breast fillets shelf-life, Molecules 26 (2021). https://doi.org/10.3390/molecules26061585.

[419] M.M. Abd Al-Ghani, R.A. Azzam, T.M. Madkour, Design and development of enhanced antimicrobial breathable biodegradable polymeric films for food packaging applications, Polymers (Basel). 13 (2021). https://doi.org/10.3390/polym13203527.

[420] X. Chen, X. Wang, S. Wang, X. Zhang, J. Yu, C. Wang, Mussel-inspired polydopamine-assisted bromelain immobilization onto electrospun fibrous membrane for potential application as wound dressing, Mater. Sci. Eng. C 110 (2020) 110624. https://doi.org/10.1016/j.msec.2019.110624.

[421] S. Chao, Y. Li, R. Zhao, L. Zhang, Y. Li, C. Wang, X. Li, Synthesis and characterization of tigecycline-loaded sericin/poly(vinyl alcohol) composite fibers via electrospinning as antibacterial wound dressings, J. Drug Deliv. Sci. Technol. 44 (2018) 440–447. https://doi.org/10.1016/j.jddst.2018.01.022.

[422] F. Wang, S. Hu, Q. Jia, L. Zhang, Advances in Electrospinning of Natural Biomaterials for Wound Dressing, J. Nanomater. 2020 (2020). https://doi.org/10.1155/2020/8719859.

[423] F. Shahverdi, A. Barati, E. Salehi, M. Arjomandzadegan, Biaxial electrospun nanofibers based on chitosan-poly (vinyl alcohol) and poly (Ɛ-caprolactone) modified with CeAlO3 nanoparticles as potential wound dressing materials, Int. J. Biol. Macromol. 221 (2022) 736–750. https://doi.org/10.1016/j.ijbiomac.2022.09.061.

[424] E.R. Kenawy, M.S.A. El-Moaty, M. Ghoneum, H.M.A. Soliman, A.A. El-Shanshory, S. Shendy, Biobran-loaded core/shell nanofibrous scaffold: a promising wound dressing candidate, RSC Adv. 14 (2024) 4930–4945. https://doi.org/10.1039/d3ra08609g.

[425] I. Bonadies, F. Di Cristo, A. Valentino, G. Peluso, A. Calarco, A. Di Salle, Ph-responsive resveratrol-loaded electrospun membranes for the prevention of implant-associated infections, Nanomaterials 10 (2020) 1–18. https://doi.org/10.3390/nano10061175.

[426] Y. Fang, X. Zhu, N. Wang, X. Zhang, D. Yang, J. Nie, G. Ma, Biodegradable core-shell electrospun nanofibers based on PLA and γ-PGA for wound healing, Eur. Polym. J. 116 (2019) 30–37. https://doi.org/10.1016/j.eurpolymj.2019.03.050.

[427] L. Bauer, A. Rogina, M. Ivanković, H. Ivanković, Medical-Grade Poly(Lactic Acid)/Hydroxyapatite Composite Films: Thermal and In Vitro Degradation Properties, Polymers (Basel). 15 (2023). https://doi.org/10.3390/polym15061512.

[428] F. Zou, X. Sun, X. Wang, Elastic, hydrophilic and biodegradable poly (1, 8-octanediol-co-citric acid)/polylactic acid nanofibrous membranes for potential wound dressing applications, Polym. Degrad. Stab. 166 (2019) 163–173. https://doi.org/10.1016/j.polymdegradstab.2019.05.024.
[429] M. Zarei, A. Samimi, M. Khorram, M.M. Abdi, S.I. Golestaneh, Fabrication and characterization of conductive polypyrrole/chitosan/collagen electrospun nanofiber scaffold for tissue engineering application, Int. J. Biol. Macromol. 168 (2021) 175–186. https://doi.org/10.1016/j.ijbiomac.2020.12.031.
[430] D.I. Sánchez-Machado, J. López-Cervantes, C.A. Vega-Cázarez, K.L. Hernández-Ruiz, O.N. Campas-Baypoli, A. Soto-Cota, T.J. Madera-Santana, Functional and antibacterial characterization of electrospun nanofiber membranes made of chitosan and polyvinyl alcohol, Results Chem. 7 (2024). https://doi.org/10.1016/j.rechem.2024.101314.
[431] S. Baishal, J. Prakash, M.S. Marvaan, M. Sundar, B. Pannerselvam, G.D. Venkatasubbu, Naringin and graphene oxide incorporated Moringa oleifera gum/poly(vinyl) alcohol patch for enhanced wound healing, Int. J. Biol. Macromol. 259 (2024). https://doi.org/10.1016/j.ijbiomac.2024.129198.
[432] K.H. Sun, Z. Liu, C. Liu, T. Yu, T. Shang, C. Huang, M. Zhou, C. Liu, F. Ran, Y. Li, Y. Shi, L. Pan, Evaluation of in vitro and in vivo biocompatibility of a myo-inositol hexakisphosphate gelated polyaniline hydrogel in a rat model, Sci. Rep. 6 (2016) 1–11. https://doi.org/10.1038/srep23931.
[433] A.C. Caroprese, A.N.C. Navarrete, S.J.G. Prieto, J.C. Villamil, O.A.C. Uribe, J.C.S. Reyes, H.A.M. Pinzón, Cytotoxic effects on human dental pulp stem Cells after exposure to adhesive bonding agents, Braz. Dent. J. 35 (2024) 1–13. https://doi.org/10.1590/0103-6440202405529.
[434] K. Das, S. Sharma, S. Kumar, S. Mahajan, S.K. Banerjee, International Journal of Biological Macromolecules Chitosan nanoparticles and neem essential oil functionalized pullulan / gum arabic active edible biocomposites for fresh-cut guava preservation, Int. J. Biol. Macromol. 283 (2024) 136936. https://doi.org/10.1016/j.ijbiomac.2024.136936.
[435] S. Hashemi, R. Nahidi, H. Ansari, K. Firoozi, R. Rokhshad, Comparative analysis of cytotoxicity effects of two denture hard lining materials on human gingival fibroblasts: an in vitro study, Saudi Dent. J. 36 (2024) 765–769. https://doi.org/10.1016/j.sdentj.2024.02.005.
[436] Y.R. Choi, M.K. Kang, Evaluation of Cytotoxic and Antibacterial Effect of Methanolic Extract of Paeonia lactiflora, Med. 58 (2022) 1–9. https://doi.org/10.3390/medicina58091272.
[437] F.L.A. Cardoso, L.L.S. Soares, D.B.A. Silva, N.M. Argôlo Neto, E.C. Silva Filho, A.S. Silva, D.O. Bezerra, M.S.P. Cruz, F.C. Nunes, W.G.G. Melo, J.M.C. Sousa, A.C. Reis, M.A.M. Carvalho, Cytotoxicity and genotoxic impacts of LAPONITE® on murine adipose stem cells, Appl. Clay Sci. 261 (2024). https://doi.org/10.1016/j.clay.2024.107572.
[438] C. Liu, Q. Zhang, Z. Liu, D. Zhuang, S. Wang, H. Deng, Y. Shi, J. Sun, J. Guo, F. Wei, X. Wu, miR-21 Expressed by Dermal Fibroblasts Enhances Skin Wound Healing Through the Regulation of Inflammatory Cytokine Expression, Inflammation 47 (2024) 572–590. https://doi.org/10.1007/s10753-023-01930-2.
[439] O.G. Virijević, K., Živanović, M.N., Nikolić, D., Milivojević, N., Pavić, J., Morić, I., Šenerović, L., Dragačević, L., Thurner, P.J., Rufin, M. and Andriotis, AI-Driven Optimization of PCL/PEG Electrospun Scaffolds for Enhanced In Vivo Wound Healing, (2024) 22989–23002.
[440] E.F. dos Reis, F.S. Campos, A.P. Lage, R.C. Leite, L.G. Heneine, W.L. Vasconcelos,

Z.I.P. Lobato, H.S. Mansur, Synthesis and characterization of poly (vinyl alcohol) hydrogels and hybrids for rMPB70 protein adsorption, Mater. Res. 9 (2006) 185–191. https://doi.org/10.1590/s1516-14392006000200014.

[441] H.S. Mansur, C.M. Sadahira, A.N. Souza, A.A.P. Mansur, FTIR spectroscopy characterization of poly (vinyl alcohol) hydrogel with different hydrolysis degree and chemically crosslinked with glutaraldehyde, Mater. Sci. Eng. C 28 (2008) 539–548. https://doi.org/10.1016/j.msec.2007.10.088.

[442] C.T. Chen, K.I. Chen, H.H. Chiang, Y.K. Chen, K.C. Cheng, Improvement on Physical Properties of Pullulan Films by Novel Cross-Linking Strategy, J. Food Sci. 82 (2017) 108–117. https://doi.org/10.1111/1750-3841.13577.

[443] A. Koohkhezri, M., Lotfi, R., Zandi, N., Emami, Z., Tamjid, E. and Simchi, Drug-Eluting and Antibacterial Core–Shell Polycaprolactone/Pectin Nanofibers Containing Ti3C2Tx MXene and Medical Herbs for Wound Dressings, ACS Appl. Bio Mater. 1 (2021) 2–5. https://doi.org/10.1021/acsabm.4c00880.

[444] N. Reddy, R. Reddy, Q. Jiang, Crosslinking biopolymers for biomedical applications, Trends Biotechnol. 33 (2015) 362–369. https://doi.org/10.1016/j.tibtech.2015.03.008.

[445] X. Li, Q. Li, C. Zhao, Zero-Order Controlled Release of Water-Soluble Drugs Using a Marker Pen Platform, ACS Omega 6 (2021) 13774–13778. https://doi.org/10.1021/acsomega.1c01141.

[446] F. Ciftci, Release kinetics modelling and in vivo-vitro, shelf-life study of resveratrol added composite transdermal scaffolds, Int. J. Biol. Macromol. 235 (2023) 123769. https://doi.org/10.1016/j.ijbiomac.2023.123769.

[447] M.L. Laracuente, M.H. Yu, K.J. McHugh, Zero-order drug delivery: State of the art and future prospects, J. Control. Release 327 (2020) 834–856. https://doi.org/10.1016/j.jconrel.2020.09.020.

[448] T. Hou, X. Li, Y. Lu, J. Zhou, X. Zhang, S. Liu, B. Yang, Fabrication of hierarchical porous ethyl cellulose fibrous membrane by electro-centrifugal spinning for drug delivery systems with excellent integrated properties, Int. J. Biol. Macromol. 242 (2023) 125141. https://doi.org/10.1016/j.ijbiomac.2023.125141.

[449] A.E. Erickson, D. Edmondson, F.C. Chang, D. Wood, A. Gong, S.L. Levengood, M. Zhang, High-throughput and high-yield fabrication of uniaxially-aligned chitosan-based nanofibers by centrifugal electrospinning, Carbohydr. Polym. 134 (2015) 467–474. https://doi.org/10.1016/j.carbpol.2015.07.097.

[450] N.A. Norzain, W.C. Lin, Orientated and diameter-controlled fibrous scaffolds fabricated using the centrifugal electrospinning technique for stimulating the behaviours of fibroblast cells, J. Ind. Text. 51 (2022) 6728S-6752S. https://doi.org/10.1177/1528083720988127.

[451] H. Peng, Y. Liu, S. Ramakrishna, Recent development of centrifugal electrospinning, J. Appl. Polym. Sci. 134 (2017) 1–10. https://doi.org/10.1002/app.44578.

[452] H. Chen, X.L. Li, N. Li, B. Yang, Electrostatic-assisted centrifugal spinning for continuous collection of submicron fibers, Text. Res. J. 87 (2017) 2349–2357. https://doi.org/10.1177/0040517516671121.

[453] T. Hou, X. Li, Y. Lu, B. Yang, Highly porous fibers prepared by centrifugal spinning, Mater. Des. 114 (2017) 303–311. https://doi.org/10.1016/j.matdes.2016.11.019.

[454] X. Zhang, Y. Lu, Centrifugal spinning: An alternative approach to fabricate nanofibers at high speed and low cost, Polym. Rev. 54 (2014) 677–701. https://doi.org/10.1080/15583724.2014.935858.

[455] M.R. Badrossamay, H.A. McIlwee, J.A. Goss, K.K. Parker, Nanofiber assembly by rotary jet-spinning, Nano Lett. 10 (2010) 2257–2261. https://doi.org/10.1021/nl101355x.

[456] H. Xu, S. Yagi, S. Ashour, L. Du, M.E. Hoque, L. Tan, A Review on Current Nanofiber Technologies: Electrospinning, Centrifugal Spinning, and Electro-Centrifugal Spinning, Macromol. Mater. Eng. 308 (2023) 1–13. https://doi.org/10.1002/mame.202200502.
[457] A. Gholipour-Kanani, P. Daneshi, A Review on Centrifugal and Electro-Centrifugal Spinning as New Methods of Nanofibers Fabrication, J. Text. Polym. 10 (2022) 41–55.
[458] A.R. Hashemi, A.R. Pishevar, A. Valipouri, E.I. Părău, Numerical and experimental study on the steady cone-jet mode of electro-centrifugal spinning, Phys. Fluids 30 (2018). https://doi.org/10.1063/1.5001808.
[459] B. Zhou, X. Bu, J. Li, C. Gao, X. Saitaer, J. Guo, Electro–centrifugal spinning of core–sheath composite yarns with micro/nano structures for self–powered sensing, Compos. Commun. 53 (2025) 102141. https://doi.org/10.1016/j.coco.2024.102141.
[460] N.A. Norzain, W. Chih Lin, Electrostatic Force and Centrifugal Force for Fiber Fabrication, ICECOS 2019 - 3rd Int. Conf. Electr. Eng. Comput. Sci. Proceeding (2019) 112–116. https://doi.org/10.1109/ICECOS47637.2019.8984455.
[461] L. Wang, M.W. Chang, Z. Ahmad, H. Zheng, J.S. Li, Mass and controlled fabrication of aligned PVP fibers for matrix type antibiotic drug delivery systems, Chem. Eng. J. 307 (2017) 661–669. https://doi.org/10.1016/j.cej.2016.08.135.
[462] F. Müller, S. Jokisch, H. Bargel, T. Scheibel, Centrifugal Electrospinning Enables the Production of Meshes of Ultrathin Polymer Fibers, ACS Appl. Polym. Mater. 2 (2020) 4360–4367. https://doi.org/10.1021/acsapm.0c00853.
[463] Y. Zhang, P. Wang, Q. Shi, X. Ning, J. Zheng, Y.Z. Long, Research progress and prospect of centrifugal electrospinning and its application, J. Alloys Compd. 990 (2024) 174433. https://doi.org/10.1016/j.jallcom.2024.174433.
[464] J. Gu, S. Yagi, J. Meng, Y. Dong, C. Qian, D. Zhao, A. Kumar, T. Xu, A. Lucchetti, H. Xu, High-efficiency production of core-sheath nanofiber membrane via co-axial electro-centrifugal spinning for controlled drug release, J. Memb. Sci. 654 (2022). https://doi.org/10.1016/j.memsci.2022.120571.
[465] M. Hamidi, J.F. Kennedy, F. Khodaiyan, Z. Mousavi, S.S. Hosseini, Production optimization, characterization and gene expression of pullulan from a new strain of Aureobasidium pullulans, Int. J. Biol. Macromol. 138 (2019) 725–735. https://doi.org/10.1016/j.ijbiomac.2019.07.123.
[466] R.S. Singh, N. Kaur, M. Hassan, J.F. Kennedy, Pullulan in biomedical research and development - A review, Int. J. Biol. Macromol. 166 (2021) 694–706. https://doi.org/10.1016/j.ijbiomac.2020.10.227.
[467] D. Poudel, S. Swilley-sanchez, O. Sean, J. Matson, T. Long, C. Fern, Novel electrospun pullulan fibers incorporating hydroxypropyl-β-cyclodextrin: morphology and relation with rheological properties, Polymers (Basel). 12 (2020) 2558.
[468] M. Zhang, J. Lidder, M. Bahri, H. Zhang, Preparation of PLGA-Coated Porous Silica Nanofibers for Drug Release, Pharmaceutics 14 (2022). https://doi.org/10.3390/pharmaceutics14122660.
[469] A. Kongprayoon, G. Ross, N. Limpeanchob, S. Mahasaranon, W. Punyodom, P.D. Topham, S. Ross, Bio-derived and biocompatible poly(lactic acid)/silk sericin nanogels and their incorporation within poly(lactide-co-glycolide) electrospun nanofibers, Polym. Chem. 13 (2022) 3343–3357. https://doi.org/10.1039/d2py00330a.
[470] A. Tuanchai, P. Iamphring, P. Suttaphakdee, M. Boupan, J. Mikule, J. Pablo, P. Worajittiphon, Y. Liu, G.M. Ross, S. Kunc, P. Mikeš, M. Unno, S. Ross, Bilayer Scaffolds of PLLA/PCL/CAB Ternary Blend Films and Curcumin-Incorporated PLGA Electrospun Nanofibers: The Effects of Polymer Compositions and Solvents on Morphology and Molecular Interactions, Polymers (Basel). 16 (2024) 1679.
[471] A. Guzmán-Soria, V. Moreno-Serna, D.A. Canales, C. García-Herrera, P.A. Zapata,

P.A. Orihuela, Effect of Electrospun PLGA/Collagen Scaffolds on Cell Adhesion, Viability, and Collagen Release: Potential Applications in Tissue Engineering, Polymers (Basel). 15 (2023). https://doi.org/10.3390/polym15051079.

[472] Z. Ude, K. Kavanagh, B. Twamley, M. Pour, N. Gathergood, A. Kellett, C.J. Marmion, A new class of prophylactic metallo-antibiotic possessing potent anti-cancer and anti-microbial properties, Dalt. Trans. 48 (2019) 8578–8593. https://doi.org/10.1039/c9dt00250b.

[473] Y. Fu, Y. Yang, S. Zhou, Y. Liu, Y. Yuan, S. Li, C. Li, Ciprofloxacin containing Mannich base and its copper complex induce antitumor activity via different mechanism of action, Int. J. Oncol. 45 (2014) 2092–2100. https://doi.org/10.3892/ijo.2014.2611.

[474] D.F. Jaber, M.A.N. Jallad, A.M. Abdelnoor, The effect of ciprofloxacin on the growth of B16F10 melanoma cells, J. Cancer Res. Ther. 13 (2017) 956–960. https://doi.org/10.4103/0973-1482.180610.

[475] O. Aranha, D.P. Wood, F.H. Sarkar, Ciprofloxacin mediated cell growth inhibition, S/G2-M cell cycle arrest, and apoptosis in a human transitional cell carcinoma of the bladder cell line, Clin. Cancer Res. 6 (2000) 891–900.

[476] E. Somekh, Eli, Douer, Dan, Shaked, Nili, and Rubinstein, In Vitro Effects of Ciprofloxacin and Pefloxacin on Growth of Normal Human Hematopoletic, J. Pharmacol. Exp. Ther. 0415502 (1989) 0–3.

[477] S.A. Aldaghi, R. Jalal, Concentration-Dependent Dual Effects of Ciprofloxacin on SB-590885-Resistant BRAF V600E A375 Melanoma Cells, Chem. Res. Toxicol. 32 (2019) 645–658. https://doi.org/10.1021/acs.chemrestox.8b00335.

[478] A. Beberok, D. Wrześniok, A. Minecka, J. Rok, M. Delijewski, Z. Rzepka, M. Respondek, E. Buszman, Ciprofloxacin-mediated induction of S-phase cell cycle arrest and apoptosis in COLO829 melanoma cells, Pharmacol. Reports 70 (2018) 6–13. https://doi.org/10.1016/j.pharep.2017.07.007.

[479] Q. Chen, S. Xu, S. Liu, Y. Wang, G. Liu, Emerging nanomedicines of paclitaxel for cancer treatment, J. Control. Release 342 (2022) 280–294. https://doi.org/10.1016/j.jconrel.2022.01.010.

[480] S. Asnaashari, E. Amjad, B. Sokouti, Synergistic effects of flavonoids and paclitaxel in cancer treatment: a systematic review, Cancer Cell Int. 23 (2023) 1–32. https://doi.org/10.1186/s12935-023-03052-z.

[481] F. Zahedipour, P. Kesharwani, A. Sahebkar, Mechanisms of multidrug resistance in cancer, Aptamers Eng. Nanocarriers Cancer Ther. 596 (2023) 51–83. https://doi.org/10.1016/B978-0-323-85881-6.00002-6.

[482] C.P. Wu, C.H. Hsieh, Y.S. Wu, The emergence of drug transporter-mediated multidrug resistance to cancer chemotherapy, Mol. Pharm. 8 (2011) 1996–2011. https://doi.org/10.1021/mp200261n.

[483] P. Gupta, H.L. Gao, Y. V. Ashar, N.M. Karadkhelkar, S. Yoganathan, Z.S. Chen, Ciprofloxacin enhances the chemosensitivity of cancer cells to ABCB1 substrates, Int. J. Mol. Sci. 20 (2019). https://doi.org/10.3390/ijms20020268.

[484] J. Gu, S. Luposchainsky, S. Yagi, L. Du, Y. Dong, S. Sakurai, H. Xu, Ultralong and highly axially aligned nerve guide conduits produced by electro-centrifugal spinning, Polymer (Guildf). 303 (2024) 2–12. https://doi.org/10.1016/j.polymer.2024.127110.

[485] C.B. Weldon, J.H. Tsui, S.A. Shankarappa, V.T. Nguyen, M. Ma, D.G. Anderson, D.S. Kohane, Electrospun drug-eluting sutures for local anesthesia, J. Control. Release 161 (2012) 903–909. https://doi.org/10.1016/j.jconrel.2012.05.021.

[486] S.F. Chou, K.A. Woodrow, Relationships between mechanical properties and drug release from electrospun fibers of PCL and PLGA blends, J. Mech. Behav. Biomed. Mater. 65 (2017) 724–733. https://doi.org/10.1016/j.jmbbm.2016.09.004.

[487] S. Fujita, H. Xu, Y. Dong, Y. Okahisa, Reconstruction of fibroin nanofibers (Fnfs) via electrospinning: Fabrication of poly(vinyl alcohol)/fnfs composite nanofibers from aqueous solution, Polymers (Basel). 14 (2022) 4–15. https://doi.org/10.3390/polym14010043.
[488] J. Gu, S. Luposchainsky, S. Yagi, L. Du, Y. Dong, S. Sakurai, H. Xu, Ultralong and highly axially aligned nerve guide conduits produced by electro-centrifugal spinning, Polymer (Guildf). 303 (2024) 127110. https://doi.org/10.1016/j.polymer.2024.127110.
[489] M. Mehdi, S. Hussain, B. Bin Gao, K.A. Shah, F.K. Mahar, M. Yousif, S. Hussain, F. Ahmed, Fabrication and characterization of rizatriptan loaded pullulan nanofibers as oral fast-dissolving drug system, Mater. Res. Express 8 (2021). https://doi.org/10.1088/2053-1591/abff0b.
[490] C.H. Lee, K.C. Hung, M.J. Hsieh, S.H. Chang, J.H. Juang, I.C. Hsieh, M.S. Wen, S.J. Liu, Core-shell insulin-loaded nanofibrous scaffolds for repairing diabetic wounds, Nanomedicine Nanotechnology, Biol. Med. 24 (2020) 102123. https://doi.org/10.1016/j.nano.2019.102123.
[491] Y. Liu, X. Chen, Y. Gao, Y. Liu, D. Yu, P. Liu, Electrospun Core–Sheath Nanofibers with Variable Shell Thickness for Modifying Curcumin Release to Achieve a Better Antibacterial Performance, Biomolecules 12 (2022). https://doi.org/10.3390/biom12081057.
[492] Y. Khattab, M.M. and Dahman, Functionalized bacterial cellulose nanowhiskers as long-lasting drug nanocarrier for antibiotics and anticancer drugs, (2019) 2594–2607.
[493] M. Fan, S. Chen, Y. Weng, X. Li, Y. Jiang, X. Wang, M. Bie, L. An, M. Zhang, B. Chen, G. Huang, J. Wu, M. Zhu, Q. Shi, Ciprofloxacin promotes polarization of CD86+CD206- macrophages to suppress liver cancer, Oncol. Rep. 44 (2020) 91–102. https://doi.org/10.3892/or.2020.7602.
[494] L. He, G. Wang, S. Deng, Y. Yang, S. Ding, Y.R. Guo, J. Hao, D. Wang, Tibetan tea extract exerts anti-tumor effects and potentiate paclitaxel-induced cytotoxicity and apoptosis in human hepatocellular carcinoma cells HepG2, South African J. Bot. 173 (2024) 380–387. https://doi.org/10.1016/j.sajb.2024.08.028.
[495] E. Mukhtar, V.M. Adhami, H. Mukhtar, Targeting microtubules by natural agents for cancer therapy, Mol. Cancer Ther. 13 (2014) 275–284. https://doi.org/10.1158/1535-7163.MCT-13-0791.
[496] Y.H. YANG, J.W. MAO, X.L. TAN, Research progress on the source, production, and anti-cancer mechanisms of paclitaxel, Chinese J. Nat. Med. 18 (2020) 10–17. https://doi.org/10.1016/S1875-5364(20)60032-2.
[497] R.B. Tishler, P.B. Schiff, C.R. Geard, E.J. Hall, Taxol: A novel radiation sensitizer, Int. J. Radiat. Oncol. Biol. Phys. 22 (1992) 613–617. https://doi.org/10.1016/0360-3016(92)90888-O.
[498] N.L. Elstad, K.D. Fowers, OncoGel (ReGel/paclitaxel) - Clinical applications for a novel paclitaxel delivery system, Adv. Drug Deliv. Rev. 61 (2009) 785–794. https://doi.org/10.1016/j.addr.2009.04.010.
[499] S. Ramalingam, C.P. Belani, Paclitaxel for non-small cell lung cancer, Expert Opin. Pharmacother. 5 (2004) 1771–1780. https://doi.org/10.1517/14656566.5.8.1771.
[500] K.N. Bhalla, Microtubule-targeted anticancer agents and apoptosis, Oncogene 22 (2003) 9075–9086. https://doi.org/10.1038/sj.onc.1207233.
[501] H.B. Nirmal, S.R. Bakliwal, S.P. Pawar, In-Situ gel: New trends in controlled and sustained drug delivery system, Int. J. PharmTech Res. 2 (2010) 1398–1408.
[502] S. Naderlou, M. Vahedpour, D.M. Franz, Functionalization Strategy in 2D Flexible Zn(BTTB)-MOF for Improving Storage and Release of Anticancer Drugs: A Comprehensive Computational Investigation, Organometallics (2024).

https://doi.org/10.1021/acs.organomet.3c00535.
[503] Z. Zhang, L. Mei, S.S. Feng, Paclitaxel drug delivery systems, Expert Opin. Drug Deliv. 10 (2013) 325–340. https://doi.org/10.1517/17425247.2013.752354.
[504] Y. Lu, D. Cheng, B. Niu, X. Wang, X. Wu, A. Wang, Properties of Poly (Lactic-co-Glycolic Acid) and Progress of Poly (Lactic-co-Glycolic Acid)-Based Biodegradable Materials in Biomedical Research, Pharmaceuticals 16 (2023). https://doi.org/10.3390/ph16030454.
[505] P. Wróblewska-Łuczka, J. Cabaj, W. Bąk, J. Bargieł, A. Grabarska, A. Góralczyk, J.J. Łuszczki, Additive Interactions between Betulinic Acid and Two Taxanes in In Vitro Tests against Four Human Malignant Melanoma Cell Lines, Int. J. Mol. Sci. 23 (2022). https://doi.org/10.3390/ijms23179641.
[506] J. Fischer, D. Pröfrock, N. Hort, R. Willumeit, F. Feyerabend, Reprint of: Improved cytotoxicity testing of magnesium materials, Mater. Sci. Eng. B 176 (2011) 1773–1777. https://doi.org/10.1016/j.mseb.2011.06.002.
[507] K. Das, S. Sharma, S. Kumar, S. Mahajan, S.K. Banerjee, V. Katiyar, Chitosan nanoparticles and neem essential oil functionalized pullulan/gum arabic active edible biocomposites for fresh-cut guava preservation, Int. J. Biol. Macromol. 283 (2024) 136936. https://doi.org/10.1016/j.ijbiomac.2024.136936.
[508] S. Saleki Baghban, N. Zarrabi Ahrabi, S.M. Tabaie, Evaluation of the Synergistic Effects of Ciprofloxacin and Low-Power Laser on Apoptosis, Cell Viability, and Reactive Oxygen Species Levels in Skin Cancer (A375 Cancer Cells), Gene, Cell Tissue 9 (2021) 1–6. https://doi.org/10.5812/gct.116856.
[509] T.M. Ho, A. Razzaghi, A. Ramachandran, K.S. Mikkonen, Emulsion characterization via microfluidic devices: A review on interfacial tension and stability to coalescence, Adv. Colloid Interface Sci. 299 (2022) 102541. https://doi.org/10.1016/j.cis.2021.102541.
[510] F. Calvo, J.M. Gómez, L. Ricardez-Sandoval, O. Alvarez, Integrated design of emulsified cosmetic products: A review, Chem. Eng. Res. Des. 161 (2020) 279–303. https://doi.org/10.1016/j.cherd.2020.07.014.
[511] R.S. Singh, N. Kaur, D. Singh, S.S. Purewal, J.F. Kennedy, Pullulan in pharmaceutical and cosmeceutical formulations: A review, Int. J. Biol. Macromol. 231 (2023) 123353. https://doi.org/10.1016/j.ijbiomac.2023.123353.
[512] K.K. Dubey, Insights of microbial pullulan production: A bioprocess engineer assessment, Curr. Biotechnol. 7 (2018) 262–272.
[513] B. Senizza, G. Rocchetti, K.I. Sinan, G. Zengin, M.F. Mahomoodally, J. Glamocilja, M. Sokovic, D. Lobine, O.K. Etienne, L. Lucini, The phenolic and alkaloid profiles of Solanum erianthum and Solanum torvum modulated their biological properties, Food Biosci. 41 (2021) 100974. https://doi.org/10.1016/j.fbio.2021.100974.
[514] N.K. Joseph, T. Anatole, I.B.J. Séverin, K. Fernique, G. Nathalie, A.K. Jean-Claude, Antibacterial Properties of an Aqueous Extract of Solanum torvum (Solanaceae) on a Few Multidrug Resistant Bacterial Strains to Common Antibiotics, Am. Sci. Res. J. Eng. Technol. Sci. 54 (2019) 137–146. https://www.semanticscholar.org/paper/731bcea3ead0b6f626c362ebb2f85b784b1f934c.
[515] D. Khunbutsri, N. Naimon, K. Satchasataporn, N. Inthong, S. Kaewmongkol, S. Sutjarit, C. Setthawongsin, N. Meekhanon, Antibacterial Activity of Solanum torvum Leaf Extract and Its Synergistic Effect with Oxacillin against Methicillin-Resistant Staphyloccoci Isolated from Dogs, Antibiotics 11 (2022). https://doi.org/10.3390/antibiotics11030302.
[516] N. Naimon, U. Pongchairerk, A. Suebkhampet, Phytochemical analysis and antibacterial

activity of ethanolic leaf extract of solanum torvum sw. against pathogenic bacteria, Kasetsart J. - Nat. Sci. 49 (2015) 516–523.
[517] J. Boonen, L. Veryser, L. Taevernier, N. Roche, K. Peremans, C. Burvenich, B. De Spiegeleer, Risk evaluation of impurities in topical excipients: The acetol case, J. Pharm. Anal. 4 (2014) 303–315. https://doi.org/10.1016/j.jpha.2013.12.006.
[518] A.M. Aboelenin, R. Hassan, E.S. Abdelmegeed, The effect of EDTA in combination with some antibiotics against clinical isolates of gram negative bacteria in Mansoura, Egypt, Microb. Pathog. 154 (2021) 104840. https://doi.org/10.1016/j.micpath.2021.104840.
[519] K.R. Raghupathi, R.T. Koodali, A.C. Manna, Size-dependent bacterial growth inhibition and mechanism of antibacterial activity of zinc oxide nanoparticles, Langmuir 27 (2011) 4020–4028. https://doi.org/10.1021/la104825u.
[520] B. Dréno, T. Zuberbier, C. Gelmetti, G. Gontijo, M. Marinovich, Safety review of phenoxyethanol when used as a preservative in cosmetics, J. Eur. Acad. Dermatology Venereol. 33 (2019) 15–24. https://doi.org/10.1111/jdv.15944.
[521] U. Poddębniak, P. and Kalinowska-Lis, A survey of preservatives used in cosmetic products, Appl. Sci. 14 (2024) 1581. https://doi.org/10.4324/9781315232140-14.
[522] A.H. Delcour, Outer membrane permeability and antibiotic resistance, Biochim. Biophys. Acta - Proteins Proteomics 1794 (2009) 808–816. https://doi.org/10.1016/j.bbapap.2008.11.005.
[523] B.M. Samad, Comparative Analysis of Antimicrobial and in Vitro Cytotoxic Studies in Regenerative and AntioxidantContaining Products, Am. J. Biomed. Sci. Res. 22 (2024) 693–699. https://doi.org/10.34297/ajbsr.2024.22.003004.
[524] Shanthi, D. and Saravanan, R., Evaluation of cytotoxicity of normal vero and anticancer activity of human breast cancer cell lines by aqueous unripe fruit extract of Solanum torvum, Res. J. Pharm. Technol. 14 (2021) 3504–3508.
[525] N. Zerbinati, S. Sommatis, C. Maccario, S. Di Francesco, M.C. Capillo, G. Grimaldi, R. Rauso, M. Herrera, P.L. Bencini, R. Mocchi, A practical approach for the in vitro safety and efficacy assessment of an anti-ageing cosmetic cream enriched with functional compounds, Molecules 26 (2021). https://doi.org/10.3390/molecules26247592.
[526] J. Deng, E.Q. Zhu, G.F. Xu, N. Naik, V. Murugadoss, M.G. Ma, Z. Guo, Z.J. Shi, Overview of renewable polysaccharide-based composites for biodegradable food packaging applications, Green Chem. 24 (2022) 480–492. https://doi.org/10.1039/d1gc03898b.
[527] S.S. Rout, K.C. Pradhan, A review on antimicrobial nano-based edible packaging: Sustainable applications and emerging trends in food industry, Food Control 163 (2024) 110470. https://doi.org/10.1016/j.foodcont.2024.110470.
[528] A. Rashid, A. Qayum, Q. Liang, L. Kang, J.N. Ekumah, X. Han, X. Ren, H. Ma, Exploring the potential of pullulan-based films and coatings for effective food preservation: A comprehensive analysis of properties, activation strategies and applications, Int. J. Biol. Macromol. 260 (2024) 129479. https://doi.org/10.1016/j.ijbiomac.2024.129479.
[529] T. Ghosh, R. Priyadarshi, C. Krebs de Souza, B.L. Angioletti, J.W. Rhim, Advances in pullulan utilization for sustainable applications in food packaging and preservation: A mini-review, Trends Food Sci. Technol. 125 (2022) 43–53. https://doi.org/10.1016/j.tifs.2022.05.001.
[530] G. Mugnaini, M. Bonini, L. Gentile, O. Panza, M.A. Del Nobile, A. Conte, R. Esposito, G. D'Errico, F. Moccia, L. Panzella, Effect of design and molecular interactions on the food preserving properties of alginate/pullulan edible films loaded with grape pomace extract, J. Food Eng. 361 (2024) 111716.

https://doi.org/10.1016/j.jfoodeng.2023.111716.
[531] L. Jiang, C. Wang, F. Zhao, S. Li, D. Sun, Q. Ma, Z. Yu, B. Zhang, Y. Liu, W. Jiang, Development of electrospun nanofiber films based on pullulan/polyvinyl alcohol incorporating bayberry pomace anthocyanin extract for aquatic products freshness monitoring, Food Biosci. 58 (2024) 103717. https://doi.org/10.1016/j.fbio.2024.103717.
[532] X. Zhang, H. Sun, S. Song, Y. Li, X. Zhang, W. Zhang, Preparation and characterization of polyvinyl alcohol/pullulan/ZnO-Nps composite film and its effect on the postharvest quality of Allium mongolicum Regel, Int. J. Biol. Macromol. 279 (2024). https://doi.org/10.1016/j.ijbiomac.2024.135380.
[533] Z. Zeng, Y.J. Yang, Q. Tu, Y.Y. Jian, D.M. Xie, T. Bai, S.S. Li, Y.T. Liu, C. Li, C.X. Wang, A.P. Liu, Preparation and characterization of carboxymethyl chitosan/pullulan composite film incorporated with eugenol and its application in the preservation of chilled meat, Meat Sci. 198 (2023) 109085. https://doi.org/10.1016/j.meatsci.2022.109085.
[534] W. Chen, H. Liu, Y. Chai, C. Guo, C. Luo, D. Chen, X. Cheng, F. Wang, C. Huang, Chitosan–pullulan films enriched with Artemisia annua essential oil: Characterization and application in grape preservation, Int. J. Biol. Macromol. 243 (2023) 125216. https://doi.org/10.1016/j.ijbiomac.2023.125216.
[535] S.V. Thangavelu, M. and Kulandhaivelu, Development and Characterization of Pullulan-Carboxymethyl Cellulose Blend Film for Packaging Applications, Int. J. Polym. Sci. 1 (2022) 9649726.
[536] J.L. López Terán, E. V. Cabrera, J. Poveda, J. Araque, M.I. Beltrán, Improving the behavior of thermoplastic starch with the addition of gum Arabic: Antibacterial, mechanical properties and biodegradability, Heliyon 10 (2024) 1–12. https://doi.org/10.1016/j.heliyon.2024.e31856.
[537] D. Hassani, I.K. Sani, S. Pirsa, Nanocomposite Film of Potato Starch and Gum Arabic Containing Boron Oxide Nanoparticles and Anise Hyssop (Agastache foeniculum) Essential Oil: Investigation of Physicochemical and Antimicrobial Properties, J. Polym. Environ. 32 (2024) 1972–1983. https://doi.org/10.1007/s10924-023-03114-3.
[538] M. Seididamyeh, S.M.O. Mantilla, M.E. Netzel, R. Mereddy, Y. Sultanbawa, Gum Arabic edible coating embedded aqueous plant extracts: Interactive effects of partaking components and its effectiveness on cold storage of fresh-cut capsicum, Food Control 159 (2024) 110267. https://doi.org/10.1016/j.foodcont.2023.110267.
[539] K. Bajaj, A. Kumar, P.P.S. Gill, S.K. Jawandha, R. Arora, Ameliorative effect of gum Arabic and essential oil coatings on postharvest preservation of Kinnow mandarin (Citrus reticulata. Blanco), J. Food Meas. Charact. 18 (2024) 7884–7893. https://doi.org/10.1007/s11694-024-02772-8.
[540] C. Peiyao, H. Shuhao, L. Yinxin, L. Cheng, Z. Xinyi, L. Xingmeng, S. Cui, S. Chongde, L. Huang, Preparation and characterization of Chitosan based edible coating containing vanillin/HPβCD inclusion complex and its application in chicken preservation, Food Control 166 (2024) 110683. https://doi.org/10.1016/j.foodcont.2024.110683.
[541] M. Singh, R. Saroj, D. Kaur, Optimized chitosan edible coating for guava and its characterization, Meas. Food 14 (2024) 100145. https://doi.org/10.1016/j.meafoo.2024.100145.
[542] R. Elahi, A. Jamshidi, A.A. Fallah, Effect of active composite coating based on nanochitosan-whey protein isolate on the microbial safety of chilled rainbow trout fillets packed with oxygen absorber, Int. J. Biol. Macromol. 277 (2024) 133756. https://doi.org/10.1016/j.ijbiomac.2024.133756.
[543] P. Dasgupta, J. Mitra, Feasibility Study of Nanochitosan Solution as a Potential Coating

for Shelf Life Extension of Apples, J. Packag. Technol. Res. 8 (2024) 139–151. https://doi.org/10.1007/s41783-024-00170-5.
[544] N.A. Al Zahrani, M.M. Gad, A.M. Fikry, A. Ezzat Ahmed, K.A. El-Tarabily, H.A. Elakkad, I. Eid Elesawi, Efficacy of chitosan nanoparticles and wax coatings on maintaining post-harvest quality of "Murcott" mandarins, Saudi J. Biol. Sci. 31 (2024) 103894. https://doi.org/10.1016/j.sjbs.2023.103894.
[545] S. Sheerzad, R. Khorrami, A. Khanjari, H. Gandomi, A.A. Basti, F. Khansavar, Improving chicken meat shelf-life: Coating with whey protein isolate, nanochitosan, bacterial nanocellulose, and cinnamon essential oil, Lwt 197 (2024) 115912. https://doi.org/10.1016/j.lwt.2024.115912.
[546] E. Ghafari, P. Ariaii, R. Bagheri, M. Esmaeili, Investigating the effect of nanochitosan-Iranian tragacanth gum composite film along with Eryngium campestre essential oil on the shelf life of goat meat, J. Food Meas. Charact. 18 (2024) 1543–1558. https://doi.org/10.1007/s11694-023-02202-1.
[547] S. Kumar, N. Singh, L.S. Devi, S. Kumar, M. Kamle, P. Kumar, A. Mukherjee, Neem oil and its nanoemulsion in sustainable food preservation and packaging: Current status and future prospects, J. Agric. Food Res. 7 (2022) 100254. https://doi.org/10.1016/j.jafr.2021.100254.
[548] Z. Liu, S. Wang, H. Liang, J. Zhou, M. Zong, Y. Cao, W. Lou, A review of advancements in chitosan-essential oil composite films: Better and sustainable food preservation with biodegradable packaging, Int. J. Biol. Macromol. 274 (2024) 133242. https://doi.org/10.1016/j.ijbiomac.2024.133242.
[549] I. Malarselvi Rajkumar, D. Asaithambi, R.R. Chidambaram, P. Rajkumar, Double Schiff bases derivatives of chitosan by selective C-6 and C-2 oxidation mediated by 5-fluorosalicylaldehyde aniline by TG-GC-MS and TG-FTIR analysis, Synth. Commun. 50 (2020) 2617–2628. https://doi.org/10.1080/00397911.2020.1780614.
[550] S. Li, J. Yi, X. Yu, Z. Wang, L. Wang, Preparation and characterization of pullulan derivative/chitosan composite film for potential antimicrobial applications, Int. J. Biol. Macromol. 148 (2020) 258–264. https://doi.org/10.1016/j.ijbiomac.2020.01.080.
[551] E. Alehosseini, H. Shahiri Tabarestani, M.S. Kharazmi, S.M. Jafari, Physicochemical, Thermal, and Morphological Properties of Chitosan Nanoparticles Produced by Ionic Gelation, Foods 11 (2022). https://doi.org/10.3390/foods11233841.
[552] S.A. Kahdestani, M.H. Shahriari, M. Abdouss, Synthesis and characterization of chitosan nanoparticles containing teicoplanin using sol–gel, Polym. Bull. 78 (2021) 1133–1148. https://doi.org/10.1007/s00289-020-03134-2.
[553] S. Bhatia, Y.A. Shah, A. Al-Harrasi, M. Jawad, E. Koca, L.Y. Aydemir, Novel applications of black pepper essential oil as an antioxidant agent in sodium caseinate and chitosan based active edible films, Int. J. Biol. Macromol. 254 (2024) 128045. https://doi.org/10.1016/j.ijbiomac.2023.128045.
[554] S. Bhatia, A. Al-Harrasi, Y.A. Shah, A.N. Saif Alrasbi, M. Jawad, E. Koca, L.Y. Aydemir, J.A. Alamoudi, Y. Almoshari, S. Mohan, Structural, mechanical, barrier and antioxidant properties of pectin and xanthan gum edible films loaded with grapefruit essential oil, Heliyon 10 (2024) e25501. https://doi.org/10.1016/j.heliyon.2024.e25501.
[555] D. Merino, A. Athanassiou, Biodegradable and Active Mulch Films: Hydrolyzed Lemon Peel Waste and Low Methoxyl Pectin Blends with Incorporated Biochar and Neem Essential Oil, ACS Sustain. Chem. Eng. 10 (2022) 10789–10802. https://doi.org/10.1021/acssuschemeng.2c01539.
[556] Y. Zhou, X. Wu, J. Chen, J. He, Effects of cinnamon essential oil on the physical, mechanical, structural and thermal properties of cassava starch-based edible films, Int. J. Biol. Macromol. 184 (2021) 574–583.

https://doi.org/10.1016/j.ijbiomac.2021.06.067.
[557] X. Li, Z.C. Tu, X.M. Sha, Y.H. Ye, Z.Y. Li, Flavor, antimicrobial activity and physical properties of gelatin film incorporated with of ginger essential oil, J. Food Sci. Technol. 59 (2022) 815–824. https://doi.org/10.1007/s13197-021-05080-x.
[558] K. Han, Y. Liu, Y. Liu, X. Huang, L. Sheng, Characterization and film-forming mechanism of egg white/pullulan blend film, Food Chem. 315 (2020) 126201. https://doi.org/10.1016/j.foodchem.2020.126201.
[559] P. Das, N. Sharma, A. Puzari, D.K. Kakati, N. Devi, Synthesis and characterization of neem (Azadirachta indica) seed oil-based alkyd resins for efficient anticorrosive coating application, Polym. Bull. 78 (2021) 457–479. https://doi.org/10.1007/s00289-020-03120-8.
[560] N. Haghighatpanah, M. Omar-Aziz, M. Gharaghani, F. Khodaiyan, S.S. Hosseini, J.F. Kennedy, Effect of mung bean protein isolate/pullulan films containing marjoram (Origanum majorana L.) essential oil on chemical and microbial properties of minced beef meat, Int. J. Biol. Macromol. 201 (2022) 318–329. https://doi.org/10.1016/j.ijbiomac.2022.01.023.
[561] Z. Najafi, C.J.F. Kahn, F. Bildik, E. Arab-Tehrany, N. Şahin-Yeşilçubuk, Pullulan films loading saffron extract encapsulated in nanoliposomes; preparation and characterization, Int. J. Biol. Macromol. 188 (2021) 62–71. https://doi.org/10.1016/j.ijbiomac.2021.07.175.
[562] Z. Zhao, X. Xiong, H. Zhou, Q. Xiao, Effect of lactoferrin on physicochemical properties and microstructure of pullulan-based edible films, J. Sci. Food Agric. 99 (2019) 4150–4157. https://doi.org/10.1002/jsfa.9645.
[563] S. Sanuja, A. Agalya, M.J. Umapathy, Synthesis and characterization of zinc oxide-neem oil-chitosan bionanocomposite for food packaging application, Int. J. Biol. Macromol. 74 (2015) 76–84. https://doi.org/10.1016/j.ijbiomac.2014.11.036.
[564] P.C. Martins, D.C. Bagatini, V.G. Martins, Oregano essential oil addition in rice starch films and its effects on the chilled fish storage, J. Food Sci. Technol. 58 (2021) 1562–1573. https://doi.org/10.1007/s13197-020-04668-z.
[565] V.P. Romani, C. Prentice-Hernández, V.G. Martins, Active and sustainable materials from rice starch, fish protein and oregano essential oil for food packaging, Ind. Crops Prod. 97 (2017) 268–274. https://doi.org/10.1016/j.indcrop.2016.12.026.
[566] M.V. Lorevice, C.G. Otoni, M.R. de Moura, L.H.C. Mattoso, Chitosan nanoparticles on the improvement of thermal, barrier, and mechanical properties of high- and low-methyl pectin films, Food Hydrocoll. 52 (2016) 732–740. https://doi.org/10.1016/j.foodhyd.2015.08.003.
[567] R. Priyadarshi, S.M. Kim, J.W. Rhim, Pectin/pullulan blend films for food packaging: Effect of blending ratio, Food Chem. 347 (2021) 129022. https://doi.org/10.1016/j.foodchem.2021.129022.
[568] Â. Luís, A. Ramos, F. Domingues, Pullulan–apple fiber biocomposite films: Optical, mechanical, barrier, antioxidant and antibacterial properties, Polymers (Basel). 13 (2021) 1–15. https://doi.org/10.3390/polym13060870.
[569] Z. Tahsiri, H. Mirzaei, S.M.H. Hosseini, M. Khalesi, Gum arabic improves the mechanical properties of wild almond protein film, Carbohydr. Polym. 222 (2019) 114994. https://doi.org/10.1016/j.carbpol.2019.114994.
[570] N. Roshandel-hesari, M. Mokaber-Esfahani, A. Taleghani, R. Akbari, Investigation of physicochemical properties, antimicrobial and antioxidant activity of edible films based on chitosan/casein containing Origanum vulgare L. essential oil and its effect on quality maintenance of cherry tomato, Food Chem. 396 (2022) 133650. https://doi.org/10.1016/j.foodchem.2022.133650.

[571] Z. An, M. Yuan, X. Xu, Z. Huang, L. Zhu, Z. Cai, Y. Shen, Active pullulan-based coatings incorporated with Auricularia auricular extracts for preserving potato fresh-cuts, Food Sci. Biotechnol. 33 (2024) 1147–1161. https://doi.org/10.1007/s10068-023-01420-z.
[572] Q. Zhou, S. Huang, L. Zou, D. Ren, X. Wu, D. Xu, Application of hydroxypropyl methylcellulose to improve the wettability of chitosan coating and its preservation performance on tangerine fruits, Int. J. Biol. Macromol. 263 (2024) 130539. https://doi.org/10.1016/j.ijbiomac.2024.130539.
[573] H. Singh, J.K. Bhasin, K.K. Dash, R. Shams, A.M. shaikh, K. Béla, Effect of chitosan based edible coating in management of post harvest losses in Papaya: A comprehensive review, Appl. Food Res. 4 (2024). https://doi.org/10.1016/j.afres.2024.100456.
[574] N. Ehyaeirad, N. Babolanimogadam, M. Dadkhah, L. Rezaie Shirmard, Polylactic acid films incorporated with nanochitosan, nanocellulose, and Ajwain essential oil: Synthesis, characterizations, with in-vitro and in-vivo antimicrobial properties for infected wound healing, Carbohydr. Polym. Technol. Appl. 7 (2024) 100425. https://doi.org/10.1016/j.carpta.2024.100425.
[575] F.M.R. Mendonça, A.E. Polloni, A. Junges, R.S. da Silva, A.F. Rubira, G.R. Borges, C. Dariva, E. Franceschi, Encapsulation of neem (Azadirachta indica) seed oil in poly(3-hydroxybutyrate-co-3-hydroxyvalerate) by SFEE technique, J. Supercrit. Fluids 152 (2019). https://doi.org/10.1016/j.supflu.2019.104556.
[576] P. de Castro e Silva, A.C.S. de Oliveira, L.A.S. Pereira, M. Valquíria, G.R. Carvalho, K.W.E. Miranda, J.M. Marconcini, J.E. Oliveira, Development of bionanocomposites of pectin and nanoemulsions of carnauba wax and neem oil pectin/carnauba wax/neem oil composites, Polym. Compos. 41 (2020) 858–870. https://doi.org/10.1002/pc.25416.
[577] P.S.X. Yap, K. Yusoff, S.H.E. Lim, C.M. Chong, K.S. Lai, Membrane disruption properties of essential oils-a double-edged sword?, Processes 9 (2021) 1–11. https://doi.org/10.3390/pr9040595.
[578] Z. Mahcene, A. Khelil, S. Hasni, P.K. Akman, F. Bozkurt, K. Birech, M.B. Goudjil, F. Tornuk, Development and characterization of sodium alginate based active edible films incorporated with essential oils of some medicinal plants, Int. J. Biol. Macromol. 145 (2020) 124–132. https://doi.org/10.1016/j.ijbiomac.2019.12.093.
[579] S. Achutha, S. Kumari Nisha, S. Barakala Pushpa, S. Andrews, Antimicrobial polyvinyl alcohol/neem oil flexible film for food packaging applications, Mater. Today Proc. (2023). https://doi.org/10.1016/j.matpr.2023.07.061.
[580] H.H. Musa, A.A. Ahmed, T.H. Musa, Chemistry, Biological, and Pharmacological Properties of Gum Arabic, Ref. Ser. Phytochem. (2019) 797–814. https://doi.org/10.1007/978-3-319-78030-6_11.
[581] G. Ghoshal, S. Sandal, Neem essential oil: Extraction, characterization, and encapsulation, Food Chem. Adv. 4 (2024) 100702. https://doi.org/10.1016/j.focha.2024.100702.
[582] S. Roy, R. Priyadarshi, Composite Films Reinforced with ZnO Nanoparticles and Propolis for Meat Packaging Applications, Foods 10 (2021).
[583] S. Roy, J.W. Rhim, Pullulan/Agar-Based Functional Film Containing Eucalyptus Essential Oil and Rutin, Coatings 13 (2023). https://doi.org/10.3390/coatings13020460.
[584] M. Zheng, Y. Zhu, Y. Zhuang, K.B. Tan, J. Chen, Effects of grape seed extract on the properties of pullulan polysaccharide/xanthan gum active films for apple preservation, Int. J. Biol. Macromol. 241 (2023) 124617. https://doi.org/10.1016/j.ijbiomac.2023.124617.
[585] M. Sharma, C.S. Saini, Postharvest shelf-life extension of fresh-cut guavas (Psidium guajava) using flaxseed protein-based composite coatings, Food Hydrocoll. Heal. 1

(2021) 100015. https://doi.org/10.1016/j.fhfh.2021.100015.
[586] J. Yu, M. Wang, Z. Li, F. Tchuenbou-Magaia, A.A. Wani, P. Zhu, T. Fadiji, Y. Liu, Preserving freshness:Innovations for fresh-eating fruit distribution and damage prevention – A review, Food Packag. Shelf Life 44 (2024) 101323. https://doi.org/10.1016/j.fpsl.2024.101323.
[587] K. Chen, R. Tian, J. Jiang, M. Xiao, K. Wu, Y. Kuang, P. Deng, X. Zhao, F. Jiang, Moisture loss inhibition with biopolymer films for preservation of fruits and vegetables: A review, Int. J. Biol. Macromol. 263 (2024) 130337. https://doi.org/10.1016/j.ijbiomac.2024.130337.
[588] W. Zhang, M. Hadidi, A.C. Karaca, S. Hedayati, M. Tarahi, E. Assadpour, S.M. Jafari, Chitosan-grafted phenolic acids as an efficient biopolymer for food packaging films/coatings, Carbohydr. Polym. 314 (2023) 120901. https://doi.org/10.1016/j.carbpol.2023.120901.
[589] S. Ali, S. Ishtiaq, A. Nawaz, S. Naz, S. Ejaz, M.W. Haider, A.A. Shah, M.M. Ali, S. Javad, Layer by layer application of chitosan and carboxymethyl cellulose coatings delays ripening of mango fruit by suppressing cell wall polysaccharides disassembly, Int. J. Biol. Macromol. 256 (2024) 128429. https://doi.org/10.1016/j.ijbiomac.2023.128429.
[590] A.B. De Aquino, A.F. Blank, L.C.L. De Aquino Santana, Impact of edible chitosan-cassava starch coatings enriched with Lippia gracilis Schauer genotype mixtures on the shelf life of guavas (Psidium guajava L.) during storage at room temperature, Food Chem. 171 (2015) 108–116. https://doi.org/10.1016/j.foodchem.2014.08.077.
[591] S.B. Murmu, H.N. Mishra, The effect of edible coating based on Arabic gum, sodium caseinate and essential oil of cinnamon and lemon grass on guava, Food Chem. 245 (2018) 820–828. https://doi.org/10.1016/j.foodchem.2017.11.104.
[592] W. Hu, W. Sarengaowa, Y. Guan, K. Feng, Biosynthesis of Phenolic Compounds and Antioxidant Activity in Fresh-Cut Fruits and Vegetables, Front. Microbiol. 13 (2022) 1–8. https://doi.org/10.3389/fmicb.2022.906069.
[593] Z. Wang, Q. Zhang, D. Bukvicki, Y. Xu, Y. Peng, F. Li, Q. Zhang, S. Liu, J. Yan, S. Lin, W. Qin, Konjac glucomannan/microcapsule of thymol edible coating reduces okra pericarp browning by regulating antioxidant activity and ROS synthesis, Int. J. Biol. Macromol. 276 (2024) 1–10. https://doi.org/10.1016/j.ijbiomac.2024.133641.
[594] E.A. Luna-zapién, R. Minjares-fuentes, E. Sierra-campos, J.E. Marszalek, S.I. Barraza-guerrero, J.A. Meza-velázquez, Conservation of commercial quality and bioactive compounds of guava pieces by application of an alginate- alginate - acemannan coating, Not. Bot. Horti Agrobot. Cluj-Napoca 51 (2023) 1–19. https://doi.org/10.15835/nbha51113080.
[595] A. Floegel, D.O. Kim, S.J. Chung, S.I. Koo, O.K. Chun, Comparison of ABTS/DPPH assays to measure antioxidant capacity in popular antioxidant-rich US foods, J. Food Compos. Anal. 24 (2011) 1043–1048. https://doi.org/10.1016/j.jfca.2011.01.008.

RESEARCH OUTPUT

List of publications/patent

Thesis-related research articles

- **Das, K.,** Sharma, S., Kumar, S., Mahajan, S., Banerjee, S.K. and Katiyar, V., 2024. Chitosan nanoparticles and neem essential oil functionalized pullulan/gum arabic active edible biocomposites for fresh-cut guava preservation. International Journal of Biological Macromolecules, 283, p.136936. ***(Published)***
- **Das, K.,** Tiwari, V., Prasannavenkadesan, V., Banerjee, S.K. and Katiyar, V., 2025. *In vitro* biocompatibility and wound healing potential of bilayered scaffold with electrospun gentamicin-loaded pullulan/PVA/Gum arabic nanofibers and solvent-casted PLA. Journal of Applied Polymer Science, 142(15), p.e56731. ***(Published)***
- **Das, K.,** Xu, H., Gu, J., Sakurai, S., Tiwari, V., Banerjee, S.K. and Katiyar, V., 2025. Coaxially Electrocentrifugally Spun Ciprofloxacin/Paclitaxel-Loaded Pullulan/PLGA Core/Sheath Nanofibers and Their *In Vitro* Cytotoxic Efficacy Toward Melanoma Cells. Journal of Applied Polymer Science, 142(16), p.e56759. ***(Published)***
- **Das, K.** and Katiyar, V. Shake-Flask Optimization of Pullulan Production by *Aureobasidium pullulans* NCIM 1049 using Sugarcane Jaggery as Substrate. ***(Under preparation)***

Patent filed:

- Katiyar, V., **Das, K.,** and Ranjan, R., 2025. Biopolymer based Cosmetic Skin Cream Formulation. (Patent application no.: 202531097797).

Other contributory publications

Research articles

- Kumar, S., Shukla, P., **Das, K.** and Katiyar, V., 2025. Chitosan/water caltrop pericarp extract reinforced active edible film and its efficacy as strawberry coating for prolonging shelf life. International Journal of Biological Macromolecules, 307, p.142115. ***(Published)***

- Bhattacharjee, S.K., Mondal, K., Singh, A., Dhal, M.K., **Das, K.,** Gupta, R. and Katiyar, V., 2025. Impact of nano-silica on thermal, mechanical, and rheological properties of melt-extruded PLA-based nanocomposites. International Journal of Biological Macromolecules, p.146077. ***(Published)***
- Roy, A., Kumar, S., Das, B., **Das, K.,** Kumar, A., Ebihara, A., Wang, C.T. and Katiyar, V., 2025. Eco-Engineered N-Methyl-2-pyrrolidone-Free Antibacterial Chitosan/Cellulose Acetate membrane Separator for Real Hospital Wastewater-fed Microbial Fuel Cells. Next Research, p.100867. ***(Published)***
- Roy, A., Kumar, S., **Das, K.,** Kumar, A., Ebihara, A., Wang, C. T., Katiyar, V. (2026). Next-Generation Per and Poly-Fluoroalkyl-Free Graphene Oxide Modified Cellulose Ether Charge Separator for Antibiotic Micropollutant Removal and Energy Recovery in Hospital Wastewater-Fed Microbial Fuel Cell. Journal of Polymer Science. ***(Published)***
- Bhattacharjee, S.K., Chakraborty, G., Mondal, K., Boruah, P., Singh, A., **Das, K.,** Gupta, R. and Katiyar, V., 2025. Development of poly (lactic acid) (PLA) based bio-nanocomposite reinforced with cellulose nanocrystals (CNC) for sustainable packaging: Thermal, mechanical, rheological properties evaluation. ***(Under preparation)***

Book chapters

- Bora, S., **Das, K.,** Saini, P., Katiyar, V. and Ghosh, T., 2025. Application of nanoemulsion for improving quality and safety of fruits and vegetables. In Advancements in Nanotechnology for Food and Packaging (pp. 53-78). Elsevier. ***(Published)***
- Bora, S., Revathi, V., **Das, K.,** Katiyar, V. and Ghosh, T., 2025. Nanotechnology in functional food developments. In Advancements in Nanotechnology for Food and Packaging (pp. 133-157). Elsevier. ***(Published)***
- Afzia, N., **Das, K.,** Revathi, V., Katiyar, V. and Ghosh, T., 2025. Nanocomposites in food packaging. In Advancements in Nanotechnology for Food and Packaging (pp. 191-228). Elsevier. ***(Published)***

Achievements

- Qualified Graduate Aptitude Test in Engineering (GATE) 2018 in Biotechnology.

- Received Ministry of Human Resource Development, India (MHRD) scholarship during Ph.D., July, 2020 – July 2025.
- Received the Japan Student Services Organization (JASSO) scholarship for Global Human Resource Development Program, 2023 Short-Term Student Exchange Program at Kyoto Institute of Technology, Japan, during April 2023 – September 2023.

List of conferences attended

Poster presentation

- **Kuhelika Das,** Vimal Katiyar, "Studies on Production of Pullulan and its Industrial Applications", North-East Research Conclave (NERC) 2022, 20th – 22nd May 2022, IIT Guwahati, India.
- **Kuhelika Das,** Vimal Katiyar, "Pullulan: A Comprehensive Review on its Properties, Production and Multifaceted Applications", SPSI-MACRO 2023, 10th – 13th December, 2023, IIT Guwahati, India.
- **Kuhelika Das,** Vimal Katiyar, "Chitosan Nanoparticles and Neem Essential Oil Functionalised Pullulan/Gum Arabic Biocomposites for Guava Preservation", Japan-NER Sustainable Technologies Co-operation Symposium 2025, 3rd – 5th March 2025, IIT Guwahati, India.

Oral presentation

- **Kuhelika Das,** Jincheng Gu, Huaizhong Xu, Shinichi Sakurai, Vimal Katiyar, "Coaxially Electro-Centrifugally Spun Core-Sheath Nanofibers With Dual Drug Loading For Use in Cancer Treatment", SPSI-MACRO 2023, 10th – 13th December, 2023, IIT Guwahati, India.
- **Kuhelika Das,** Vimal Katiyar, "Dual-layered Antibacterial Scaffold with Zero-Order Release for Critical Wound Healing", IIChE-CHEMCON 2023, 27th – 30th December, 2023, Heritage Institute of Technology, Kolkata, India.

Outreach activities

- Organizing Committee Member and Student Coordinator of North-East Research Conclave (May 2022).
- Organizing Committee Member of Indo-Taiwan International Exchange Workshop (September 2022).

- Organizing Committee Member of Y20 Youth Inception Meet as a part of the G20 Presidency of India (February 2023).
- Organizing Committee Member of SPSI-MACRO (December 2023).